AD NUMBER

ADB025970

NEW LIMITATION CHANGE

TO

Approved for public release, distribution unlimited

FROM

Distribution authorized to U.S. Gov't. agencies only; Test and Evaluation; JAN 1978. Other requests shall be referred to Rome Air Development Center, ATTN: OCTS, Griffiss AFB, Ny 13441.

AUTHORITY
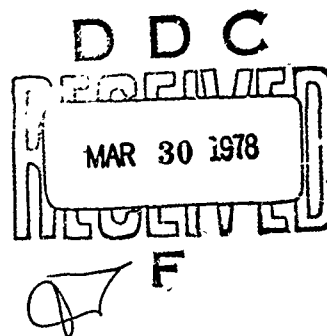
RADC ltr dtd 18 Jun 1978

RADC-TR-78-14
Final Technical Report
January 1978

MONOPULSE TRACKING WITH ADAPTIVE ARRAYS

George G. Rassweiler
Eduardo H. Villaseca
Samuel L. Earp
Carl E. Giesler
Charles L. Zahm

Harris Corporation

D D C

MAR 30 1978

F

This report contains a large percentage of machine-produced copy which is not of the highest printing quality but because of economical consideration, it was determined in the best interest of the government that they be used in this publication.

RADC-TR-78-14 has been reviewed and is approved for publication.

APPROVED: *Vincent Vannicola*

VINCENT VANNICOLA
Project Engineer

APPROVED: *Joseph L. Ryerson*

JOSEPH L. RYERSON
Technical Director
Surveillance Division

FOR THE COMMANDER: *John P. Huss*

JOHN P. HUSS
Acting Chief, Plans Office

REPORT DOCUMENTATION PAGE		READ INSTRUCTIONS BEFORE COMPLETING FORM
1. REPORT NUMBER RADC-TR-78-14	2. GOVT ACCESSION NO.	3. RECIPIENT'S CATALOG NUMBER
4. TITLE (and Subtitle) MONOPULSE TRACKING WITH ADAPTIVE ARRAYS		5. TYPE OF REPORT & PERIOD COVERED Final Technical Report 14 Jun 76 – 14 Jun 77
		6. PERFORMING ORG. REPORT NUMBER N/A
7. AUTHOR(s) George G. Rassweiler, Carl E. Giesler Eduardo H. Villaseca, Charles L. Zahm Samuel L. Earp		8. CONTRACT OR GRANT NUMBER(s) F30602-76-C-0292
9. PERFORMING ORGANIZATION NAME AND ADDRESS Harris Electronic Systems Division P.O. Box 37 Melbourne FL 32901		10. PROGRAM ELEMENT, PROJECT, TASK AREA & WORK UNIT NUMBERS 62702F 45060495
11. CONTROLLING OFFICE NAME AND ADDRESS Rome Air Development Center (OCTS) Griffiss AFB NY 13441		12. REPORT DATE January 1978
		13. NUMBER OF PAGES 229
14. MONITORING AGENCY NAME & ADDRESS(if different from Controlling Office) Same		15. SECURITY CLASS. (of this report) UNCLASSIFIED
		15a. DECLASSIFICATION/DOWNGRADING SCHEDULE N/A

16. DISTRIBUTION STATEMENT (of this Report)

Distribution limited to U.S. Government agencies only; test and
evaluation; January 1978. Other requests for this document must
be referred to RADC (OCTS), Griffiss AFB NY 13441.

17. DISTRIBUTION STATEMENT (of the abstract entered in Block 20, if different from Report)

Same

18. SUPPLEMENTARY NOTES

RADC Project Engineer: Vincent C. Vannicola (OCTS)

19. KEY WORDS (Continue on reverse side if necessary and identify by block number)

Monopulse Tracking
Adaptive Arrays
Radar Arrays

20. ABSTRACT (Continue on reverse side if necessary and identify by block number)

    This technical report assesses the effectiveness of monopulse tracking
while cancelling jammers in the sidelobes using practical null steering
techniques.
    In monopulse tracking systems using adaptive arrays, two adaptive
receiving beams with nulls on the sidelobe jammers are formed: a sum beam
(Σ) and a difference beam (Δ). In this report, antenna pattern decomposition
of the sum and difference beams allows first-order estimates of the boresight

shift error due to null steering when the jammer locations and the adaptive weights are known. Measurements on a small fully adaptive amplitude comparison monopulse array are presented and compared with computer simulations including both random construction errors and null steering errors. Computer simulation results are also presented for larger arrays.

In most cases, random construction errors in the monopulse tracking array cause more monopulse boresight shift error than will be caused by optimal null steering of the sidelobes.

TABLE OF CONTENTS

TABLE OF CONTENTS (Cont'd)

Paragraph	Title	Page

APPENDICES

iv

LIST OF ILLUSTRATIONS

LIST OF ILLUSTRATIONS (Cont'd)

LIST OF ILLUSTRATIONS (Cont'd)

LIST OF ILLUSTRATIONS (Cont'd)

LIST OF ILLUSTRATIONS (Cont'd)

LIST OF ILLUSTRATIONS (Cont'd)

LIST OF ILLUSTRATIONS (Cont'd)

LIST OF ILLUSTRATIONS (Cont'd)

LIST OF TABLES

EVALUATION

This contractual effort provides insight to target angle tracking performance for arrays that are null tracking noise sources through adaptive means. The work which included both computer simulations and experimental evaluations is of general value for all angle tracking radar systems which contain adaptive aperture capability. It supports RADC Technology Plan TPO R4B by providing a technical basis for adaptive radar operation in a hostile electromagnetic environment. The results derived herein will serve as back-up information and design criteria for tracking radars in jammer environment.

VINCENT C. VANNICOLA
Project Engineer

SECTION I

INTRODUCTION

1.1   Statement of the Problem

The problem addressed in this study is to determine the effectiveness of monopulse tracking while cancelling jammers in the sidelobes using practical null steering techniques. The areas studied to determine whether or not radar tracking accuracy improves with adaptive processing include theoretical analysis of optimum adaptive arrays, but emphasize practical, though perhaps non-optimum, null steering techniques. In the study of practical null steering techniques the effects of typical array construction errors and the effects of null steering errors have been included.

1.2   Background

Adaptive sidelobe cancellers (references 1 and 2), and adaptive optimum null steering antennas (references 3, 4, and 5) have obtained significant anti-jam protection by steering nulls on jammers. The antenna pattern distortions due to the null steering have been calculated for several array configurations. For the most part, null steering techniques have been applied to single beams, rather than, to monopulse beams. However, recently, a theory was developed by Technology Services Corporation (reference 6) for obtaining an optimum maximum likelihood angular error estimate in an adaptive monopulse array. It was shown that the solution to the maximum likelihood estimate allowed a decomposition into a sum and a difference beam.

The practicality of this and other null steering techniques needed to be fully explored and a comparison of null steering effects with normal construction error effects had to be made.

SECTION II

SUMMARY OF RESULTS

a. Measurements on a fully adaptive amplitude comparison monopulse array with phase-only weights typically recorded the following boresight shift data, as a function of the location of the jammer.

Jammer Location	Boresight Shift
● First sidelobe (-10 dB)	0.036 Beamwidth
● Second sidelobe (-11 dB)	0.015 Beamwidth
● Lower and further-out sidelobes	<0.01 Beamwidth

b. Computer simulations with the same adaptive array, including both random construction errors and null steering boresight errors, predicted the same magnitude of boresight shift as was measured. This good agreement allows us to extend the simulation computer program to larger arrays than the 8-element array measured. For example, Figure 2-1 shows the computer simulation results with and without adaptive processing for larger arrays having random construction errors.

c. A comparison of boresight shift errors was made assuming no random construction errors, for the following array configurations:

● Optimum, complex weighted arrays

● Optimum, phase only weighted arrays

● Omni sidelobe level canceller

The results are given in Table 2-1 for the jammer

2
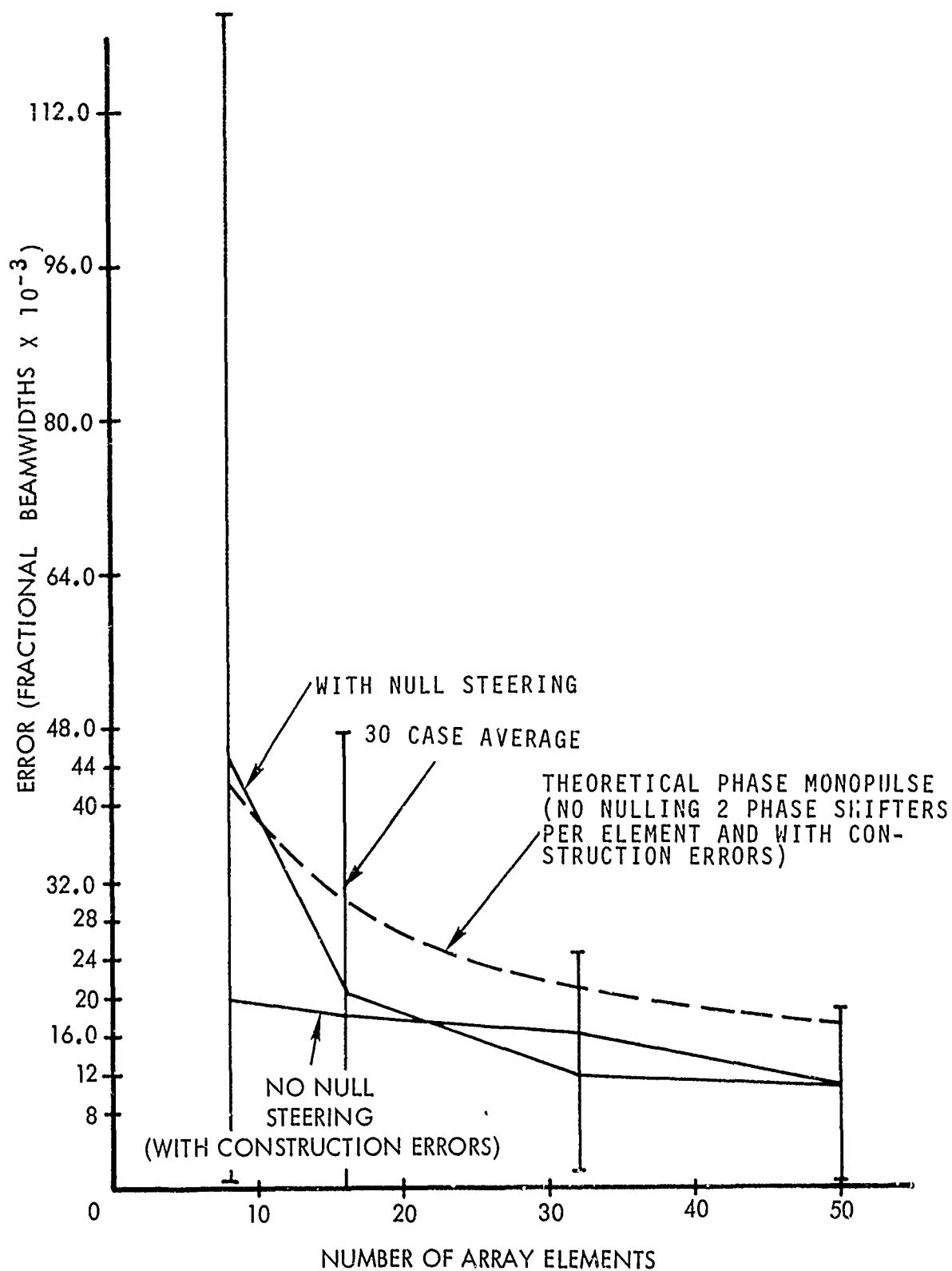
Figure 2-1 Boresight Shift Error Due to Random
Phase and Amplitude Errors with Null Steering

3

appearing at three sidelobe   levels of the
difference monopulse pattern.

Table 2-1. Boresight Shift Error for Optimal Versus Omni Null Steering

First Near-In Sidelobe Level to be Cancelled*	Optimal Nulling with Complex Weights		Optimal Nulling with Phase-Only Weights		Omni Cancelling Beam
	Beam Level Boresight	Boresight Shift**	Beam Level Boresight	Boresight Shift	Boresight Shift
-20 dB	-33.5 dB	0.015 beamwidths	-30 dB	0.022 beamwidths	0.06
-30 dB	-47.9 dB	0.003 beamwidths	-45 dB	0.004 beamwidths	0.022
-35 dB	-56 dB	0.0011 beamwidths	-53 dB	0.0015 beamwidths	0.015

*All levels relative to sum beam peak.
**These are worst-case boresight shifts found by matching sidelobes. Interference entering the first sidelobe (-20 dB) of a mainbeam would have a worst-case shift due to the first sidelobes of the cancelling beam, etc.

5

SECTION III

CONCLUSIONS

a. In most cases, random construction errors in the
    array cause more monopulse boresight shift error
    than will be caused by optimal null-steering of the
    sidelobes. For example, random construction errors
    causing far-out sidelobe limitations of -35 dB
    cause rms boresights shift errors of 0.015 beam-
    widths approximately, whereas optimal null steering
    would cause rms boresight shift errors of 0.001
    beamwidths.

b. Nulling of close-in sidelobes (1st, 2nd) can cause,
    with most nulling approaches, more boresight shift
    error than construction errors. However, even in
    the case of omni sidelobe cancellers, the boresight
    shift error will be less than 0.03 beamwidths.

c. Mainbeam null steering causes severe boresight
    shift error, and thus is probably impractical in
    most cases. However, the use of a correction fac-
    tor to compensate for this error is possible, if
    required. Nevertheless, accuracy will greatly
    deteriorate with mainbeam null steering.

d. Using weights at each element in adaptive arrays
    causes far less boresight shift error than omni
    sidelobe cancellers, especially when nulling high
    close-in sidelobes. Worst-case shift error much
    less than 0.003 beamwidths can be obtained even
    nulling close-in, sidelobes of -15 dB or higher,
    when optimal null steering is used. Nulling of
    further-out sidelobes will cause even less error.

e. Pattern decomposition allows first-order estimates of boresight shift error due to null steering for most null steering approaches. At least part of the null steering boresight shift error can be removed by using a correction factor computed when the adaptive weights are known.

f. All errors tend to diminish with increasing array size for fixed location of the jammers, so that tracking accuracy using adaptive arrays is limited only by the size of the array, as in the case of ordinary monopulse arrays.

SECTION IV

ANALYSIS OF NULL STEERING EFFECTS ON MONOPULSE TRACKING

This section illustrates the utilization of the cancelling beam concept to determine the monopulse boresight errors resulting from different kinds of null steering. The following specific null steering techniques are analyzed.

a. Monopulse tracking system using complex weights

b. Monopulse tracking system using phase only weights

These results are then extended to the monopulse tracking system using large arrays.

4.1 Optimum Complex Weight Nulling Effects on Monopulse Tracking

A simple analysis of the effects of null steering on monopulse accuracy can be obtained by producing a decomposition of the null-steered antenna patterns into two antenna patterns as follows;

a. The original unperturbed antenna pattern without null steering or boresight error, and

b. A "cancelling" pattern that is equal to the negative of the original pattern in the direction of the jammer.

The superposition of these two patterns produces a null toward the jammer. This concept of pattern decomposition applies to the sum and difference monopulse antenna patterns.

There are two important reasons for using antenna pattern decomposition;

a. The effects on boresight shift can be immediately estimated from the magnitude of cancelling beam in

8

the vicinity of boresight of the monopulse difference pattern.

b. An algorithm can be used in the simulations and experiments which adjusts the amplitude and phase of a cancelling beam to form a null toward the jammer (beam space algorithm).

4.1.1   Complex Weight Nulling of Monopulse Sum Beams

It is shown in Appendix A, and in References 2 and 5, that the optimum LMS (or S/N) antenna pattern (sum beam) can be decomposed into a beam toward the desired signal, and one toward each jammer. Both patterns can be described as being formed from linearly phased uniform illumination functions. For the case of a broadside array of equally spaced elements, from Equation 17 and 19 of Appendix A; the total optimally null-steered sum pattern can be written as:

$$\Psi_\Sigma (\zeta, \theta) = A \; \frac{\sin \frac{N}{2} (\zeta)}{\sin \frac{1}{2} (\zeta)} + K \; \frac{\sin \frac{N}{2} \{\zeta - \theta\}}{\sin \frac{1}{2} \{\zeta - \theta\}} \qquad (4.1.1-1)$$

where

Ψ = the far field null-steered sum pattern

ζ, θ = electrical phase corresponding to the mechanical angle of the target and the jammer, respectively

A, K = complex weights of the main beam and cancelling beam, respectively

N = number of elements

The constant K is calculated specifically in Appendix A. However, for purposes of this report, we note that K is approximately the sidelobe level of the main pattern in the

9

direction of the jammer, as depicted in Figure 4.1.1-1, if the jammer power is large. This follows also by noting that the total pattern in the direction of the jammer must be approximately zero, i.e., the second term of Equation (4.1.1-1) should cancel the first term in the direction of jammer. Since at $\varsigma = \theta$, the first term of Equation (4.1.1-1) is the sidelobe of a main beam toward the jammer and the second term equals K. Therefore, K must be approximately the negative of the sidelobe level toward the jammer in order to achieve cancellation. The second term of Equation (4.1.1-1) is often called a cancelling beam and achieves nulling of the sidelobe level.

Using the cancellation beam concept, it is now possible to show the basic "beam-space" algorithm.

In the "beam-space" technique a weight vector, W^S, is first formed in computer software corresponding to a beam pointed toward the desired signal. For an array using a uniform amplitude distribution, this weight vector is composed of the complex unit phasors corresponding to each element phase shifter setting, and is given by:

$$W^S = \left\{ \begin{array}{c} 1 \\ e^{j \, \phi_i^S} \\ \cdot \\ \cdot \\ \cdot \\ e^{j \, \phi_m^S} \end{array} \right\}$$

where ϕ_i^S is the phase shifter setting of the ith element of an m element linear array. The values of ϕ_i^S are determined by the direction of arrival (DOA) of the signal through the following relationship:

$$\phi_i^S = \frac{2\pi}{\lambda} \, d_i \, \sin \theta_s$$

10
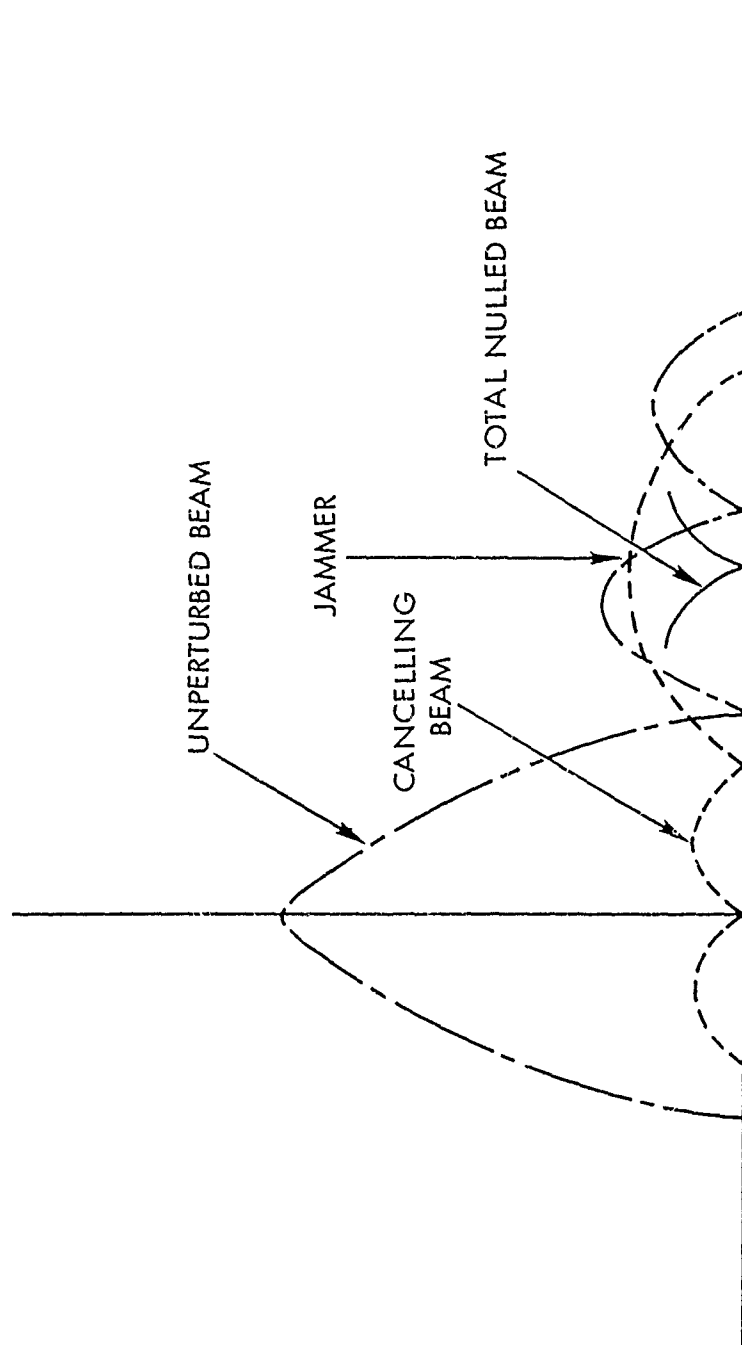
Figure 4.1.1-1 Illustration of Cancelling Beam Concept

UNPERTURBED BEAM

JAMMER

CANCELLING BEAM

TOTAL NULLED BEAM

11

where d_i is the array element location (relative to the end element) and θ_s is the angle of arrival (measured from array boresight) of the desired signal. The beam-space algorithm assumes that θ_s is known. A second weight vector, W^j is also formed in computer software corresponding to each jammer. These weight vectors are similar in form to the signal weight vector above, except that they form a beam in the direction of each jammer and are given by:

$$W^j = \left\{ \begin{array}{c} 1 \\ e^{j\,\emptyset_i^{j}} \\ \cdot \\ \cdot \\ \cdot \\ e^{j\,\emptyset_m^{\,j}} \end{array} \right\}$$

where again $\emptyset_i^j = \frac{2\pi}{\lambda}\, d_i\, \sin\theta_j$ and where θ_j corresponds to the angle of arrival of the jammer source. The DOA of these jamming sources are assumed to be known via a jammer finder beam or some other source. Although this information is not essential to the basic operation of the beam-space algorithm, it substantially reduces the number of iterations required to form an antenna pattern null in the direction of the jammer source.

A weighted sum of the weight vector, W^S and W^j yield the total weight vector that controls the array. For a given signal source and one jammer source, the total weight vector is given by:

$$W^T = W^S + K\,W^j \quad .$$

12

For the case where both amplitude and phase weighting are available, the amplitude and phase of the complex weighting constant K are varied by the computer until the software jammer beam formed by KW^j matches the side-lobe level of the desired signal pattern (formed by W^s) in the direction of the jammer source. When a match occurs, subtraction of these two software beams forms a null toward the jammer. This procedure is illustrated in Figure 4.1.1-2. Note that the subtraction occurs in software by subtracting weight vectors and not in RF hardware. This total weight vector is then implemented on the array by setting the complex weights to values corresponding to this weight vector. The resultant antenna pattern will then exhibit a null in the direction of the jammer source. For multiple jammers, the total weight vector takes the form:

$$W^T = W^S + \sum_{i=1}^{M} K_i W_i^j$$

where M is the number of jammer sources and $K_i W_i^j$ is the weight vector the ith jammer source.

4.1.2   Complex Weight Nulling of Monopulse Difference Beams

The same optimal pattern decomposition associated with null steering applies to not only the sum pattern, but also the difference pattern. This is proven in Appendix A of this report.

The effect of null steering on boresight accuracy of a monopulse system can be estimated by simply obtaining the amplitude of the cancelling pattern in the region of the unperturbed difference pattern null, as depicted in Figure 4.1.2-1. The cancelling beam, when superimposed on the unperturbed difference pattern, will destroy the unperturbed null and cause a somewhat higher minima closeby, which is approximately the location of the new monopulse boresight. The

(1) MAIN BEAM BEFORE JAMMER CANCELLATION (USING WEIGHT VECTOR, W_S)

S

(2) A "FINDER BEAM" AUXILIARY BEAM CAN AID JAMMER NULLING SPEED BY LOCATING JAMMERS (NOT ESSENTIAL TO BASIC METHOD)

(4) TOTAL PATTERN COMMAND FROM COMPUTER: $W_T = W_S + K W_J$

A NULL IN THE TOTAL PATTERN TOWARD THE JAMMER IS FORMED BY VARYING K TO MINIMIZE OUTPUT POWER

(3) A JAMMER-CANCELLING BEAM IS FORMED IN THE COMPUTER, VIA WEIGHT VECTOR, W_J

Figure 4.1.1-2 "Beam Space" Weight Search for Nulling Jammers.

14
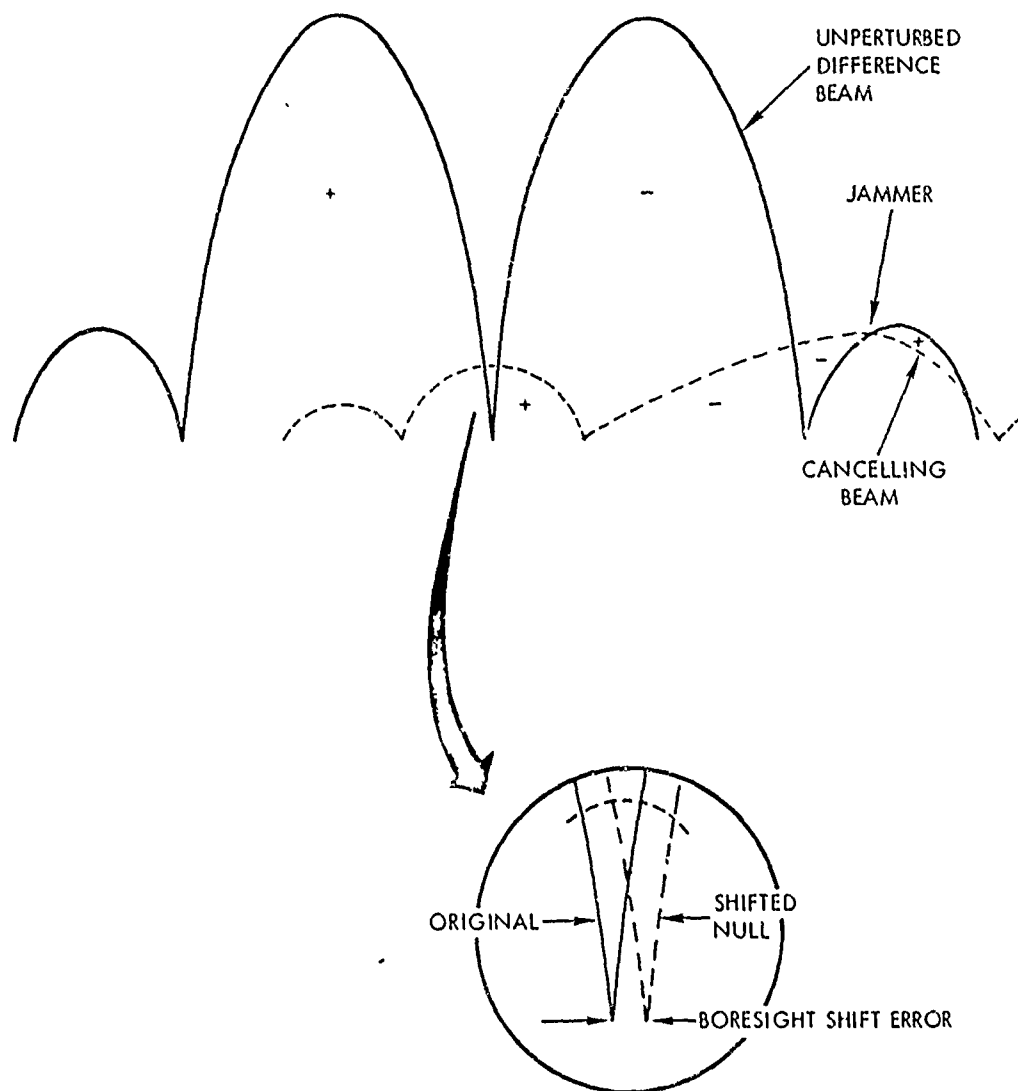
Figure 4.1.2-1 Boresight Shift Error Due to Cancelling Beam.

depth and the shift of the resultant null depends on relative phase and amplitude of the cancelling beam with respect to the unperturbed difference pattern. For example, if the cancelling pattern is negative real as shown in Figure 4.1.2-1, in order to cancel a positive real sidelobe, the new shifted null must be formed where the unperturbed difference pattern intersects the positive lobe of the cancelling beam. This is the maximum (worst-case) boresight shift error. If the cancelling beam side lobe around boresight is at a 90° phase with respect to the difference pattern little boresight shift would occur, but the difference pattern null would decrease to the value approximately equal to the cancelling pattern side lobe at boresight. The product detector that is used to sense monopulse boresight in actual monopulse systems would still have a tracking null at the same position as in the unperturbed pattern. In general, the product detector null, which takes into consideration the phase relation between the sum and difference pattern, will be close to, but will not coincide with, the difference pattern null.

Figure 4.1.2-2 shows a calculation of boresight shift resulting from the cancelling beam in a complex weighted array, as taken from Appendix A. This plot is a boresight shift versus jammer-signal separation angle. The figure has been normalized to beamwidths to remove the effect of array size from statements about boresight shift versus location of the jammers. As shown in the figure, the worst-case boresight shift for the jammer appearing at the first sidelobe is approximately -0.0375 beamwidths. After the first several (4-5) sidelobes, the boresight shift is less than 0.01 beamwidths.

In extrapolating this calculation to a more practical array, it is important to note that this was a calculation for a uniformly illuminated array with a 13 dB first sidelobe level. Nulling antenna patterns with lower sidelobe levels would require

16
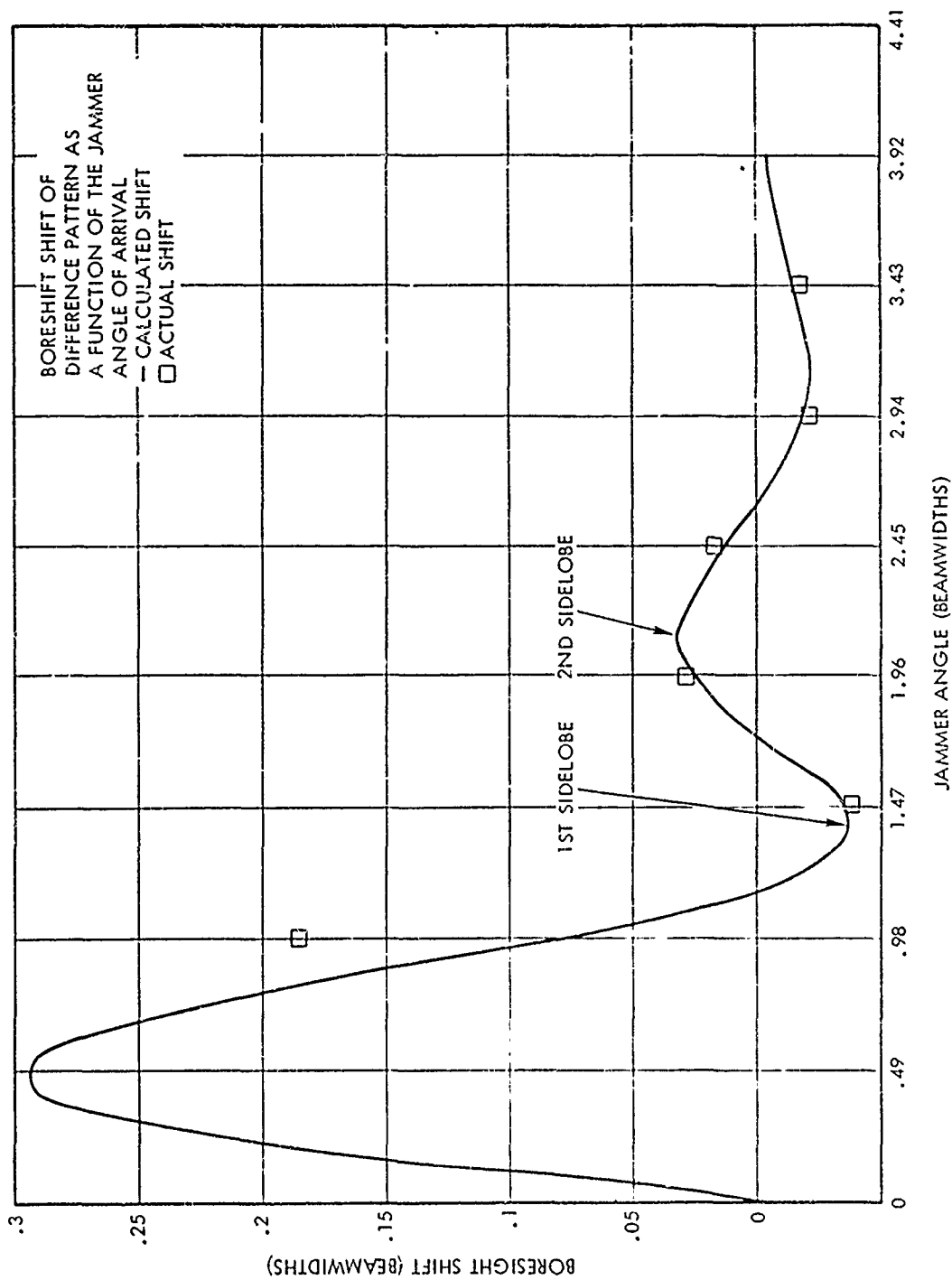
Figure 4.1.2-2. Boresight Shift Error of Difference Pattern as a Function of Jammer Angle of Arrival

17

a lower cancelling beam; and would cause less boresight shift. Another method to cancel a jammer in a monopulse tracking system is to use a sidelobe canceller array with complex weights. The sidelobe level canceller uses an omni cancelling pattern that is adjusted in amplitude and phase to create a null toward the jammer.

In the case of the fully adaptive array, the amplitude level of the cancelling beam, in the region of the difference pattern boresight, varies as the product of the sidelobe level being cancelled and the sidelobe level of the cancelling beam at boresight. The situation is that the cancelling beam peak is at the sidelobe level being cancelled, and its sidelobe level at the difference pattern boresight is still lower by approximately the same sidelobe ratio. On the other hand, the amplitude of the omnidirectional cancelling beam of a sidelobe canceller array at the difference pattern boresight is approximately the same as the sidelobe level beam cancelled. Since the omnidirectional antenna also produces an amplitude approximately equal to the sidelobe level of the beam cancelled (at boresight), the boresight error will be far greater than with the fully adaptive array.

Random error effects can also be represented by an omni directional pattern added to the unperturbed antenna pattern, such as depicted i   .gure 4.1.2-3. The expected value of the pattern, taken over all possible random errors, is omnidirectional with a mean value determined from the variance of the random errors. The far-out rms sidelobe level of most antennas is usually at this level, since the far-out sidelobes are usually dominated by random construction errors rather than the diffraction effects. Thus, the effect of random errors on boresight shift is approximately that of an omnicancelling pattern with an

18

RMS LEVEL OF ERROR
LIMITED SIDELOBES
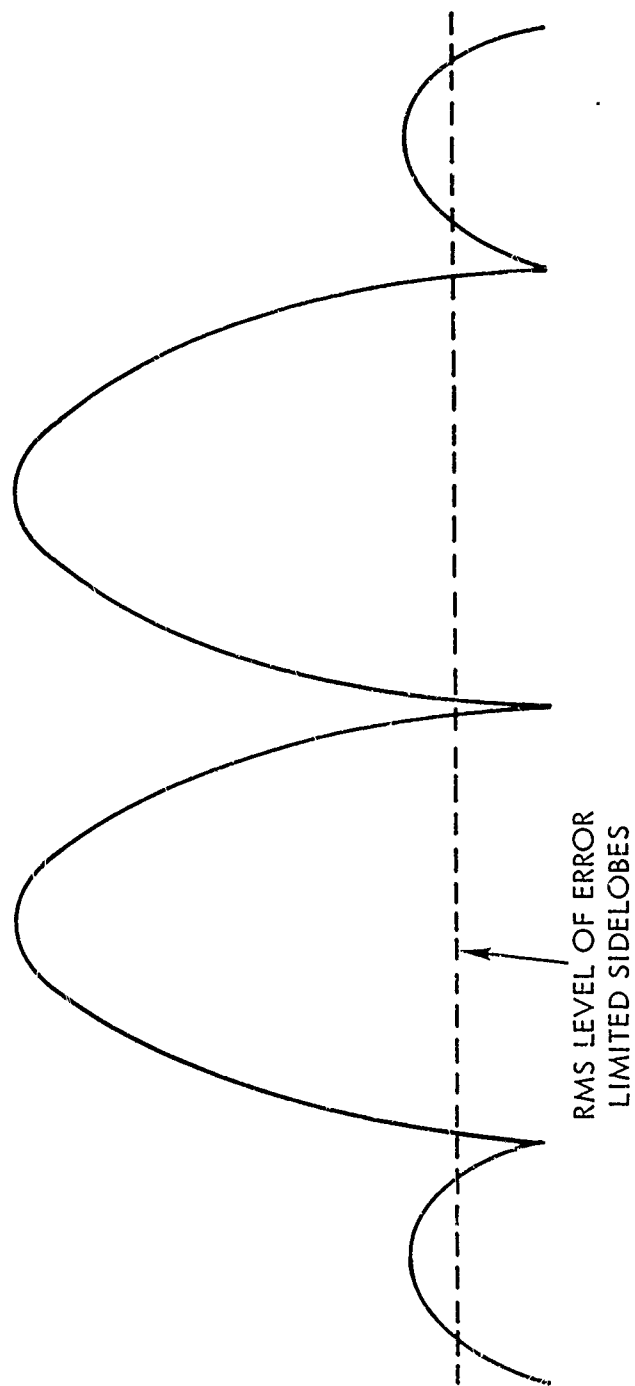
Figure 4.1.2-3 Random Error Representation

amplitude given by the random construction errors of the array. These random errors cause much larger boresight errors than the fully adaptive cancelling patterns that would cancel jammers arriving on far-out sidelobes. Specific calculations of the effect of random errors on monopulse errors are reported in Reference 7.

The actual boresight shift error due to a cancelling beam amplitude in the region of the difference beam null can be obtained using Figure 4.1.2-**4.**(a typical unperturbed difference pattern). The figure shows several examples of cancelling beam amplitudes resulting from a null steering operation. For example, if an omnidirectional cancelling beam at a level of 20 dB below the unperturbed sum beam peak is required to cancel a jammer in the difference pattern, then a worst-case difference pattern boresight shift of 0.06 beamwidths will result. Typical random construction errors, which originate sidelobe levels of the order of 25 to 35 dB below the unperturbed sum peak, cause shifts of 0.035 to 0.01 beamwidths. On the other hand, a fully adaptive cancelling pattern would create the amplitude errors at boresight approximately equal to the product of the sidelobe level being cancelled and the sidelobe level of the cancelling beam at boresight. This amplitude level would cause <0.01 beam-width shift of the difference pattern boresight for a 20 dB side-lobe. Of course, nulling in the main beam would cause very large boresight errors.

Another method of calculating boresight shift, due to the cancelling pattern, is to divide the amplitude of the cancelling beam, evaluated at boresight, by the slope of the monopulse difference pattern, as has been demonstrated in Equation (A-21) in Appendix A.
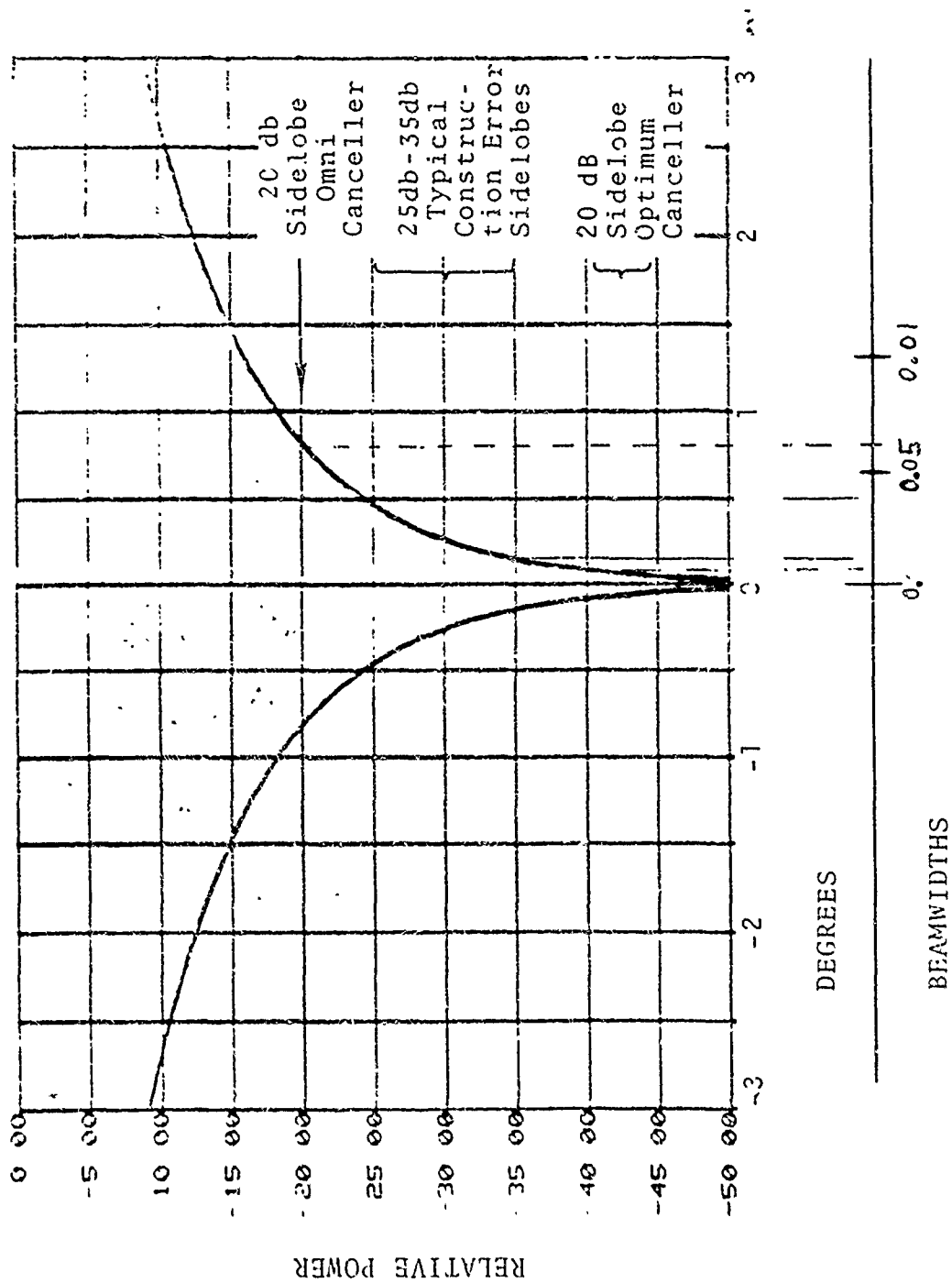
Figure 4.1.2-4 Typical Monopulse Boresight Null Region
(Unperturbed Pattern)

21

4.2 Optimum Phase-Only Weight Nulling Effects on Monopulse Tracking

The previous section considers adaptive monopulse tracking arrays, as well as monopulse tracking arrays with only a few sidelobe level cancellers. For large fully adaptive arrays, the complex weights can be very expensive.

On the other hand, the sidelobe cancellers introduce large boresight errors. However, null steering can be accomplished with less expense using only phase shifters at each element. The phase-only null steering is a relatively new technique developed at Harris ESD in a series of recent contracts (Reference 8-11).

This technique has the advantage of incorporating adaptive weights at each element, as opposed to a few auxiliary omni-directional elements, thus achieving near optimum cancelling beams with low boresight shift errors. Also, this technique is believed to require somewhat less complexity and expense than using complete amplitude and phase complex weights, while maintaining the potential for nulling many jammers. In addition, a digital search optimization was used in order to eliminate the expensive analog correlation control used in most proposed adaptive arrays and coherent sidelobe cancellors.

The emphasis of this contract has been on a detailed computer analysis and experimental measurement program of the boresight shift error (in practical amplitude monopulse arrays) in the presence of array construction errors. Optimum null steering was used with phase-only weight constraints. It is not proposed that the phase-only weighting or the digital search null-steering techniques utilized are the best for all applications; rather, the results of this study are representative of a class of optimum null steering algorithms.

4.2.1   Phase-Only Nulling of Monopulse Sum Beams

It has been shown that if only phase shifters are available for adaptive weights (i.e., magnitude of all weights are constrained to unity), that the optimum sum pattern under such weight constraints can be decomposed into an unperturbed pattern, and a two-lobed cancelling beam (References 10 and 12).

Figure 4.2.1-1a shows calculations performed for the final pattern after nulling and the two-lobed cancelling beam for a uniformly illuminated array without construction errors. Figure 4.2.1-1b shows the nulled sum beam and the two-lobed cancelling beam for an amplitude tapered array when array construction errors are included in the calculation (Reference 7).

The two-lobed cancelling pattern results from using phase-only adaptive weights, and has also been derived by the analogy of phase modulation theory that results in two sidebands (Reference 13).

The null steering algorithm used in the computer simulations for this contract was a "beam-space" algorithm similar to that previously described in Paragraph 4.1.1. However, when phase-only weights are used, certain small angle approximations (that simplify the beam-space calculations) can be made, as detailed in Reference 12.

4.2.2   Phase-Only Nulling of Monopulse Difference Beams

The subject of using phase-only weights for null steering in monopulse tracking arrays has not been discussed, to our knowledge, in the literature. There are many possible forms of monopulse tracking arrays. The one investigated in this contract was an amplitude tracking array monopulse with phase-only null steering of left and right beams.

ANGLE FROM END FIRE (DEGREES)

Final pattern with null at 108°.

ANGLE FROM END FIRE (DEGREES)

Interference cancelling beam for ideal array
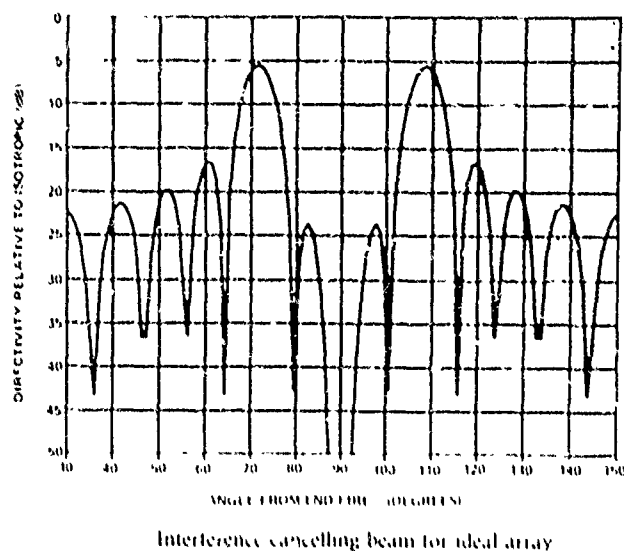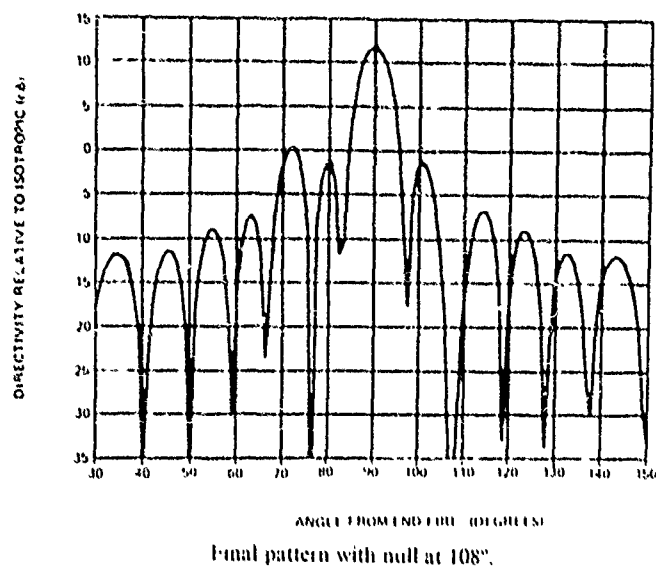
(a) Uniform Amplitude Taper without Construction Errors

Figure 4.2.1-1. Phase-Only-Weight Nulling of Sum Beams (Ref. 12)

24
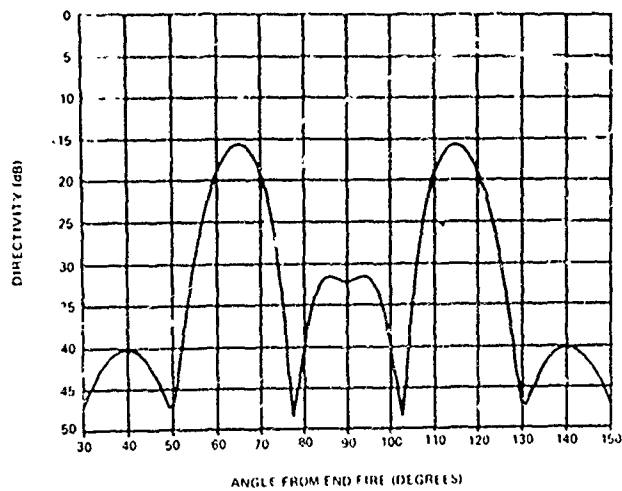
Interference cancelling beam for array with errors.
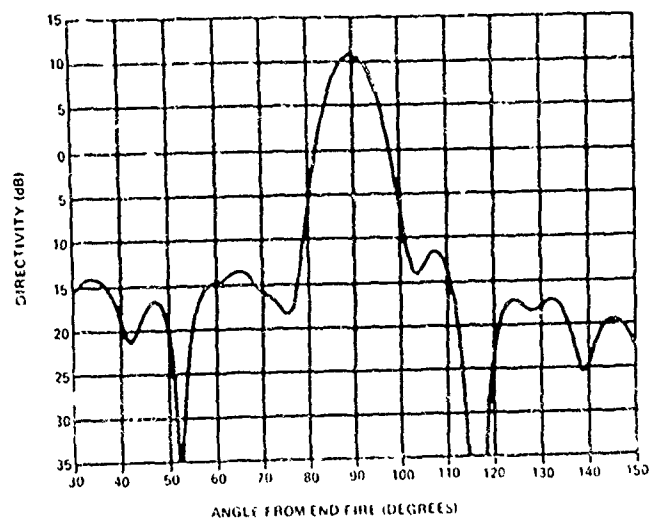
Final pattern after nulling interference at 115.

(b) Amplitude Taper with Construction Errors

Most of the emphasis of this contract was on an amplitude monopulse technique, since it represents a class of more efficient sum and difference pattern illuminations with lower sidelobes than the phase monopulse techniques. In addition, the past knowledge of phase-only nulling of a sum beam can be applied directly to the nulling of the left and right beams of amplitude monopulse. There was also a brief study of a phase tracking monopulse array, with null steering of the sum and difference beams formed by adding and subtracting the left and right array halves, but there was not sufficient time to investigate it in detail.

Figure 4.2.2-1 depicts the amplitude tracking monopulse array which was analyzed in detail and measured for this contract. The output of the antenna elements are power divided to feed two summing networks which create the left and right squinted beams of the amplitude monopulse. Each array consisting of phase shifters and summers, is separately protected from jamming by adaptive null steering, as indicated by the null steering control loops shown on the diagram.

Since both the left and right beams have nulls toward each jammer, only residual jamming occurs in either beam. Thus, any linear combination of these beams, such as the sum and difference monopulse channels, are also protected by this null steering.

The application of cancelling beam concepts to amplitude monopulse is conceptually no more different than the single beam case. However, because of the two to four beams necessary for a monopulse system, the mechanics of computing the cancelling beam become considerably more complicated. The cancelling beam application presented below, however complicated, does present a method that is easily visualized and leads to a simple and accurate prediction of the boresight shift due to adaptive null steering.

26
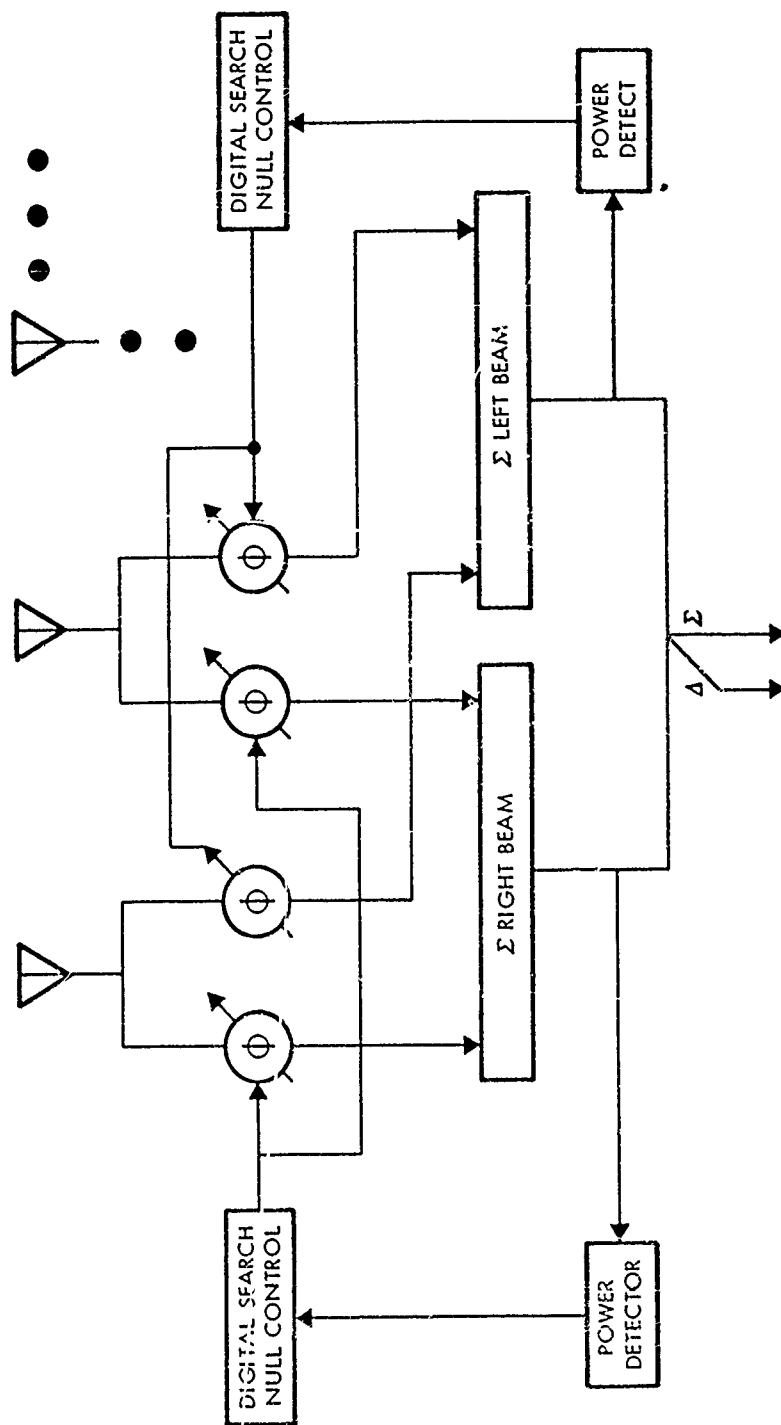
Figure 4.2.2-1 Amplitude Monopulse Null Steering Approach (analyzed and measured in this contract)

The adaptive null steering procedure employed was to null the right beam, then null the left beam, and finally form the sum and difference beams. Separate cancelling beams were then generated for the right and left beams. The cancelling beam for the difference pattern is then just the difference between these two cancelling beams.

The forms of these cancelling beams are shown in Figure 4.2.2-2, and are valid as long as the small angle approximation is valid. The cancelling beams have nulls at the peaks of the left and right main beams (not boresight, because the beams are squinted) and symmetric maxima near the interference direction of arrival, and the opposite side of the main beams. Note that both cancelling beams have a finite gain at boresight. As is shown, the interference enters the left beam at a different level (even a different sidelobe) than the right beam. This means that while the cancelling beams have the same general shape, they are different due to the squinting of the beams. The cancelling patterns will then have different levels at boresight, and their difference, which forms the cancelling beam for the difference pattern, will also be nonzero at boresight. This perturbation of the main difference pattern produces a boresight shift, as discussed in Paragraph 4.1.2.

Simulations of an amplitude-monopulse array were performed at Harris. The beam space search algorithm employed has been already described. These simulations permitted the computation of boresight shifts due only to null steering. The computer simulation results for random errors are discussed in Paragraph 4.3. The agreement with breadboard results was good, and the above analysis allowed the prediction of boresight errors due to null steering when the small-angle

28
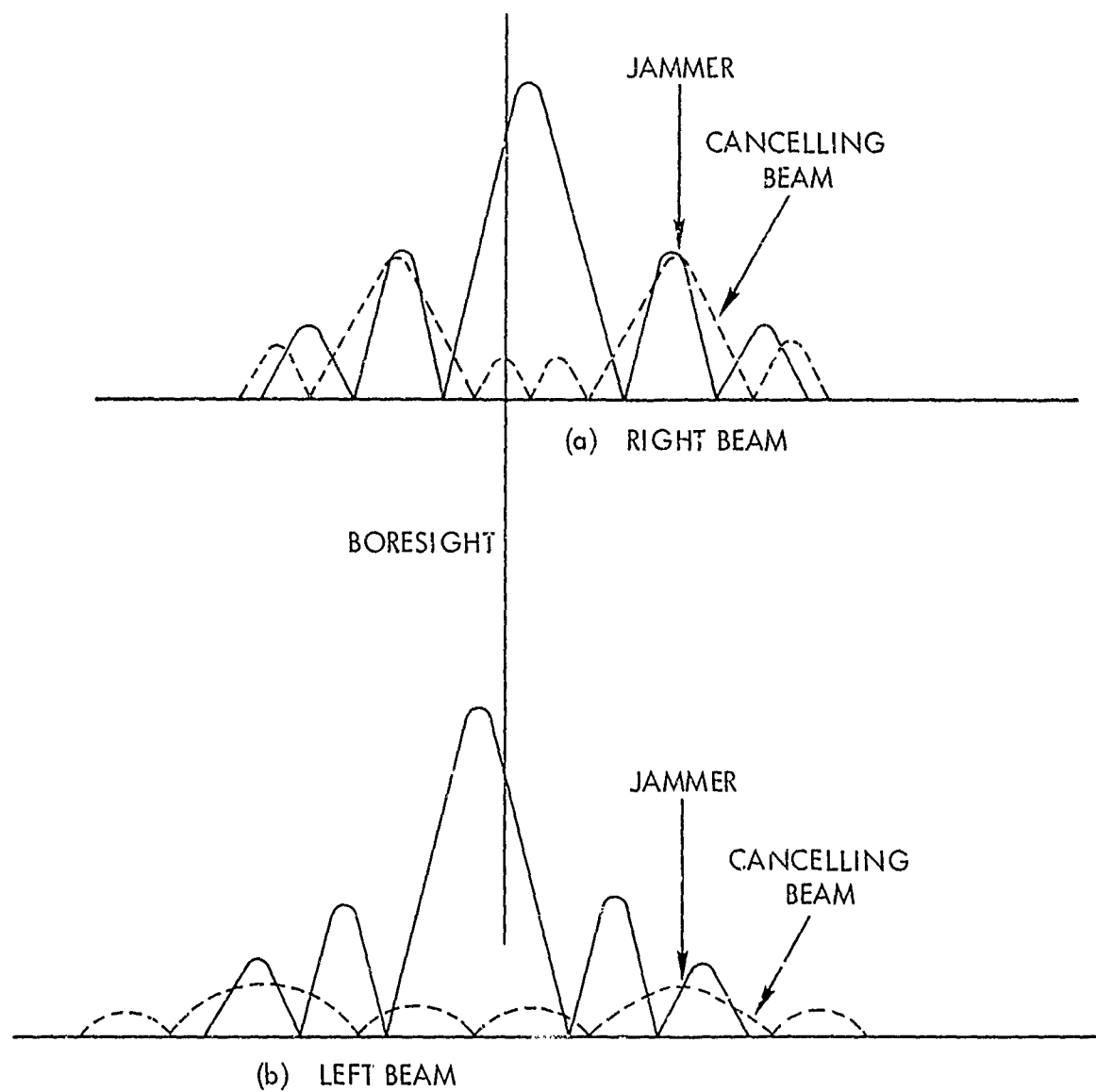
Figure 4.2.2-2 Cancelling Beams for Monopulse Arrays

approximation was valid. The simple small-angle approximation uses real beam space coefficients; an exact analysis requires complex coefficients. Complex coefficients were used in the simulation, however, for interference entering low sidelobes the complex coefficients are very nearly real. All simulations were for an 8-element linear array with an interelement spacing of 0.488λ.

One case to be presented in detail is a jammer entering a sidelobe at 45^0 from boresight. The unadapted difference pattern is shown in Figure 4.2.2-3, and the pattern after a computer null-steering simulation in Figure 4.2.2-4. A blow-up of boresight for the adapted pattern is shown in Figure 4.2.2-5, and illustrates a boresight shift of 0.3^0. This result pertains to an ideal array as no random errors were included initially in this simulation. To see if cancelling beams can be used to predict this boresight shift, and to observe their form, cancelling patterns for the two squinted beams and the cancelling pattern for the monopulse difference beam were calculated. These patterns are shown in Figures 4.2.2-6 and 4.2.2-7, respectively. The cancelling beam for the difference pattern is asymmetrical. This is not surprising, as it is the difference between two unequal beams each one symmetrical about its own squint angles, not about boresight. The calculations performed with these patterns are given in Table 4.2.2-1. These rather rough calculations agree. very well with the simulation results. The ratio of the level of the left cancelling beam to the right cancelling beam level at 45^0 indicated that there would be a peak in the difference cancelling beam. The difference-beam sidelobe that was cancelled is about -15 dB. This implies a relatively small perturbation of the unadapted difference pattern (about 17% in voltage) so the small angle approximation is valid.
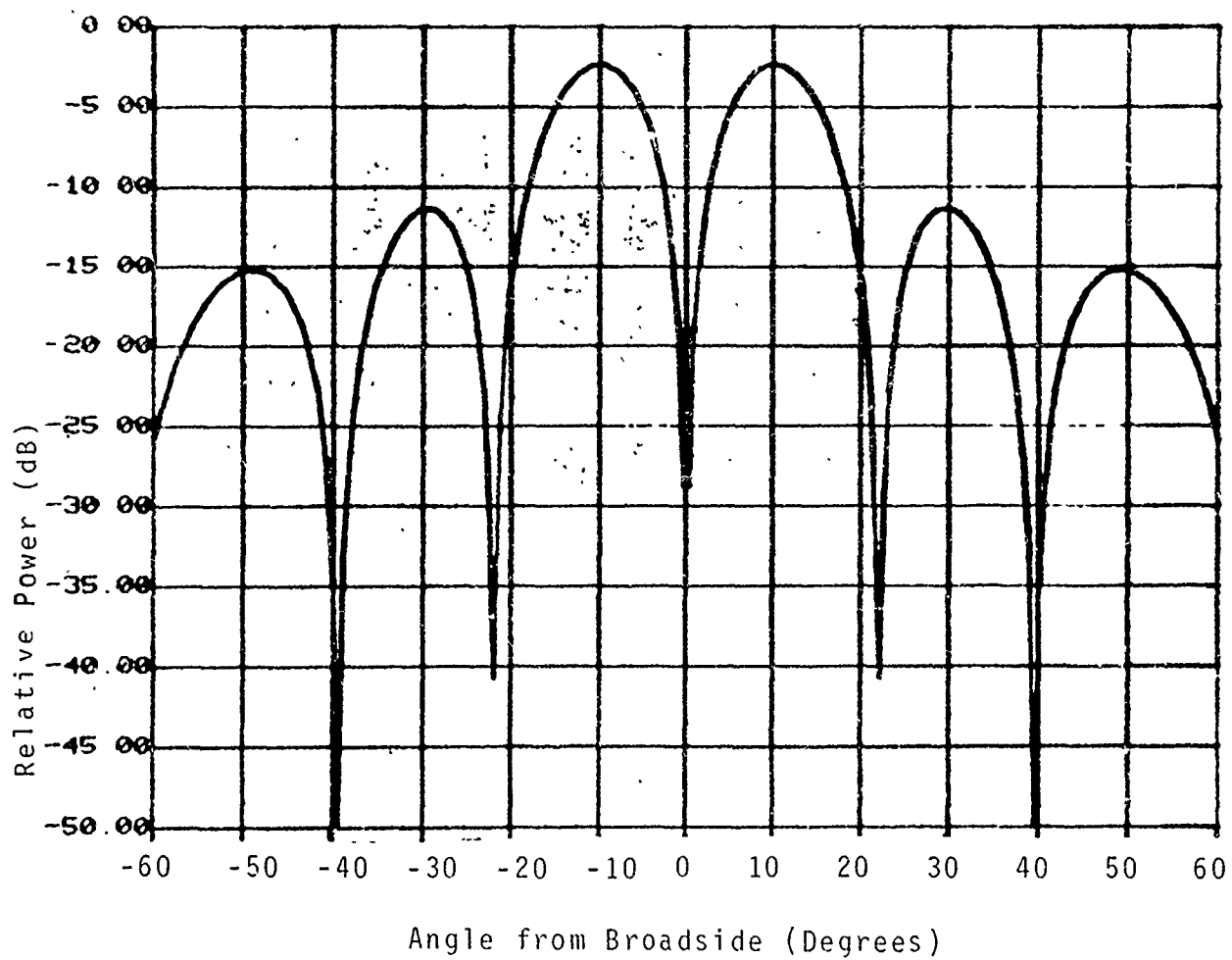
Figure 4.2.2-3. Unadapted Difference Pattern

31
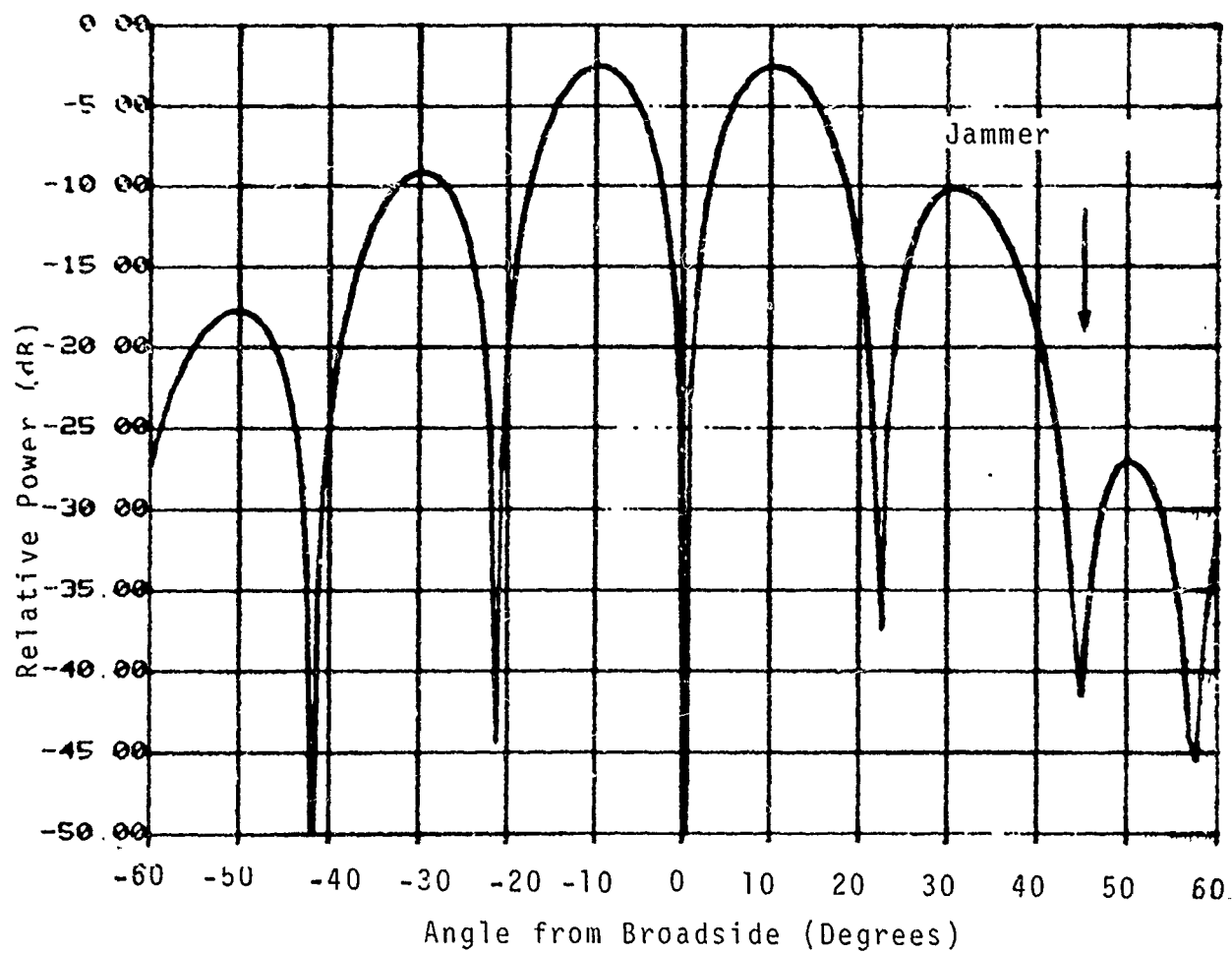
Figure 4.2.2-4. Nulled Difference Pattern
(Full Scale)

32
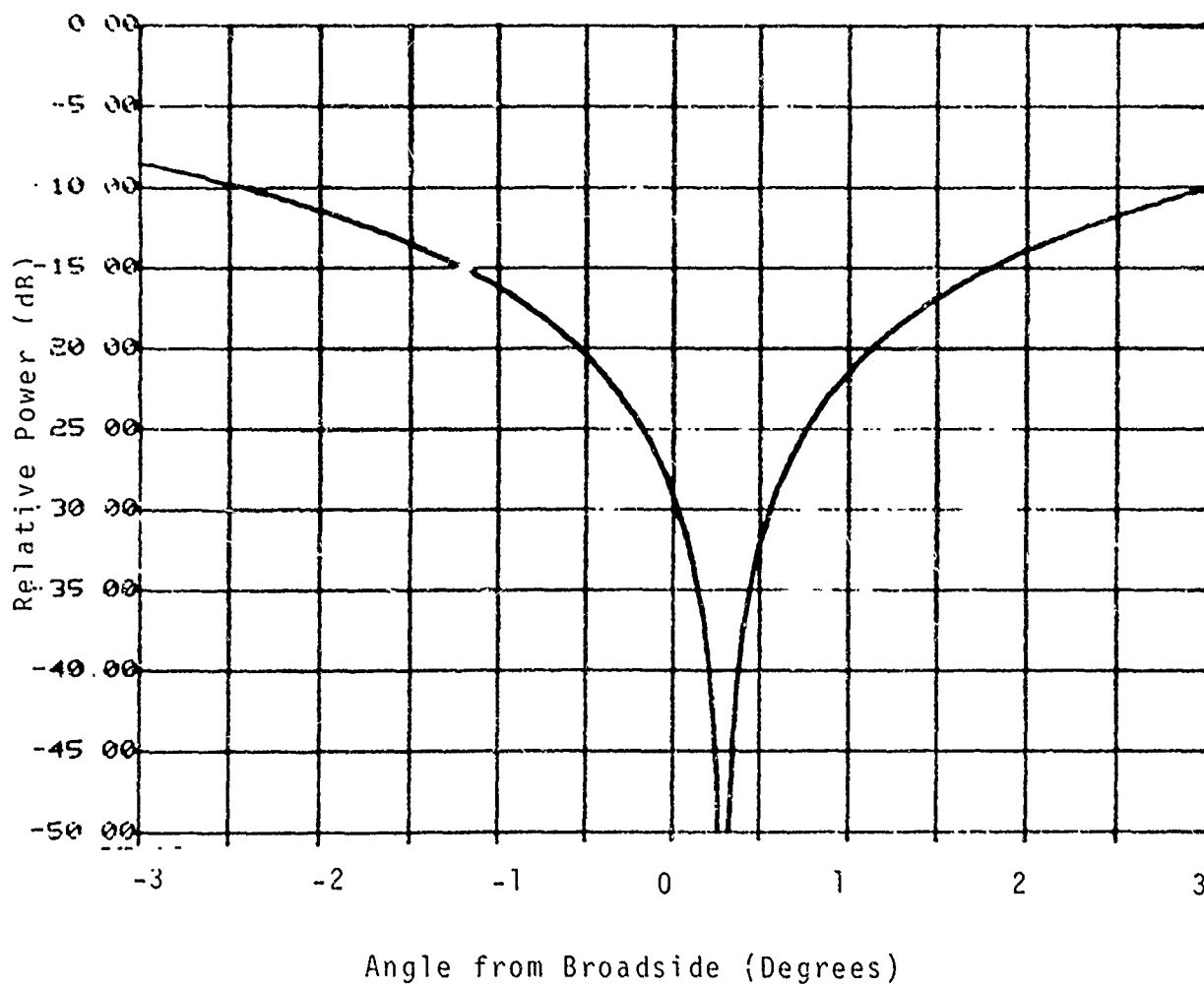
Figure 4.2.2-5.   Difference Pattern Null
(Boresight Region Expanded)

33
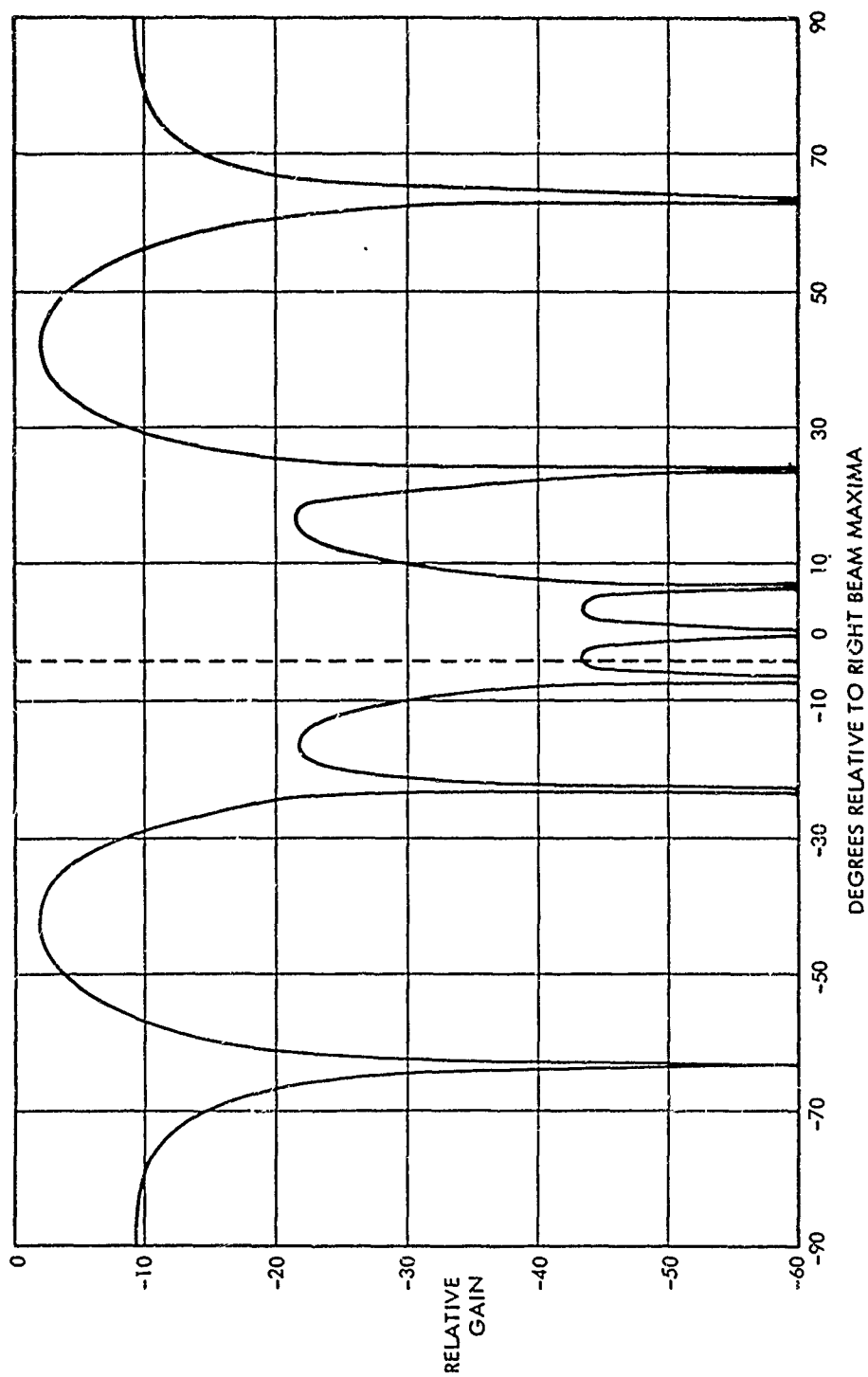
Figure 4.2.2-6 Perfect Cancelling Beam for Right Beam, $\theta_j = 45^o$, Squint Angle = 5.33^o

34
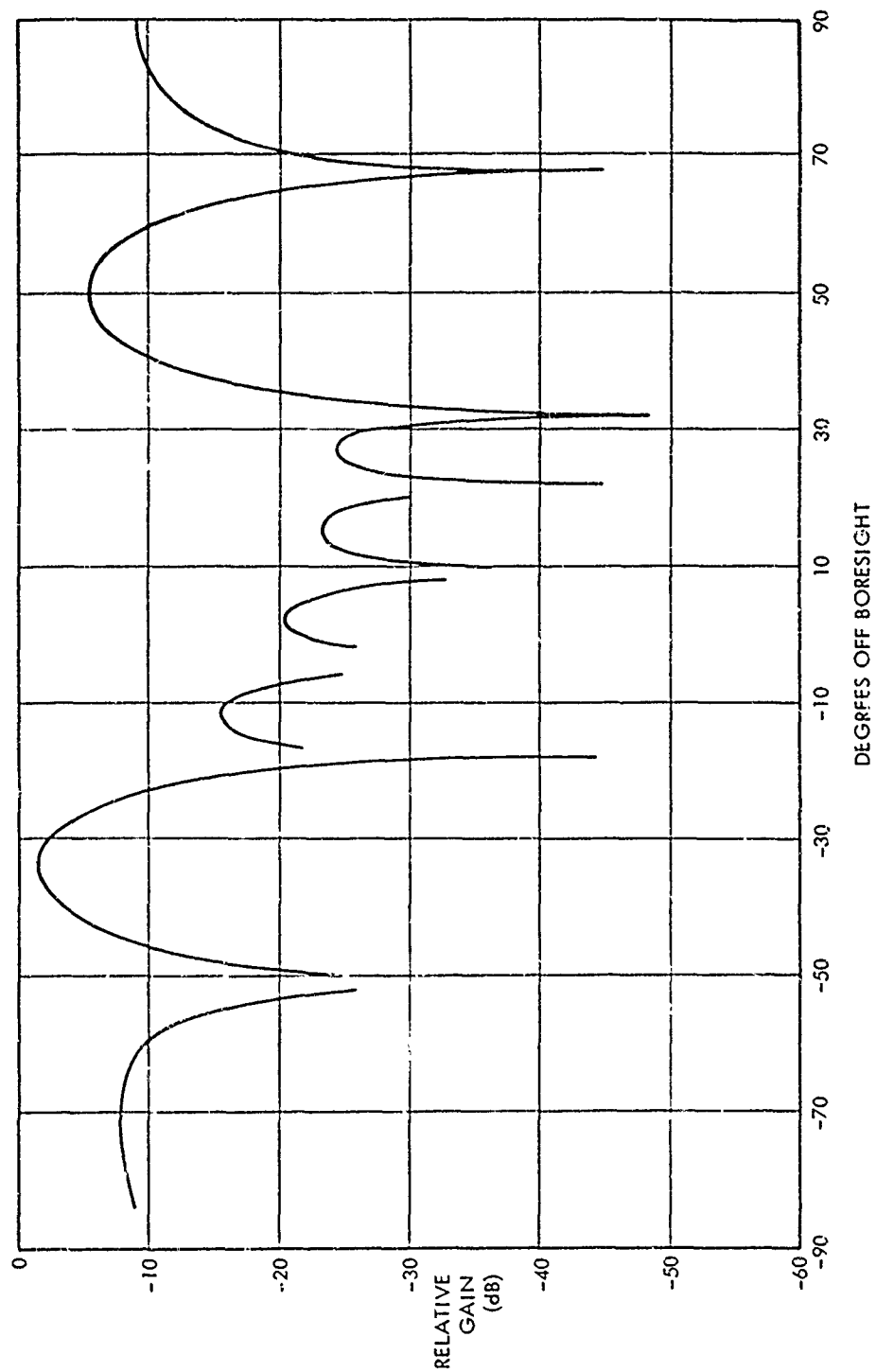
Figure 4.2.2-7 Perfect Cancelling Pattern for Difference Beam, $\theta_j = 45°$, (8 element array).

Table 4.2.2-1. Specific Calculation Values for 45°
Jammer Cancelling Beam

Ratio SLL 45°/Peak of Right Beam: -18 dB

Right Level of Cancelling Beam at 45°: -18 dB

Ratio SLL 45°/Peak of Left Beam: -25 dB

Left Level of Cancelling Beam at 45°: -26 dB

$\dfrac{\text{Left Cancelling Beam Level}}{\text{Right Cancelling Beam Level}}$: -8 dB

Ratio of Δ Cancelling Beam Level at Boresight

  to Level at 45°: -13.275 dB

Ratio of Δ Beam Level at 45°/Peak: -15 dB

Level of Cancelling Beam at Boresight: -28.275 dB

Azimuth Angle for -28.275 dB Level of Unadapted

  Δ Pattern: 0.30^O

Boresight: 0.3^O

The next case illustrates the limitations of the
theory when the small angle approximation is not valid. For
this case, the interference was entering a sidelobe 27° from
boresight. Figure 4.2.2-8 shows the unadapted difference
patterns. The jammer is entering very close to the main beam.
The pattern shown in Figure 4.2.2-9, is the adapted difference
pattern for a jammer entering at 27°. The blow-up around
boresight of this pattern, Figure 4.2.2-10, indicates a bore-
sight shift of about 0.6^O. The appropriate cancelling beams
are shown in Figure 4.2.2-11 and 4.2.2-12. The cancelling
pattern for the difference beam depicted in Figure 4.2.2-12
shows a very high level at boresight, so a large boresight
shift error might be expected. The cancelling beam calculations
for this case are not very good, for several reasons. The
sidelobe level at 27° is about -10 dB from the peak of the
difference beam, implying a perturbation of the unadapted
pattern of about 32% in voltage. The other major reason for
inaccuracies in the calculation is that the cancelling beam of
the difference pattern shown in Figure 4.2.2-12 is varying very
rapidly about boresight, so the approximation that the
cancellation pattern level is constant near boresight leads to
large errors. This case is a worst-case, and illustrates two
important facts. The boresight shift is strongly dependent on
the level and rate of change of the cancelling beam about
boresight, which in turn is dependent on the level of the side-
lobe to be cancelled, and the separation of that sidelobe from
boresight. It is to be stressed that these are practical
limitations to approximate cancelling beam calculations, not
theoretical problems. Table 4.2.2-2 shows the specific values
used in the 27° cancelling beam calculation.
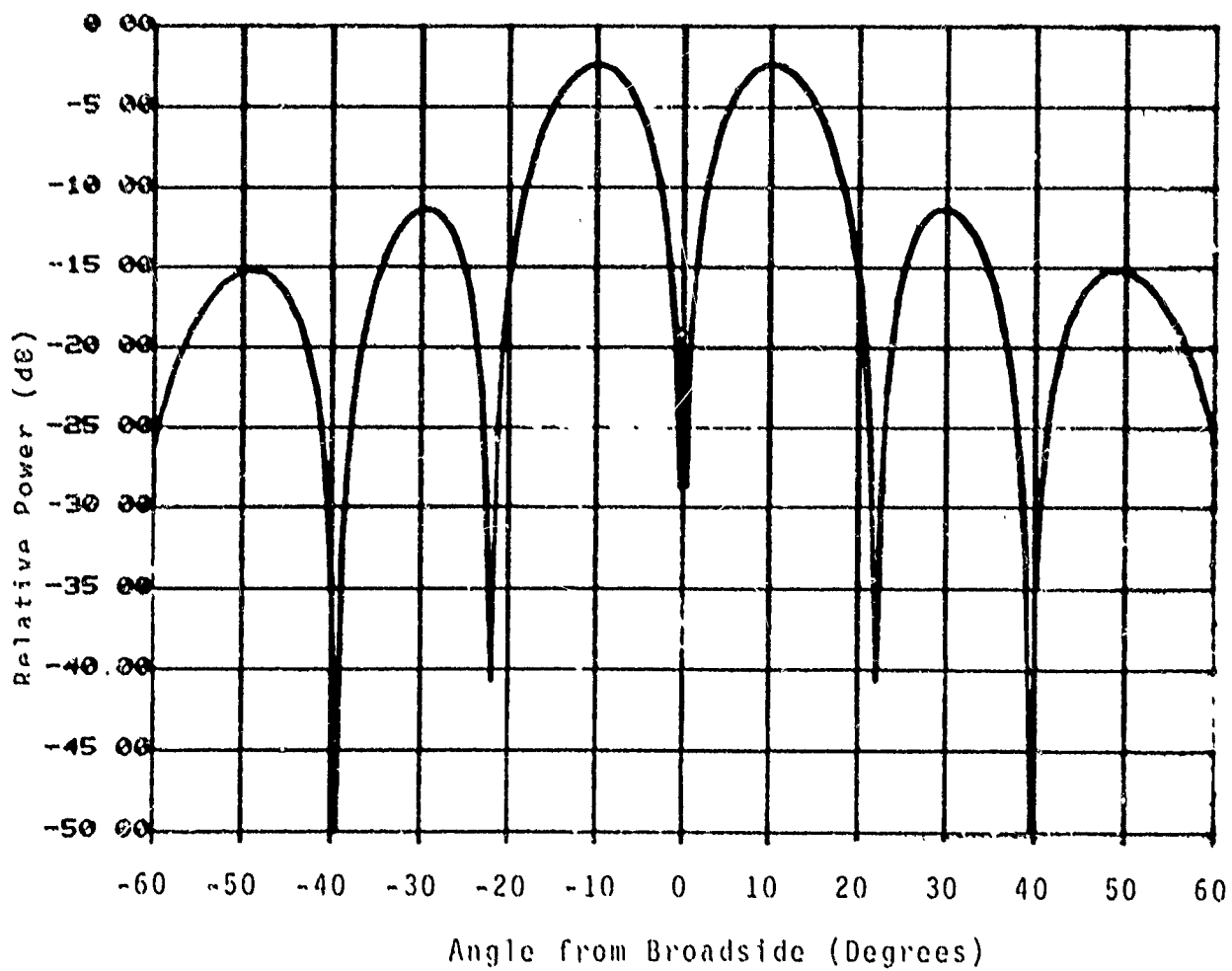
Figure 4.2.2-8.   Unadapted Pattern

38
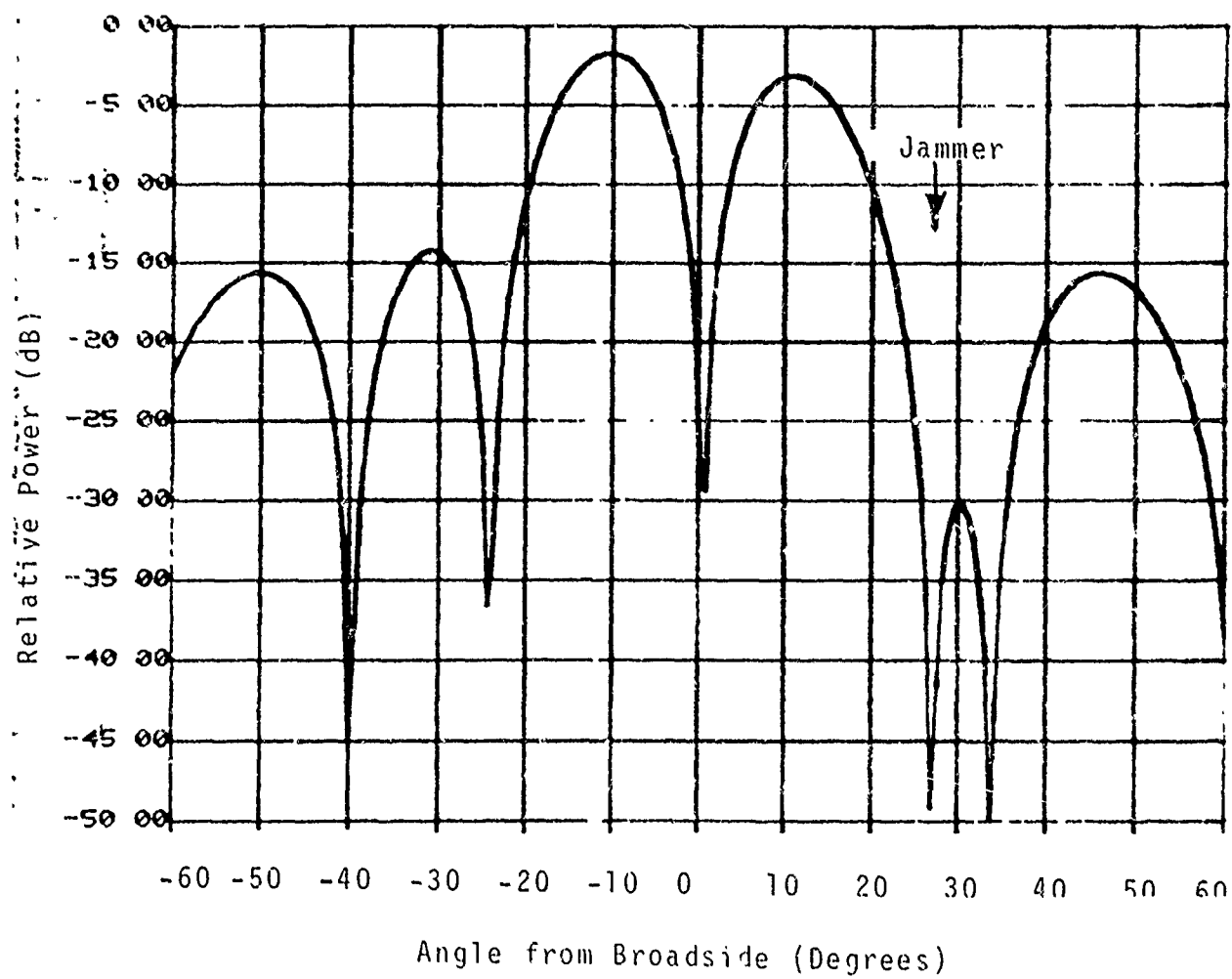
Figure 4.2.2-9. Adapted Difference Pattern for
27^C Jammer

39
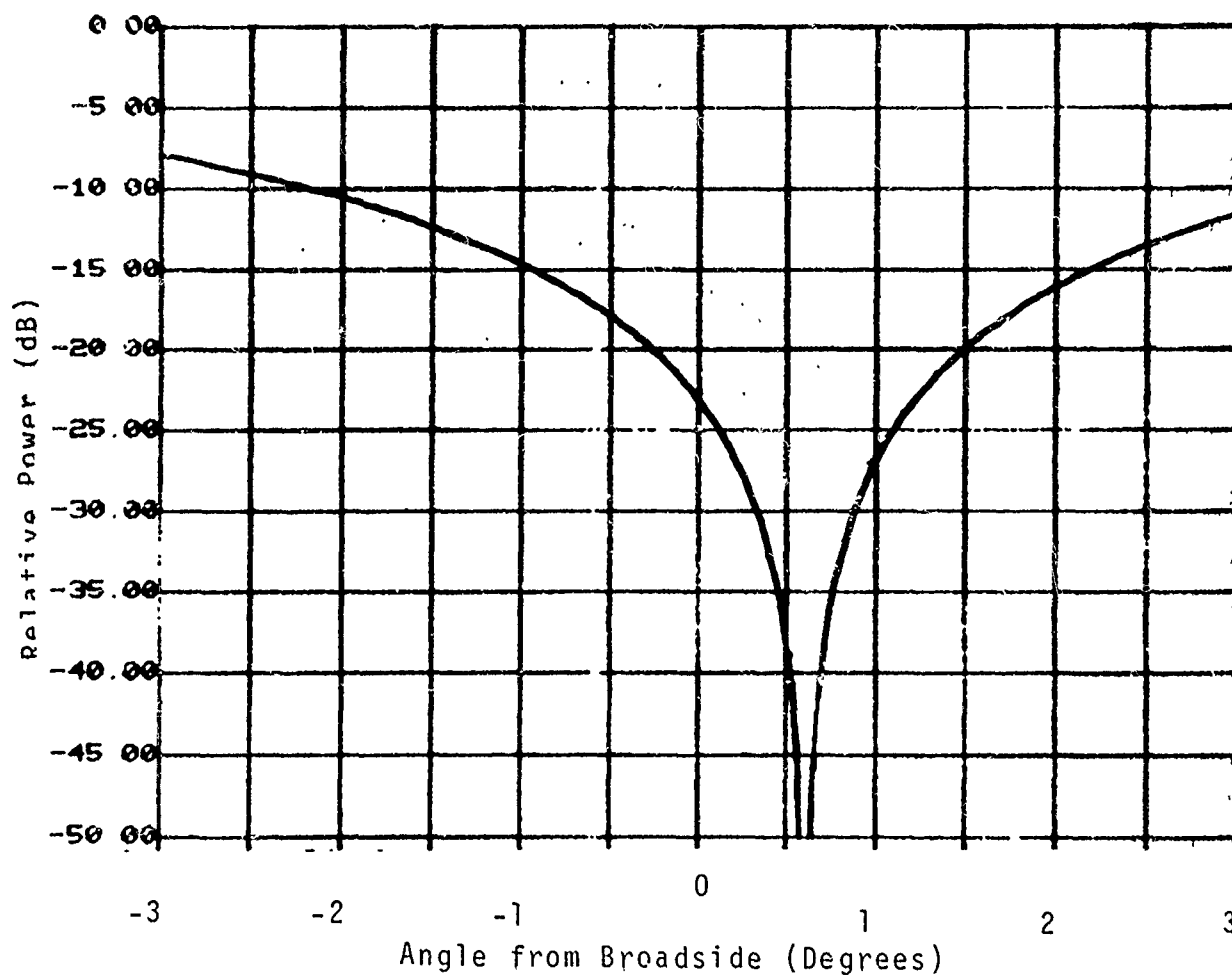
Figure 4.2.2-10.   Adapted Difference Pattern
Expanded Near Boresight

40
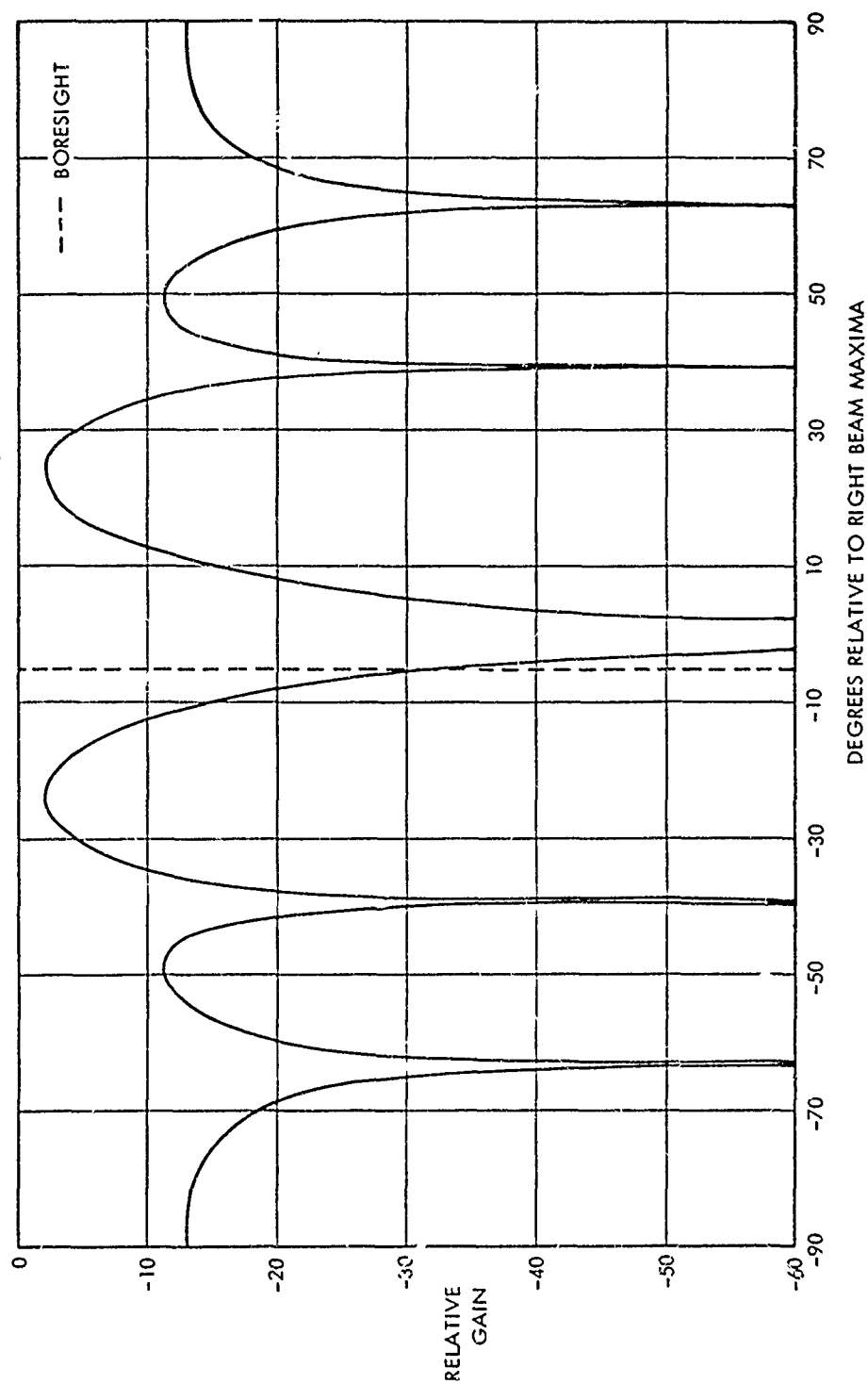
Figure 4.2.2-11 Perfect Cancelling Beam for Right Beam, $\theta_j = 27^0$
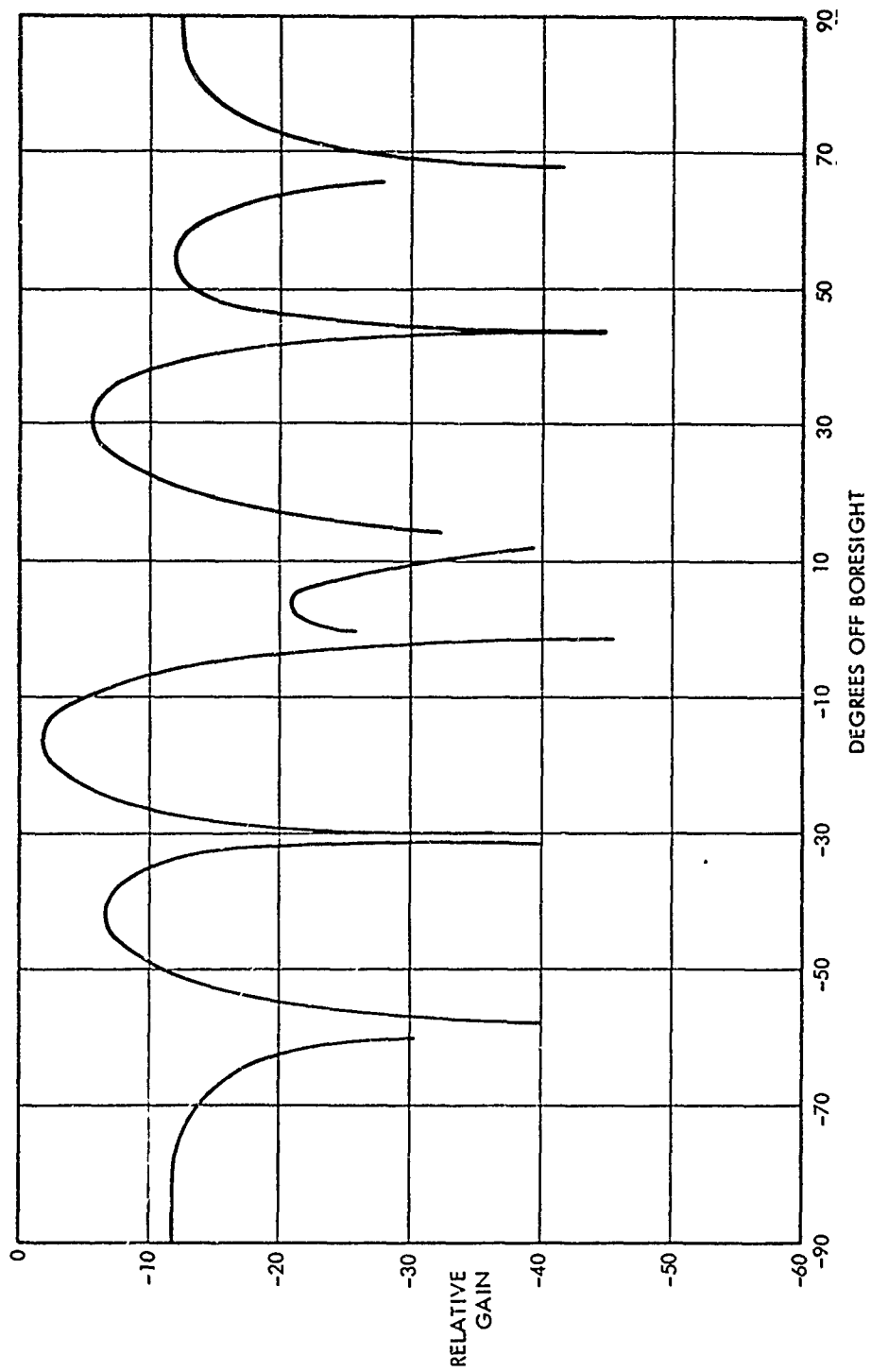
Figure 4.2.2-12 Perfect Cancelling Pattern for a Difference Beam, $\theta_j = 27°$, (8-element array)

42

Table 4.2.2-2. Specific Calculation Values for 27° Jammer
Cancelling Beam

Ratio of SLL 27°/Peak of Right Beam: -13.5 dB

Level of Right Cancelling Beam at 27°: -13.5 dB

Ratio of SLL 27°/Peak of Left Beam: -23.0 dB

Level of Left Cancelling Beam at 27°: -23.0 dB

$\dfrac{\text{Left Cancelling Beam 27}^O}{\text{Right Cancelling Beam 27}^O}$: -9.5 dB

$\dfrac{\Delta \text{ Cancelling Beam Level at Boresight}}{\Delta \text{ Cancelling Beam 27}^O}$: -19.58 dB

Ratio of Δ Beam Level at 27°/Peak: -9.0 dB

Level of Cancelling Beam at Boresight: -28.58 dB

Azimuth Angle for -28.58 dB Level of Unadapted

Δ Beam: 0.28^O

Boresight Shift: 0.28^O

4.3   Extrapolation of Results to Larger Arrays

The results given in this report are mostly for small arrays. A practical monopulse array might have hundreds of elements, and for this reason it is necessary to extrapolate the results presented here. This can be done easily, as there is no basic theoretical difference between a large array and a small array. For clarity, the boresight shift error due to null steering and due to random errors will be discussed separately.

4.3.1   Optimal Complex Weight Nulling for Larger Arrays

In Appendix A, an expression is given for the boresight shift error due to optimal null steering,

$$\Delta n \; (rad) = \frac{\frac{-J/\sigma^2}{1+NJ/\sigma} \sin\left(\frac{N\theta}{2}\right)\left(\frac{N-1}{4}\sin\left(\frac{N+1}{4}\theta\right) - \frac{N+1}{4}\sin\left(\frac{N-1}{2}\theta\right)\right)}{\frac{\pi N}{12}(N^2-1)\sin^3\frac{\theta}{2}}$$

$$(4.3.1-1)$$

where:

N = the number of elements

J = the input jammer power

θ = the jammer electrical DOA

σ^2 = thermal noise

The boresight shift error is inversely proportional to N^3. If this boresight shift is normalized to the beamwidth which is proportional to $1/N$, then the result 's a $1/N^2$ dependence. This dependence can be explained using cancelling beam concepts. At a fixed jammer DOA, as the size of an array is increased, the sidelobe structure of the antenna pattern is squeezed towards boresight, so the jammer enters an increasingly lower sidelobe level. The sidelobe gain, with respect to

44

isotropic conditions, is decreasing in power level by $1\sqrt{N}$. Further, the main beam voltage gain of the array is increasing by $\sqrt{N}$. Thus, the ratio of sidelobe voltage to the main beam voltage is proportional to $1/N$, as shown by the well known pattern function for N element arrays with uniform illuminations. The same sidelobe dependence of $1/N$ occurs for the cancelling beam, so the net effect is a $1/N^2$ dependence of the cancelling beam sidelobe voltage at boresight. This type of dependence means that the boresight shift due to optimal null steering becomes very small for far-out sidelobes in large arrays. Therefore, the source of boresight shifts is almost entirely due to random errors.

4.3.2 <u>Optimal Phase-Only Weight Nulling for Large Arrays</u>

Extrapolation of phase-only null steering to larger arrays represents a more complicated situation. Analytic expressions, such as that given above, are extremely cumbersome. Simulation results show that the sidelobe structure of the cancelling beam is approximately 3 dB higher than the optimal complex weight cancelling beam. The boresight shift error is strongly dependent on array size as is indicated by the results of Paragraph 4.2.2. The dependence on array size using phase-only weights is approximately the same as using complex weights although the sidelobe levels of the cancelling beam for this can be somewhat higher than for the complex weight. This might be expected, since by forming two lobe cancelling beams when using phase-only weights, there is a possibility that side-lobe level of the two lobe cancelling beams near boresight will be 6 dB higher than the cancelling beam using complex weights.

It must be emphasized that for a "reasonable" main beam sidelobe level of -20 dB, either type of cancelling beam will be down -35 dB from the main beam peak near boresight,

thus causing boresight shift errors of less than 0.015 beam-
widths. Since random construction errors may create amplitudes
of this level near boresight, they dominate the boresight shift
error even when the adaptive process is cancelling jammers at
sidelobe levels of less than -20 dB of large arrays. A com-
parison between a fully adaptive complex weight array and a fully
adaptive phase-only weight array is given in Table 4.3.2-1, for
the case of nulling a jammer entering at the peak of the first
sidelobe.

4.3.3   Omni Canceller Nulling

A somewhat different and less desirable situation
arises when omnidirectional cancelling beams are used for null
steering. In this case, the cancelling beam has no sidelobe
structure, so the boresight shift error dependence on array
size is that of the sidelobes of the main beam (that is 1/N).
The magnitude of the boresight shift error for a given jammer
DOA is higher because the omnidirectional beam at boresight
is at least 10 to 15 dB above the optimal cancelling beam.
This optimum cancelling beam is produced by either complex
weights or phase-only weights. Because the level of an omni-
directional beam is independent of the jammer DOA, it is
possible to find the boresight shift as a function only of side-
lobe level to be nulled. This is plotted in Figure 4.3.3-1
using some simulation results.

4.3.4   Random Construction Error Effects

The group of simulations presented here calculates
the boresight shift due to random excitation errors across the
array. These random errors were introduced at each adaptive
weight, and the resulting boresight shift error was calculated.

46

Table 4.3.2-1 Boresight Shift for Optimal Versus Omni-Null Steering

First Near-In Sidelobe Level to be Cancelled*	Optimal Nulling with Complex Weights		Optimal Nulling with Phase-Only Weights		Omni Cancelling Beam
	Beam Level Boresight	Boresight Shift**	Beam Level Boresight	Boresight Shift	Boresight Shift
-20 dB	-33.5 dB	0.015 Beamwidths	-30 dB	0.022 Beamwidths	0.06
-30 dB	-47.9 dB	0.003 Beamwidths	-45 dB	0.004 Beamwidths	0.022
-35 dB	-56 dB	0.0011 Beamwidths	-53 dB	0.0015 Beamwidths	0.015

*All levels relative to sum beam peak
**These are worse-case boresight shifts found by matching sidelobes. Interference entering the first sidelobe (-20 dB) of a mainbeam would have a worse-case shift due to the first sidelobes of the cancelling beam, etc.

BORESIGHT SHIFT (FRACTIONAL BEAMWIDTHS)
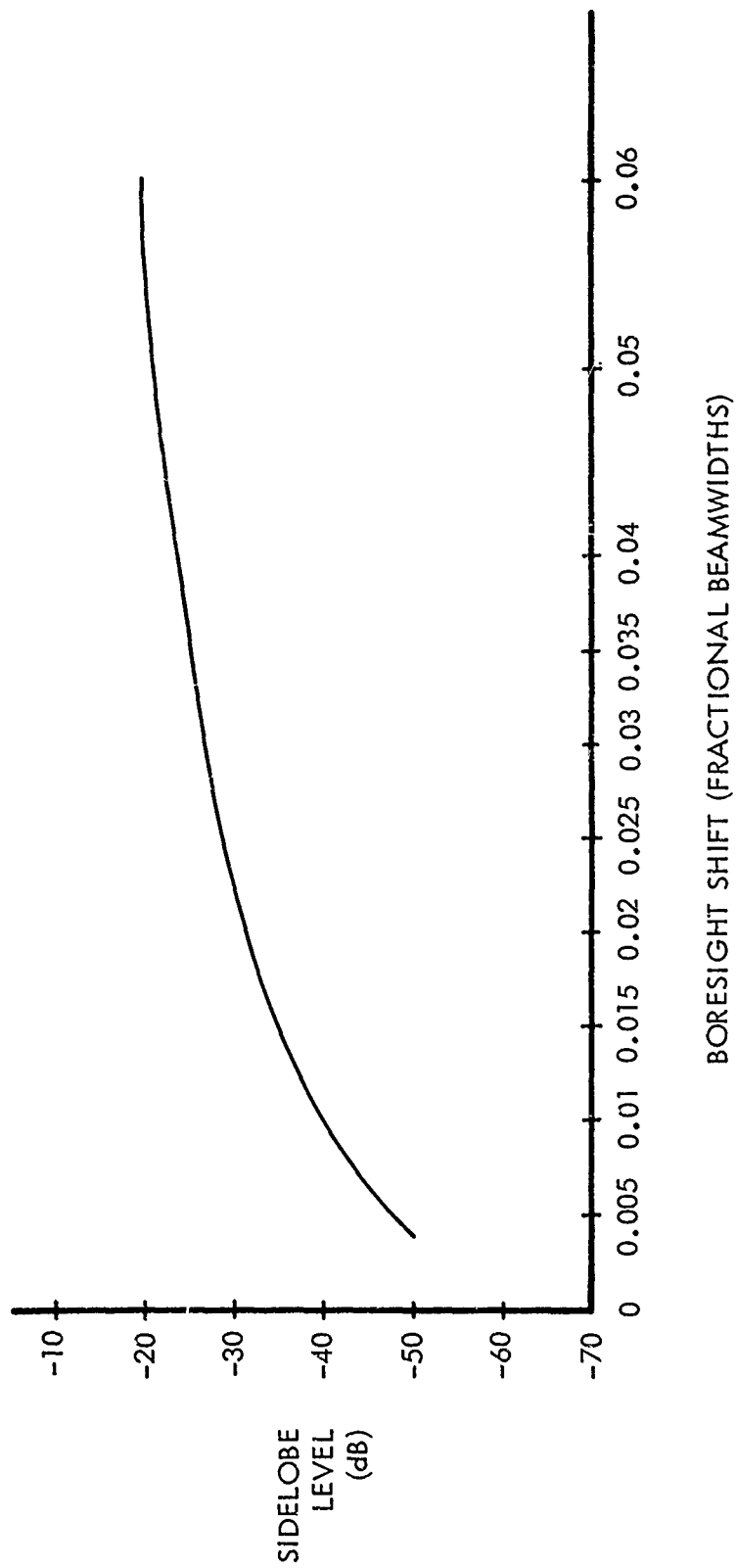
Figure 4.3.3-1   Boresight Shift Vs. Sidelobe Level for
Omnidirectional Cancelling Beams.

48

This process was repeated 30 times and averaged. The results of this calculation are plotted in Figures 4.3.4-1 through 4.3.4-4 and consist of boresight shifts with random phase errors, random amplitude errors, random phase and amplitude errors together, and random phase and amplitude errors with null steering, respectively. William H. Nester has computed the expected boresight shift due to these types of errors for phase comparison monopulse arrays (Reference 2). His results are also plotted on these graphs. The general result is that the effect of these errors should decrease as the square root of the degrees of freedom. The amplitude comparison monopulse array simulated here had two phase shifters per element; the number of degrees of freedom can then be considered to be twice the number of elements.

The theoretical results of Nester have been extended to include two degrees of freedom per element, and are also shown on the same graph. The agreement between the simulation results and extended theoretical calculations is satisfactory although the theoretical calculations are for phase comparison monopulse arrays instead of for amplitude comparison monopulse arrays.

The cases of random phase and amplitude construction errors with and without null steering are plotted in Figure 4.3.4-4. This figure shows that for eight elements the boresight shift due to random construction errors and the boresight shift due to null steering tend to add. However, for the larger array, the random construction errors across the array completely dominate as the source of boresight shift and there are no significant contributions due to null steering.

It is possible to explain random errors with cancelling beam concepts. The effect of random errors across an array is to cause error-limited sidelobes. These sidelobes are usually fairly low level, but they cannot be lowered relative to omnidirectional gain by increasing array size.
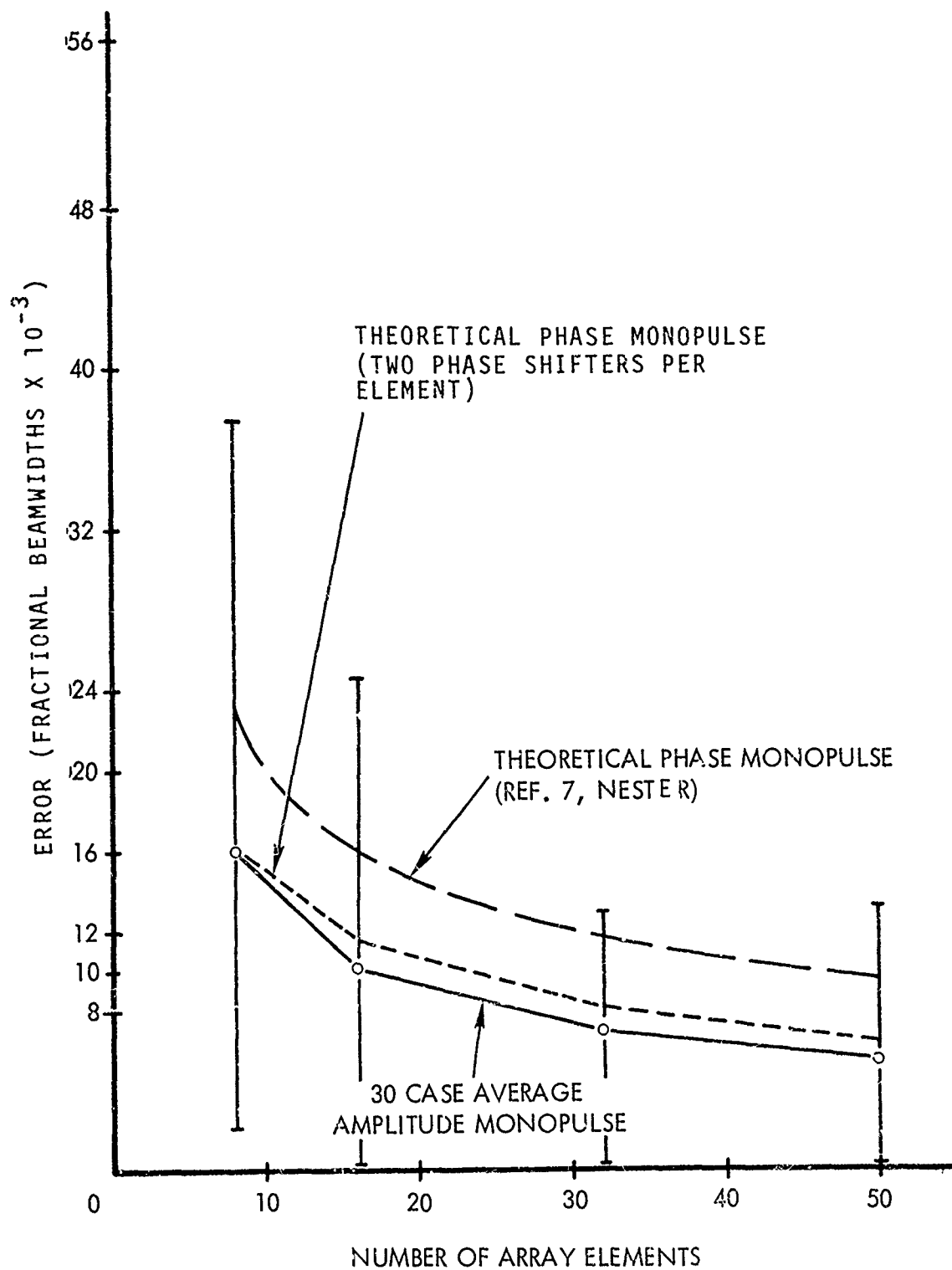
Figure 4.3.4-1   Boresight Shift Error Due to
Random Phase Error of 6°

50
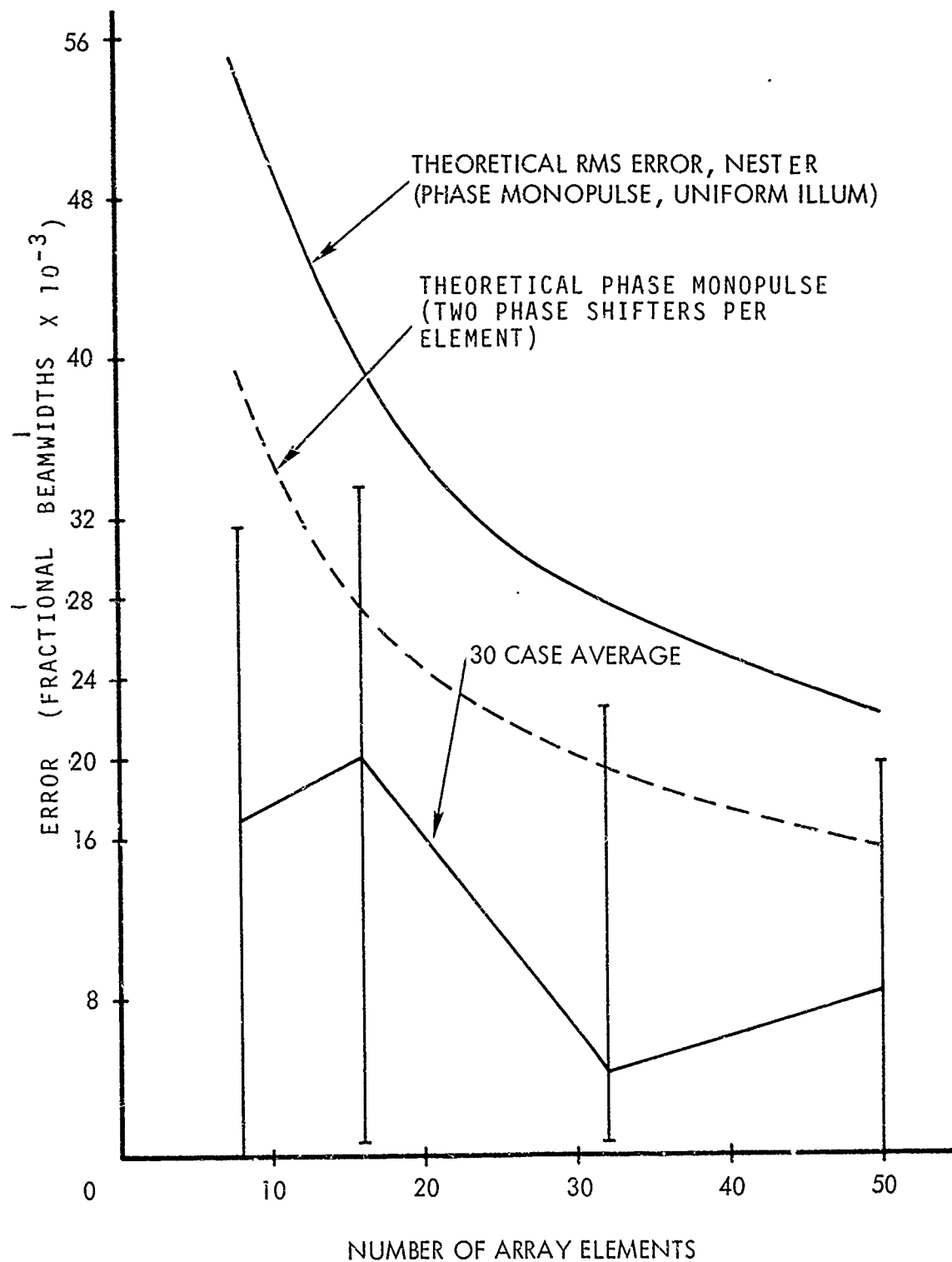
Figure 4.3.4-2 Boresight Error Due to Random Amplitude Errors of 0.1

51
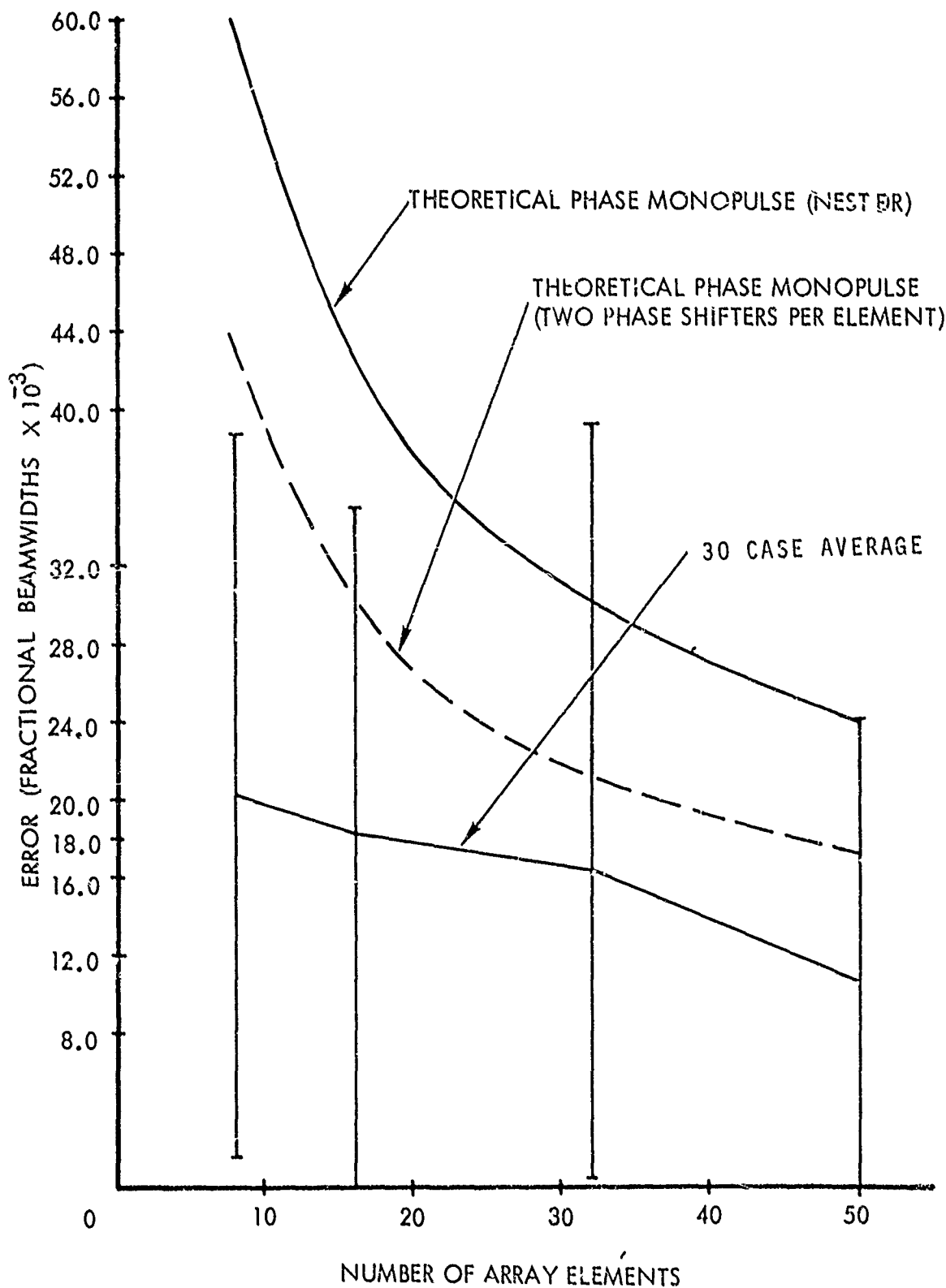
Figure 4.3.4-3. Boresight Error Due to Random Phase and
Amplitude Errors (6° and 0.1)
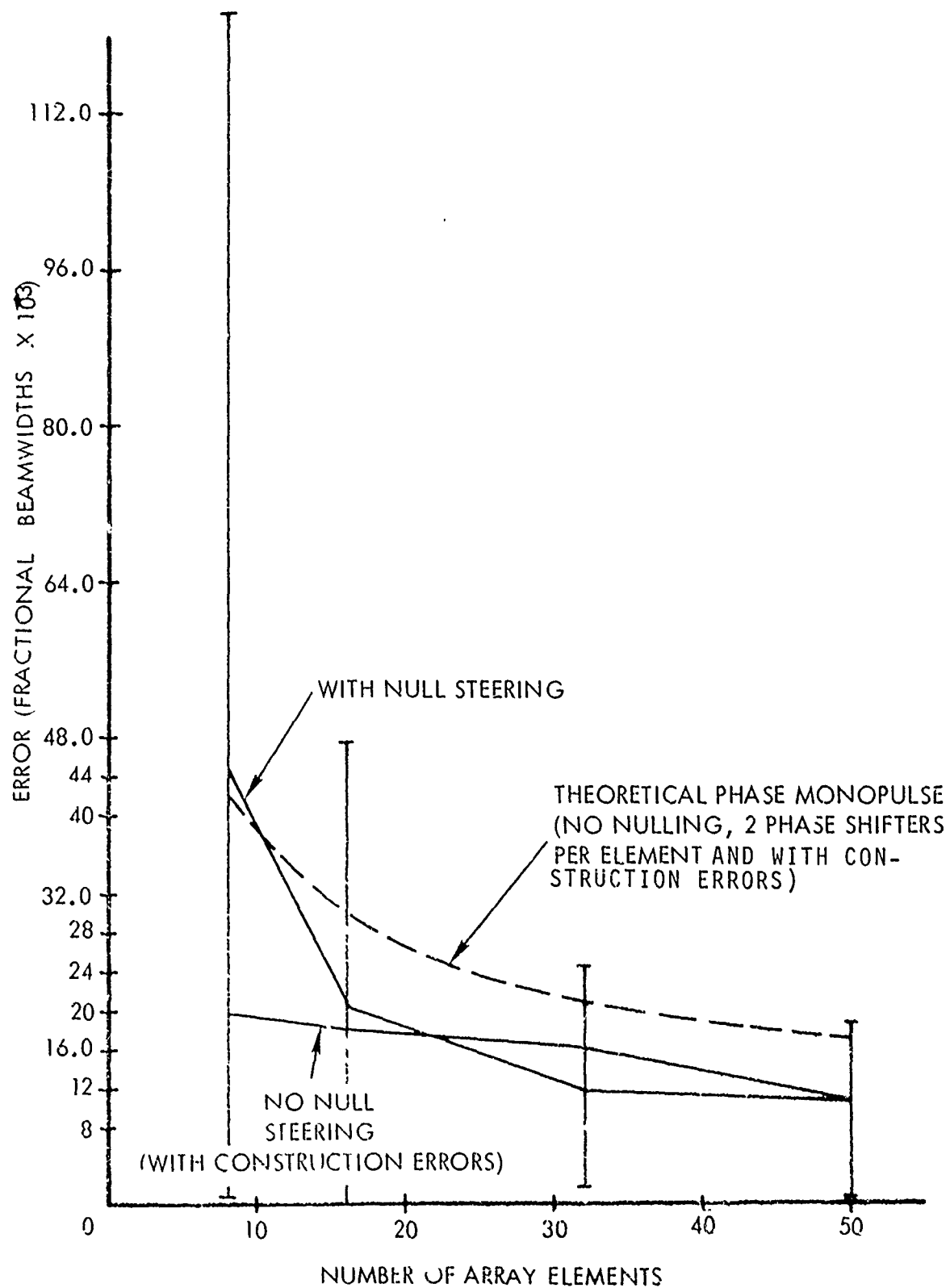
Figure 4.3.4-4 Boresight Shift Error Due to Random
Phase and Amplitude Errors with Null Steering

53

Therefore, their relative level with respect to the array gain decreases as 1/N. The boresight shift error caused by these random errors might be regarded as being due to an omni-directional beam at the level of the error limited sidelobes. Although these sidelobes are low, the undesirability of an omnidirectional, cancelling beam, as discussed above, means the boresight shift due to these errors could be relatively large. By interpreting Figure 4.3.3-1 as a plot of boresight shift due to error limited sidelobes, it can be seen that an error limited sidelobe -40 dB from main beam will produce a boresight shift error of approximately 0.01 beamwidths. Also, because the boresight shift error due to these construction errors decreases only by the square root of N, it is the dominant source of error for large arrays, while optimal null steering effects become negligible except perhaps for highest close-in sidelobes.

4.3.5   Main Beam Nulling

Finally, it is important to realize the limitations of null steering techniques in monopulse tracking. It is shown in this report that if null steering is performed in the main beam of a difference pattern, the concept of having a boresight rapidly becomes meaningless because of pattern distortion. We have shown in Appendix B that the first order expressions for boresight error by Technology Services Corporation, are not useful for main beam null steering. However, it may be possible in the future to rather accurately predict the main beam distortions, and thus regain monopulse tracking even when nulling in the main beam.

SECTION V

EXPERIMENTAL MEASUREMENTS

This section describes the experimental amplitude comparison monopulse breadboard and the monopulse null-steering measurements taken to determine boresight shift errors due to the null steering.

5.1 Description of Experimental Breadboard

The phased array used for the monopulse null-steering measurements was a modified version of the 16-element phased array used on the Null-Steering Feasibility Demonstration Contract F33615-74-C-1100 from Air Force Avionics Laboratory (AFAL). This breadboard was chosen for the monopulse measurements because it was available, and also because it represents an important class of fully-adaptive arrays.

5.1.1 Description of the Basic Phased Array Breadboard

A photograph of the complete breadboard array test setup is shown in Figure 5.1.1-1. The test setup consists of four basic components: 1) array chassis, 2) a unit containing all computer input and output buffers, 3) Datacraft general purpose computer, and 4) ASR 33 teletype unit. The array chassis components are shown in Figure 5.1.1-2.

The overall block diagram of the originally unmodified breadboard array is shown in Figure 5.1.1-3. The antenna aperture consists of a linear array of 16 C-band spiral antenna elements. The breadboard array was designed to operate over a frequency range of 4.4 to 4.6 GHz. A phase shifter (phase weight) located behind each antenna element was used to control the main beam and to form antenna pattern nulls in the direction of undesired signals. In order to obtain vernier phase control, a 9-bit phase shifter design was utilized as shown in Figure

55
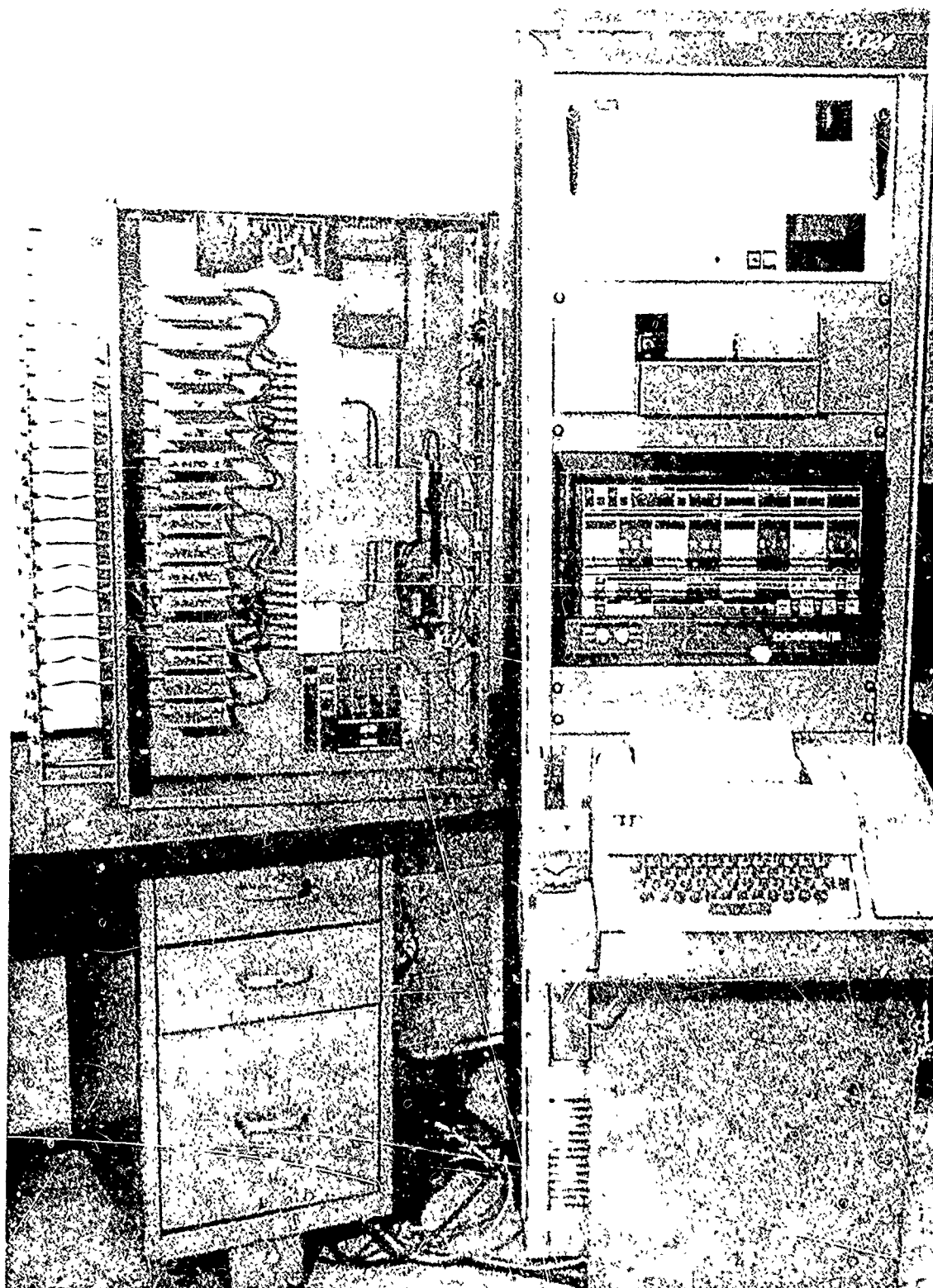
Figure 5.1.1-1   Breadboard Array Model
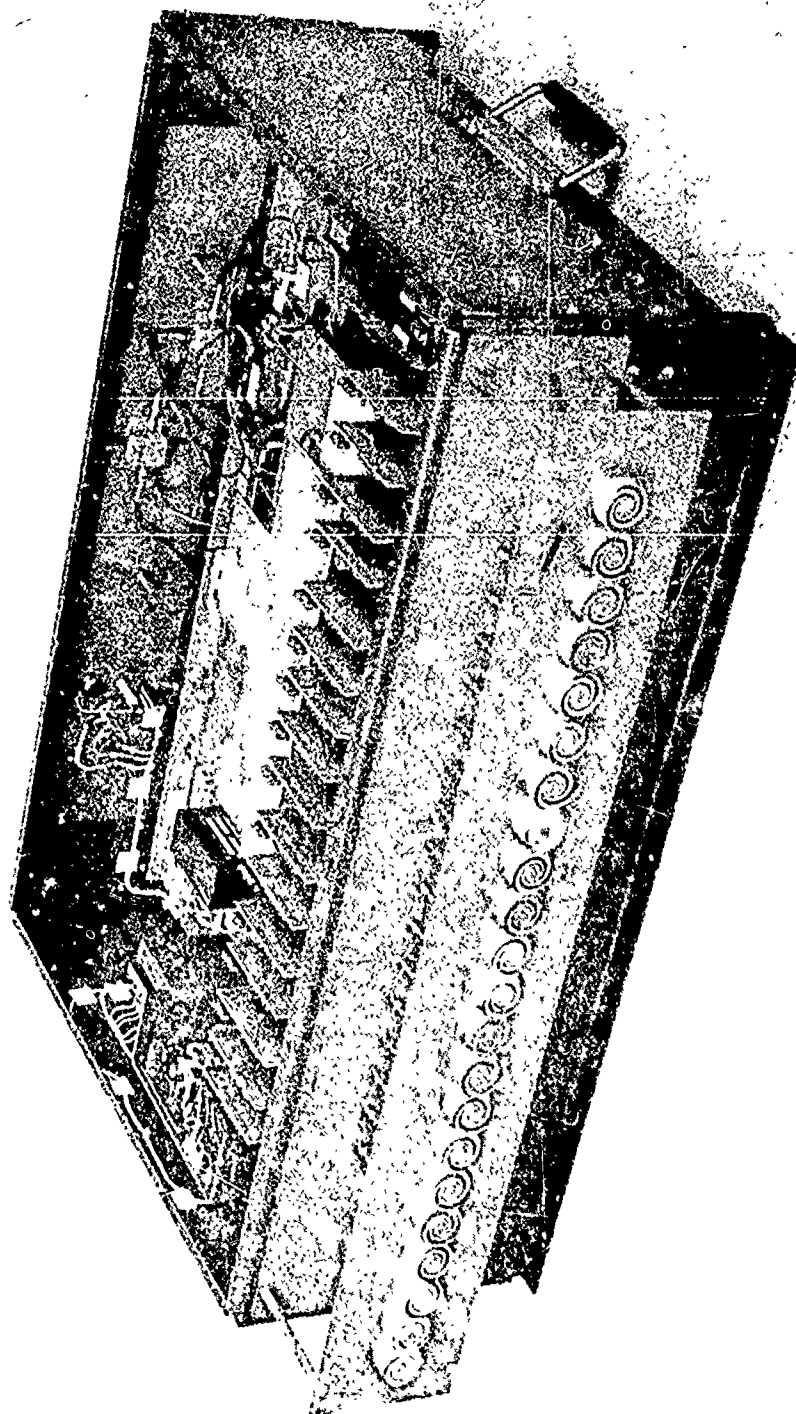
Figure 5.1.1-2 Breadboard Array Chasis

Figure 5.1.1-3 Block Diagram of Breadboard Null-Steering Array.

5.1.1-4. Four of these bits were obtained with a digital phase shifter and the remaining five bits were derived from an analog varactor diode phase shifter through an analog-to-digital (A/D) converter. The array elements were combined through a 16-to-1 power combiner forming the array RF output. The RF output was then mixed down to 300 MHz, amplified and power detected. The detected array output was sampled by the computer using an analog-to-digital (A/D) converter. This digitized (12-bit) output power was then used by the computer software as a performance measure. The breadboard array was under computer control with various optional manual inputs. The 9-bit phase shifter commands were controlled by the computer through an analog-to-ditigal converter and phase shifter drivers. The beam space algorithm that controls this rray was discussed in Section 4.1.1.

5.1.2   Amplitude Monopulse Reconfiguration of the Phased Array

The original 16-element phased array was a sing,2 beam array. It was necessary to reconfigure the phased array to have a monopulse capability. The reconfiguration effort was quite significant and required several months work. It consisted of modifying the array network, constructing and mounting better elements, calibrating and measuring all phase shifters, and calibrating the power detector, as well as measuring a new phase-error detector. It was also necessary to mount the amplitude comparator equipment, and modify the digital control circuitry that had been used together with the original phased array. In addition, it was necessary to modify the control software for the digital computer that would perform the null steering algorithm.

The original array was   reconfigured into an amplitude comparison monopulse array with a left and right beam. Each beam consisted of an 8-element array, and 8 phase shifters,
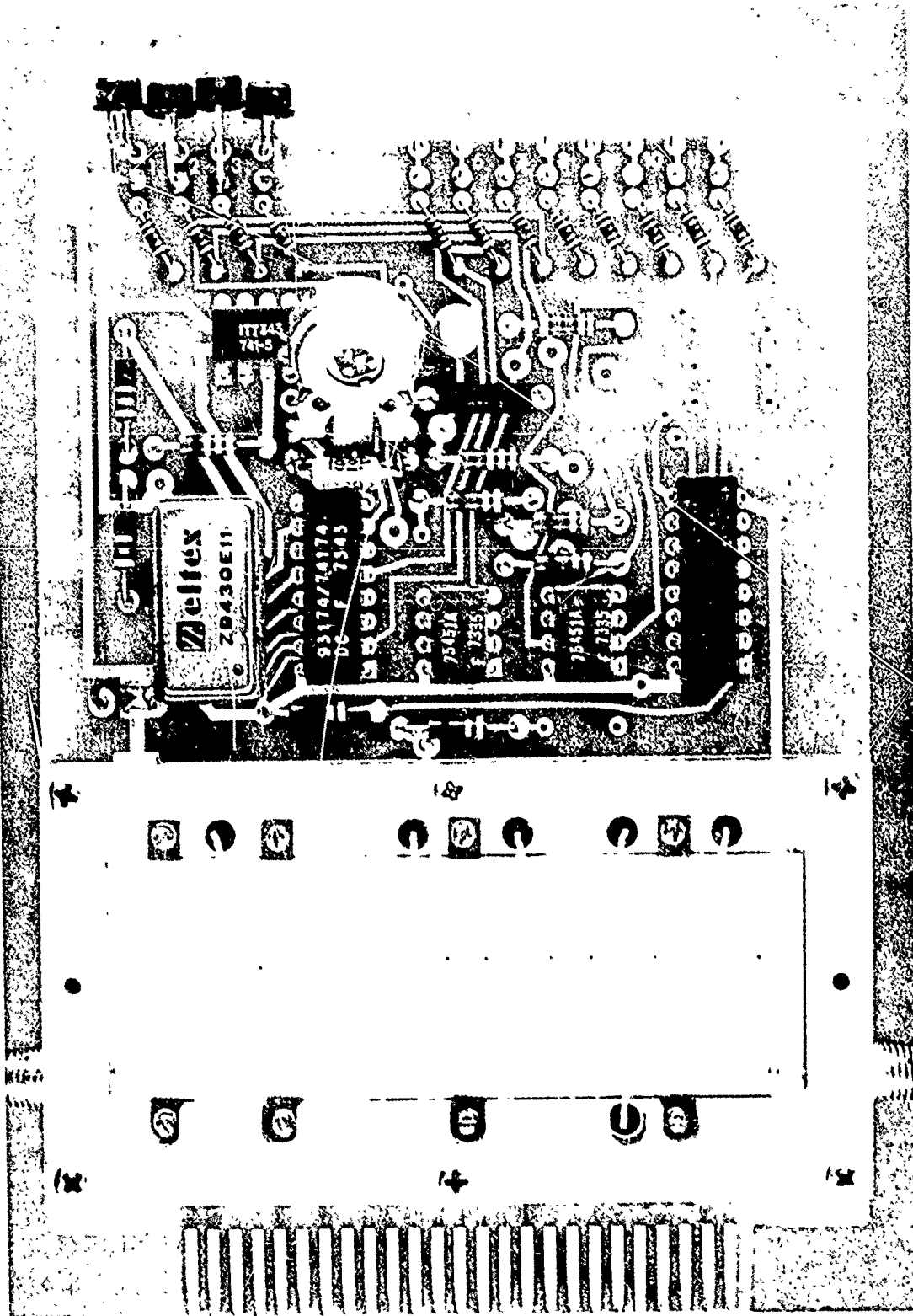
Figure 5.1.1-4 Nine-Bit Phase Shifter

60

summed together to form a beam. Figure 5.1.2-1 indicates how
the amplitude monopulse beams were formed. Eight elements were
shared for both the left and right beams. After each element,
a power divider split the signals into a component that would
form the left beam and one that would form the right beam. After
splitting, a phase shifter was used to align the phase of each
element for each beam, and then an 8-way summer was used to
combine the power for that beam. Normally, an amplifier would
precede the power divider to assure that no S/N degradation
could take place, but in this breadboard the S/N degradation was
accepted since it was not a significant part of the experiment.
A photograph of the front view of the array after being recon-
figured for amplitude monopulse, is shown in Figure 5.1.2-2.
Although many array elements are shown, most are passive and
terminated in a 50-ohm resistance to ensure that the central 8
elements have terminated neighbors such as would occur in a large
phase array. In addition, some absorber is shown on the top
and bottom of the array. The absorber was used to reduce the
effects of reflections in the chamber and outdoor range where
measurements were made. Figure 5.1.2-3 shows a photograph of
a top view of the reconfigured array. To the right of the photo-
graph are the phased array elements, followed by 8 two-way
dividers that split the element signals into the left and right
beam components. Inside the main box, these signals are phase
shifted by the 16 modules shown in the middle right part of the
photograph. Following this, in the left part of the photograph,
there are the hybrids used for 8-way summation. At the top part
of the photograph there is the digital control equipment, which
consists of the D/A and A/D converters that interface with the
digital computer.

Figure 5.1.2-4 is the block diagram of the sum and
difference circuitry used for the monopulse study. RF left and
right beams obtained at the outputs of the eight-way power

61
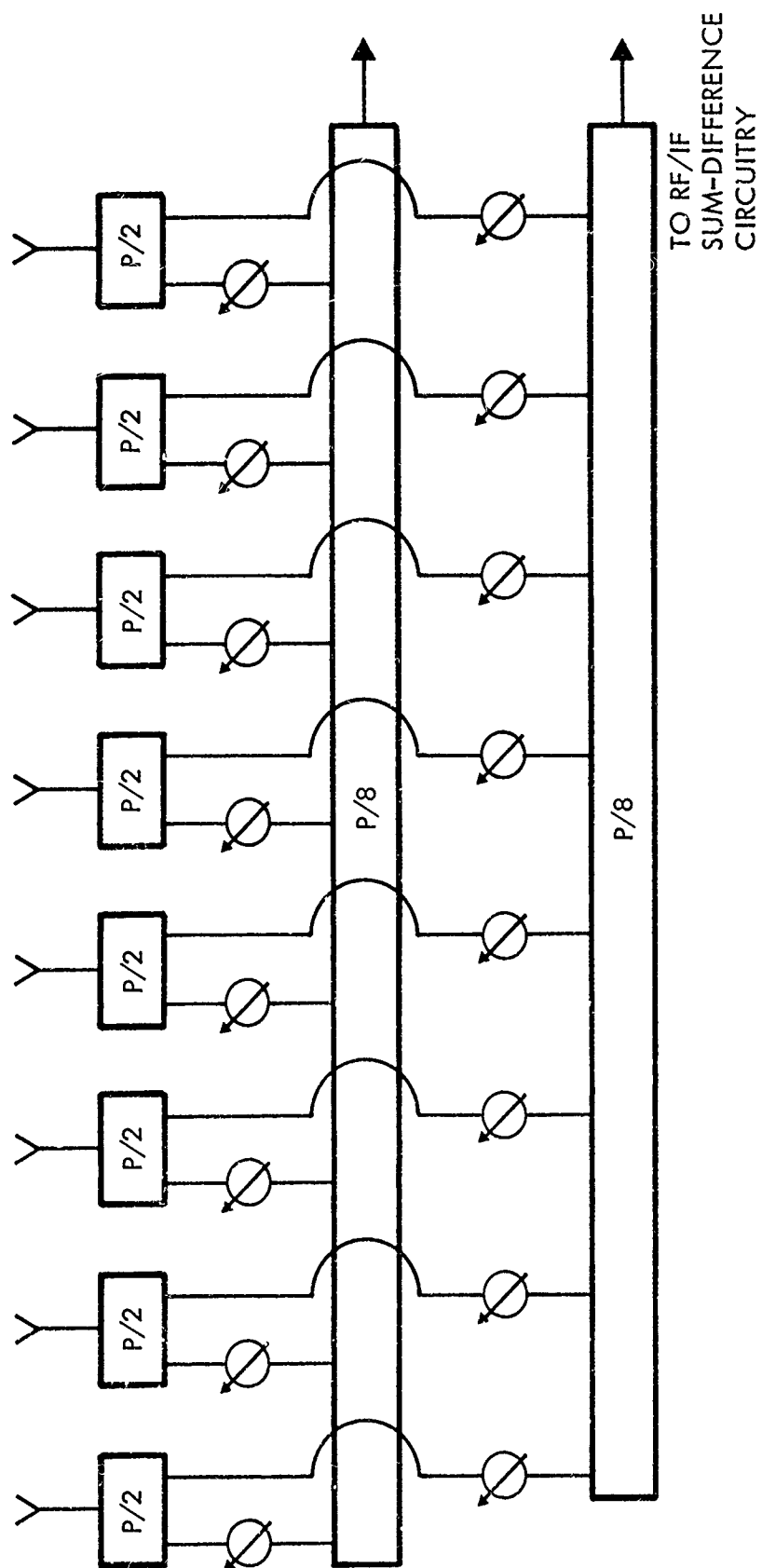
Figure 5.1.2-1 Diagram of Amplitude Monopulse Configuration
of Array Breadboard

62
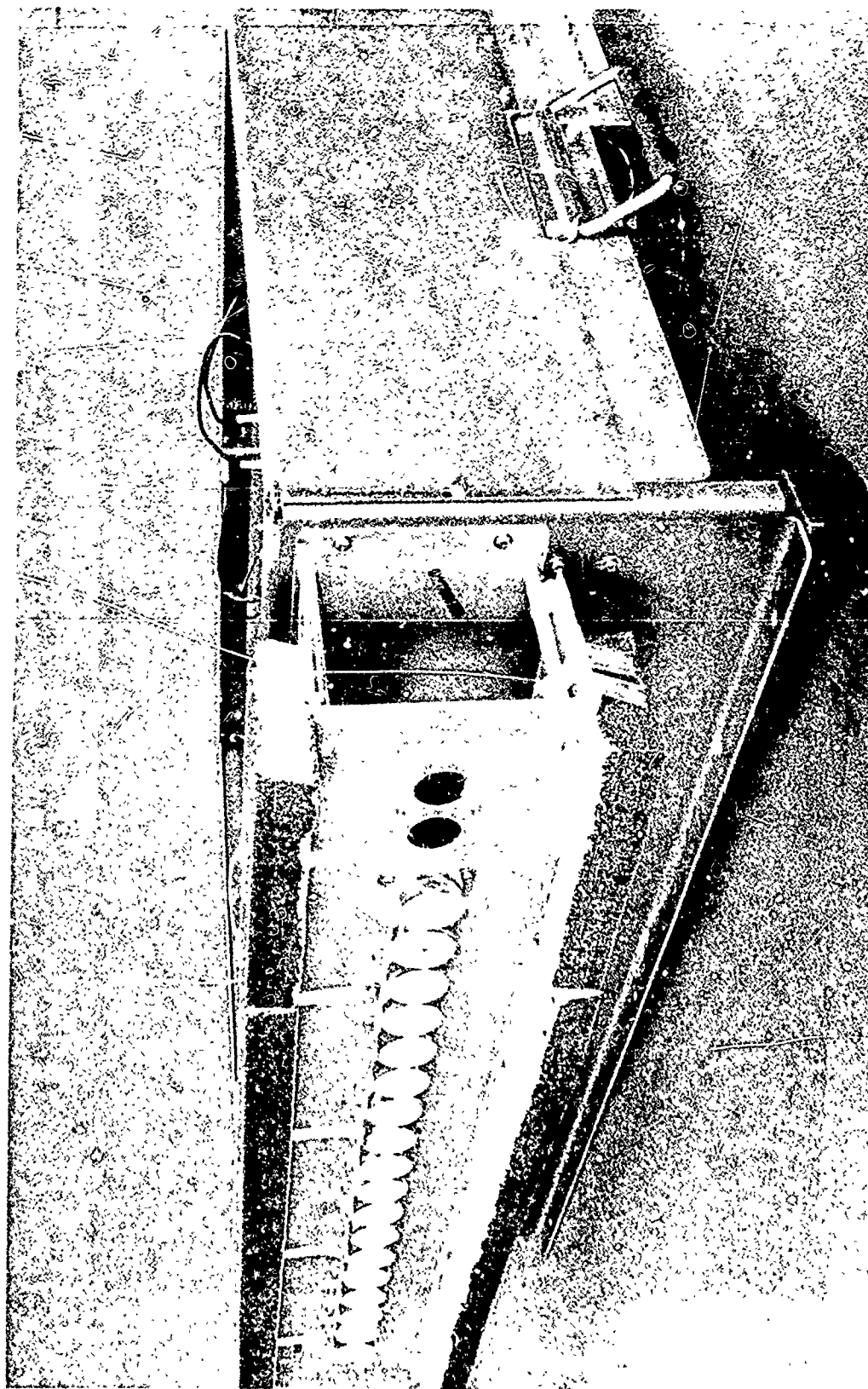
Figure 5.1.2-2   Front View of 16-Element Array Reconfigured
For Amplitude Monopulse
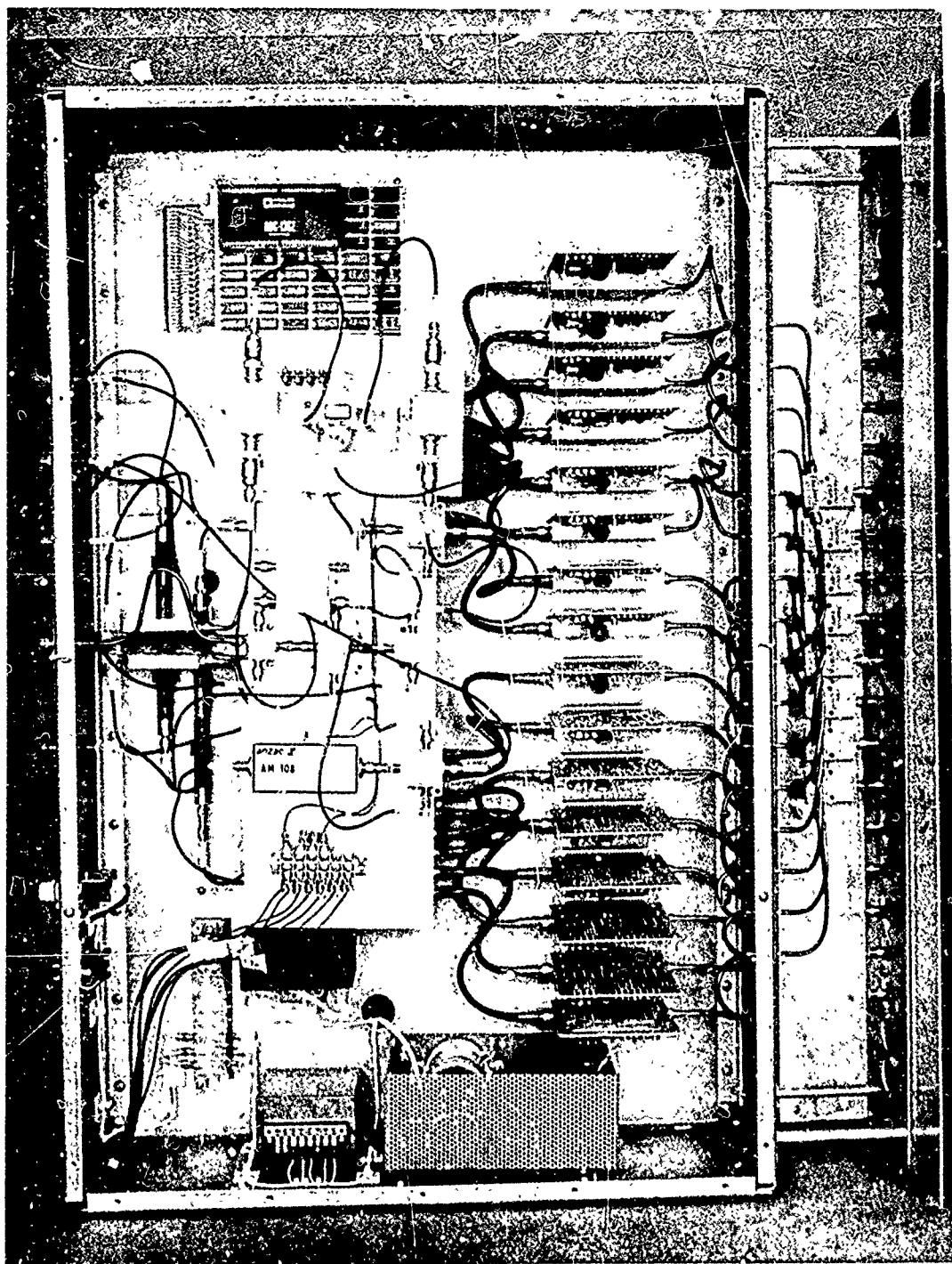
Figure 5.1.2-5 Top View of Reconfigured Array

64
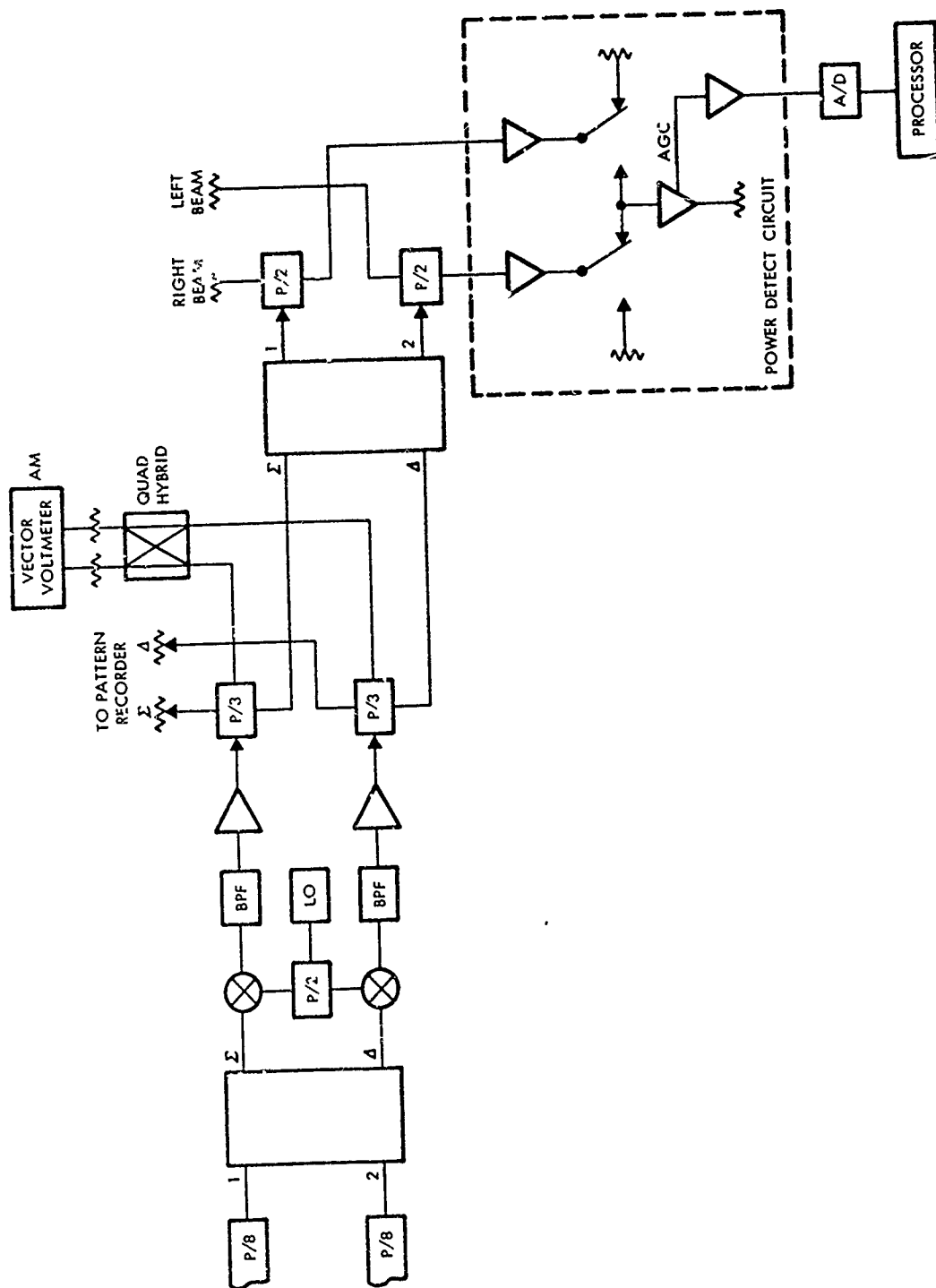
Figure 5.1.2-4 Sum and Difference IF Circuits

65

combiners are fed to ports 1 and 2 of a C-Band sum and difference hybrid. The outputs of the sum and difference hybrid are down-converted to a 300 MHz IF frequency. Band pass filters with a 120 MHz BW are connected after the mixers and, in turn, followed by 27 dB gain amplifiers. The 300 MHz circuits are setup to be used for amplitude or phase monopulse measurements. The amplified IF sum and difference signals are power divided three ways. One set of outputs are used to measure sum and difference antenna patterns. The second set of sum and difference outputs are combined in a quad hybrid. This converts the amplitude monopulse RF network to a phase monopulse output and allows a vector voltmeter to be used as the angle detector for amplitude monopulse measurements. The third set of sum and difference outputs are combined in a sum and difference hybrid to reform the left and the right beam outputs so that patterns could be measured at IF frequency. The left and right beam outputs are divided two ways. One set of left and right array outputs are fed to a recorder to measure the right and left antenna pattern beams. The other set of left and right beam outputs are used to feed the power detector circuit used for null steering the left and right beams in Figure 5.1.2-4. The beam space algorithm employs the total power detected of either the left or the right beam of the array as a performance measure. The algorithm varies the cancelling beam amplitude and phase until a minimum in output power occurs, which indicates a null formed toward the jammer. Only one power detecting circuit is used. This power detector is an amplifier which has an AGC voltage response proportional to the logarithm of the input power. This AGC voltage is digitized by an A/D converter and made available to the computer. The input to the AGC amplifier is switched from the right beam to the left beam, depending upon which beam is being nulled at a given time. A 10 dB gain amplifier is used in both the left and right beam outputs. The purpose of these amplifiers is to isolate the channels from

66

reflections that might cause errors in the power detecting circuit upon switching between the right and left beams.

Extensive calibration of the equipment was performed, and is detailed in Appendix E.

5.1.3   Control Software Development

The software to produce null steering in the breadboard array was a modification of the main monopulse null-steering simulation, previously developed, as described in Appendix C. One of the major differences between the software that is used for simulation of the monopulse array and the software that is used to control the monopulse array breadboards is that the latter continuously controls the 16 phase shifters while the former uses only 8 phase shifters at any one time to perform null steering. The monopulse software in the breadboard array completes null steering on one beam, stores the resulting information and then uses the same memory location for nulling the other beam. In addition, it was found that the software controlling the actual breadboard array had to take into account the beam coupling problem. For example, after the right beam had been properly null steered, the left beam was then null steered. In modifying the phase shifters of the left beam in order to achieve nulls, the beam coupling caused the null to be shallower or to occasionally disappear in the right beam. Thus, it was necessary to make several passes through each beam in order to assure that nulls were formed simultaneously in both beams in the actual breadboard array. The process proved to be convergent, in that a few passes achieved good nulls in both beams, which implies that the coupling was low.

A final, rather significant difference between the software that controlled the breadboard array and the simulation software is that complex beam weights were used in the software that controlled the breadboard. It has been long known that,

with random phase and amplitude errors in an array, the phase
of the sidelobe to be cancelled is random. Thus, the beam space
constant that is required to cancel this sidelobe must also have
an arbitrary phase capability. In contrast, for simulations not
employing phase and amplitude errors, the beam space constant
can be a real constant, and need not have arbitrary phase. Thus,
for the initial simulations, which were developed without ampli-
tude and phase errors, the beam space constant was real. How-
ever, it was necessary to use the software developed for con-
trolling the breadboard in order to perform the final amplitude
monopulse simulations that are presented in Section 4.2.3
because the random amplitude and phase errors simulated made
necessary a complex beam space constant.

In parallel with the development of the beam space
algorithm software, the array-controlling software that controls
weights and forms the actual bits to control the phase shift
drivers was reconstituted using an earlier controlling software
utilized in previous contracts. Using very simple teletyped
inputs, the array was controlled with software in order to test
if the measured calibration corrections included in the software
were successful in producing a good steered beam, as measured
by the antenna patterns. Due to a relatively poor measured null
depth in the left beam, recalibrations had to be performed. The
final steered beam patterns were quite good, thus assuring that
the calibrations of the array errors had been successful.

The null steering software was then linked with the
array-controlling software in order to successfully perform
null steering. First, antenna patterns were taken both before
and after nulling for single jammer locations in several side-
lobes. It was clear from these initial measurements that the
usual antenna pattern on a 360° pattern scale could not be
used to measure the boresight shift in the monopulse pattern,
since this shift was too small to measure on the larger
scale.

68

Thus, the expanded scale of the antenna pattern plotter was used, to accurately measure the boresight shift. The full-scale patterns show the various nulls being formed and the general shapes and changes of the patterns before and after null steering. The following procedure was developed for measuring boresight shift:

a) The monopulse array was commanded with linear phase shifts to form the left and right beams,

b) The antenna was rotated for a null in the amplitude of the difference pattern, as indicated on the expanded scale of the antenna pattern recorder.

c) The vector voltmeter, as shown in Figure 5.1.2-4, was set to 0° phase shift (with the antenna at this angle).

d) The null steering algorithms were employed to simultaneously null the jammers in both the left and right beams.

e) The antenna was rotated until 0° phase was again indicated on the vector voltmeter to get the true boresight null position after null steering.

f) The mechanical angle and the vector voltmeter phase readings were measured and plotted.

g) In several cases, the difference pattern amplitude was plotted both before and after nulling, on the expanded scale of the antenna pattern plotter.

5.2   Measured Boresight Shift and Antenna Patterns

This section consists of the summary of the boresight shift error measurement results followed by a discussion of the corresponding antenna patterns.

5.2.1   Summary of Results

A summary of several of the most important and comprehensive boresight shift error measurements is shown in Table 5.2.1-1. This table summarizes five cases of scan angle and jammer

69

TABLE 5.2.1-1

Summary of Several Boresight
Shift Measurements After Nulling

Case No.	Scan Angle	Jammer Angle	Difference Pattern Sidelobe Level	Difference Sidelobe Number Being Nulled	Boresight Shift Degrees	Fractional Beamwidths*
1	0°	27°	-10dB	1st	0.47°	0.036
2	0°	45°	-11dB	2nd	0.2°	0.0154
3	0°	40°+	-19dB	Minima Between 1st 2nd	0.1°	0.0077
4	0°	-66°	-18.5dB	3rd	0.13°	0.01
5	-30°	30°	-11.5dB	3rd	0.083°	0.0064

NOTES

* Beamwidth $\cong$ 13°

+ Cancelling Beam Pointed Off-Jammer at 50°

70

angle that were investigated. The sidelobe level of the
difference pattern is shown in the table, followed by the differ-
pattern sidelobe number that is being nulled (i.e., first
sidelobe, second sidelobe, etc.). Finally, the boresight shift
error of the monopulse array is shown, both in degrees, and in
fractional beamwidths (where a beamwidth is approximately 13°
for the 8 element array). In each case, the array was preset
and zeroed before null steering. Then only the boresight shift
error resulting from the null steering was measured and
recorded, as discussed in the previous section. The cases are
presented in approximately decreasing order of boresight shift
error. The first four cases pertain to a 0° scan angle for
the main beam of the array, that is normal or perpendicular to
the array face. The fifth case is one in which the beam was
scanned off 30°.

The first case, with the larger boresight shift error,
had a jammer at the first sidelobe which was located 27° off
boresight. The difference pattern sidelobe level at the angle
of the jammer was approximately -10 dB as shown on the table.
The boresight shift error (details of these measurements are
presented later) measured after nulling the jammer was 0.47^O or
0.036 beamwidths.

The case, for this position of the jammer, (first
sidelobe) was discussed analytically in some detail in Section
4.2-2. The computer simulation used did not account for any
array or tolerance errors but yielded a predicted boresight
shift error of $.6^O$. This case exhibits the worst shift error
due to the jammer's position being near the main beam of the
array. This means a high level of sidelobe must be cancelled
near boresight. This position of the jammer requires the can-
celling beam to be very near boresight which, in turn, causes
the greatest boresight shift of any of the cases illustrated.

The second case, shown in Table 5.2,1-1, consisted of
a jammer on the second sidelobe, occuring at 45° and at a -11 dB

71

level with respect to the peak of the difference pattern. The
boresight shift error measured in this case was 0.2° or 0.0154
beamwidths. In this situation, a second sidelobe rather than
a first sidelobe was being nulled. Although the sidelobe level
was still approximately as high as in the first case discussed
above, its angular separation from boresight was greater. The
cancelling beam, then, was also further removed from boresight
thus a lower level of cancelling beam sidelobe existed at bore-
sight. This explains the fact that the boresight shift error
was found to be less than half that of the first case.

The third case, in Table 5.2.1-1, consisted of the jam-
mer existing at a relative minima between the first and second
sidelobes of the difference pattern (a relatively low sidelobe
level of -19 dB at 40°). In this case, the sidelobe level to
be cancelled was lower than previous cases, and the angles of
the cancelling beam and jammer were in between those of the
previous two cases. A still lower boresight shift resulted,
due largely to the lower sidelobe level being cancelled. The
cancelling beam amplitude needed was less. In addition, lower
cancelling beam sidelobes in the region of boresight resulted
in less boresight shift. One particular observation should be
noted about this case. The cancelling beam was not pointed
directly at the jammer, but off the jammer at 50°, even though
the jammer was positioned at 40°. This did not prevent can-
cellation of the sidelobe in the direction of the jammer, but
simply required a somewhat larger cancelling beam in order to
match the sidelobe level and thus obtain a null toward the
jammer. The boresight shift was quite small even with a
relatively large 10° error in the cancelling beam pointing angle,
which indicates that the tolerance of the direction of the can-
celling beam is quite high. Therefore, significant errors can
be made in this beam and still achieve   good nulling with low
boreshift shift error.

The fourth case in Table 5.2.1-1 consisted of a jammer on the third sidelobe, occurring at -66° and at a -18.5 dB level with respect to the peak of the difference pattern. The boresight shift was 0.13^O or 0.01 beamwidths. In this case, both the separation of the cancelling beam from boresight and the low level of the third sidelobe combined to yield a relatively small boresight shift error.

The last case in Table 5.2.1-1 is one in which the main beam was scanned away from boresight to -30°, and the jammer angle was $+30^O$. Thus, the separation between jammer angle and the main beam angle was 60° which was similar to the previous case. Again, the jammer was positioned on the third sidelobe, but due to the relatively poor array properties of the breadboard, the sidelobe level was higher than in the last case (-11.5 dB). However, the measured boresight shift was less than in the last case; 0.083^O or 0.0064 beamwidths. The main reason that the boresight shift was low must again be due to the angular distance between the cancelling beam and the boresight, even if the sidelobe level is considerably higher. Thus, one can conclude that when nulling in sidelobes past the first or second sidelobe, considerably less boresight shift can be expected. This is exactly as predicted and discussed in Sections 4.2.2.1 and 4.2.2.

In summary, it is felt that the above results are quite encouraging for at least two reasons;

a. The actual worst case boresight shift, 0.036 beamwidths, corresponds to approximately 0.1^O monopulse tracking error for a 3° beamwidth. A 50 element linear multiple beam array that Harris built for the ICNS Program has a beamwidth of approximately 3° and a tracking accuracy of 0.1^O due to random phase shifter and construction errors alone.

73

b. This worse case boresight shift error resulted
    from nulling a sidelobe level of -10 dB, which
    is certainly unacceptably high for an opera-
    tional array. The array tested was strictly
    a breadboard non-optimized array with uniform
    amplitude distribution for the left and right
    beams. Although the amplitude comparison
    monopulse array used produced fairly good
    illuminations for both sum and difference patterns,
    the design was certainly not optimized for low
    difference pattern sidelobes. In the case that
    a lower difference pattern sidelobe were nulled,
    as would be the case in an operational array, a
    much lower boresight shift error would be
    encountered. The measurements made with lower
    and further out sidelobes certainly indicate
    that much lower boresight shift errors are
    obtained in these cases.

c. As we will show in later sections, a significant
    portion of the boresight shift error due to null
    steering can be predicted, and thus corrected with
    open loop calculations. Therefore, by such open
    loop "calibrations", still further reduction in
    boresight shifts due to null steering could be
    obtained if required. Nevertheless, the previous
    discussion has indicated that acceptable accuracy
    can be obtained in many cases even without open
    loop corrections.

A great deal of time was involved in each measurement
of boresight shift error since considerable manual switching
and data taking was required in this breadboard test setup.
Thus, due to the extensive time involved, only a few complete
cases were measured that included both boresight shift error

74

and detailed patterns for the left, right, sum, and difference beams. These are discussed in the next section.

5.2.2 Detailed Results

This section discusses the details of the measurements that have been summarized in the previous section, and presents certain other cases for which patterns were taken, but accurate boresight shift measurements not made.

The detailed data presented in Figure 5.2.2-1 is for the first case of a 0^0 scan angle and a jammer located at 27^0. Figure 5.2.2-1a is a plot of the phase detector output both before and after nulling the monopulse array. This phase detector output describes approximately the slope from the conventional monopulse product detector or angle error detector. The plot is of mechanical angle on the abscissa and electrical phase on the ordinate. The plot is taken by varying the mechanical angle and measuring the electrical phase with a vector voltmeter as discussed in Section 5.1. The dashed part of the plot always represents data taken before null steering. The plot was constructed so that a 0^0 electrical phase occurred at 0^0 mechanical angle. The 0^0 mechanical angle corresponds approximately to the mechanical boresight of the array which is perpendicular to the array face.

Thus, this reference angular position should faithfully show the changes in the array that occur during null steering although it may not be exact in terms of mechanical boresight. A conventional monopulse feedback tracking loop will approximately track the 0^0 electrical phase point, and thus have an error of zero mechanical degrees as shown on the "before" plot. After null steering, points were taken manually for the plot of mechanical angle versus electrical angle which is also shown on the phase detector output plot. One can see that the electrical 0^0 phase point which is tracked by the

Figure 5.2.2-1a. Phase Detector Output Before and After Nulling (0° Scan Angle & 270° Jammer Angle)

76

Figure 5.2.2-10. Difference Pattern Before and After Nulling (0° Scan Angle and 27° Jammer Angle)

Figure 5.2.2-1C. Difference Pattern in Expanded Scale at Boresight
(0° Scan Angle and 270° Jammer Angle)

78

conventional monopulse feedback loop occurred at approximately +0.47°, which is a boresight shift error resulting from the null steering process. It was this value that was entered in Table 5.2.1-1.

It is also worth noting that essentially no change in the slope of the error occurred due to the null steering process. Thus, in this case, the sensitivity of the feedback control loop of the monopulse tracking circuitry was not affected by the null steering process since this sensitivity depends upon the slope of the error curve.

Figure 5.2.2-1b shows the difference pattern of the breadboard array plotted at full scale (i.e., ±180° on the lowest angle scale shown on the chart). Approximately ±72° of the antenna pattern is shown. Again, the dashed line shows the pattern taken before null steering. The solid line is the pattern taken after null steering. The pattern after null steering clearly shows that the jammer at 27° has been deeply nulled by nulling the sidelobe at this angle. Note that very little boresight shift occurred in the difference pattern null. However, the angle scale of this chart is too small to accurately measure the boresight shift. It merely confirms that less than 0.5° of boresight error occurred. The precision measurement of all boresight shift errors was done with the phase detector output plot previously shown. Figure 5.2.2-1c shows the difference pattern taken near boresight on the expanded top scale, of the antenna pattern chart. Approximately ±4° of mechanical angle is shown on this chart. Again, the dashed line shows the null of the difference pattern before null steering the jammer, while the solid line shows the pattern after nulling the jammer. As usual, the 0° mechanical angle was set before nulling the jammer so that it occurred at 0°, as shown on the chart. This does not imply that the array was perfectly aligned before null steering, but merely acts as a
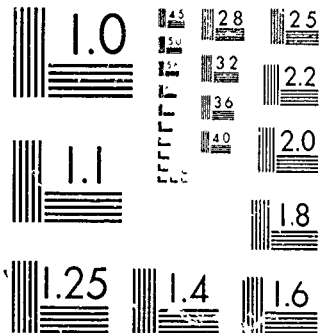
MICROCOPY RESOLUTION TEST CHART

NATIONAL BUREAU OF STANDARDS-1963-A

reference for the <u>differential</u> caused by the null steering itself. As is shown, the shift in null is approximately one-half of one degree, as was more accurately measured by the phase detector output in Figure 5.2.2-1a. Unfortunately, in this measurement, the synchro was reversed so that a "left" shift in this plot is a right shift in the $+72^O$ plot. Note that, as usual, the difference pattern does not necessarily have a deep null, and thus is not used for actual tracking purposes in monopulse arrays. The product or angle detector output, as measured in Figure 5.2.2-1a, is used for all closed loop monopulse tracking.

The next set of antenna patterns illustrated are those corresponding to the second case in Table 5.2.T-1; that of a $\bar{0}^O$ main beam scan and a 45° jammer angle. Figure 5.2.2-2a shows the phase detector output for this case. It is clear from the figure that less boresight shift error occurred, since the shift of the electrical zero (the tracking point of the monopulse feedback loop) is approximately 0.2 mechanical degrees or 0.0154 beamwidths. This boresight shift error is smaller than in the previous case because the second sidelobe rather than the first sidelobe was nulled at 45°. Figure 5.2.2-2b shows the difference pattern taken before and after nulling the jammer, again indicating qualitatively that the main beam boresight region of the antenna pattern was affected very little by the null steering process. Note that the sidelobes were more significantly affected by the null steering process. In particular, as is usual in phase-only null steering, the left side of the antenna pattern raised somewhat as the right side was lowered by nulling, due to the two-lobed cancelling beam. In addition, we note that even the first sidelobe was considerably raised by the null steering process. These sidelobe effects become more significant when nulling a very high sidelobe, such as the -11 dB sidelobe nulled in this case. Especially with phase-only null steering in an operational array, such
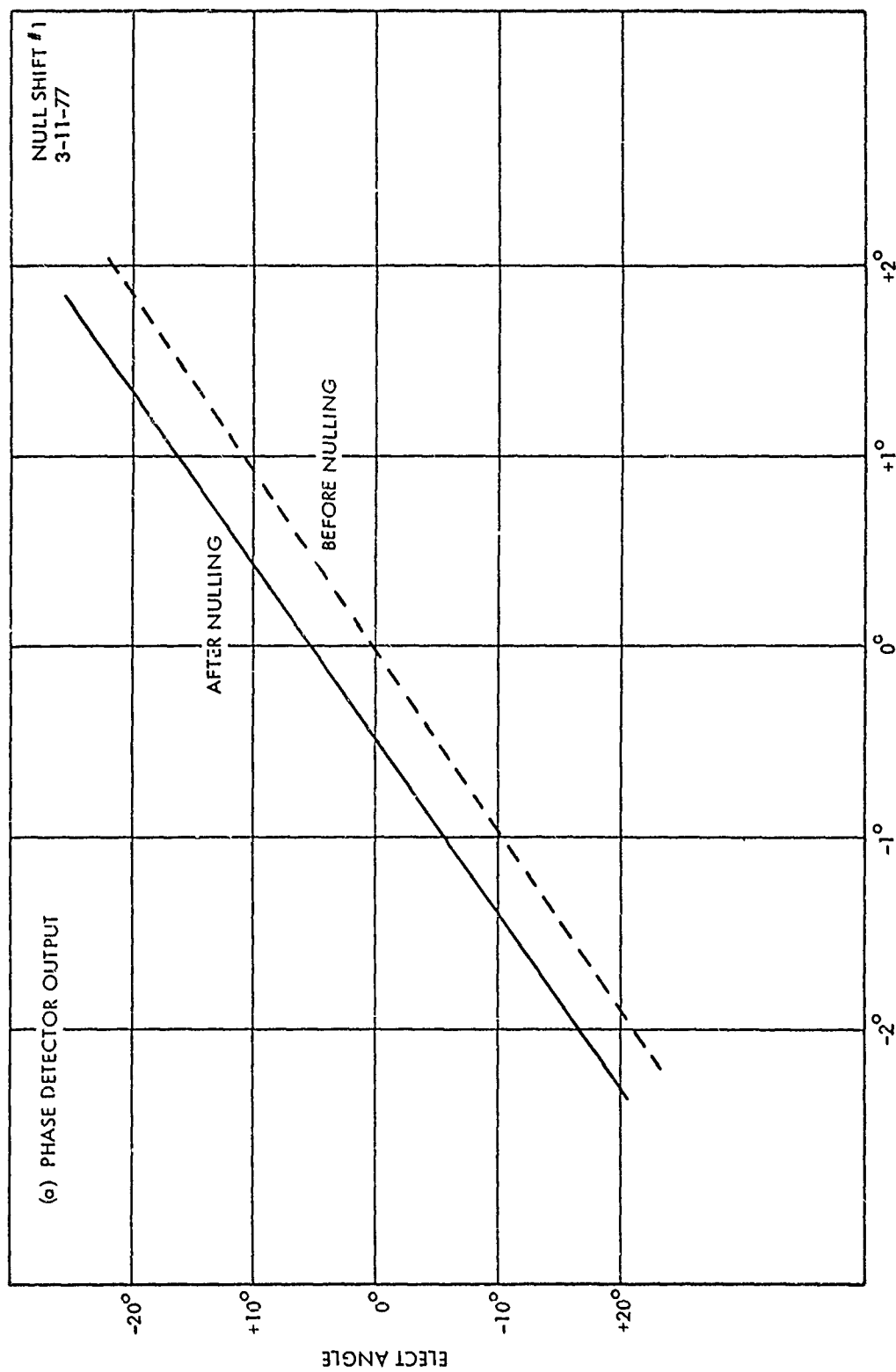
80

Figure 5.2.2-2a. Phase Detector Output Before and After Nulling
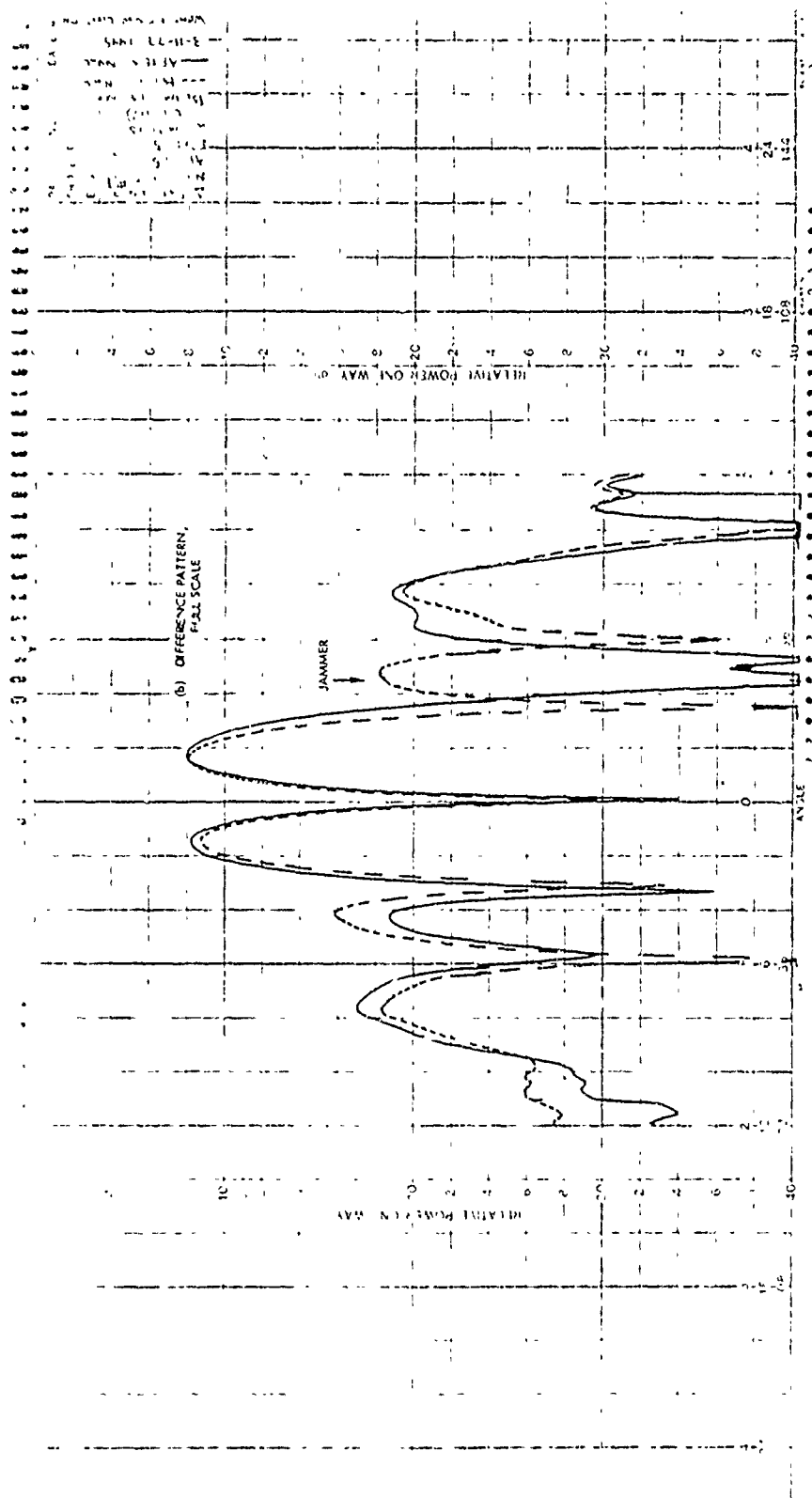(0° Scan Angle and 45° Jammer Angle)
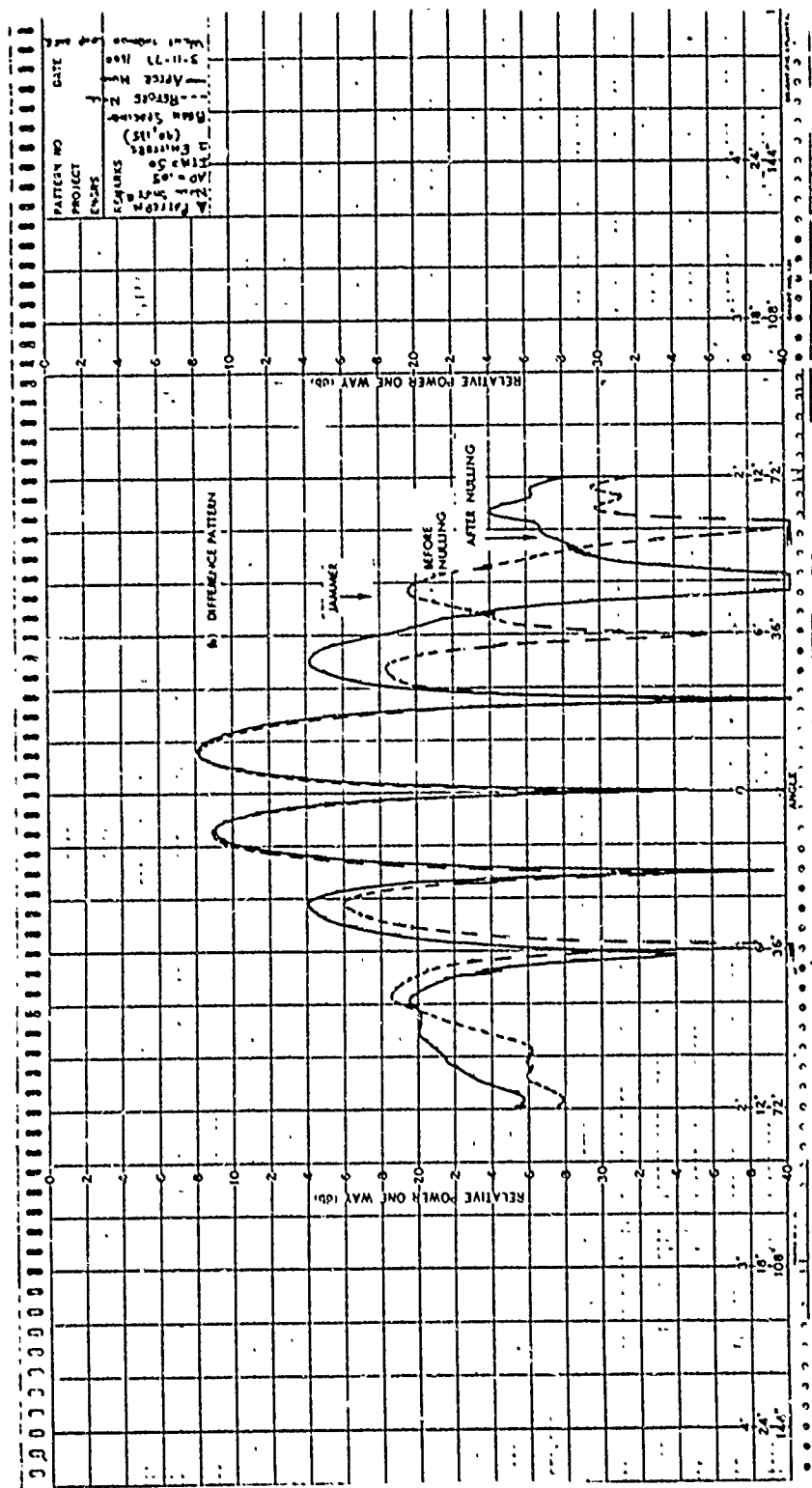
Figure 5.2.2-2b. Difference Pattern Before and After Nulling
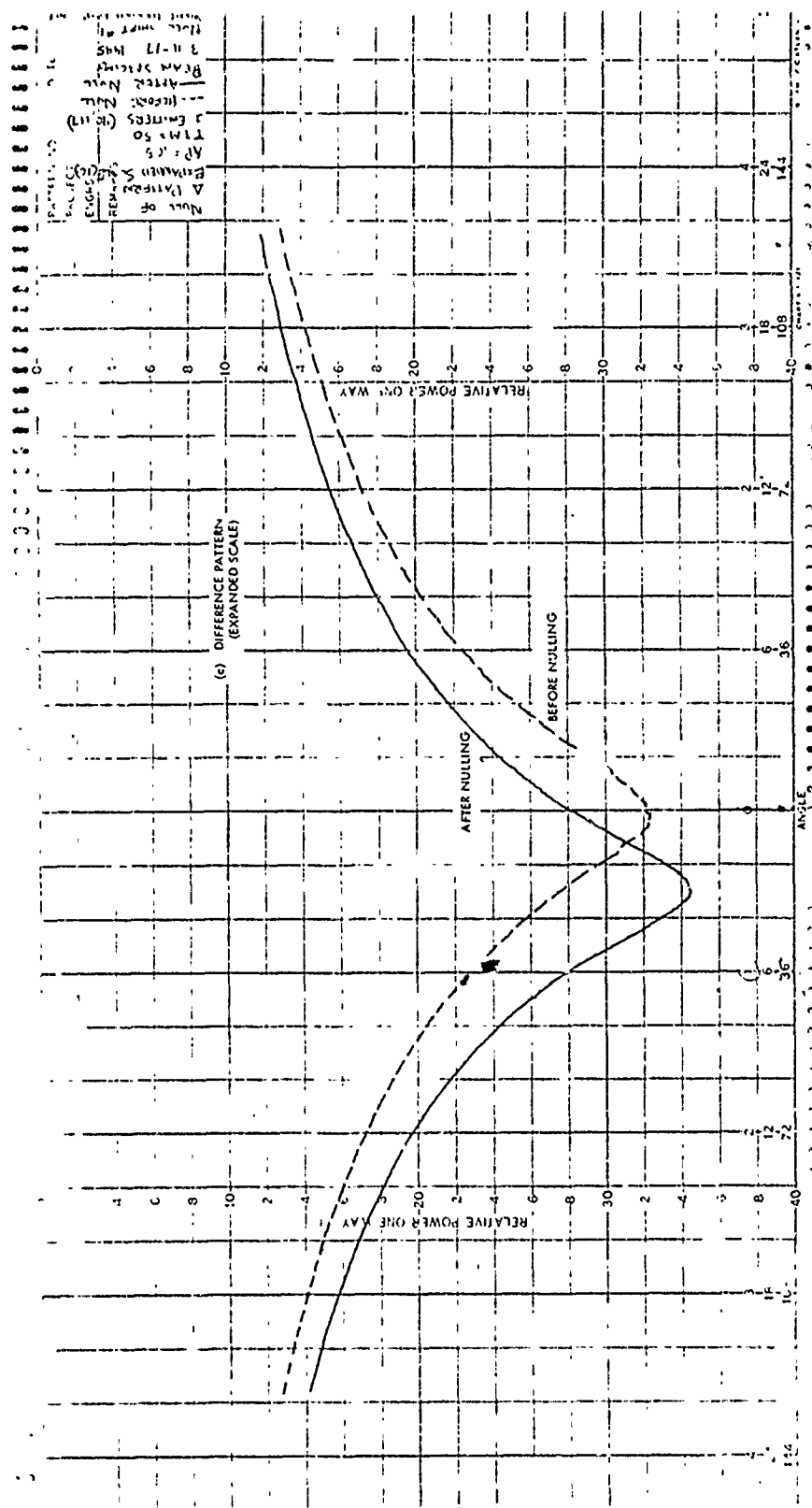(0° Scan Angle and 45° Jammer Angle)

82

Figure 5.2.2-2c. Difference Pattern in Expanded Scale at Boresight
(0° Scan Angle and 45° Jammer Angle)

83
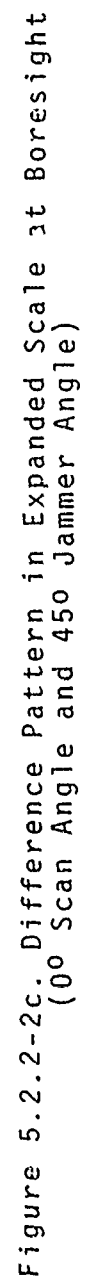
sidelobes are higher than desired. Much smaller changes in
antenna patterns were noted when nulling lower sidelobe regions.
Figure 5.2.2-2c again shows the expanded scale difference
pattern, confirming the null shift indicated and measured more
accurately in the phase detector output plot in Figure 5.2.2-2a.

A more detailed set of patterns for the same case
of nulling a jammer at 45° with 0° scan angle shows the effects
of nulling on all four of the beams that are formed in this
monopulse array: the difference, the sum, the right, and the
left beams, respectively. Figure 5.2.2-3 shows this set of 4
patterns. This particular case was a separate run of the null
steering algorithm. The difference pattern is illustrated in
Figure 5.2.2-3a and the sum pattern in Figure 5.2.2-3b. Again
indicating that the left portion of the sidelobe structure was
raised by the action of null steering on the right hand portion
of the sidelobe structure. Very little change in the main lobe
structure occurred from null steering in the sidelobe region,
as was expected. Figure 5.2.2-3c shows the right-squinted beam,
One should recall that nulling was actually performed on the
right and left beams, not the sum and difference beams directly.
The sum and difference beams were then formed and, thus, had
the corresponding nulls toward the jammer. The sidelobe level
of the right beam actually being nulled was somewhat lower
than that of the difference pattern (approximately 17 dB below
the peak of the main beam). The original sidelobe structure
is seen to be considerably better than was indicated in the
difference pattern, as is usual in the case of difference
patterns formed non-optimally by combining two beams. Again,
the phase-only null steering action on the second right side-
lobe caused a clear raising of the second left sidelobe. This
would not occur with the use of complex weights, but it is a
characteristic limitation of null steering using phase only
weights (as discussed in Section 4.2.2). Nevertheless, the

84
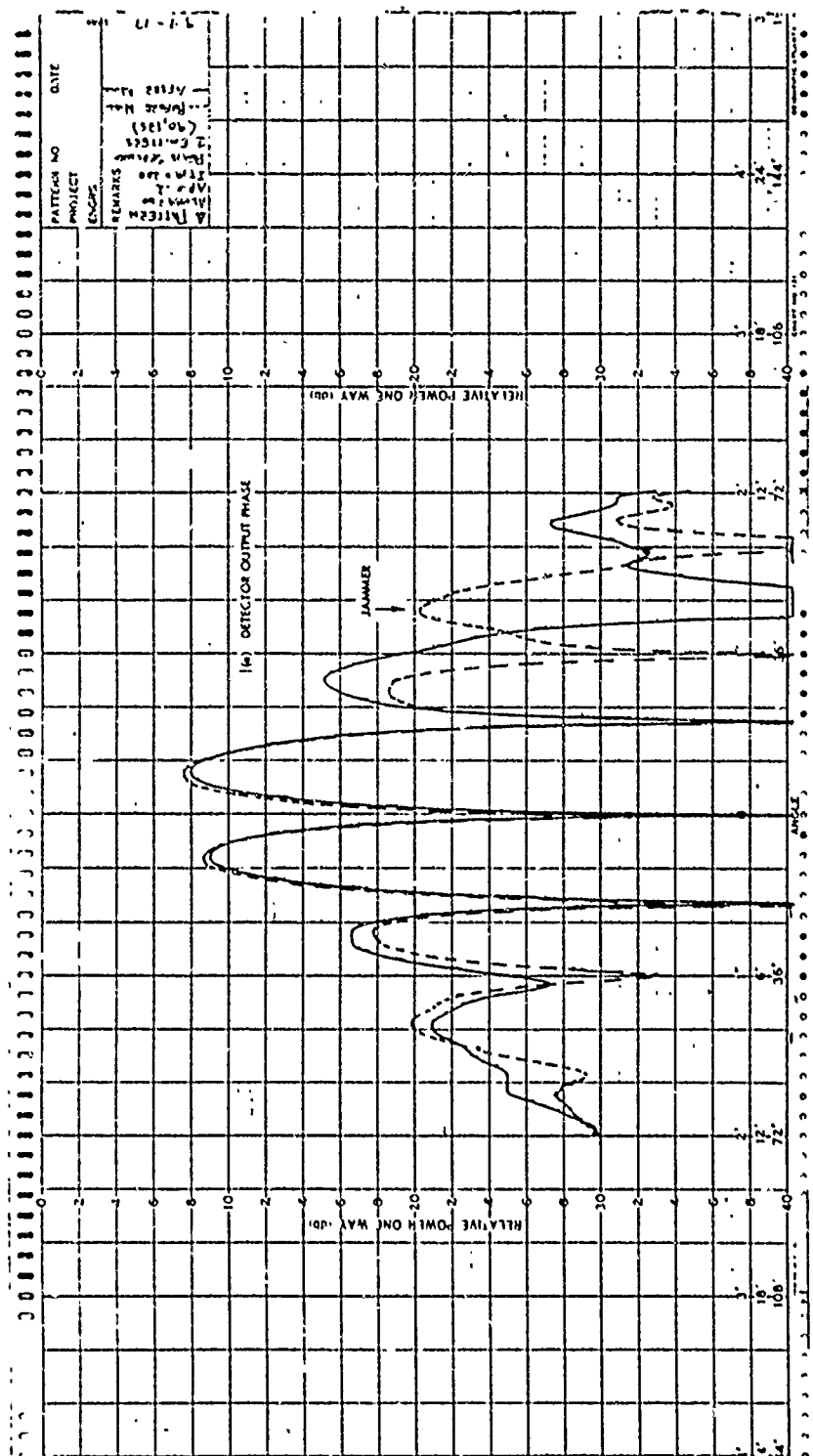
Figure 5.2.2-3a. Difference Pattern Before and After Nulling
(0° Scan Angle and 45° Jammer Angle)
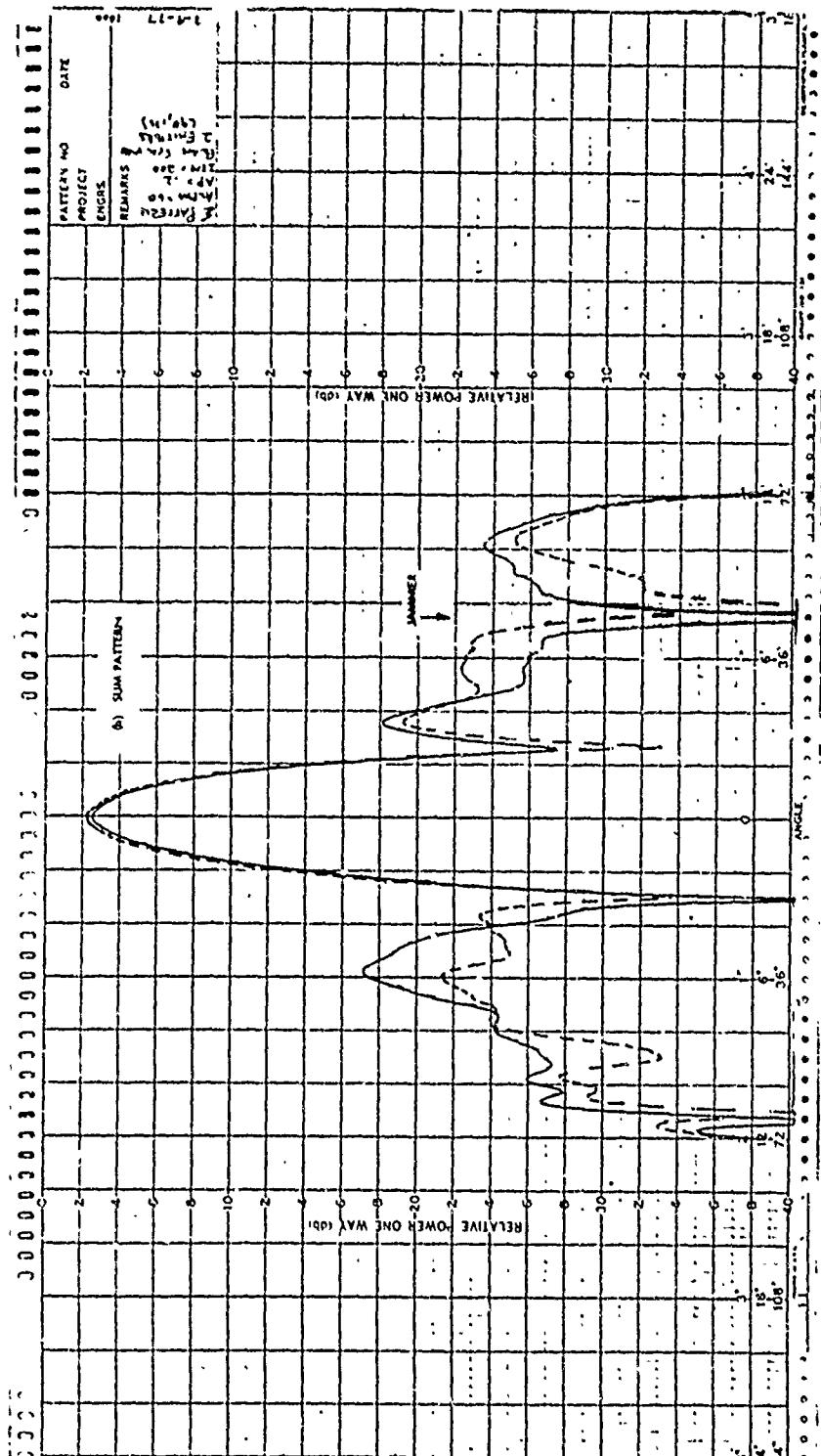
85

Figure 5.2.2-30. Sum Pattern Before and After Nulling
(0⁰ Scan Angle and 45⁰ Jammer Angle)

86

Figure 5.2.2-3c. Right-Squinted Beam Before and After Nulling
(0° Scan Angle and 45° Jammer Angle)

87
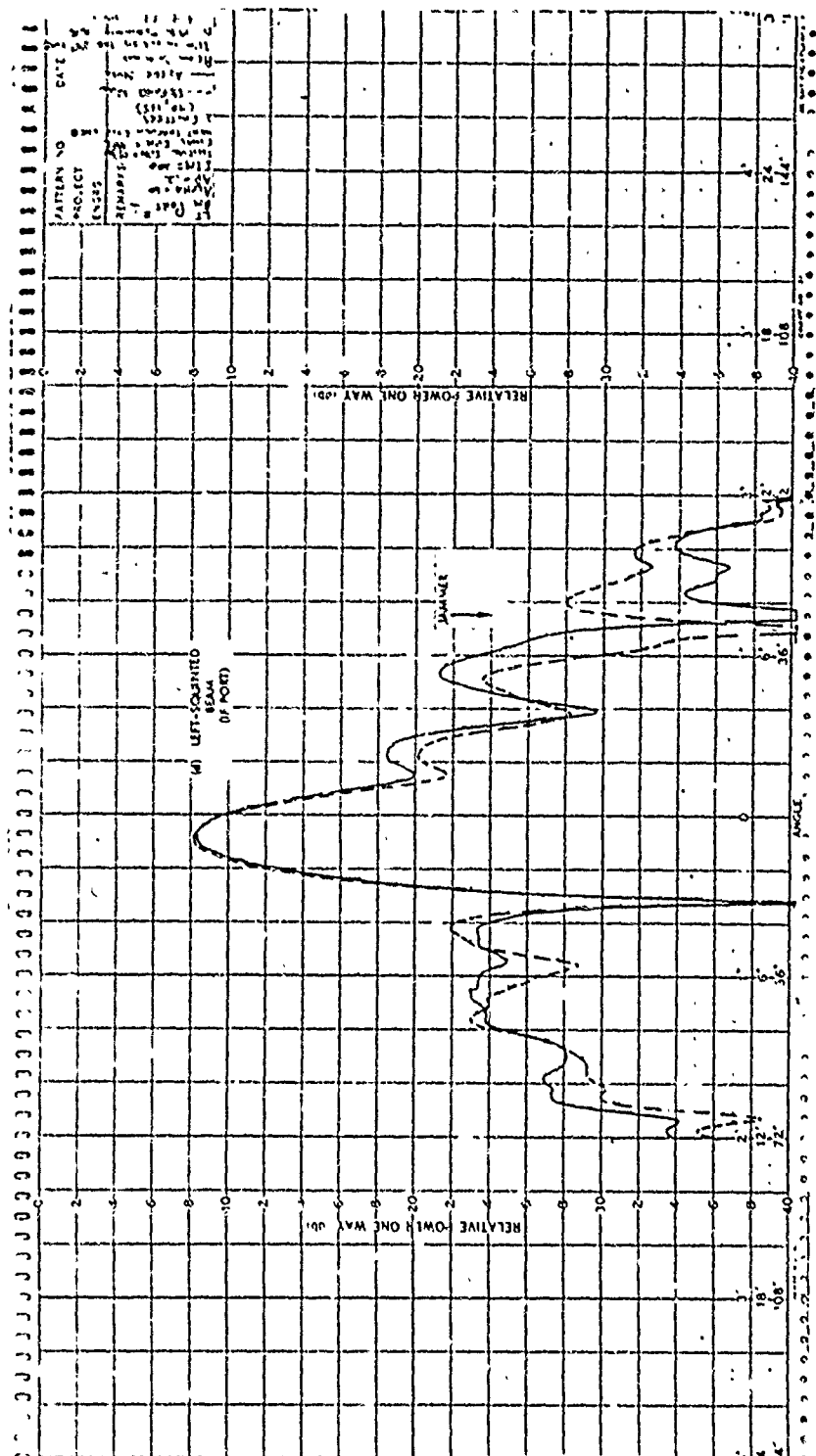
Figure 5.2.2-3d. Left-Squinted Beam Before and After Nulling
(0° Scan Angle and 45° Jammer Angle)

right beam is preserved, with its main beam relatively
unaffected and sidelobe structure only modestly altered by
the null steering action. Figure 5.2.2-3c shows the right
squinted beam before and after null steering, again indicating
relatively little effect due to the null steering. In the case
of the left beam, a considerably lower sidelobe level was nulled
than in the right beam, and even less effect on the other side-
lobes and main beam structure resulted. It can be seen that the
pattern structure at the left beam before nulling is somewhat
poorer than the right beam, indicating more uncorrected phase
and amplitude errors at least partially due to a poor phase
calibration. Nevertheless, it was felt the beam was adequate
for performing the basic null steering tests. Finally, it should
be noted that both the left and right beams were measured at IF,
after having been reconstituted by passing the sum and difference
channels through another sum-difference channels through another
sum-difference hybrid. Thus, the patterns shown were not
actually obtained from the RF right and left channels, but from
the reconstituted right and left beams at IF. Slight errors in
reproduction of the left and right beams were expected from con-
siderations pertaining to the hybrids and IF network used. These
errors, however, are not considered significant here since the
difference beam and, particularly, its shift due to null
steering are the important quantities measured in these investi-
gations.

The sets of data to follow are very similar to the pre-
vious sets, and will be discussed in less detail. Figure
5.2.2-4 shows the third case of Table 5.2.1-1, that of 0° scan
angle and a 40° jammer angle. From Figure 5.2.2-4a very little
boresight shift error occurred (approximately 0.1°). The reason
that boresight shift error is low (as was discussed in Section
5.2.2) is that the jammer was brought in at a relatively low
sidelobe level (between the first and second sidelobes) as
indicated in Figure 5.2.2-4b. This is a plot of the difference
pattern, showing the jammer angle corresponding to a fairly low
sidelobe level (as shown by the dashed part of the pattern),

89
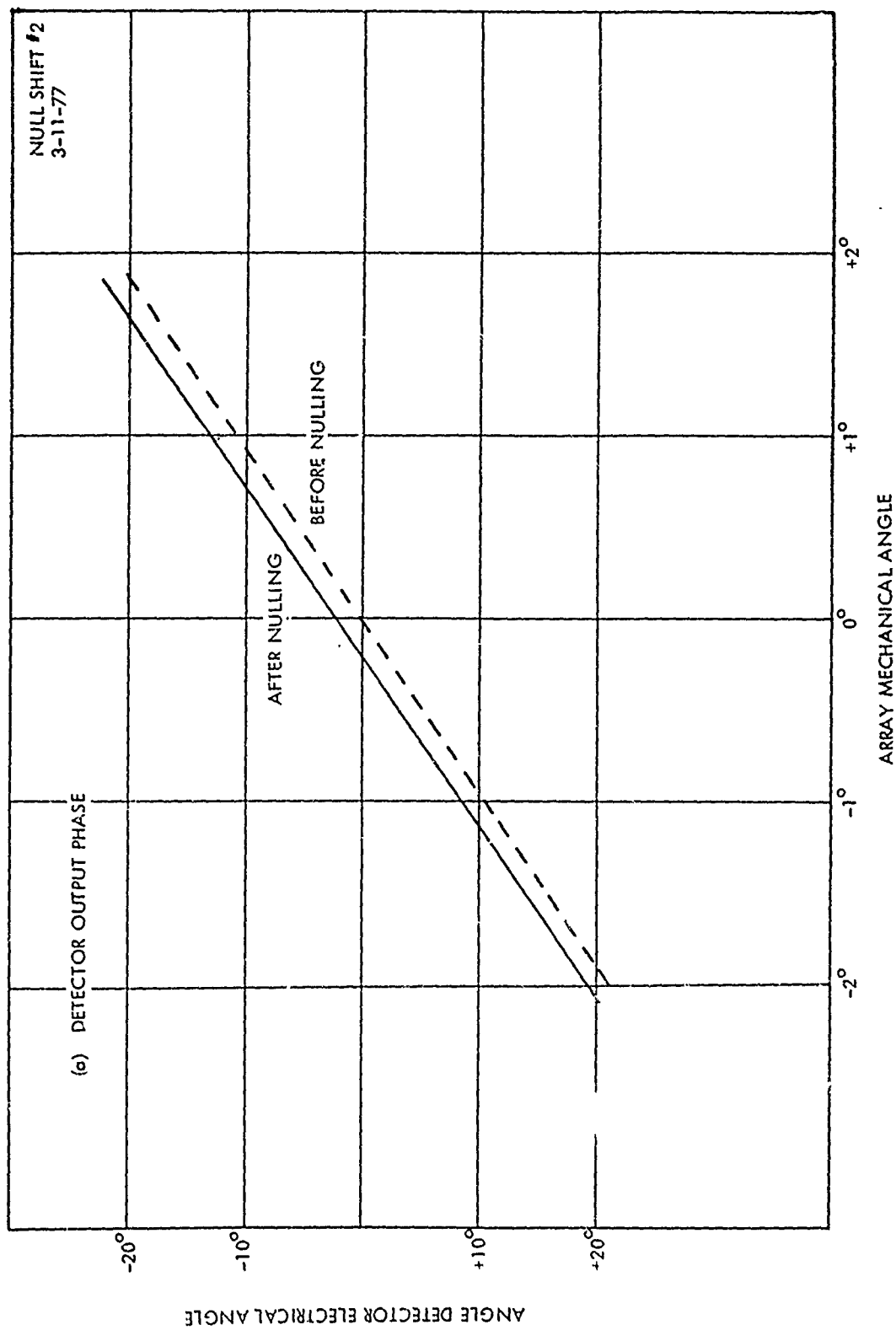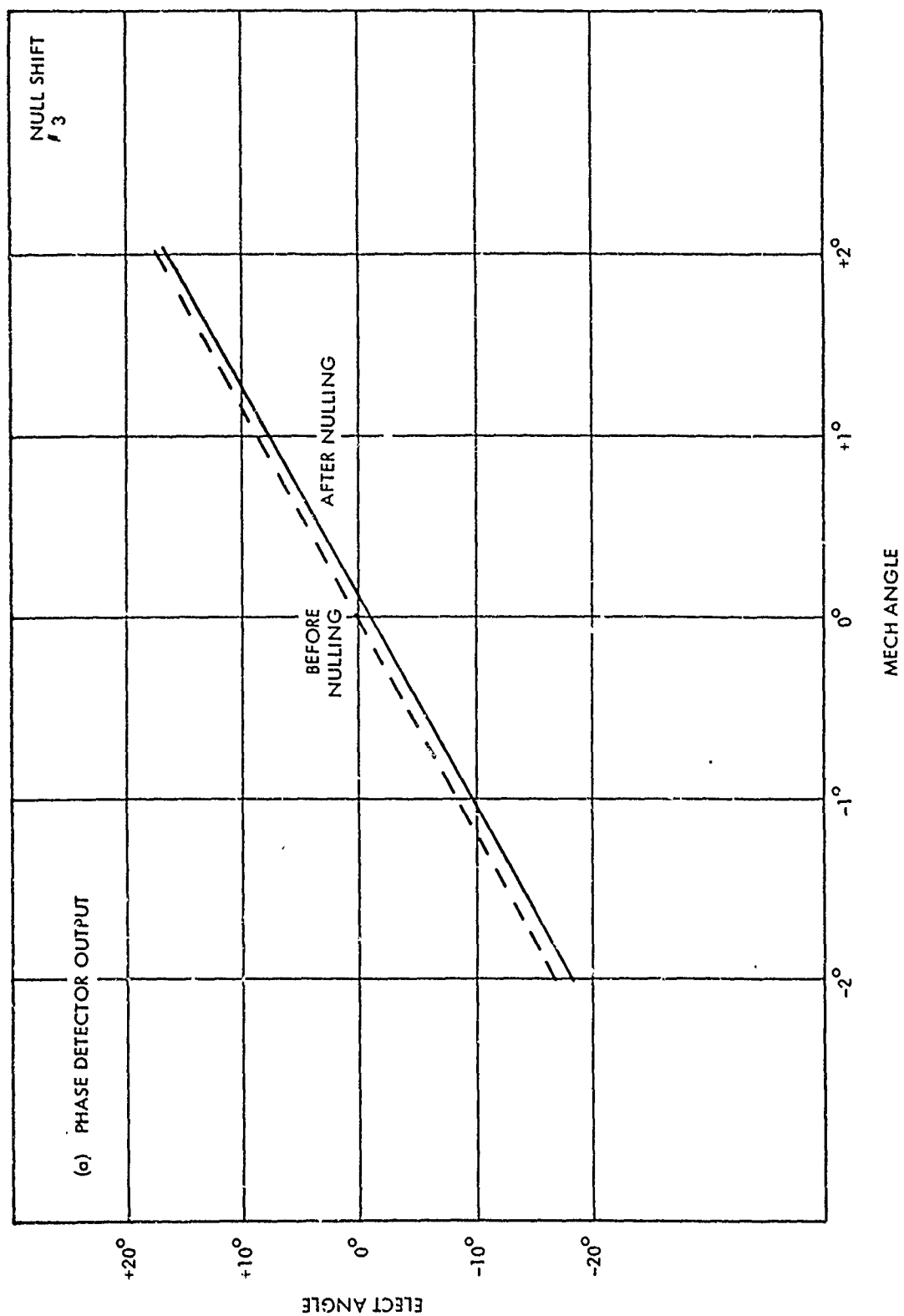
Figure 5.2.2-4a. Phase Detector Output Before and After Nulling
(00 Scan Angle and 400 Jammer)

Figure 5.2.2-4b Difference Pattern Before and After Nulling (0° Scan Angle and 40° Jammer)
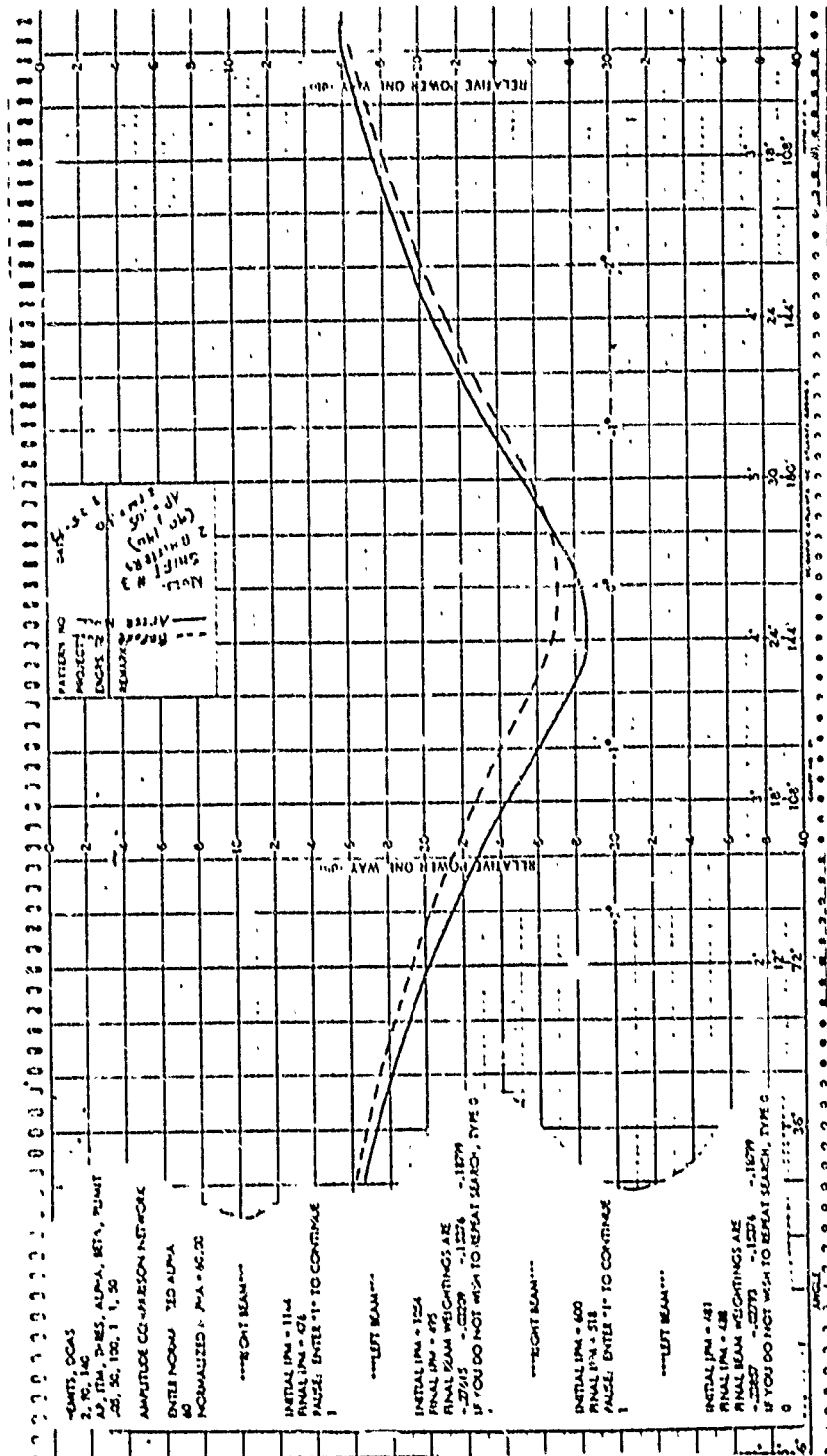
Figure 5.2.2-4c. Difference Pattern in Expanded Scale at Boresight
(0° Scan Angle and 40° Jammer Angle)

92

nulled to a still lower amplitude (as shown by the solid pattern). Note, as was stated before, that the cancelling beam in this particular case was not aligned with the jammer, but was steered 10^0 away from the jammer at 50^0 from boresight. Still, it can be seen that null steering was accomplished with good accuracy, although significant sidelobe perturbations occurred. These perturbations were mainly due to the higher intensity of the cancelling beam needed since the beam was not aligned optimally with the jammer.

Figure 5.2.2-5 shows the fourth case in Table 5.2.2-1, that of a jammer at -66^0 with 0^0 scan angle. In this case, the phase detector output again showed a relatively low boresight shift error. Figure 5.2.2-5b shows the difference pattern with a jammer entering again at the relatively low sidelobe level of approximately -18.5 dB. During null steering, relatively small perturbations in the sidelobes and essentially no perturbation in the mainlobe direction occurred.

Finally, the fifth case of Table 5.2.2-1 is illustrated in Figure 5.2.2-6, that of a -30^0 scan angle with a $+30^0$ jammer angle. Essentially no boresight shift error was seen in the phase detector output, (approximately 0.083^0 or a 0.0064 beamwidth). Figure 5.2.2-6b shows the difference pattern with a jammer positioned on the third sidelobe. Very little change in the mainbeam of the pattern was noted after null steering, as was expected. Figure 5.2.2-7 is a full pattern set of the previous case; difference, sum, right, and left beams, respectively, similar to those previously discussed.

Additional data was taken that did not include detailed phase detector measurements of the boresight shift error. They are included here as additional data of interest to show that other jammer angles were measured resulting in very low boresight shift errors (similar to those detailed data sets previously discussed.) Figure 5.2.2-8 shows the case of a

93
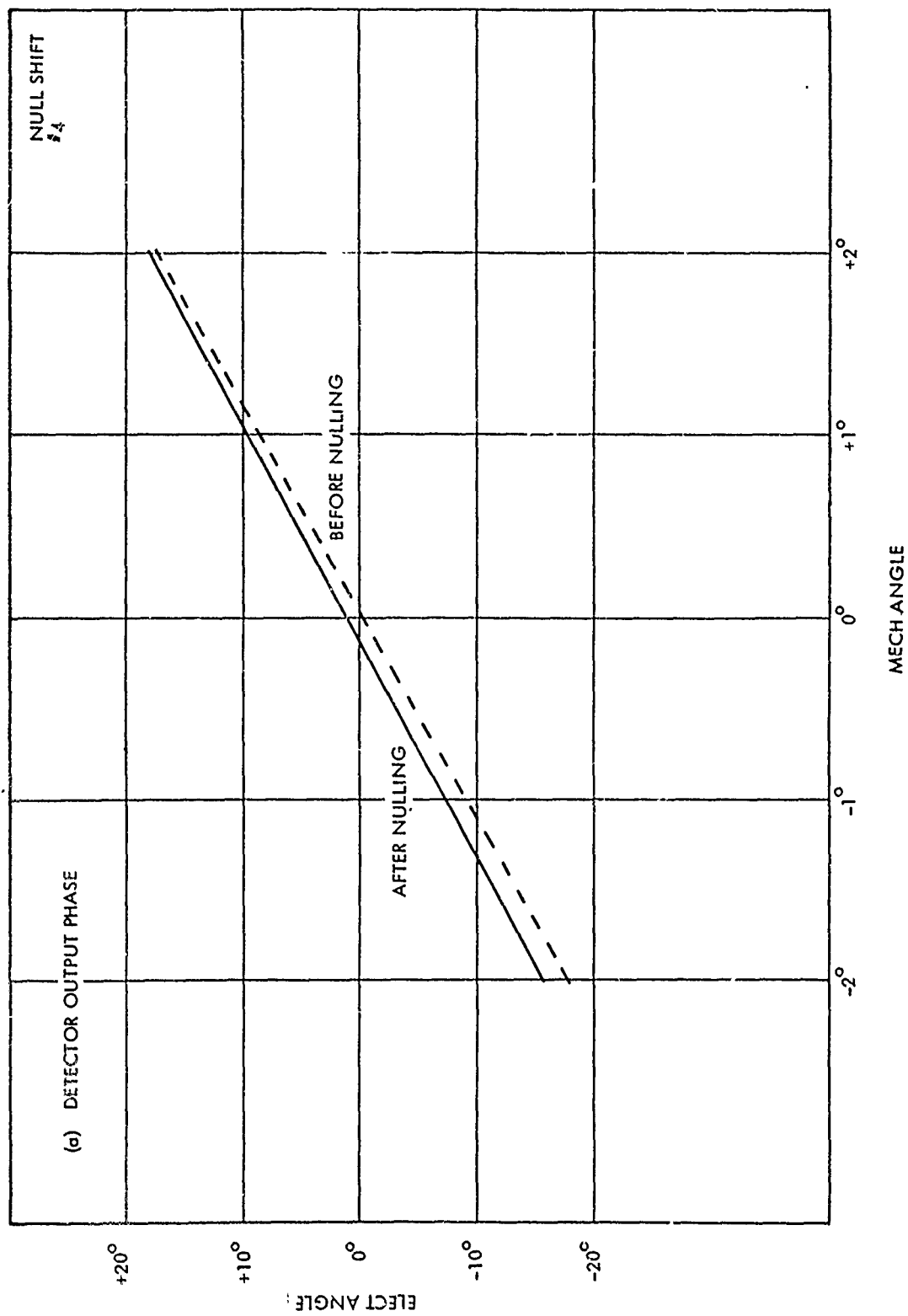
Figure -5.2.2-5a. Phase Detector Output Before and After Nulling
(0° Scan Angle and -66° Jammer)

94

Figure 5.2.2-5b. Difference Pattern Before and After Nulling
($0°$ Scan Angle and $-66°$ Jammer Angle)

Figure 5.2.2-5c. Difference Pattern in Expanded Scale at Boresight (0° Scan Angle and -60° Jammer Angle)

(a) PHASE DETECTOR OUTPUT
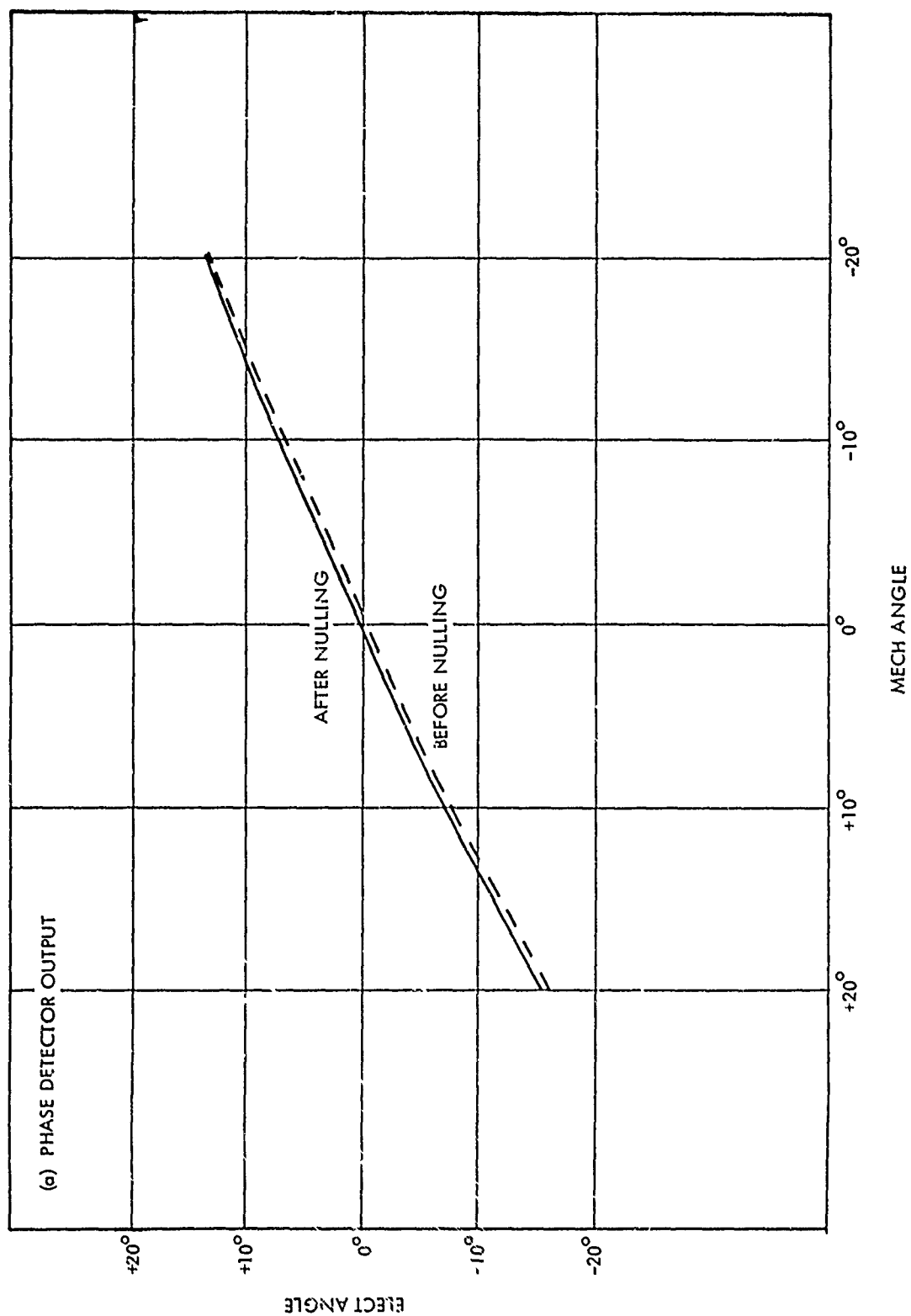
Figure 5.2.2-6a. Phase Detector Output Before and After Nulling
(-30⁰ Scan Angle and +30⁰ Jammer Angle)

Figure 5.2.2-6b. Difference Pattern Before and After Nulling
(-30° Scan Angle and +30° Jammer Angle)
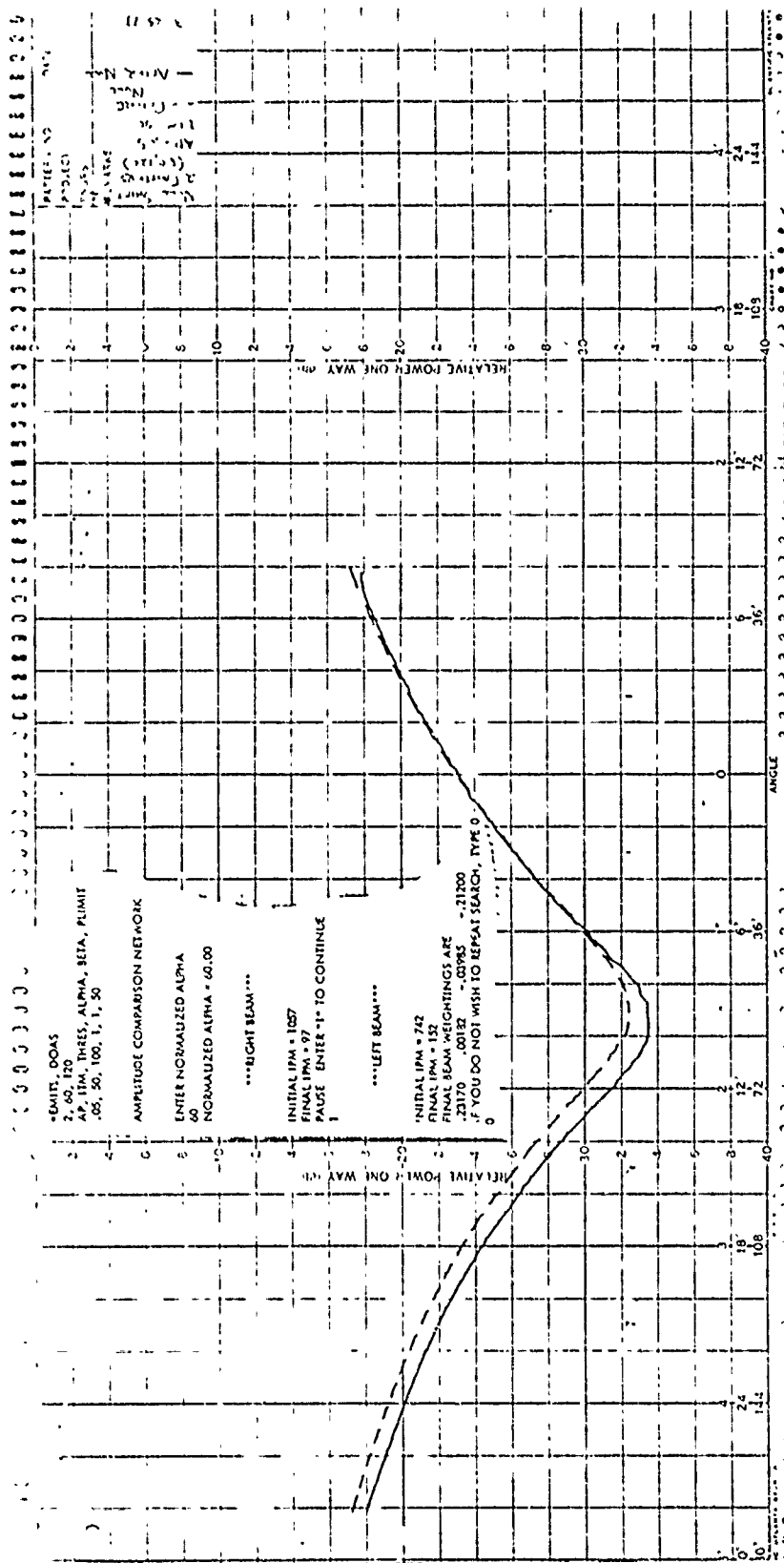
Figure 5.2.2-6c. Difference Pattern in Expanded Scale at Boresight
(-30° Scan Angle and +30° Jammer Angle)

Figure 5.2.2-7a. Difference Pattern Before and After Nulling
(-30° Scan Angle and +30° Jammer Angle)

Figure 5.2.2-7b. Sum Pattern Before and After Nulling
(-30° Scan Angle and +30° Jammer Angle)

101

Figure 5.2.2-7c. Right-Squinted Beam Before and After Nulling
(-30° Scan Angle and +30° Jammer Angle)

Figure 5.2.2-7d. Left-Squinted Beam Before and After Nulling
(-30° Scan Angle and +30° Jammer Angle)

103

Figure 5.2.2-8a. Difference Pattern Before and After Nulling
(0° Scan Angle and -48° Jammer Angle)

Figure 5.2.2-8b. Sum Pattern Before and After Nulling
(0° Scan Angle and −48° Jammer Angle)

105

Figure 5.2.2-8c. Right-Squinted Beam Before and After Nulling
(0° Scan Angle and -48° Jammer Angle)

106

Figure 5.2.2-8d. Left-Squinted Beam Before and After Nulling
(0° Scan Angle and -48° Jammer Angle)

0° scan angle with a -48° jammer angle, and the corresponding patterns. Figure 5.2.2-9 shows the case of 0° scan with a $+53^O$ jammer angle, a case in which the jammer enters, not at the peak of the sidelobe, but off to the side of the sidelobe. Since there existed very few low sidelobes in this array, this was the optimal technique for achieving low sidelobe null steering. In this case, the jammer entered the sidelobe almost 18 dB below the peak of the mainbeam, causing imperceptable boresight shifts and relatively minor sidelobe variations. Figure 5.2.2-10·shows the set of patterns for the case of a -51° jammer angle positioned at a fairly high sidelobe. Again, relatively little boresight shift error was noted.

An important effect, for the purposes of null steering, is the coupling between the left and right beams. This coupling is a more important effect in null steering than is usually the case for simple mainbeam steering. This is due to the fact that if one has steered a deep (and thus very sensitive) null in one beam, altering the second beam has significant effects through coupling on the first beam thus causing a severe change in the originally positioned null. The next two figures illustrate measurements of this effect. Figure 5.2.2-11 shows the right beam pattern both before (the dashed pattern) and after (solid pattern) null steering the left beam. The jammer was incident at -48°, as shown on the figure. The null that had been previously achieved on the right beam toward this jammer was not destroyed by null steering on the left beam, however, significant variations of the other sidelobes did occur. In other cases (for which we will not present data) significant to serious degradation of the nulls on the jammer occurred when null steering in the other beam. This became so significant that it was necessary to null each beam successively several times in order to achieve deep nulls with assurance in both beams. Fortunately, the mutual coupling
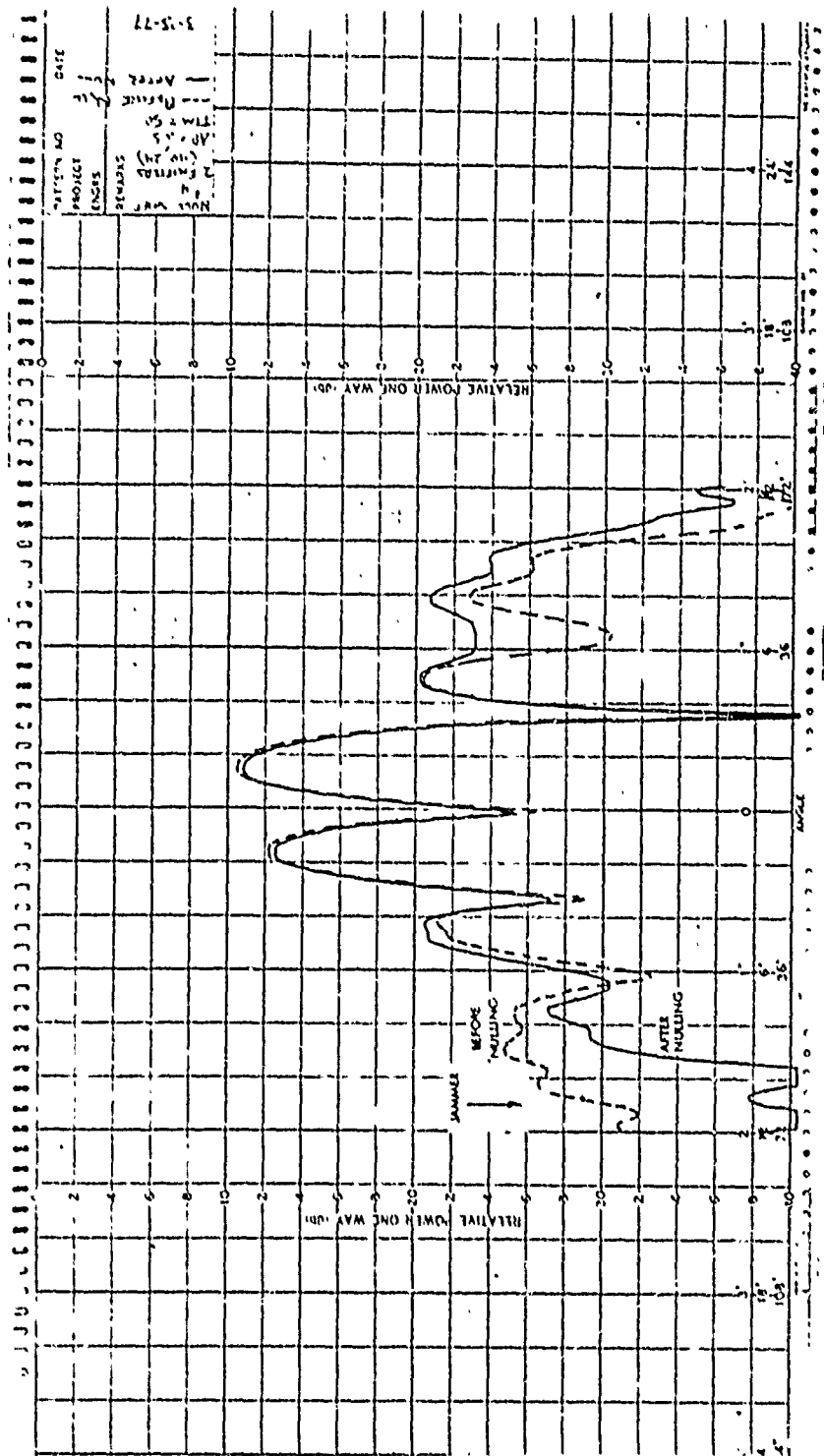
Figure 5.2.2-9. Difference Pattern Before and After Nulling
(0° Scan Angle and 53° Jammer Angle

109

Figure 5.2.2-10a. Difference Pattern Before and After Nulling
(0° Scan Angle and -51° Jammer Angle)
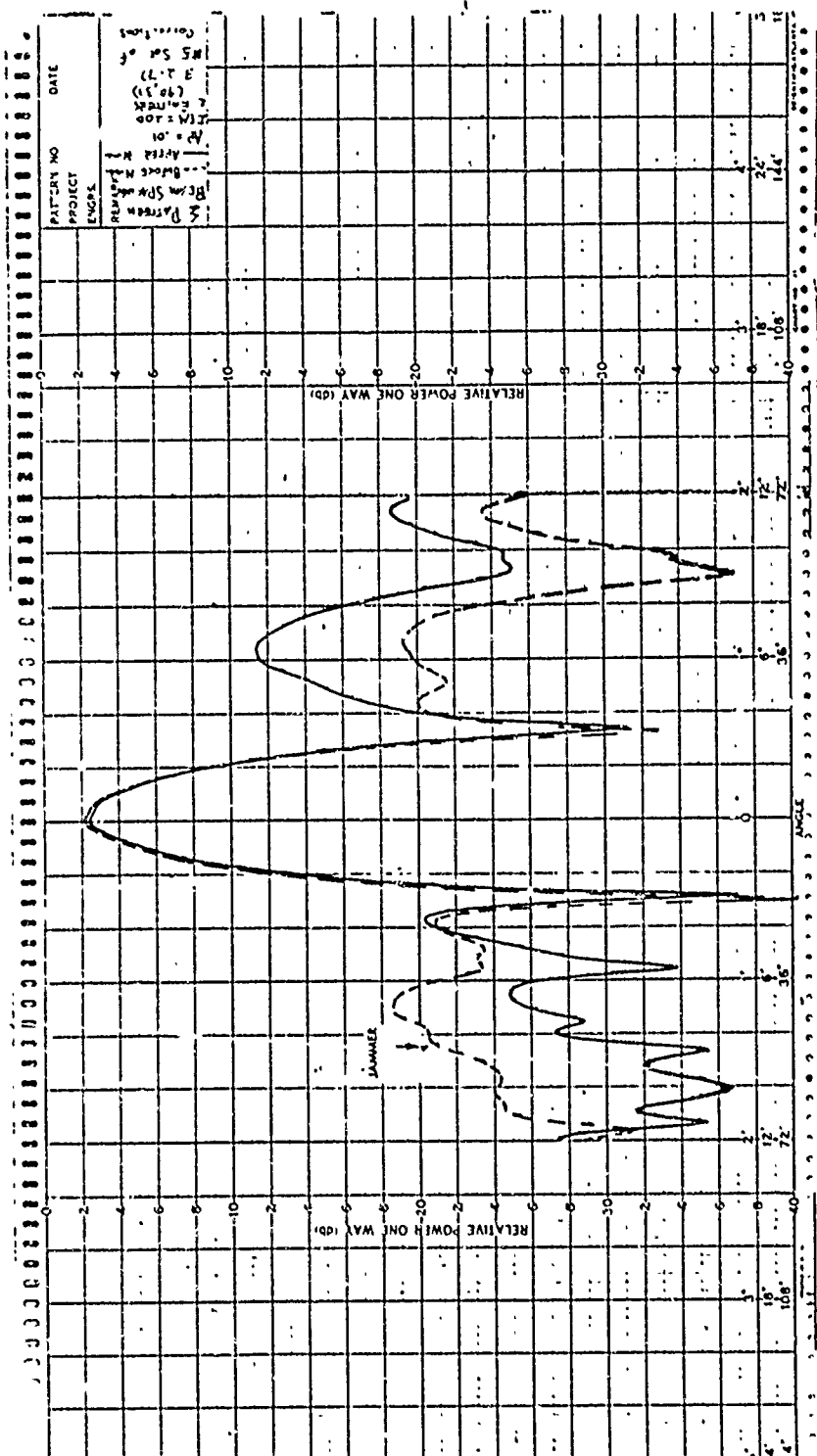
Figure 5.2.2-10b. Sum Pattern Before and After Nulling
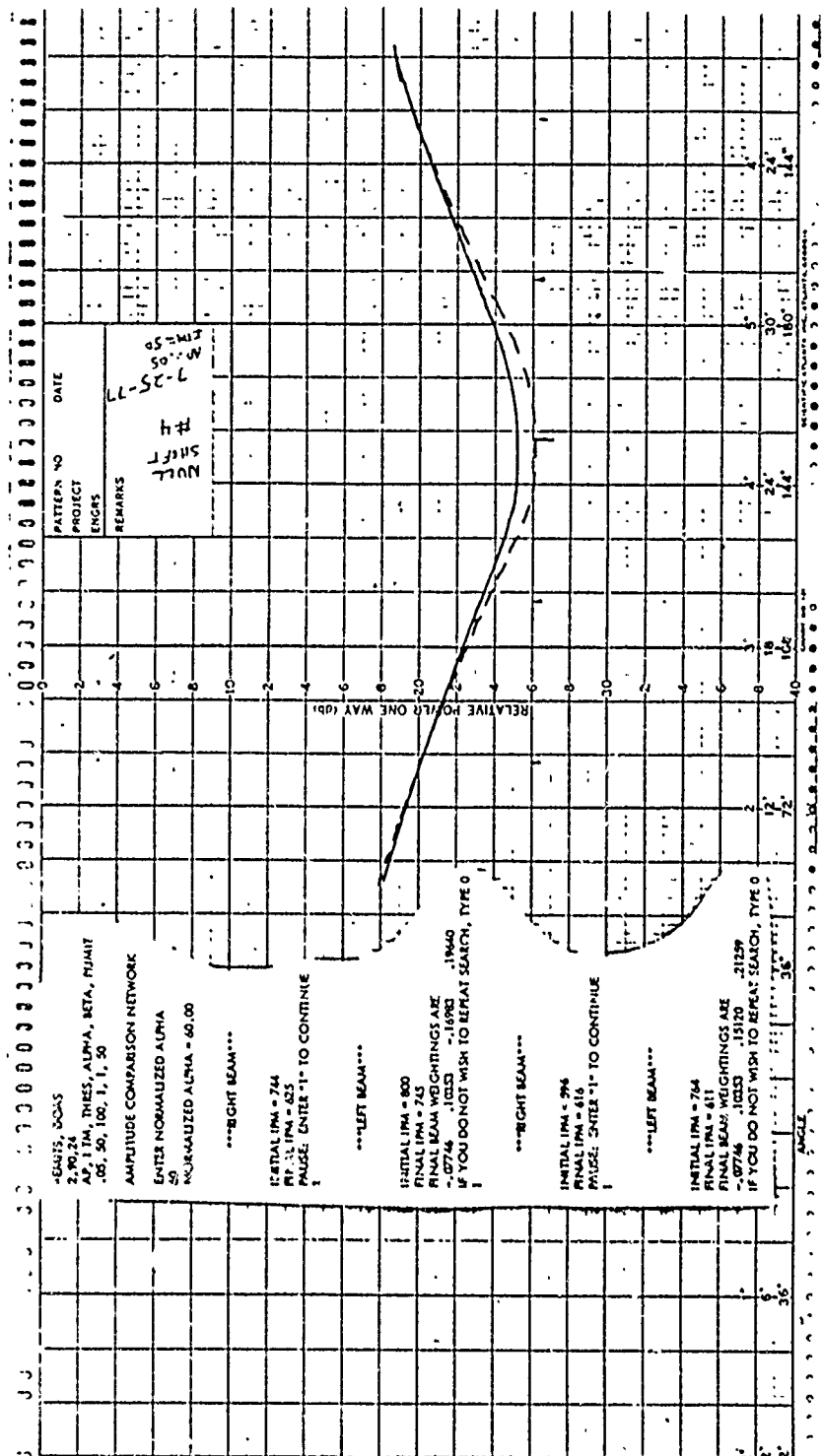(0° Scan Angle and -51° Jammer Angle)

Figure 5.2.2-10c. Right-Squinted Beam Before and After Nulling (0o Scan Angle and -51o Jammer Angle)

112

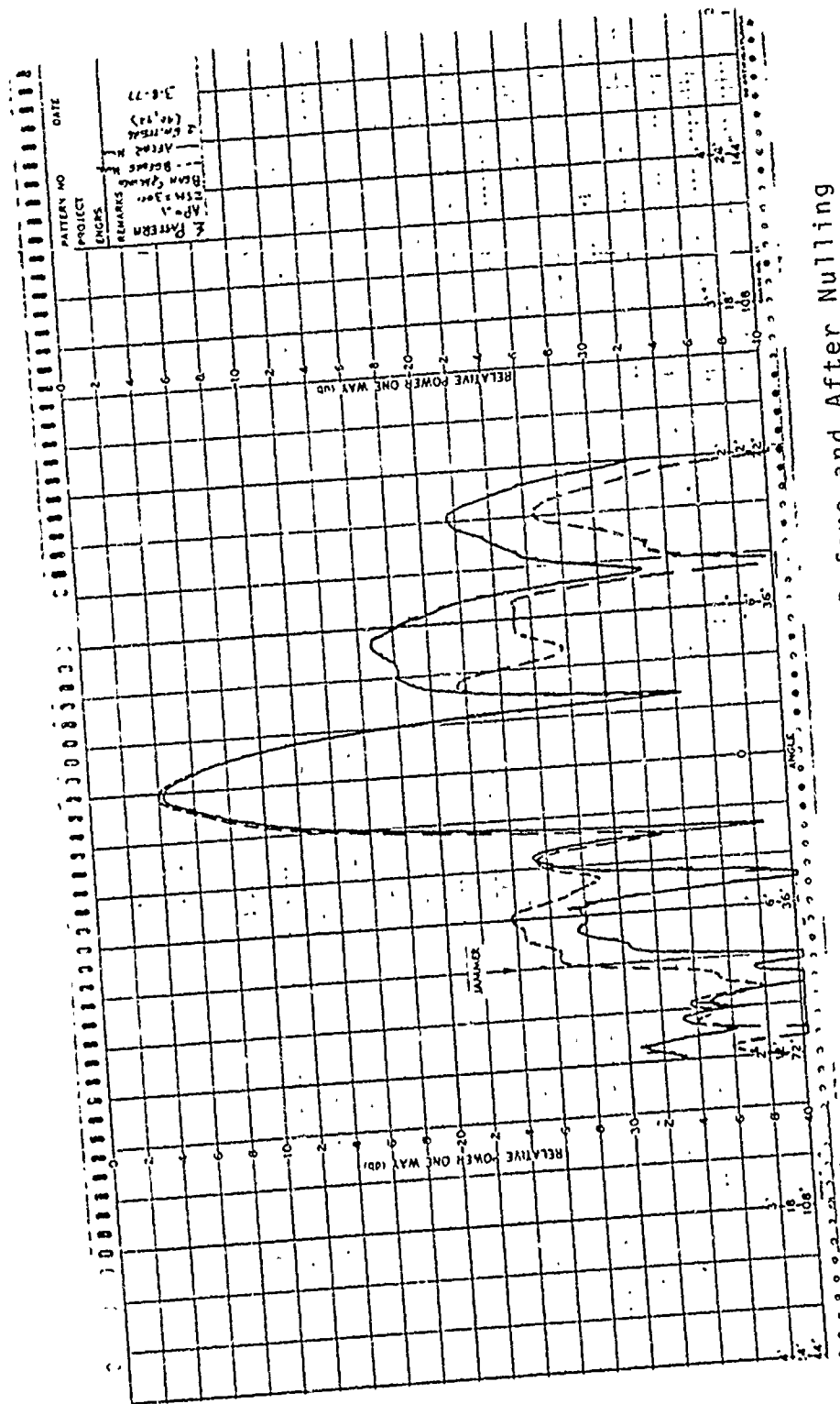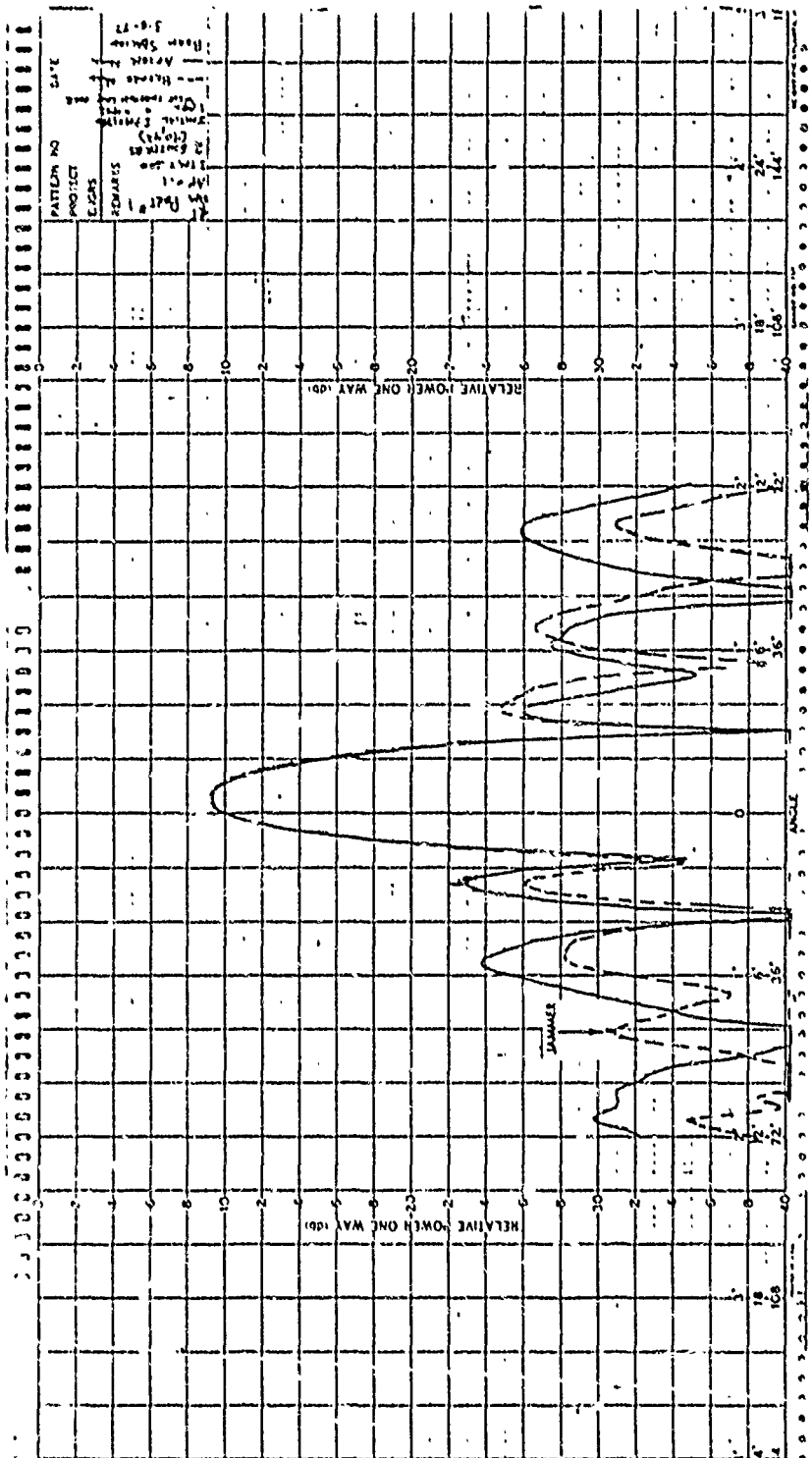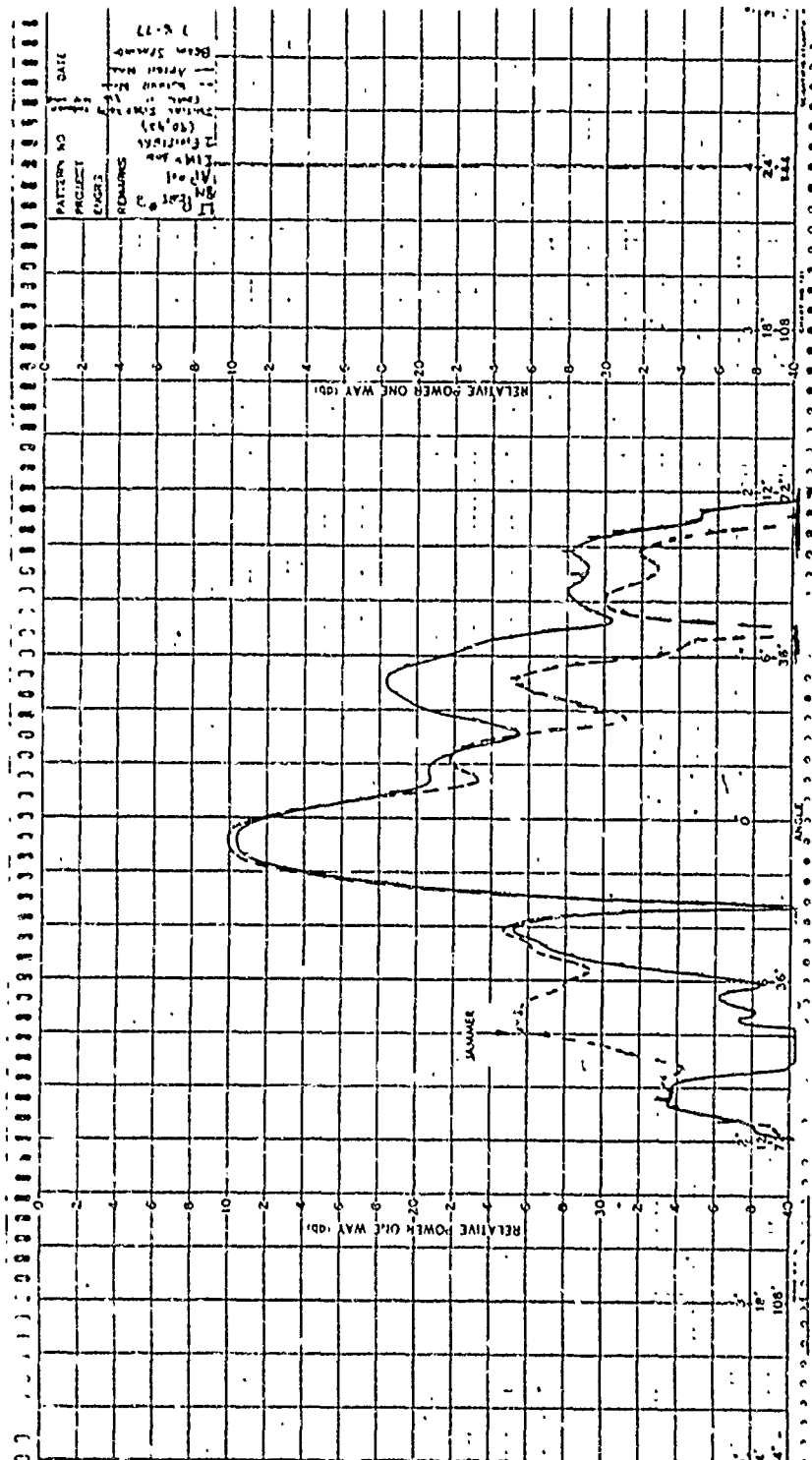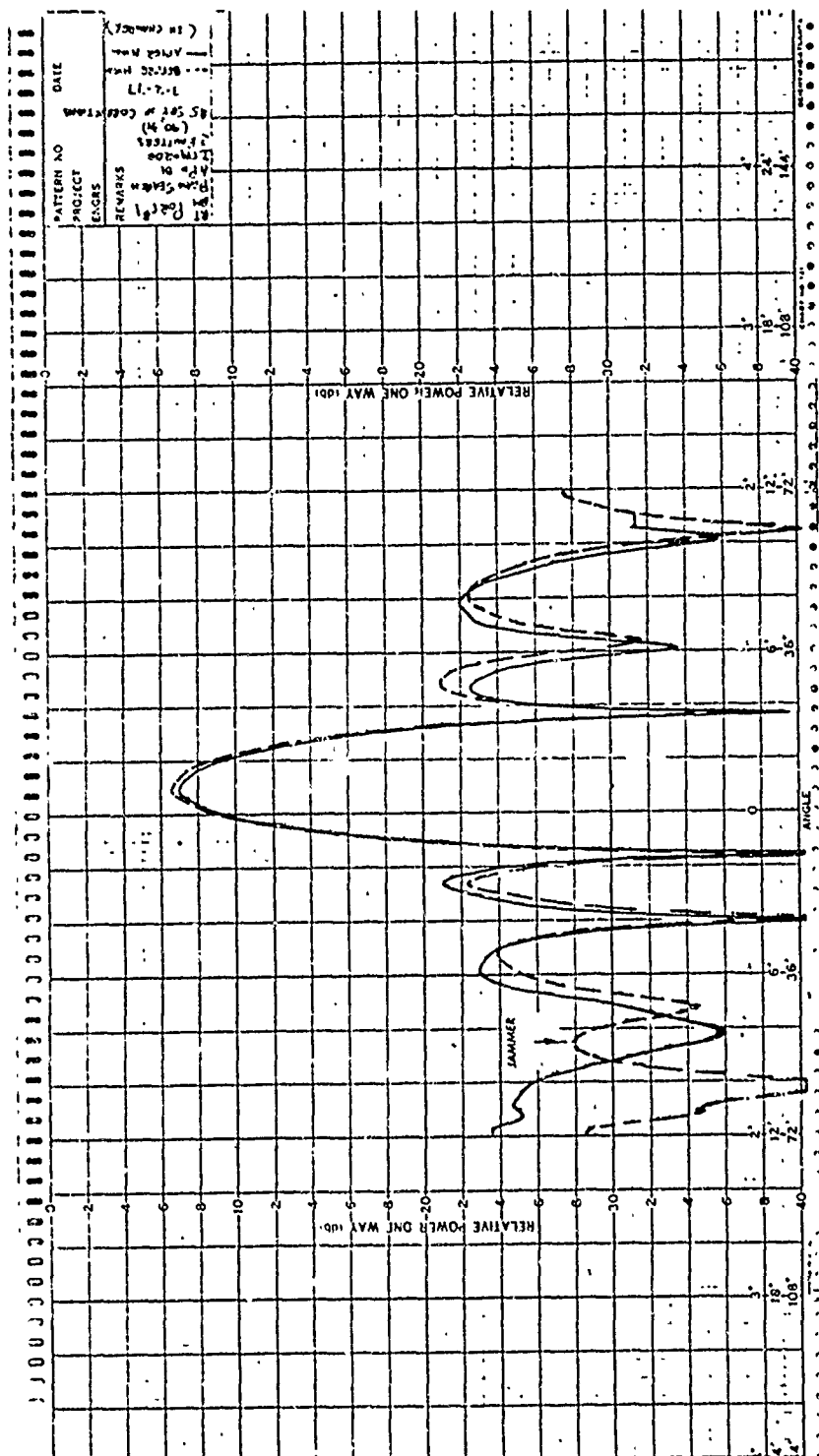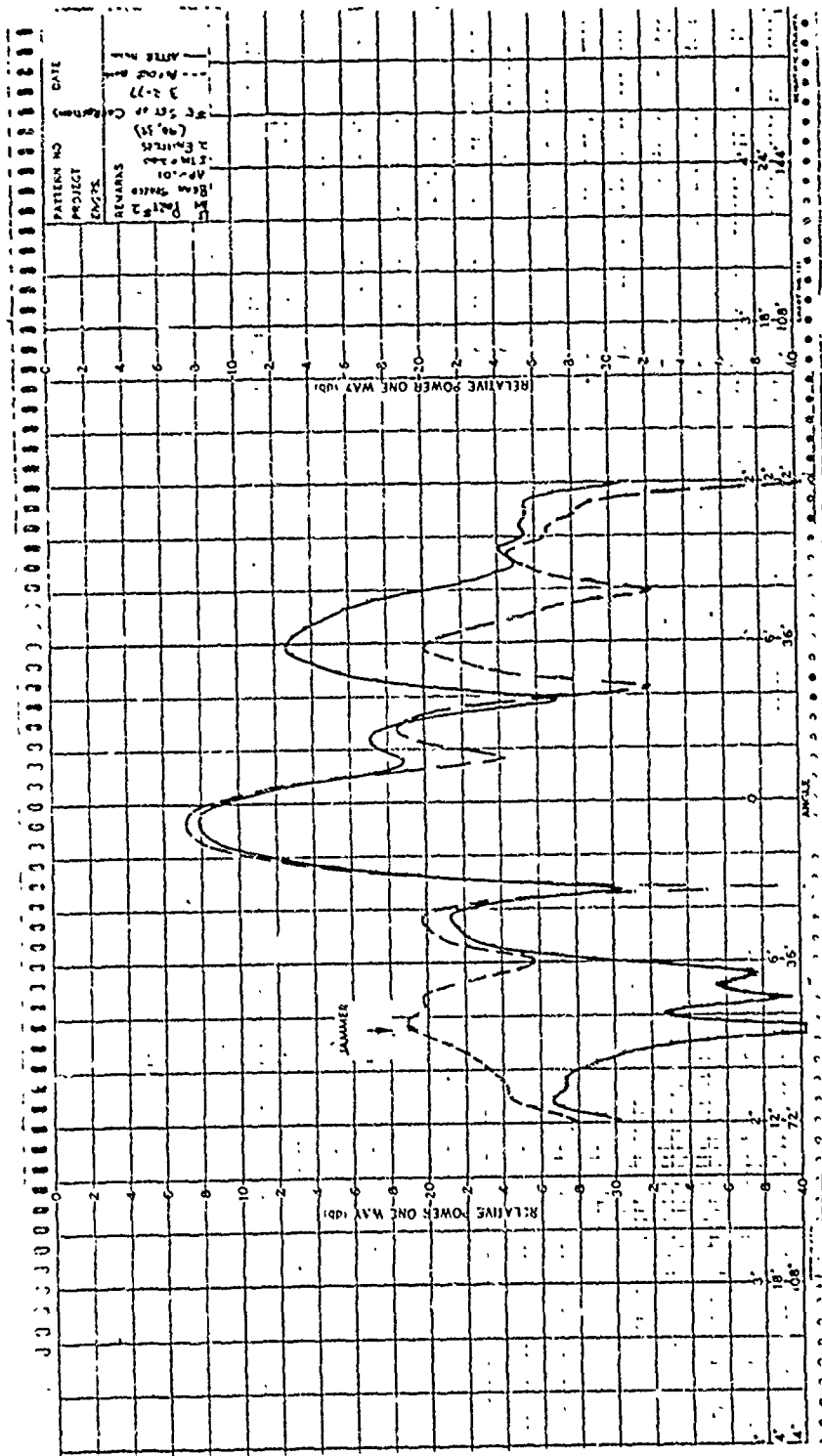Figure 5.2.2-10d. Left-Squinted Beam Before and After Nulling
(0° Scan Angle and -51° Jammer Angle)

Figure 5.2.2-11. Right-Squinted Beam Before and After Nulling the Left-Squinted Beam (0° Scan Angle and -48° Jammer Angle)

114
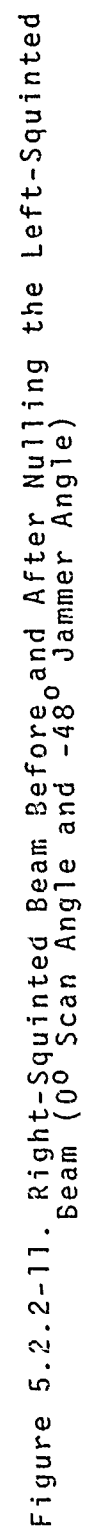
between beams was small enough so that the process of successive nulling was convergent. Figure 5.2.2-12 illustrates the mutual coupling between beams, with a right beam shown before and after nulling the left beam (jammer at 45°). In this case, very little pattern perturbation was noticed. Thus, although it may be necessary to account for coupling between beams when null steering two beams of a monopulse array, this effect will not be so overwhelming as to make the null steering process impractical.

5.2.3 Comparison of Calculated and Measured Patterns

The object of the breadboard measurements was to take sufficient data in order to assure an understanding of the basic mechanisms of boresight shift error due to null steering antenna patterns with a fully adaptive array. In particular, it was desired to demonstrate that the magnitude of boresight shift errors measured could be predicted by simple theory under the assumption of a practical array null steered by controlled phase shifters and an awareness of inherent tolerance errors. Thus the measurements of a relatively small 8-element array could be extrapolated to predict the behavior of a much larger array under various null steering configurations. It has been shown that the boresight shifts measured were small, indeed, and are of the same order of magnitude as that predicted in Section 4.2. In this section, we wish to show that the basic antenna patterns that were predicted by the simulations (as shown in this report) compare with the measured patterns within reasonable approximation. It is only rarely that one attempts to exactly calculate an antenna pattern (in the sidelobe region) and compare it with measurements. Figure 5.2.3-1 shows such a comparison of the calculated vs. measured pattern, for the first case discussed in Table 5.2.2-1, that of a 0° scan with a 27° jammer. This figure compares calculated (solid line) and measured patterns (dashed line), before null steering with a digitally-controlled algorithm. As illustrated, most of the

115
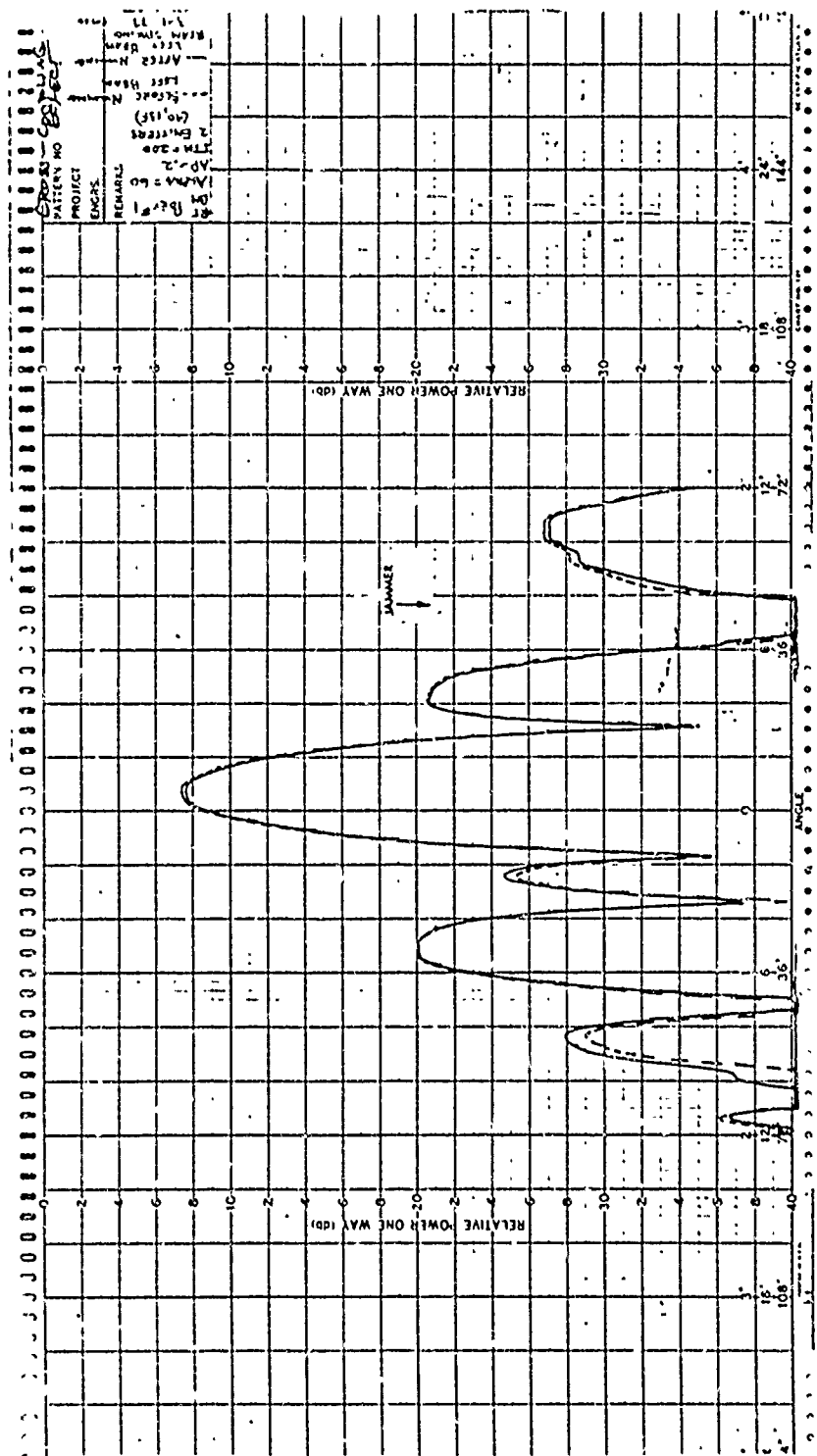
Figure 5.2.2-12. Right-Squinted Beam Before and After Nulling the Left-Squinted Beam (0° Scan Angle and 45° Jammer Angle)
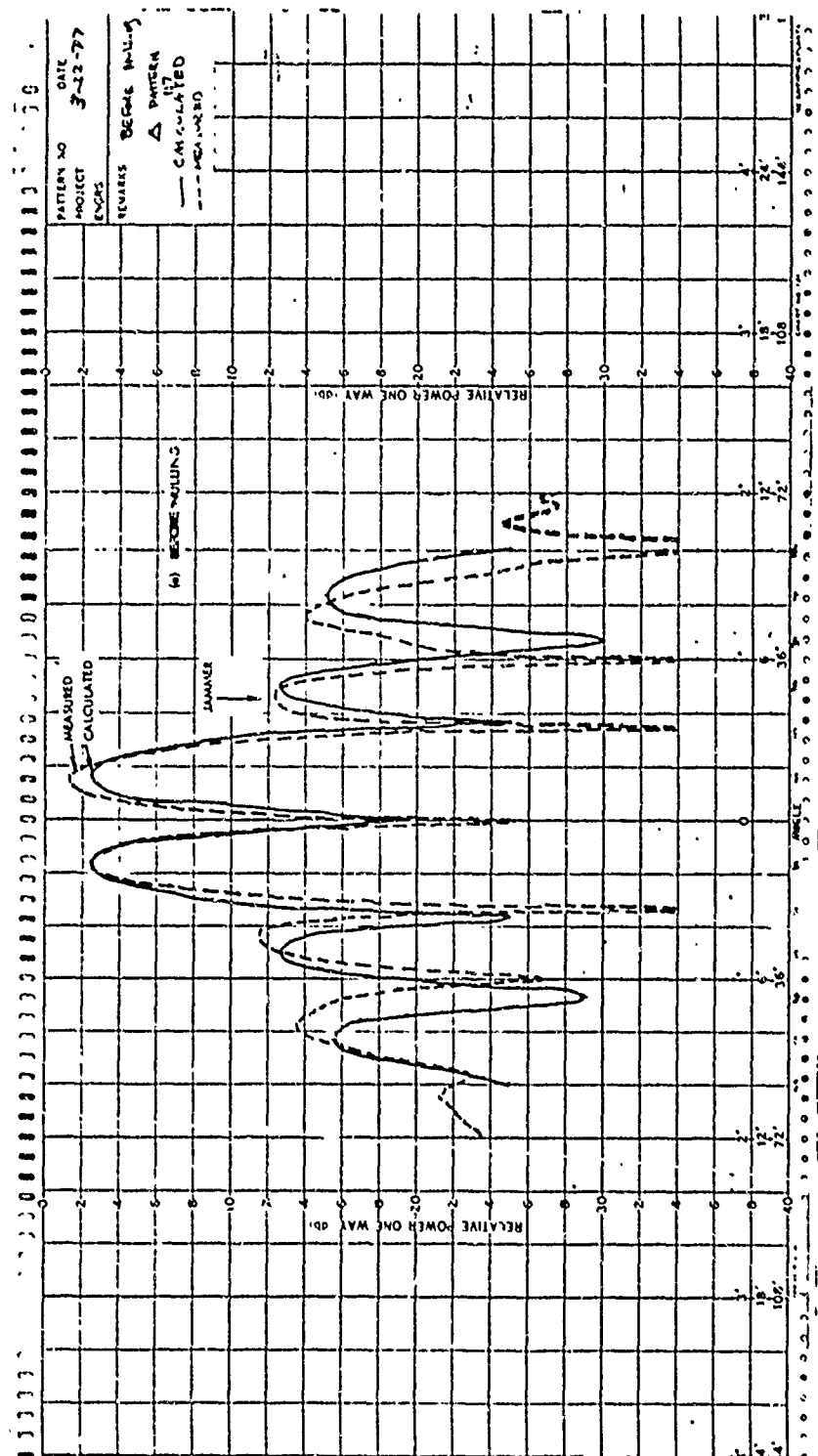
Figure 5.2.3-1. Measured and Calculated Difference Patterns Before Nulling (0° Scan Angle and 27° Jammer Angle)

117

overall details of sidelobe levels as well as beamwidths are
close to that predicted although there is a significant shift
of the sidelobe peak angles. It is expected that these
differences are due to inaccuracies in the calibrations, the
mutual coupling effects of the array which were not accounted
for by the theory, and the multipath of the relatively
inaccurate antenna range that was used for the measurements.
Figure 5.2.3-2 shows a comparison after null steering toward
a jammer, for both calculated and measured results. Again,
many aspects of the patterns are very similar, although some
angular shifts of the peaks and amplitudes were noted. Never-
theless, it is felt that these comparisons show that the simul-
ations represent a reasonable facsimile to the real breadboard
setup.

Figure 5.2.3-3 illustrates a full set of patterns with
a comparison of measured vs. calculated results for the case of
the 45^0 jammer angle previously discussed in the experimental
section. Figure 5.2.3-3a shows the difference pattern and
indicates a relatively close correspondence between the cal-
culated and measured results. Figure 5.2.3-3b, the sum pattern,
shows a reasonable correspondence in the mainbeam, but some dis-
crepancy in the details of the sidelobe region. Figure 5.2.3-3c
shows the right beam, and a very good correlation between the
calculated and measured results. Figure 5.2.3-3d shows the left
beam and a relatively poor correspondence between measured and
calculated patterns in the sidelobe region. From this pattern,
it is clear that the left pattern is not known or calibrated as
accurately as the right pattern, and thus the computations of
this beam do not accurately represent the beam. The right beam
is a much more carefully calibrated and accurately known quantity.
Since the left beam calibrations are not as accurate, the sum
beam calculations and to a lesser extent the difference beam
calculations do not correspond as well to the measured beams.
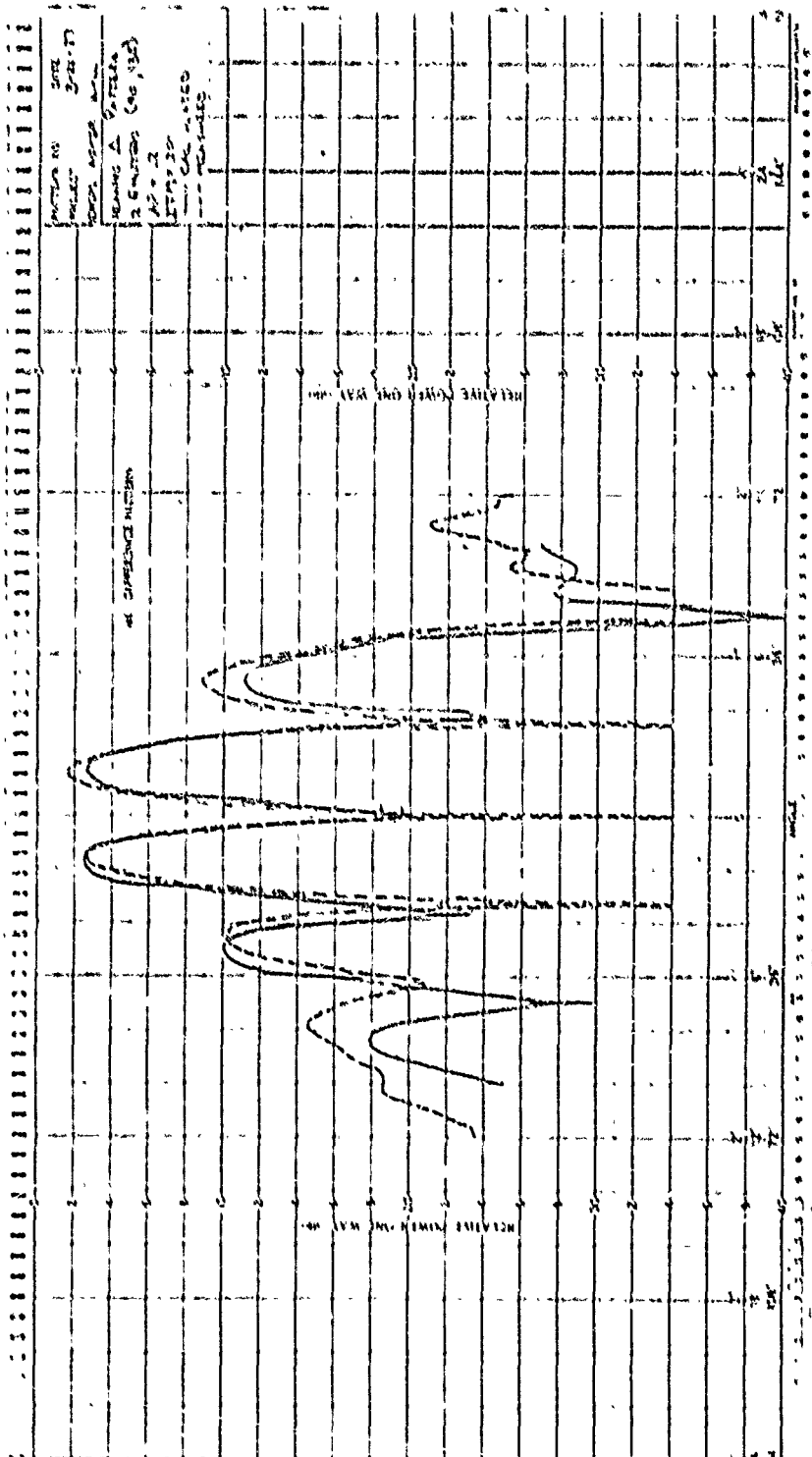
118

Figure 5.2.3-2. Measured and Calculated Difference Patterns After Nulling (0⁰ Scan Angle and 27⁰ Jammer Angle)

119

Figure 5.2.3-36. Measured and Calculated Difference Patterns After Nulling (30 Scan Angle and 450 Barrel Angle)

120
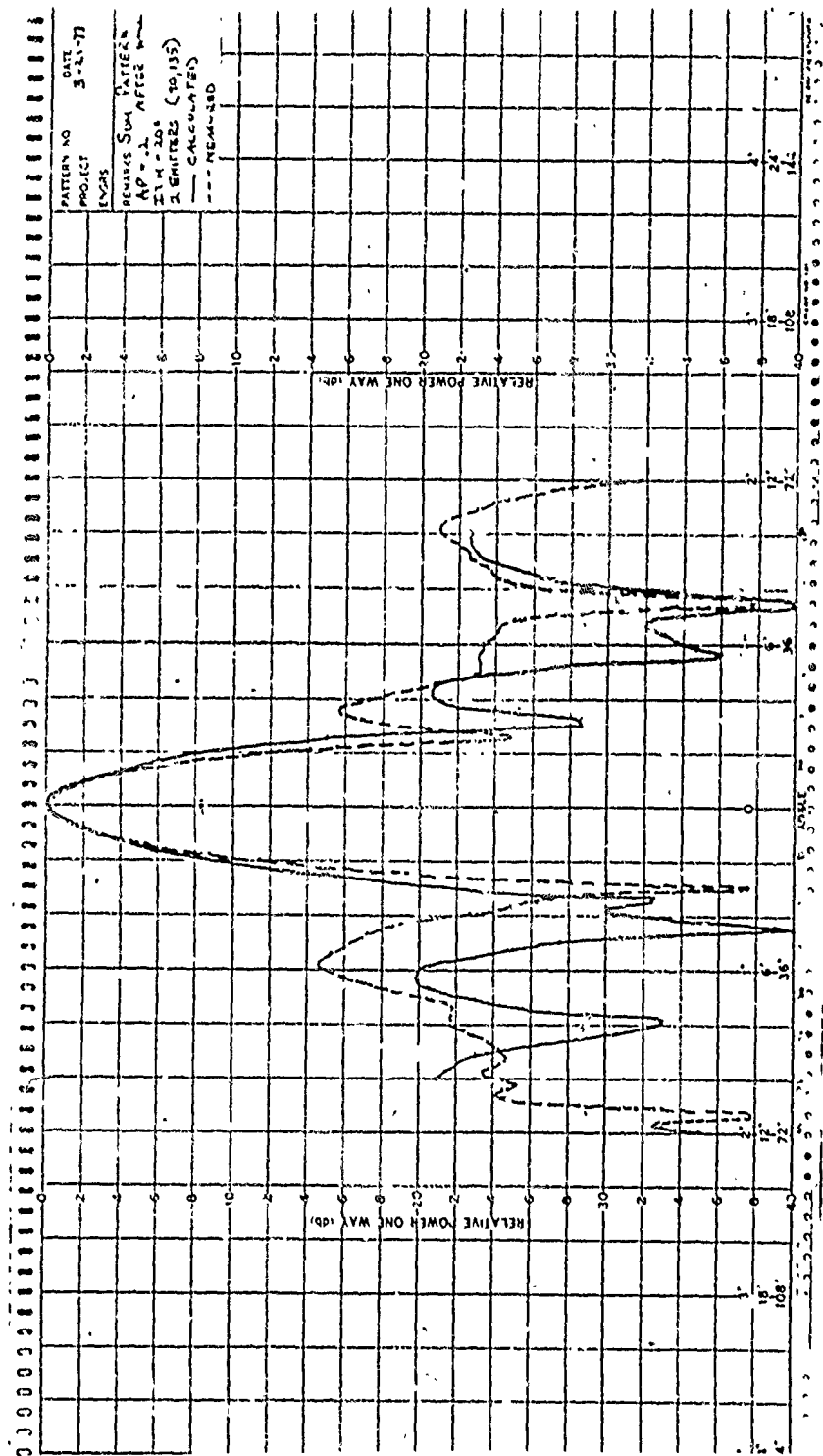
Figure 5.2.3-3b. Measured and Calculated Sum Patterns After Nulling
(0° Scan Angle and 45° Jammer Angle)
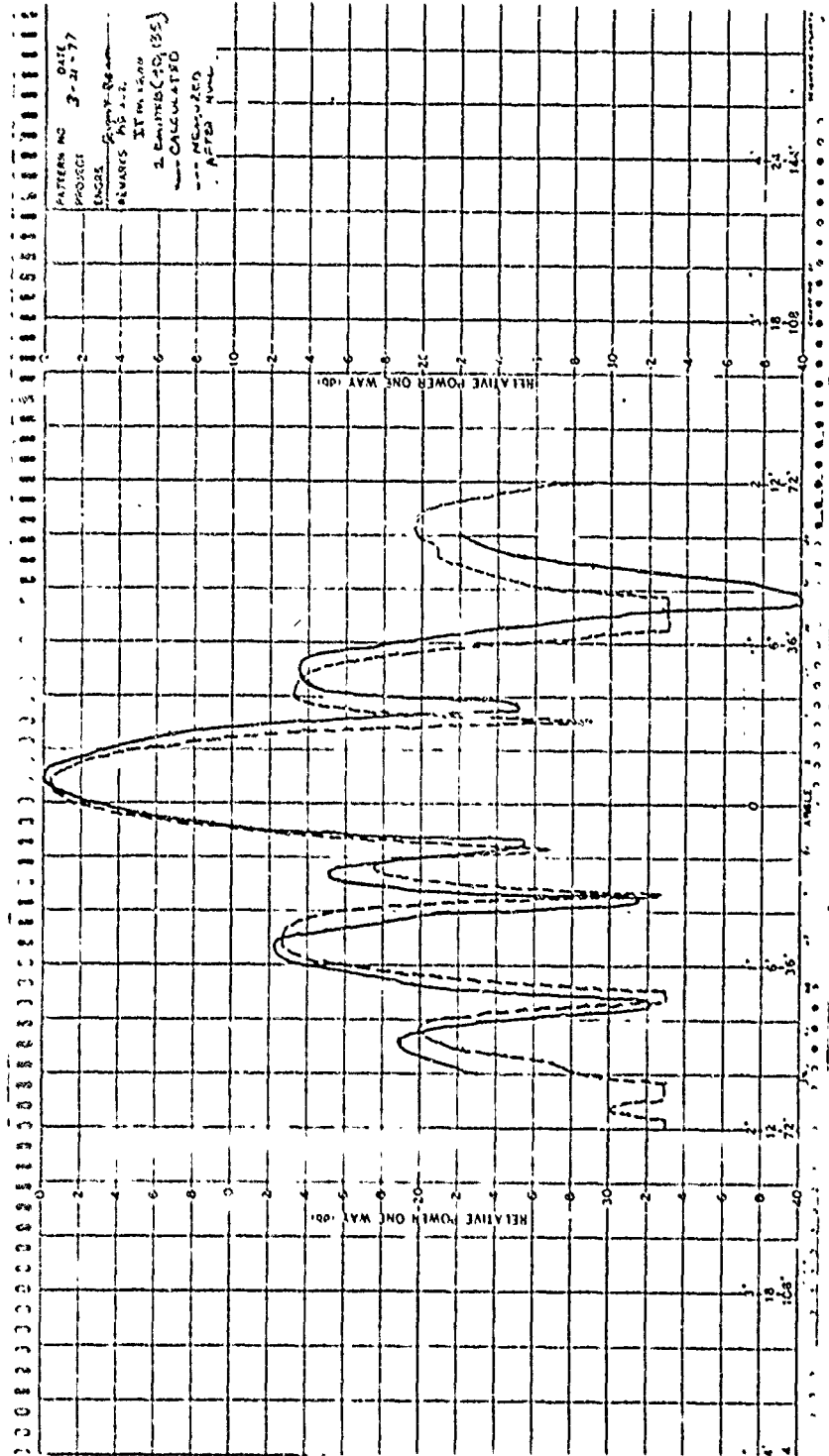
Figure 5.2.3-3c. :asured and Calculated Right-Squinted Beams After Nulling
(0° ·an Angle and 45° Jammer Angle)
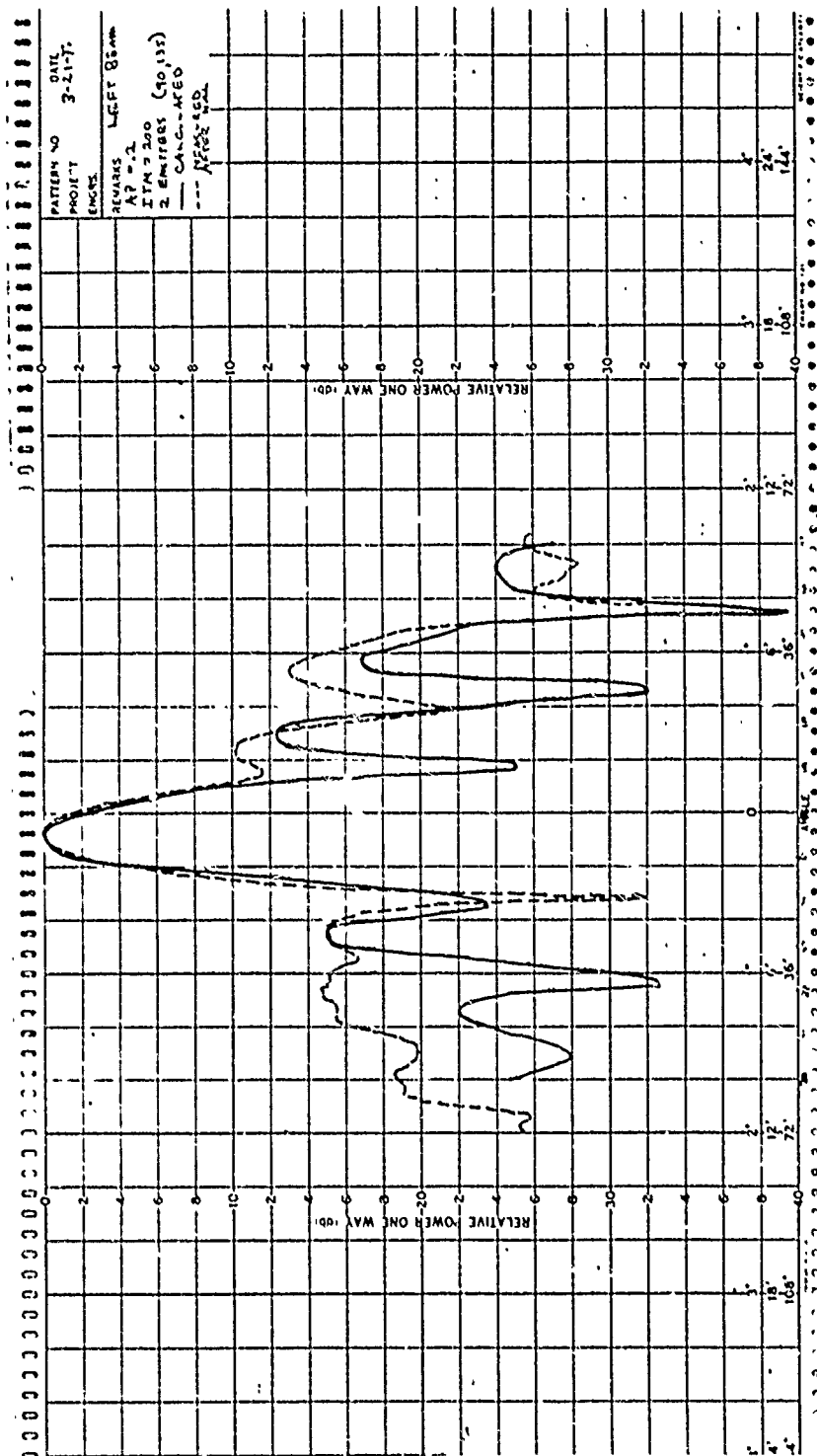
Figure 5.2.3-3d. Measured and Calculated Left-Squinted Beams After Nulling ($0°$ Scan Angle and $45°$ Jammer Angle)

123

In summary, it is felt that the patterns illustrated show that the computer simulations used in this contract have a firm basis in the actual breadboard hardware that was measured, and thus the extrapolations that were discussed in Section 4.3 to larger arrays can be accepted with some validity.

SECTION VI

SUMMARY

a. In most cases, random construction errors in the
    array cause more monopulse boresight shift error
    than will be caused by optimal null-steering of
    the sidelobes.

b. Nulling of close-in sidelobes (1st, 2nd) can cause,
    with most nulling approaches, more boresight shift
    error than construction errors.

c. Mainbeam null steering causes severe boresight
    shift error, and thus is probably impractical in
    most cases. However, the use of a correction fac-
    tor to compensate for this error is possible, if
    required. Nevertheless, accuracy will greatly
    deteriorate with mainbeam null steering.

d. Using weights at each element in adaptive arrays
    causes far less boresight shift error than omni
    sidelobe cancellers, especially when nulling high
    close-in sidelobes.

e. Pattern decomposition allows first-order estimates
    of boresight shift error due to null steering for
    most null steering approaches. At least part of
    the null steering boresight shift error can be re-
    moved by using a correction factor computed when
    the adaptive weights are known.

f. All errors tend to dimish with increasing array
    size for fixed location of the jammers, so that
    tracking accuracy using adaptive arrays is limited
    only by the size of the array, as in the case
    of ordinary monopulse arrays.

125

References

1. Howells, P. W., "Intermediate Frequency Side-Lobe Canceller," Patent No. 3,202,990, Filed 4 May 1959.

2. Applebaum, S. P., "Adaptive Arrays," SPL-TA-66-1, Syracuse University Research Corp. Syracuse, N.Y., August 1966, See also PGAP Special Issue on Adaptive Arrays, Sept. 1976.

3. Widrow, B., P. E. Mantey, L. J. Griffiths, and B. B. Goode, "Adaptive Antenna Systems," Proc. of the IEEE, Volume 55, No. 12, pp. 2143-2159, December 1967.

4. IEEE Transactions on Antennas and Propagation, Special Issue on Adaptive Arrays, September, 1976.

5. Baird, C. A., Martin, G. P., Rassweiler, G. G., and Zahm, C. L., "Adaptive Processing for Antenna Arrays," Radiation Incorporated, RADC-TR-72-174, July 1972(U), AD 748 220.

6. Technology Services Corp. "Angle Tracking with an Adaptive Array," RADC-TR-73-194, Final Technical Report, Vol. II, July, 1973, AD 767 210.

7. Nester, W. H., "A Study of Tracking Accuracy in Monopulse Phase Arrays", IEEE - PGAP, May, 1962, pp. 237-246.

8. Roy, A. G., Lehman, D. F., Rassweiler, G. G., and Oishi, R. K., "RPV Ground Terminal Antenna Study - Conceptual Design," Final Technical Report for Rome Air Development Center, Contract F30602-73-C-0117, October 1973(U). RADC-TR-130, Vol I, AD 919 853L; Vol II AD 919 854L.

9. Mikenas, V., et al., "Null-Steering Feasibility Demonstration," Final Report, Harris ESD, Contract F33615-74-C-1100, for Air Force Avionics Lab, December 1974.

10. "Hardware Investigation of RPV Null-Steering Antenna High Risk Areas", Harris ESD, Air Force Contract (AFAL)-F33615-75-C-1216, 14 September 1975(U).

11. ICNS Contract No. DAAB-7-76-C-0914.

12. Baird, C. A. and G. Rassweiler, "Adaptive Nulling Using Digitally Controlled Phase Shifters," Trans. PGAP, September 1976, pp. 638-649.

13. Marchand, N. and G. Marner, "The Theory of Spatial Sidebands Applied to Null Steering", Marchand Electronics Labs, 11 September 1975.

APPENDIX A

ANALYSIS OF MONOPULSE ARRAYS
WITH COMPLEX WEIGHTS

APPENDIX A

ANALYSIS OF MONOPULSE ARRAYS
WITH COMPLEX WEIGHTS

In this appendix we develop the mathematical expressions
for the weights, output voltages and antenna patterns for an N
element adaptive monopulse array situated in an environment
consisting of a strong jammer and a weak desired signal. It
will be evident from this discussion the manner in which the
algorithms decompose the adaptive beams into the sum of two
beams. These are the beams generated from a conventional
non-adaptive array and a cancelling beam. From this decom-
position the boresight shift due to the presence of a jammer
can be predicted.

Consider the adaptive monopulse array shown in Figure A-1.
The objective is to form a Σ and Δ beam in the boresight direc-
tion while providing spatial filtering on emitters located in
any other direction. For the case at hand we shall assume
that the environment consists of a narrowband desired signal
located at an angle $\hat{\phi}$ from boresight with power S and a narrow
band jammer located at an angle $\hat{\theta}$ from boresight with power J.
We shall also assume that there is independent uncorrelated
white noise in each channel of equal variance σ^2. Assuming
the array weights are complex it is well known that they can
be represented by the expressions

$$W_\Sigma = R_N^{-1} \underline{1} \qquad (1)$$

$$W_\Delta = R_N^{-1} D\underline{1} \qquad (2)$$

where

128
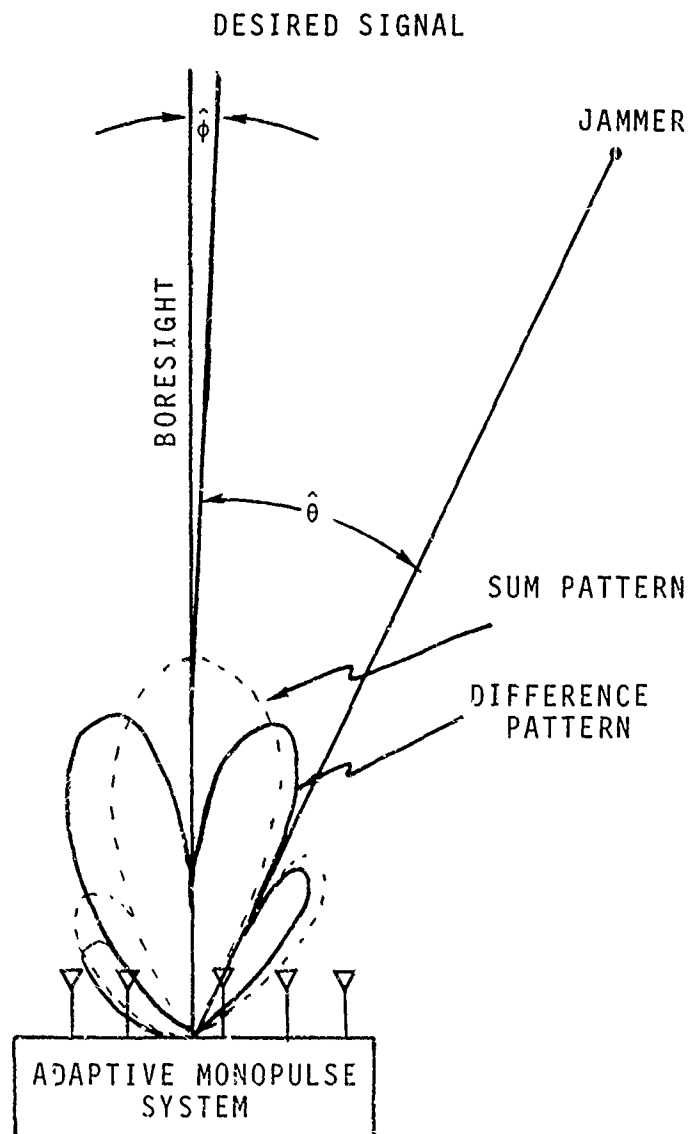
Figure A-1.   Adaptive Monopulse Array Configuration

$$D\underline{1} = \overset{\circ}{\delta}\pi \begin{bmatrix} \dfrac{-N-1}{2} \\[6pt] \dfrac{-N-3}{2} \\[4pt] \cdot \\ \cdot \\ 0 \\ \cdot \\ \cdot \\ \dfrac{-N-1}{2} \end{bmatrix} \quad ; \quad \underline{1} \sim \begin{bmatrix} 1 \\ 1 \\[2pt] \cdot \\ \cdot \\ \cdot \\ 1 \end{bmatrix} \qquad (3)$$

represent linear phase fronts across the array. The noise correlation matrix R_N can be given in terms of the jammer power, thermal noise power, and the angle of arrival of the jammer namely

$$R_N = \sigma^2 I + JVV* \qquad (4)$$

where

$$V = \begin{bmatrix} e^{j\left(\frac{N-1}{2}\right)\theta} \\[6pt] e^{j\left(\frac{N-3}{2}\right)\theta} \\[6pt] \cdot \\ \cdot \\ \cdot \\ e^{-j\left(\frac{N-1}{2}\right)\theta} \end{bmatrix} \quad ; \quad \theta = \frac{2\pi d}{\lambda}\, \sin\hat{\theta} \qquad (5)$$

with * representing complex conjugate transpose. Using the matrix inverse lemma, we can uniquely solve for the optimum weights yielding

$$W_{\Sigma} = \frac{1}{\sigma^2} \left[\underline{1} - \frac{J/\sigma^2}{1+NJ/\sigma^2} (V^* \underline{1}) V \right] \tag{6}$$

$$W_{\Delta} = \frac{1}{\sigma^2} \left[D\underline{1} - \frac{J/\sigma^2}{1+NJ/\sigma^2} (V^* D\underline{1}) V \right] \tag{7}$$

Hence it is evident that the weights can be viewed as the sum of the conventional monopulse weights plus a perturbation. That is

$$W_{\Sigma} = W_{\Sigma}^C + \delta W_{\Sigma} = \frac{1}{\sigma^2} \underline{1} + \left(-\frac{J/\sigma^4}{1+NJ/\sigma^2} (V^* \underline{1}) V \right) \tag{8}$$

$$W_{\Delta} = W_{\Delta}^C + \delta W_{\Delta} = \frac{1}{\sigma^2} D\underline{1} + \left(-\frac{J/\sigma^4}{1+NJ/\sigma^2} (V^* D\underline{1}) V \right) . \tag{9}$$

In each case the variation in the weights is proportional to the angle of arrival of the undesired signal V. Similarly the antenna pattern can be viewed as the sum of the conventional plus an additional pattern which generates nulls in the direction of the noise sources.

To demonstrate this effect, consider a unit power point source whose direction of arrival $\hat{\zeta}$ varies from -180^0 to 180. Holding the weights fixed, the output voltage due to tnis unit source generates the antenna pattern which is given by

$$\Psi_\Sigma(\hat{\xi}) = (W_\Sigma{}^C + \zeta W_\Sigma)^* \zeta = \Psi_\Sigma{}^C + \zeta \Psi_\Sigma \qquad (10)$$

$$\Psi_\Delta(\hat{\xi}) = (\dot{W}_\Delta{}^C + \zeta W_\Delta)^* \zeta = \Psi_\Sigma{}^C + \zeta \Psi_\Sigma \qquad (11)$$

where

$$\xi = \begin{bmatrix} e^{j(\frac{N-1}{2})\frac{2\pi d}{\lambda} \sin \hat{\xi}} \\ \cdot \\ \cdot \\ \cdot \\ \cdot \\ e^{-j(\frac{N-1}{2}) \frac{2\pi d}{\lambda} \sin \hat{\xi}} \end{bmatrix} . \qquad (12)$$

Substituting the expressions of the weights into those describing the antenna patterns, we see that

$$\Psi_\Sigma(\hat{\xi}) = \frac{1}{\sigma^2}(\underline{1}^*\xi) + \left(\frac{-J/\sigma^4}{1+NJ/\sigma^2}\right)(V^*\xi)(V^*\underline{1}) \qquad (13)$$

$$\Psi_\Delta(\hat{\xi}) = \frac{1}{\sigma^2}(D1)^*\xi + \left(\frac{-J/\sigma^4}{1+NJ/\sigma^4}\right)(V^*\xi)(V^*D\underline{1}) \qquad (14)$$

The first term in the above expressions represents the conventional Σ and Δ patterns whereas the last term represents the additional pattern necessary to make

$$\Psi_\Sigma(\hat{\theta}) \cong 0 \qquad (15)$$

$$\Psi_\Delta(\hat{\theta}) \cong 0 \qquad (16)$$

This is easily seen by letting $\hat{\xi}$ equal to $\hat{\theta}$ resulting in

132

$$\Psi_\Sigma(\hat{\theta}) = \frac{1}{\sigma^2}(\underline{1}^*V) + \left(-\frac{NJ/\sigma^+}{1+NJ/\sigma^2}\right)(V^*\underline{1}) \approx 0 \qquad (17)$$

$$\Psi_\Delta(\hat{\theta}) = \frac{1}{\sigma^2}(D\underline{1})^*V + \left(-\frac{NJ/\sigma^{''}}{1+NJ/c^2}\right)(V^*D\underline{1}) \approx 0 \qquad (18)$$

where we have used the fact that V*V=N. Hence we see that the
total pattern consists of the conventional pattern plus a
variation. For a linear array the variational patterns can be
written in the form

$$\delta\Psi_\Sigma(\hat{\xi}) = \frac{-J/\sigma^2}{1+NJ/\sigma^2} \Psi_\Sigma^C(\hat{\theta}) \frac{\sin N/2(\xi-\theta)}{\sin 1/2(\xi-\theta)} \qquad (19)$$

$$\delta\Psi_\Delta(\hat{\xi}) = \frac{-J/\sigma^2}{1+NJ/\sigma^2} \Psi_\Delta^C(\hat{\theta}) \frac{\sin N/2(\xi-\theta)}{\sin 1/2(\xi-\theta)} \cdot \qquad (20)$$

We note that the variational patterns consist of an amplitude
scanned $\frac{\sin NX}{\sin X}$ position centered on the jammer. It is the side-
lobes of this pattern that cause the boresight shift of the
difference pattern. The closer the jammer the more likely a
large shift will be developed. An estimation of the shift is
easily accomplished by the following expression

$$\Delta\eta \approx \frac{\delta\Psi_\Delta(0)}{\frac{d}{d\hat{\xi}}\Psi_\Delta(0)} \frac{Volts}{Volts/Rad} = rad \qquad (21)$$

which for a linear array can be written as

133

$$\Delta n(\text{RADIANS}) = \frac{\dfrac{-J/\sigma^2}{1+NJ/\sigma}\sin\left(\dfrac{N\theta}{2}\right)\left\{\dfrac{N-1}{4}\sin\dfrac{N+1}{4}\theta-\dfrac{N+1}{4}\sin\dfrac{N-1}{2}\theta\right\}}{\dfrac{\pi N}{12}(N^2-1)\sin^3\theta/2} \tag{22}$$

Note that for large jammer to thermal noise ratio's, the boresight shift (Δn) is inversely proportional to N^3. Hence, for a given jammer angle of arrival, the shift diminishes very quickly. Figure A-2 illustrates the shift in the boresight of the difference pattern as a function of the angle of arrival of the jammer for a five element linear array. The solid curve depicts the shift predicted from the previous equation while the squares illustrate the exact shift. We note the approximation gives very good results after the jammer has moved outside the main lobe of the sum pattern. For those angles which are inside the main lobe, boresight shift is a meaningless quantity since the difference pattern is no longer a useful tracking parameter.

Given the representation of the antenna pattern as a function of the jammer parameters, we now direct our efforts to develop expressions for the signal, jammer and noise voltages from the sum and difference weights.

For the desired signal, the voltage out of both arrays is given by

$$V_\Sigma^S = \sqrt{S}\ W_\Sigma^* \zeta = \frac{\sqrt{S}}{\sigma^2}\left[\underline{1}^*\zeta - \frac{J/\sigma^2}{1+NJ/\sigma^2}(V^*\underline{1})(V^*\zeta)\right] \tag{23}$$

$$V_\Sigma^S = \sqrt{S}\ W_\Delta^* \zeta = \frac{\sqrt{S}}{\sigma^2}\left[(D\underline{1})^*\zeta - \frac{J/\sigma^2}{1+NJ/\sigma^2}(V^*D\underline{1})(V^*\zeta)\right] \tag{24}$$
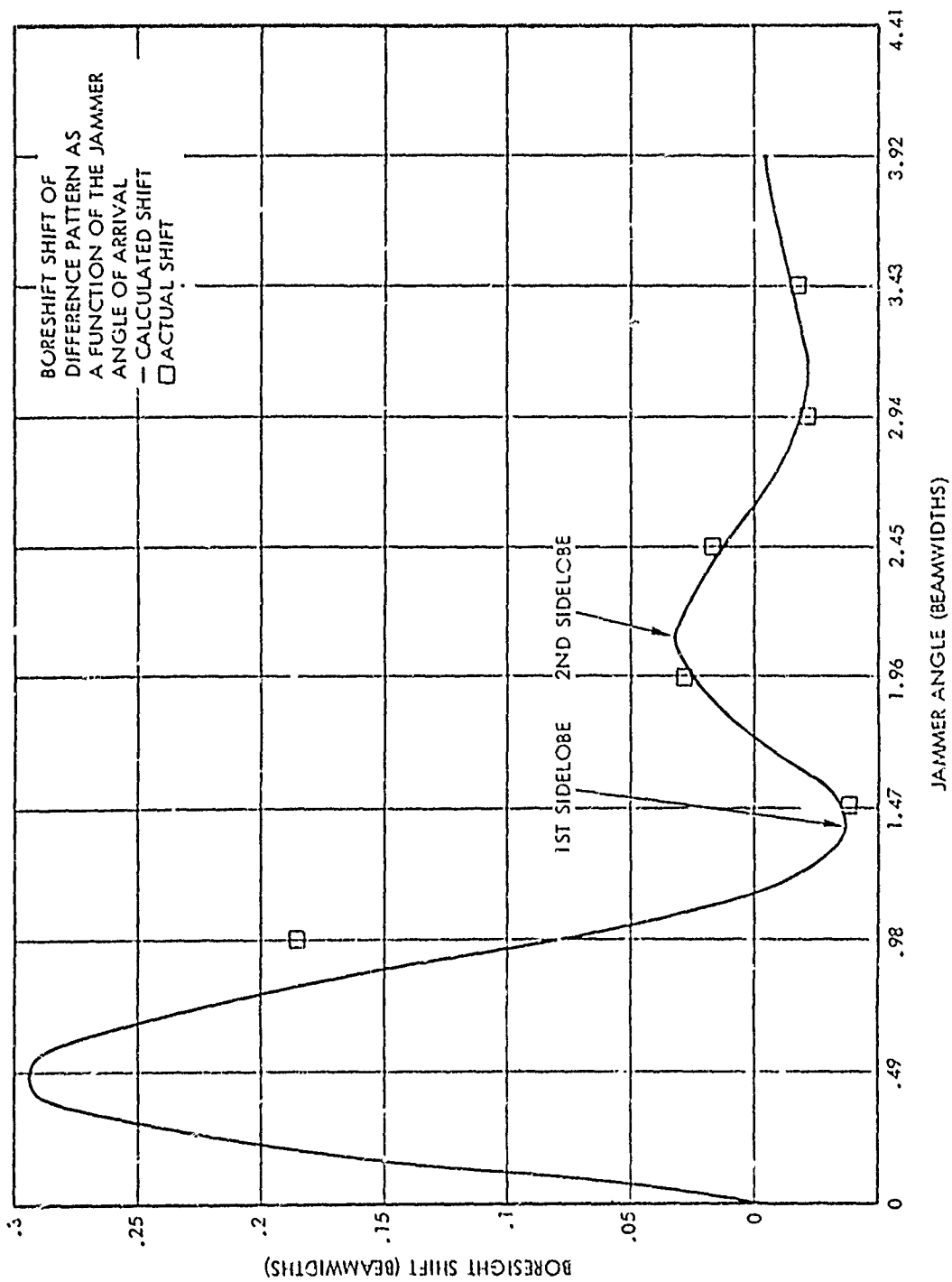
134

Figure A-2. Boresight Shift Error of Difference Pattern as a
Function of Jammer Angle of Arrival

135

where the vector ζ represents the phase front generated by the desired signal namely

$$\zeta = \begin{bmatrix} e^{j(\frac{N-1}{2})} \frac{2\pi d}{\lambda} \sin \hat{\phi} \\ \cdot \\ \cdot \\ \cdot \\ e^{-j(\frac{N-1}{2})} \frac{2\pi d}{\lambda} \sin \hat{\phi} \end{bmatrix} \tag{25}$$

Again we note the decomposition is evident in these expressions, that is, the voltage due to the desired signal is the sum of that due to a conventional array plus a term due to the perturbed weights.

Figures A-3 to A-4 illustrate the magnitude of the signal voltage in both Σ and Δ channels as a function of the angle of arrival of the jammer. It is of interest to note that although the desired signal is on boresight its output is not necessarily zero in the Δ channel. From Figure A-4 we note that it starts at zero and then increases to a maximum when the jammer is at 10° and then falls back to zero. Hence, if these patterns alone were used to track the target, there would be considerable error until the jammer was well outside the main Σ lobe.

The expressions for the jammer are similar and are given by

$$V_{\Sigma}^J = \sqrt{J} \, W_{\Sigma}^* \, V = \frac{\sqrt{J}}{\sigma^2} \left[1^T V - \frac{NJ/\sigma^2}{1+NJ/\sigma^2} (V^* 1) \right] \tag{26}$$

$$\frac{1}{\sigma^2} \frac{1}{N\sqrt{J}/\sigma^2} (1^T V)$$

$$V_{\Delta}^J = \sqrt{J} \, W_{\Delta}^* \, V = \frac{1}{\sigma^2} \frac{1}{N\sqrt{J}/\sigma^2} (V^* D 1) \tag{27}$$

136

SIGNAL U ON SUM
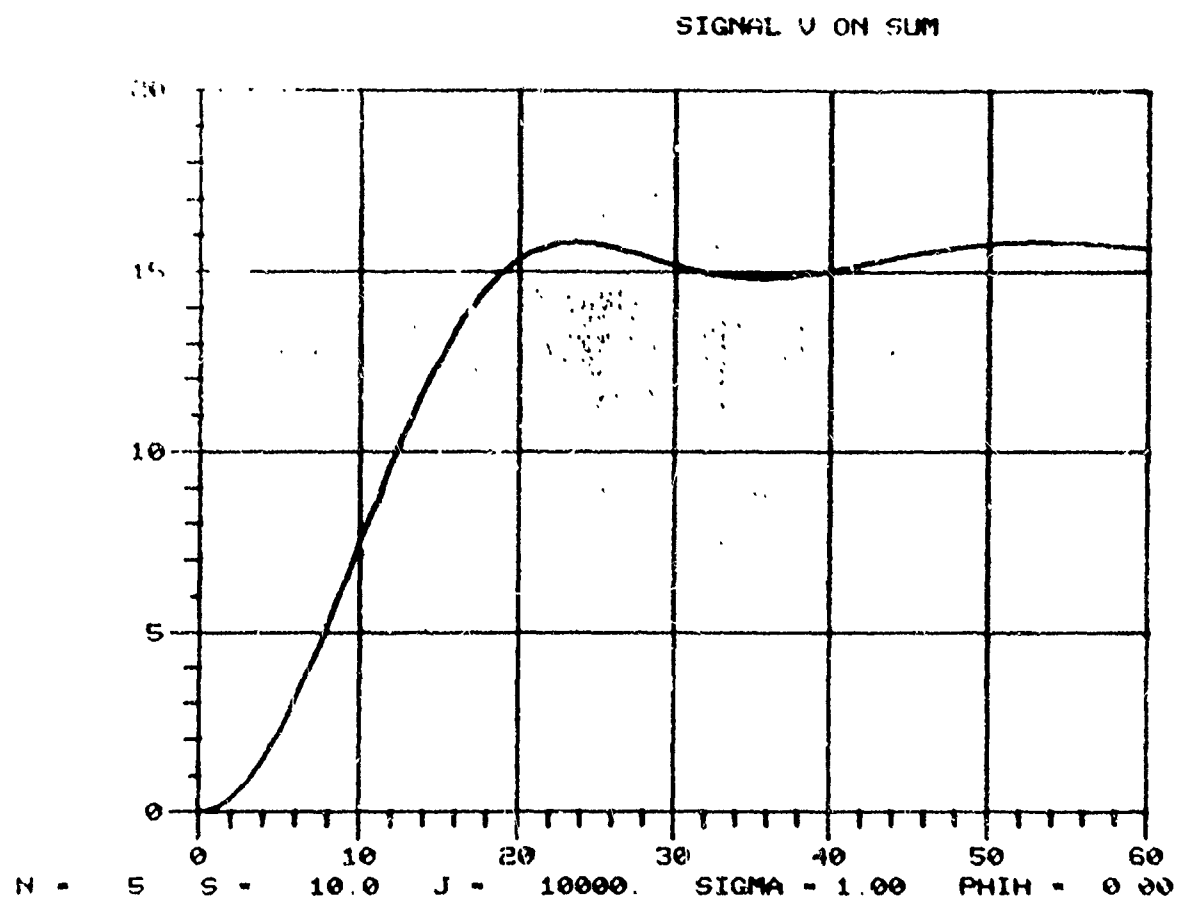
Figure A-3.   Desired Signal on Sum Channel
as a Function of the Angle of Arrival
of the Jammer

137

SIGNAL U ON DIFFERENCE
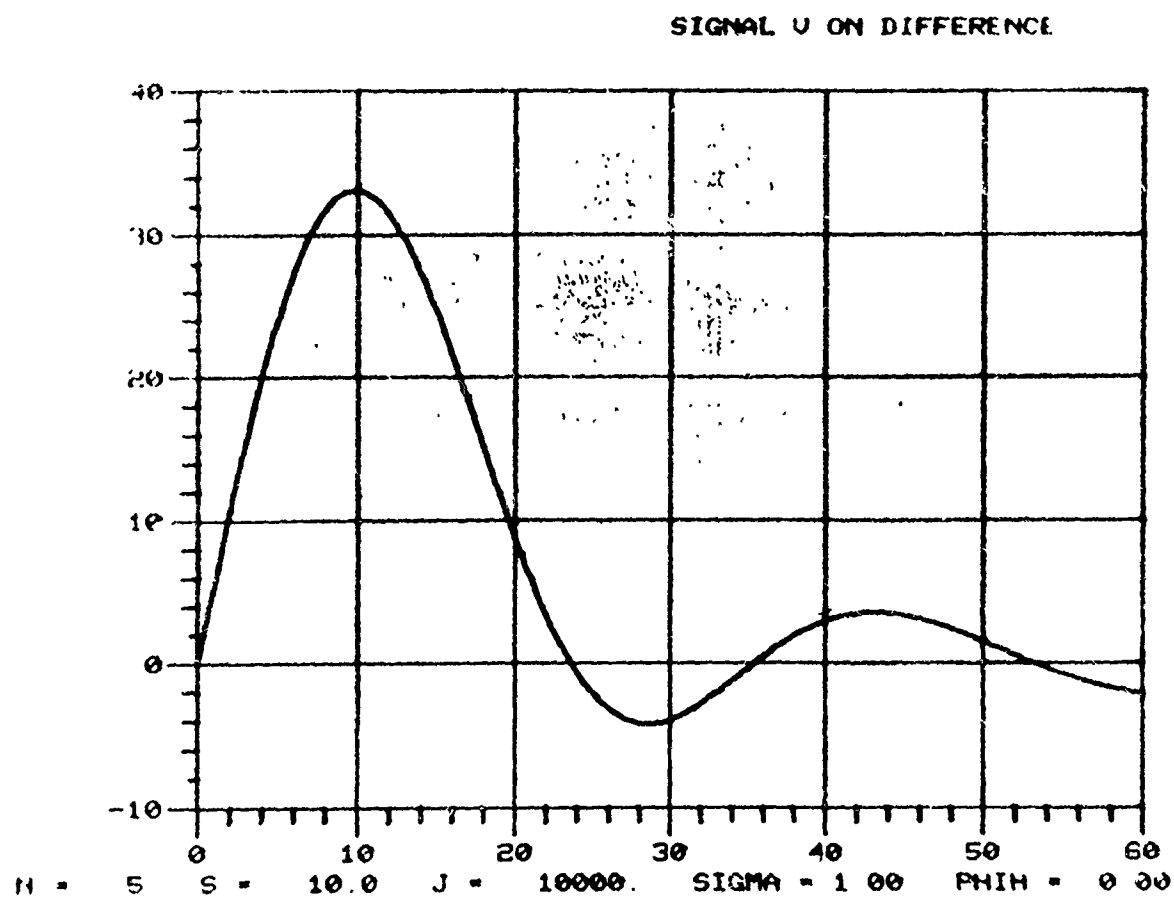
Figure A-4. Desired Signal on the Difference Channel
as a Function of the Angle of Arrival
of the Jammer

138

The adaptive nulling feature is evident from these expressions since we see that the output jammer voltage is inversely proportional to the input jammer voltage. Figures A-5 to A-6 illustrate the output jammer voltage as a function of its angle of arrival.

The average rms noise voltage for each pattern is easily computed by obtaining the norm of the weights. That is

$$V_\Sigma^N = \sigma \left[W_\Sigma{}^* W_\Sigma \right]^{\frac{1}{2}}$$

$$= \frac{\sqrt{N}}{\sigma} \left\{ 1 + |V^*\underline{1}|^2 \left[\left(\frac{J/\sigma^2}{1+NJ/\sigma^2} \right)^2 - \frac{2}{N} \left(\frac{J/\sigma^2}{1+NJ/\sigma^2} \right) \right] \right\}^{\frac{1}{2}} \quad (28)$$

and

$$V_\Delta^N = \sigma \left[W_\Delta{}^* W_\Delta \right]^{\frac{1}{2}}$$

$$= \frac{1}{\sigma} \left\{ (D\underline{1})^* D\underline{1} + |V^* D\underline{1}|^2 \left[N \left(\frac{J/\sigma^2}{1+NJ/\sigma^2} \right)^2 - 2 \frac{J/\sigma^2}{1+NJ/\sigma^2} \right] \right\}^{\frac{1}{2}} \quad (29)$$

Figures A-7 to A-8 illustrate the behavior as a function of the angle of arrival of the jammer.

139

$\times 10^{-2}$

N = 5   S = 10.0   J = 10000.   SIGMA = 1.00   PHIH = 0.00
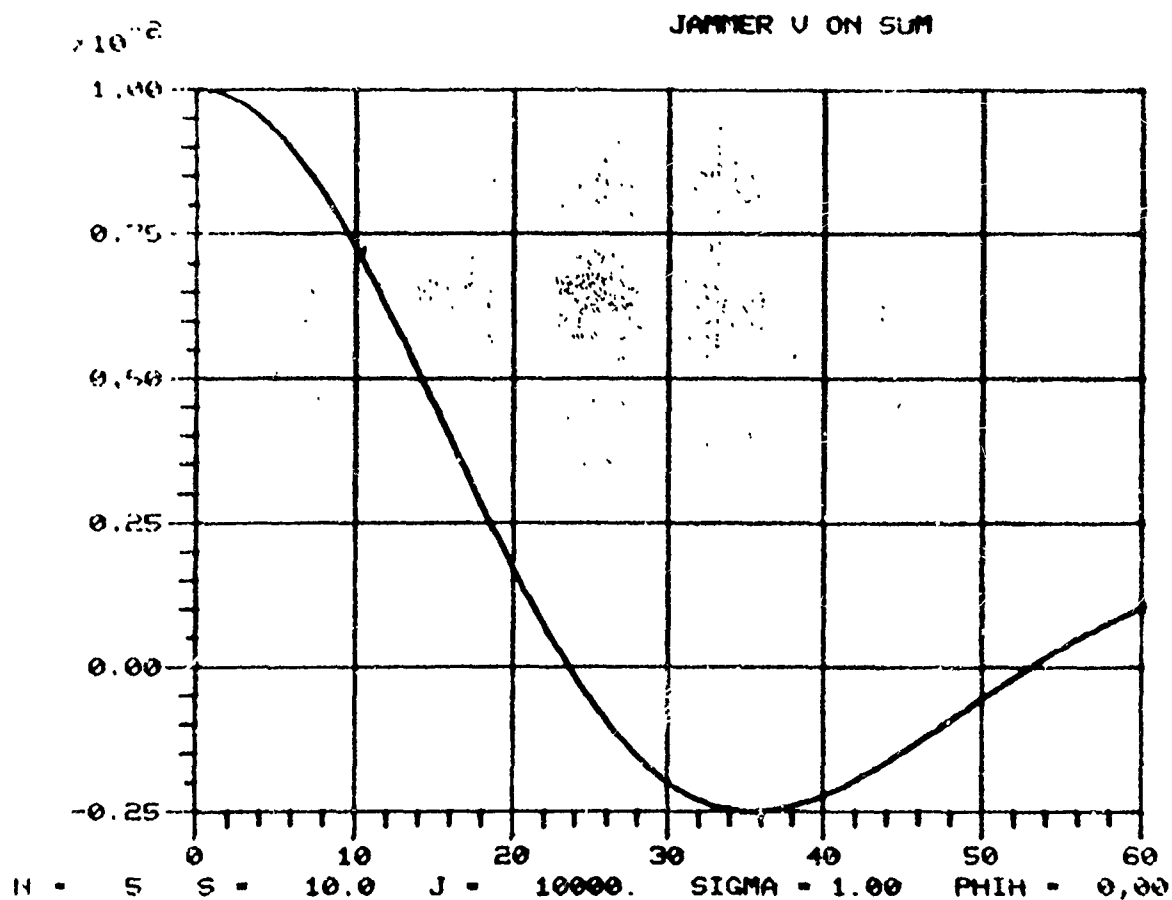
Figure A-5.   Jammer Signal on the Sum Channel
as a Function of its Angle of Arrival
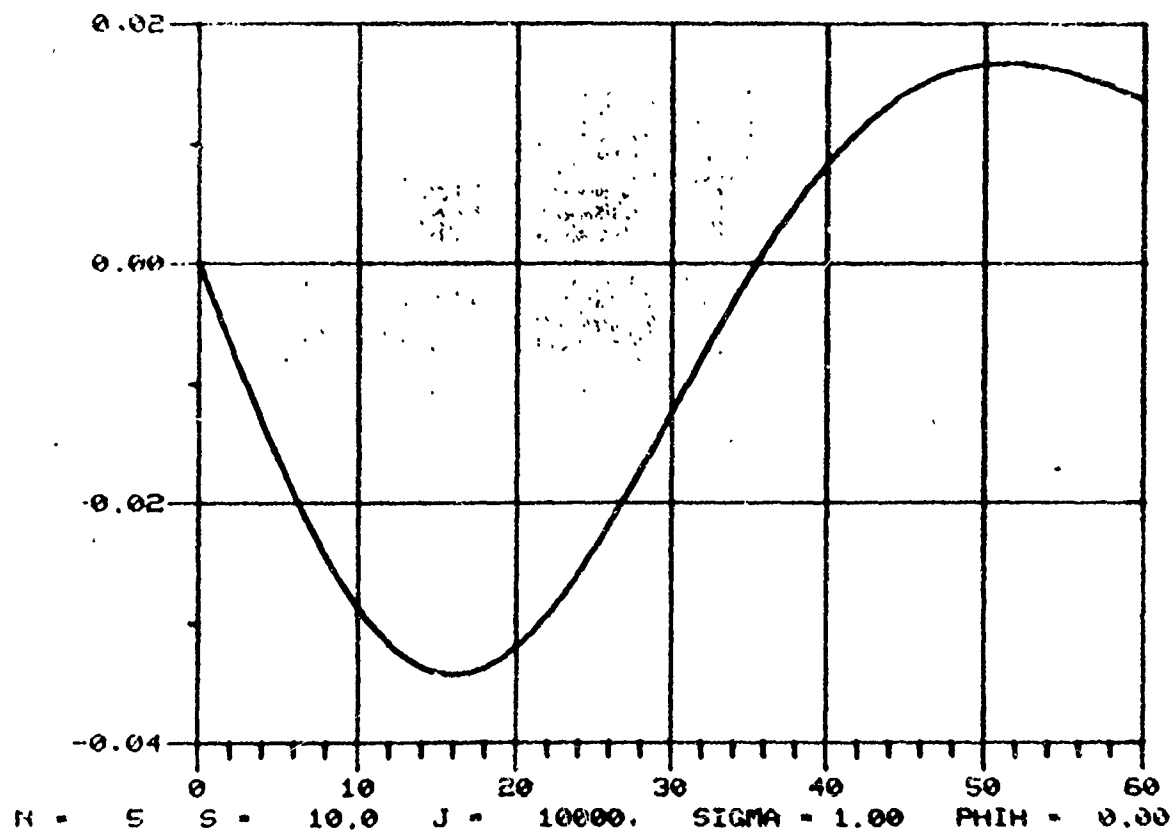
Figure A-6.   Jammer Signal on the Difference
Channel as a Function of its Angle of Arrival

N = 5   S = 10.0   J = 10000   SIGMA = 1.00   PHIH = 0.00
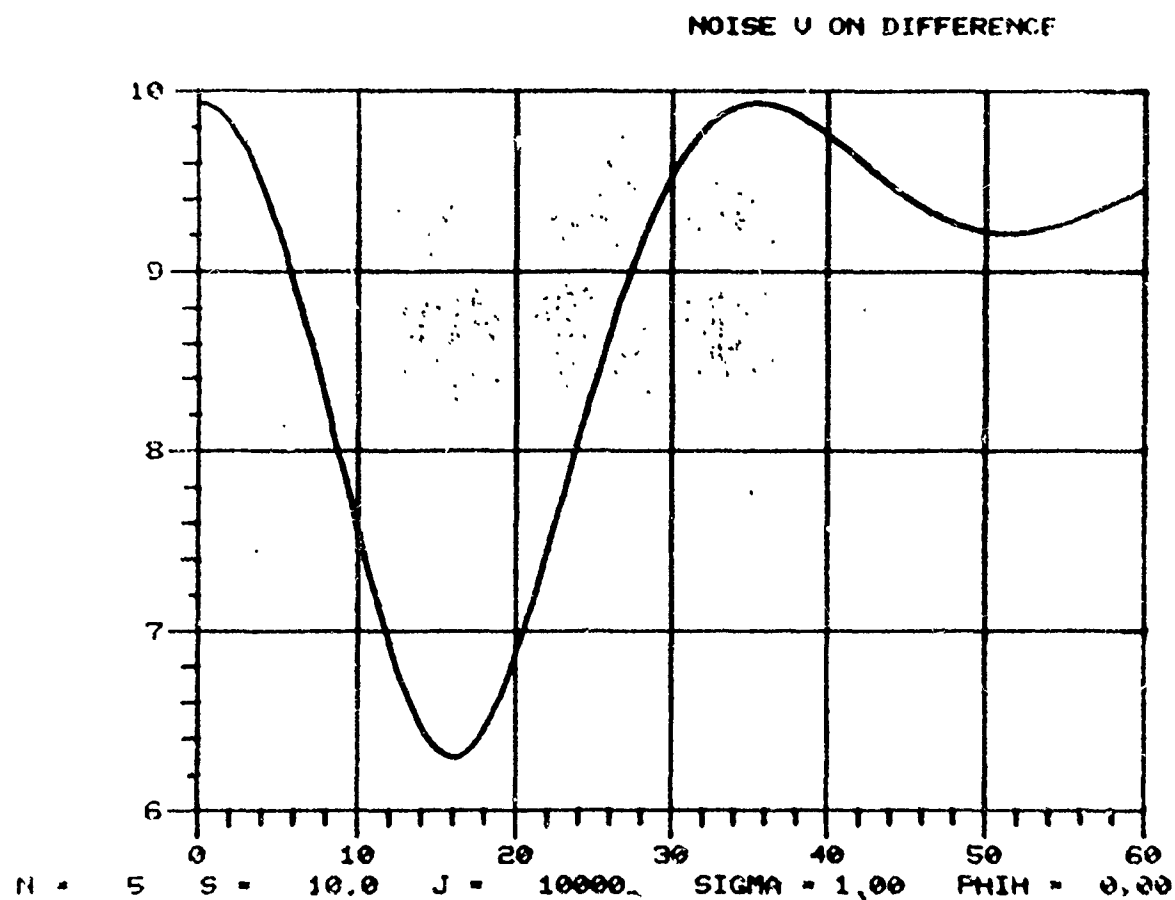
Figure A-7. RMS Noise Voltage on the Difference
Channel as a Function of the Jammer Angle of Arrival

NOISE V ON SUM
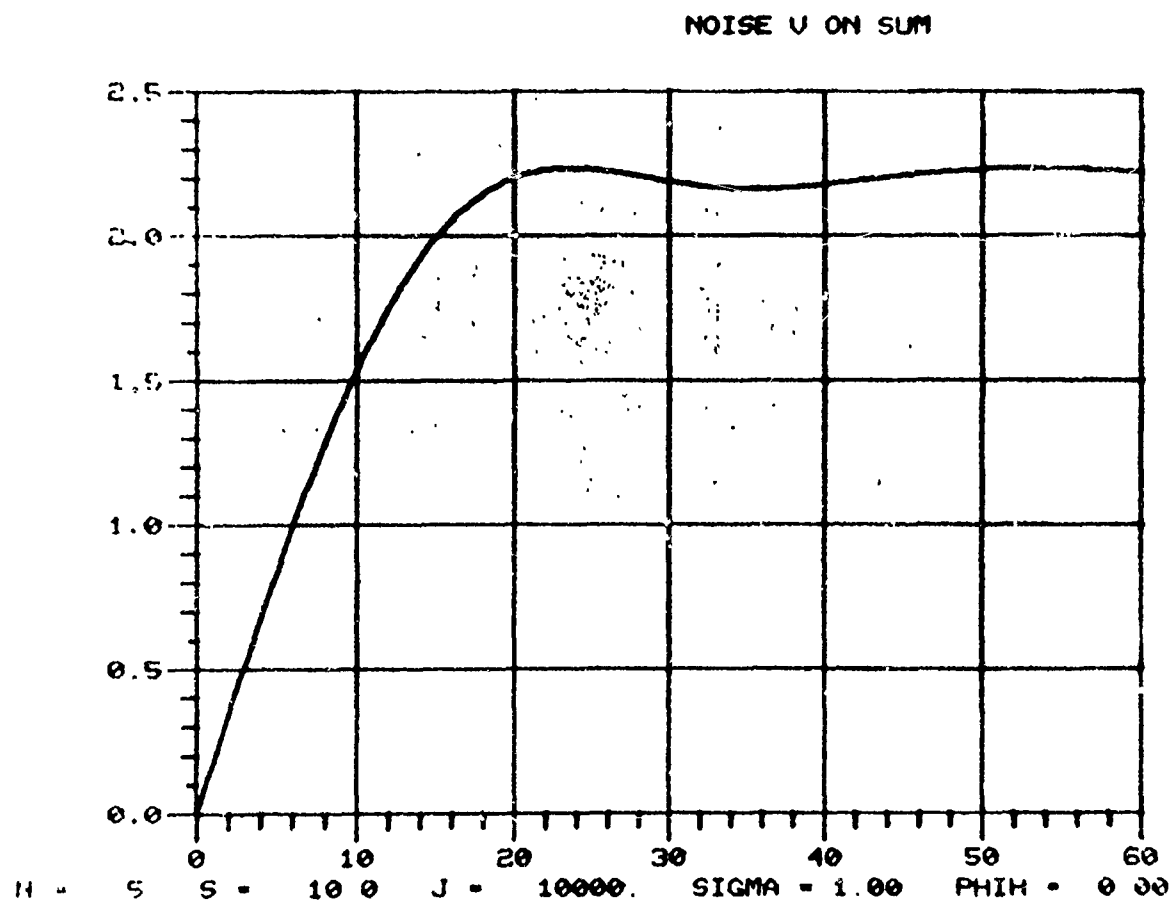
Figure A-8.   RMS Noise Voltage on the Sum Channel
            as a Function of the Jammer Angle of Arrival

143

APPENDIX B

MAXIMUM LIKELIHOOD ESTIMATES OF BORESIGHT ERROR

B1 Introduction

It is well known that the presence of sidelobe interference induces boresight shifts in nonadaptive monopulse tracking arrays there-by generating errors in its tracking capability. In an attempt to reduce this problem sum (Σ) and difference (Δ) patterns are generated with an adaptive capability such that pattern nulls are formed on all directional interference impinging on the array from directions other than boresight. However, it is easily seen that these adaptive beams also vary as a function of the external noise distribution. Hence, the error measure normally used to track (Δ/Σ) will provide erroneous angle information. Technology Services have recently devised an approach utilizing the adaptive sum and difference patterns such that if approximate knowledge of the angle of arrival of the desired signal is known then a maximum likelihood estimate of the error $K(\hat{\varepsilon}_a - \varepsilon_a)$ can be formed where $\hat{\varepsilon}_a$ and ε_a are the estimated and true angles of arrival with K denoting a random variable, the expected value of which is positive. That is, from the Σ and Δ beams an error function is generated that is sign sensitive with zero bias which can be used in a feedback loop for tracking purposes. One disadvantage of this technique noted from our simulation is that if the jammer is inside the natural sum beam the error estimate becomes very poor and may have incorrect sign information which will negate the procedure. The next section provides a brief discussion of the generation of the expression used for angle of arrival estimation.

B2 Procedure

Consider an environment consisting of a weak desired signal and noise such that at any instant in time we may represent in vector notation the signals in the array elements as

$$X = S + N$$

where

$$S = bV(\varepsilon)$$

with b representing the desired signal power and V representing

$$V = \begin{bmatrix} \exp\ (2\pi\ \frac{d}{\lambda}\ \varepsilon) \\[2ex] \exp\ (4\pi\ \frac{d}{\lambda}\ \varepsilon) \\[1ex] \cdot \\ \cdot \\ \cdot \\[1ex] \exp\ (2n\pi\ \frac{d}{\lambda}\ \varepsilon) \end{bmatrix}$$

with ε denoting the angle of arrival of the desired signal relative to the boresight of the array.

Assuming that all the noise sources are jointly Gaussian the probability density function for the signal plus noise process can be formed and is given by

$$P(x \mid S+N) = (\pi)^{-n}\ |R_N|^{-1}\ \exp\ (X-bV(\varepsilon))\ *R_N^{-1}\ (X-bV(\varepsilon))$$

where R_N is the noise convariance matrix. To obtain an estimate of ε depending on the data and R_N we utilize those values of b and ε which maximize the likelihood function. If we let

$$Q(X|b,\varepsilon) = (X-bV(\varepsilon))\ *R_N^{-1}\ (X-bV(\varepsilon))$$

then it is sufficient to maximize this expression. Maximizing this expression with respect to b reduces Q to a function of ε only namely

$$Q(\varepsilon) = X*R_N^{-1}\ X-(\mid X*R_N^{-1}V\mid^2/V*R_N^{-1}V)$$

145

The maximum likelihood estimate $\hat{\varepsilon}$ of ε can be found by finding the value of ε which makes $\left.\frac{dQ(\varepsilon)}{d\varepsilon}\right|_{\varepsilon} = 0$. The solution of this expression is very cumbersome and requires many computations of the parameters involved. Hence, the approach is to expand $Q(\varepsilon)$ about the boresight angle. If ε_1 denotes this value then

$$Q(\varepsilon) = Q(\varepsilon_1) + \left.\frac{dQ}{d\varepsilon}\right|_{\varepsilon_1} (\varepsilon - \varepsilon_1) + \tfrac{1}{2} \left.\frac{d^2Q}{d\varepsilon^2}\right|_{\varepsilon_1} (\varepsilon - \varepsilon_1)^2$$

This quantity is minimized when $\frac{dQ}{d\varepsilon}$ is zero, or

$$(\varepsilon \cdot \varepsilon_1) = Q'/Q''.$$

Hence, for small errors in the angle of arrival, the above expression provides a correction term so the optimum estimate can be obtained. A variation of the above estimate is in fact used by Technology Services namely

$$(\varepsilon - \varepsilon_1) \cong -Q'/EQ''.$$

Expanding this expression in terms of the weights in the sum and difference channels it can be shown that

$$(\hat{\varepsilon} - \varepsilon_1) = \left[W_\Sigma^* 1 (\overline{\Sigma}\Delta + \overline{\Delta}\Sigma) - |\Sigma|^2 (1^* W_\Delta + W_\Delta^* 1) \right] \Big/$$

$$\{ 2 \, W_\Delta^* R_N W_\Delta \, |\Sigma|^2 - W_\Delta^* 1 \overline{\Sigma}\Delta - 1^* W_\Delta \Sigma \overline{\Delta} + W_\Sigma^* 1 |\Delta|^2$$

$$- 2 (W_\Sigma^* 1 W_\Delta^* R_N W_\Delta - W_\Delta^* 1 \, 1^* W_\Delta) \}$$

where

$$\Sigma \overset{\Delta}{=} W_\Sigma^* X = 1^* R_N^{-1} X$$

$$\Delta = W_\Delta^* X = -1^* D R_N^{-1} X$$

146

and where D is the diagonal matrix

$$D = \frac{2\pi}{\lambda} \zeta \, diag \, (1,2,\ldots,n).$$

From these expressions it is noted that the <u>maximum likeli-</u>
<u>hood estimate</u> of the error between the true and estimated angles
of arrival can be obtained from knowledge of the adaptive
weights on the sum and difference channels as well as the
outputs of these channels. It can be easily seen that if the
external noise field is uncorrelated in each channel with equal
variance then the expressions for W_Σ and W_Λ are equal to the
usual weights for nonadaptive Σ and Δ patterns.

The following section of this appendix graphically presents
analytical results of this technique so that it can be
more easily evaluated.

B3 <u>Results</u>

For purposes of understanding the behavior of the technique
described here we shall consider a five element linear array
and an environment consisting of a desired signal and one
jammer. The SNR of the desired signal over thermal noise is
assumed to be 10 dB where as the jammer to thermal noise ratio
is 40 dB. Figures B-1 and B-2 illustrate the conventional Σ on Δ
patterns from a nonadaptive array. We note that the beam width
for this array is approximately 20^0. If a jammer is present then
the adaptive circuitry modifies the patterns so that nulls
are placed on the directional interference sources. Figures B-3
through B-28 illustrate the behavior of the Σ and Δ patterns as
the jammer is moved from 5^0 to 65^0 in increments of 5^0. From
these figures it is evident that the presence of the jammer
significantly modifies the shape of both patterns near boresight
whenever the jammer is inside the main beam of the unadaptive
array sum pattern, which is on the order of $\pm 20^0$. The difference

147

pattern is perhaps most sensitive to the jammer angle of arrival.
We note that it is almost totally destroyed when the jammer has
angle less than 15^0 relative to boresight. The eratic behavior
of the difference pattern when the jammer is located in the
main beam has an undesirable effect on the estimator used to
predict the angle of arrival of the desired signal. Figures
B-29 through B-37 illustrate the estimate of the true angle of
arrival when the target is estimated to be on boresight as a
function of jammer angle for various values of $\hat{\emptyset}$. The magnitude
of the estimate is related to the angle of arrival via

$$\hat{r} = Sin \emptyset$$

In our simulations it was noted that the estimate of the
true angle of arrival was relatively accurate for errors of a
degree or less provided the jammer was located outside the main
sum pattern. The sign of the estimate was correct for all off-
sets again provided the jammer was located outside the sum beam.
Hence, the technique proposed by Technology Services appears
useful provided the jammer comes in a sidelobe of the Σ pattern
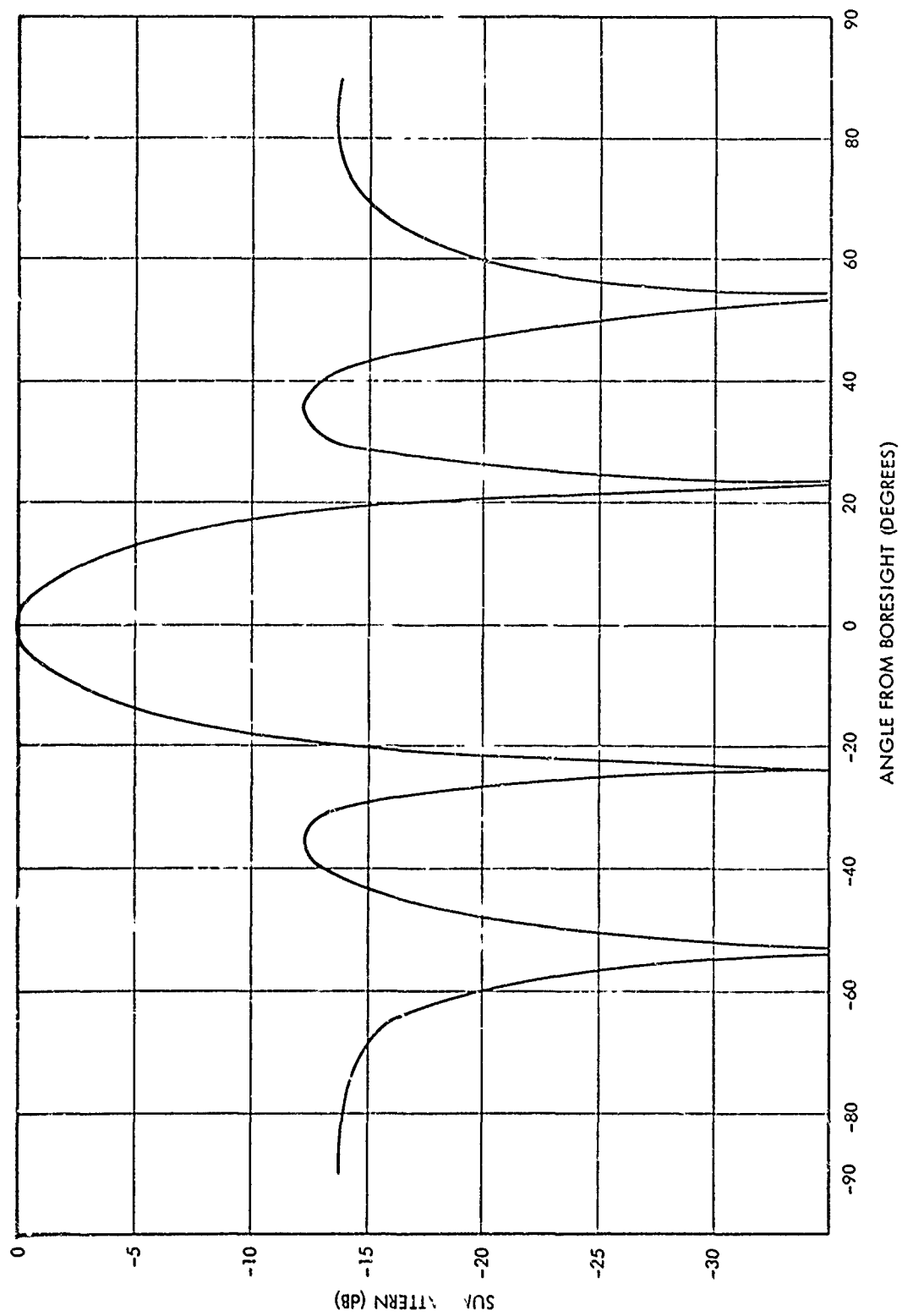and also provided the technique is used in a feedback fashion

148

Figure B-1 Conventional Sum Pattern (5 Element Array)

149

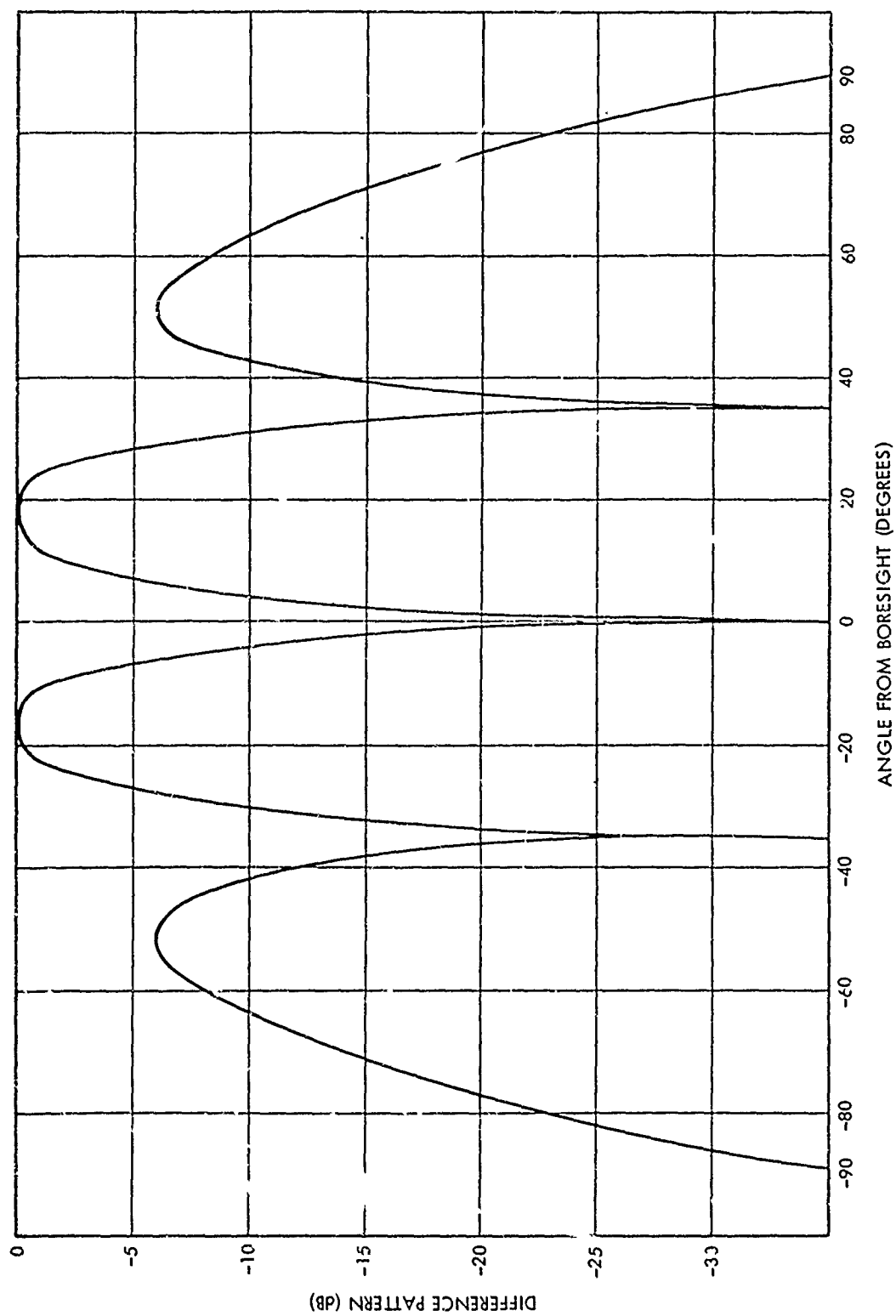Figure B-2   Conventional Difference Pattern (5 Element Array)

ANGLE FROM BORESIGHT (DEGREES)

DIFFERENCE PATTERN (dB)

150

Figure B-3. Adaptive Sum Pattern with Jammer at 5°
from Boresight

151

Figure B-4. Adaptive Difference Pattern with Jammer at 5⁰
from Boresight

Figure B-5. Adaptive Sum Pattern with Jammer at 10° from Boresight

153

Figure B-6. Adaptive Difference Pattern with Jammer at 10°
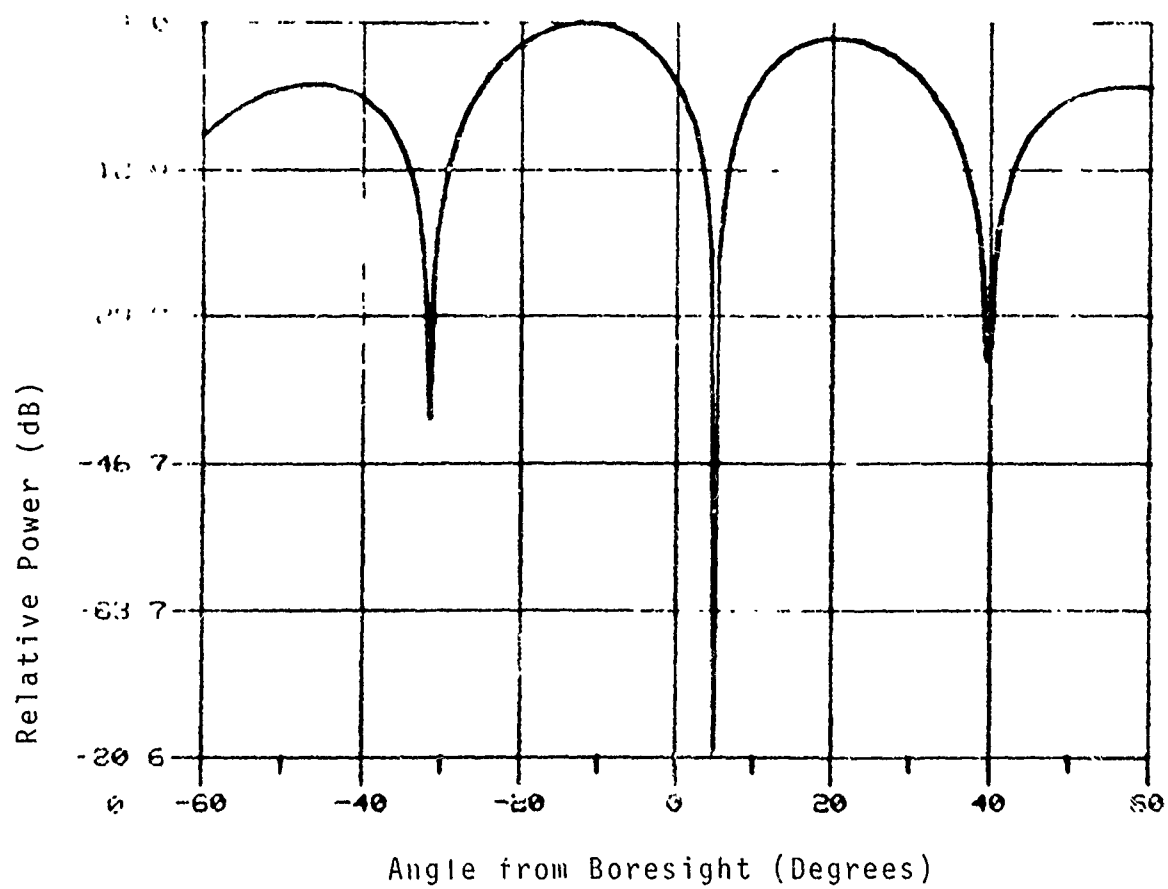from Boresight

154

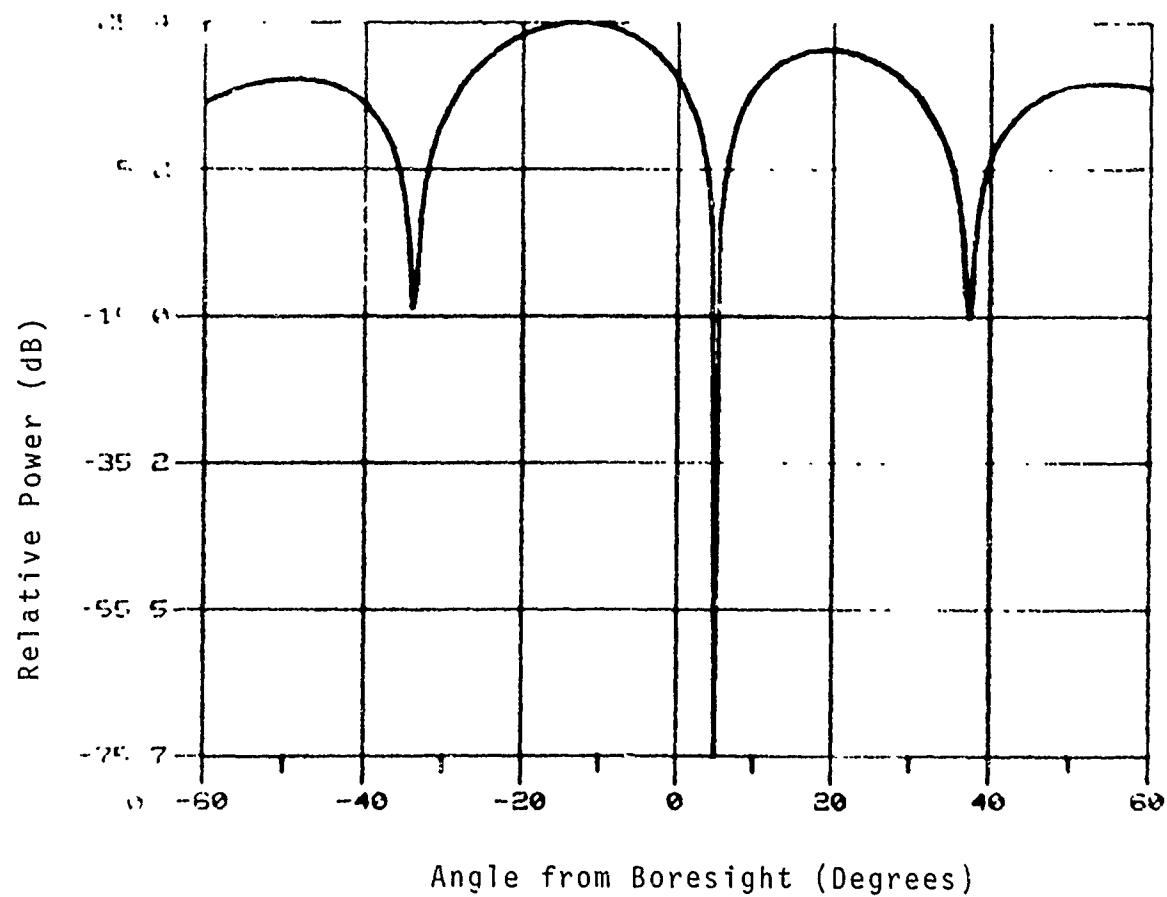Figure B-7. Adaptive Sum Pattern with Jammer at 15°
from Boresight

155

Figure B-8. Adaptive Difference Pattern with Jammer at 15° from Boresight

Figure B-9. Adaptive Sum Pattern with Jammer at 20^0
from Boresight

157

Figure B-10. Adaptive Difference Pattern with Jammer at 20°
from Boresight

158

Figure B-11. Adaptive Sum Pattern with Jammer at 25°
from Boresight

159

Figure B-12. Adaptive Difference Pattern with Jammer 25°
from Boresight
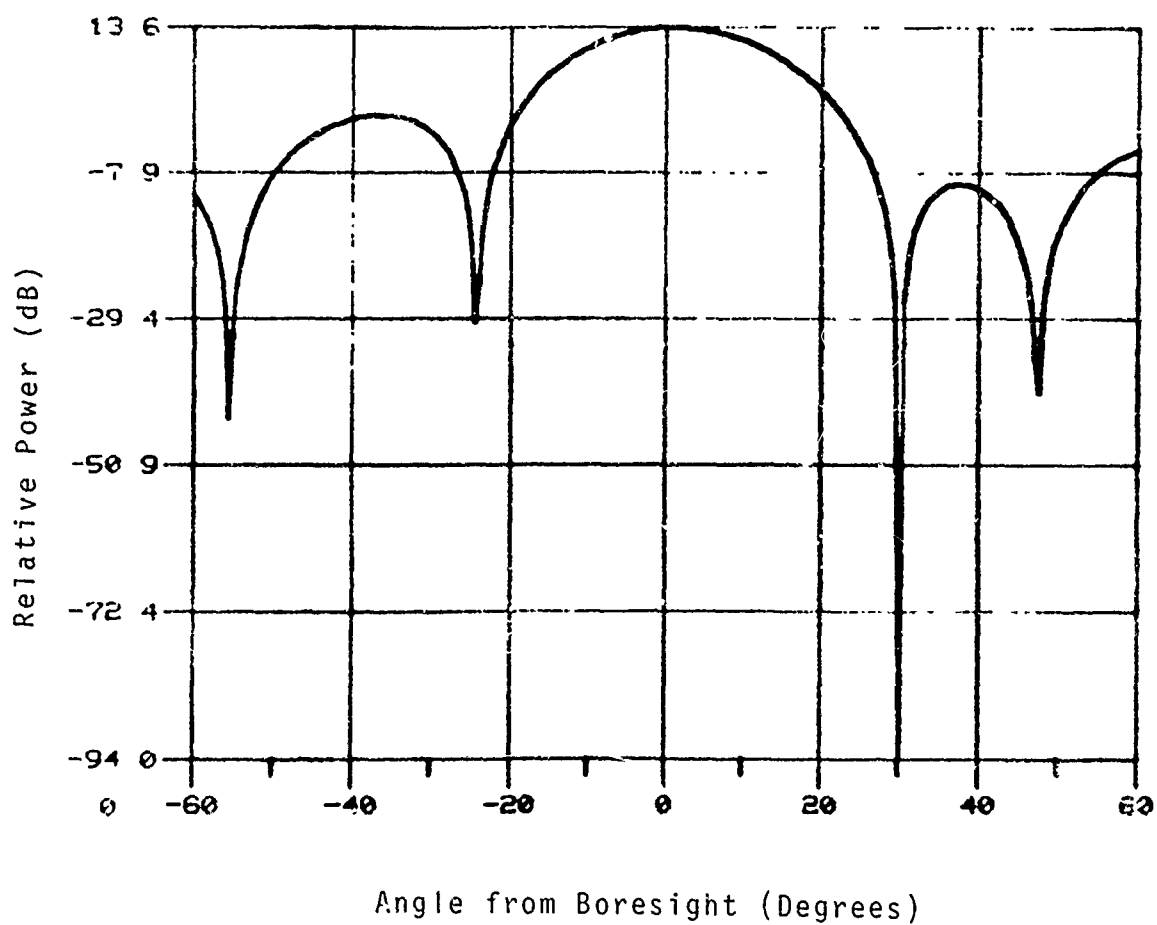
Figure B-13. Adaptive Sum Pattern with Jammer at 30^0 from Boresight

161

Figure B-14. Adaptive Difference Pattern with Jammer at 30°
from Boresight

162
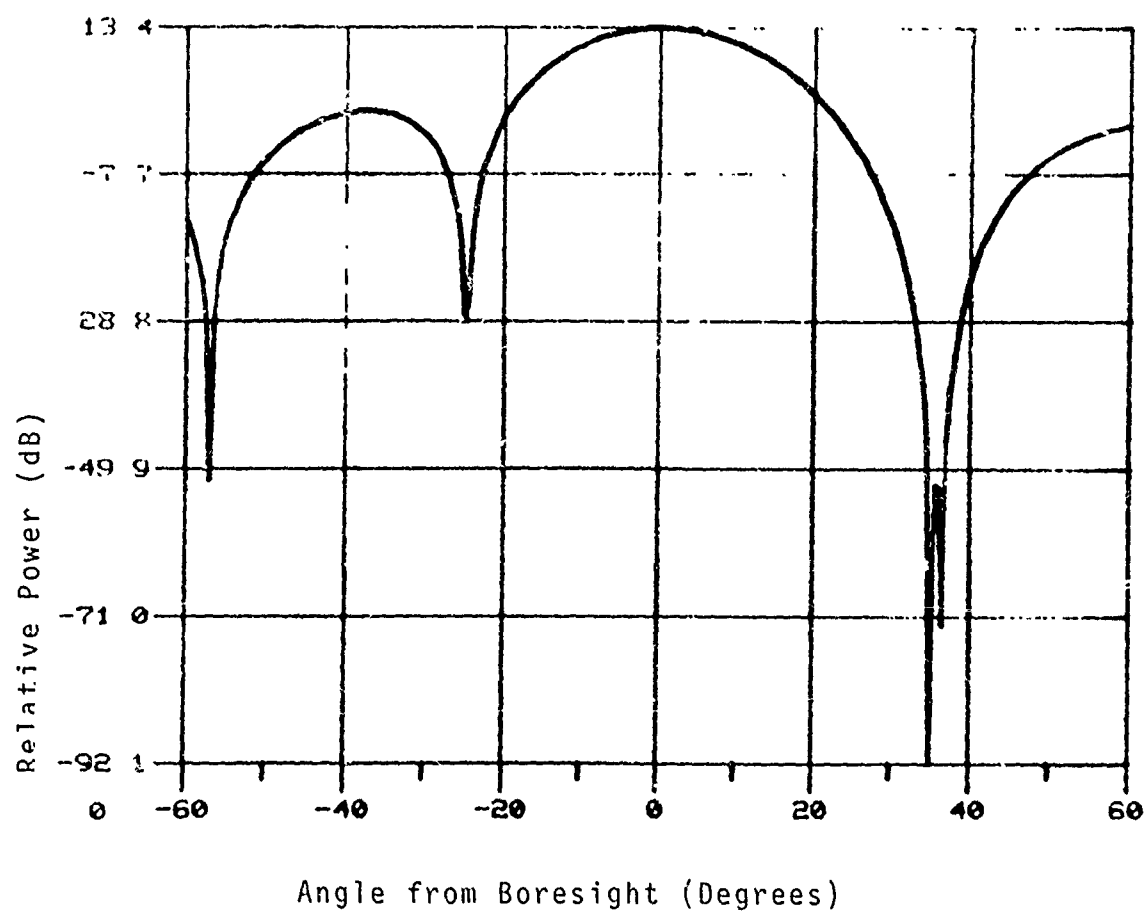
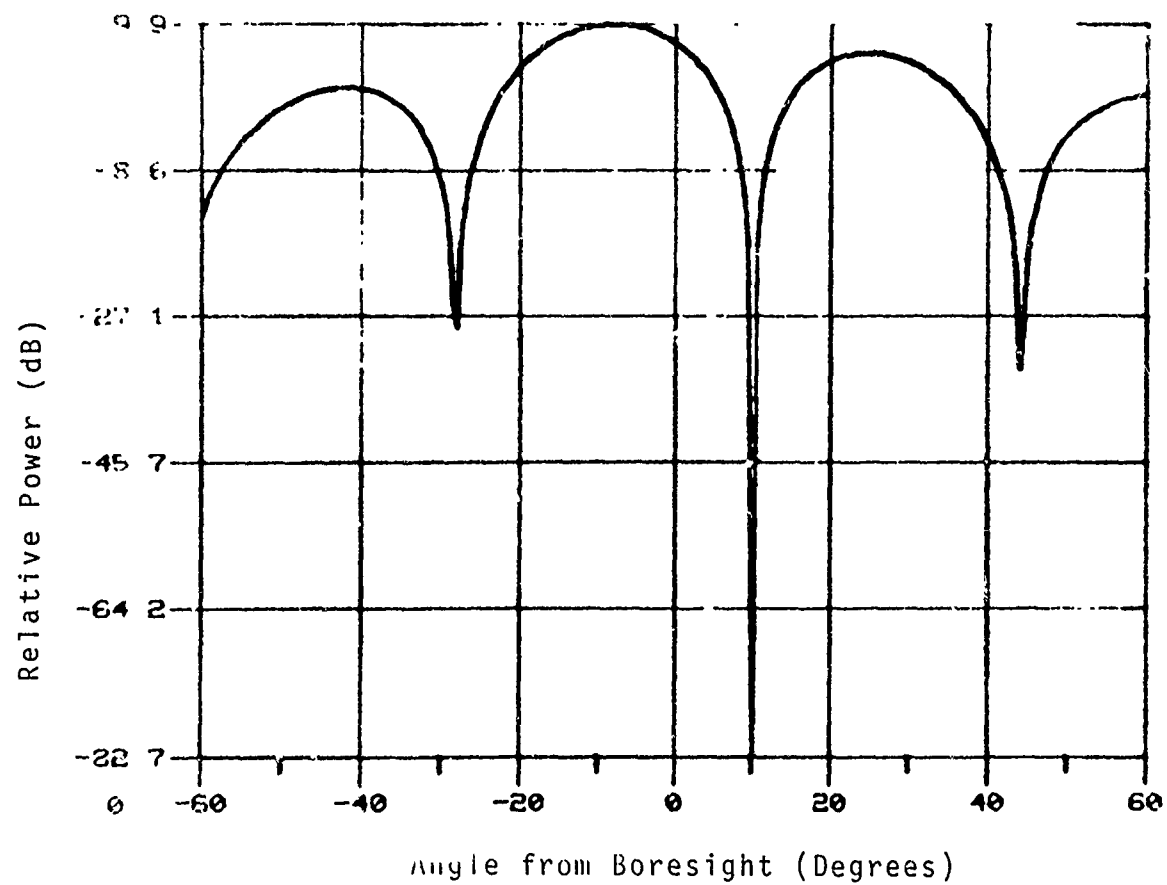Figure B-15 Adaptive Sum Pattern with Jammer at 35°
from Boresight

163
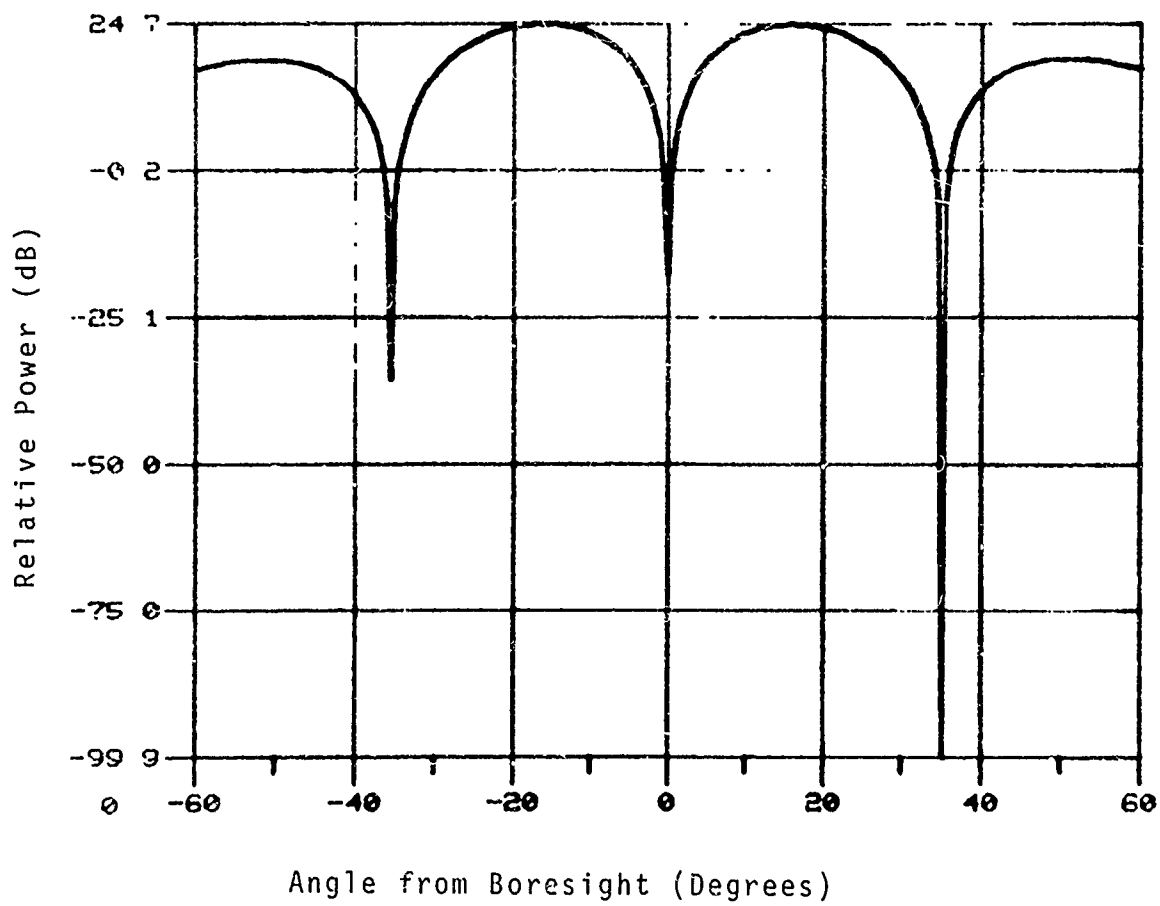
Figure B-16 Adaptive Difference Pattern with Jammer at 35°
from Boresight

164
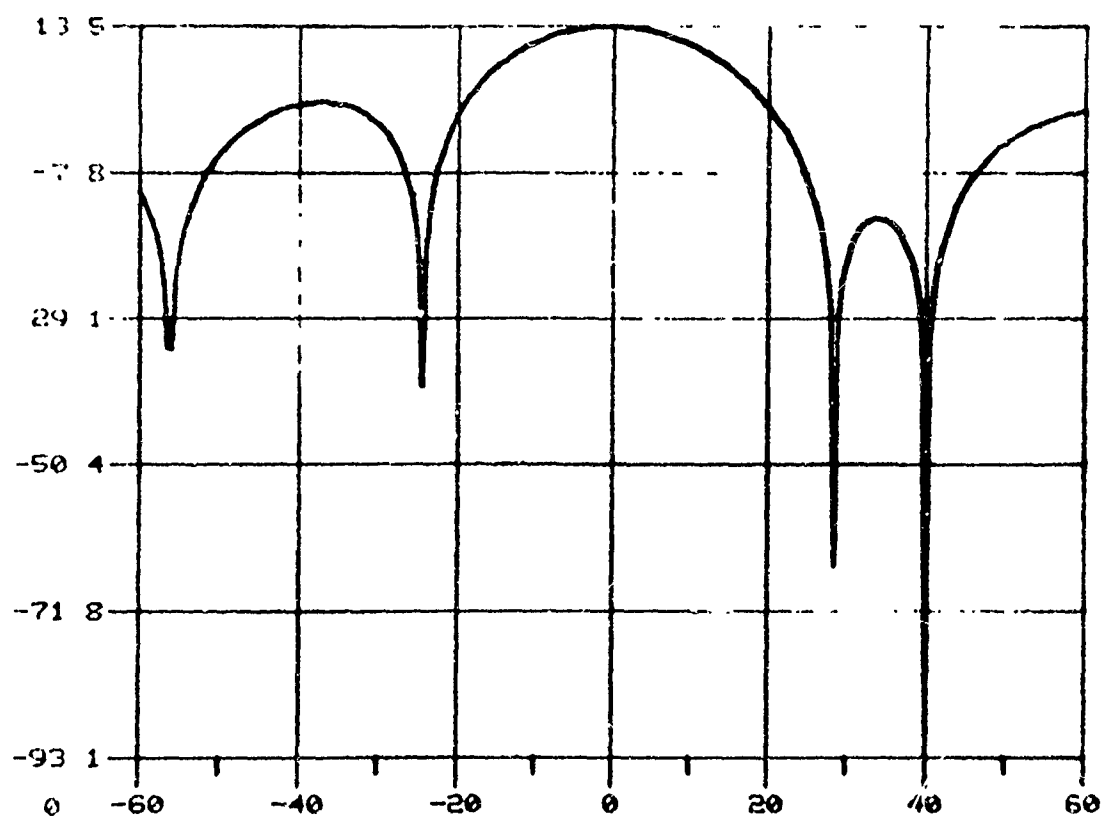
Figure B-17 Adaptive Sum Pattern with Jammer at 40^{0} from
Boresight

Figure B-13 Adaptive Difference Pattern with Jammer
at 40° from Boresight

166
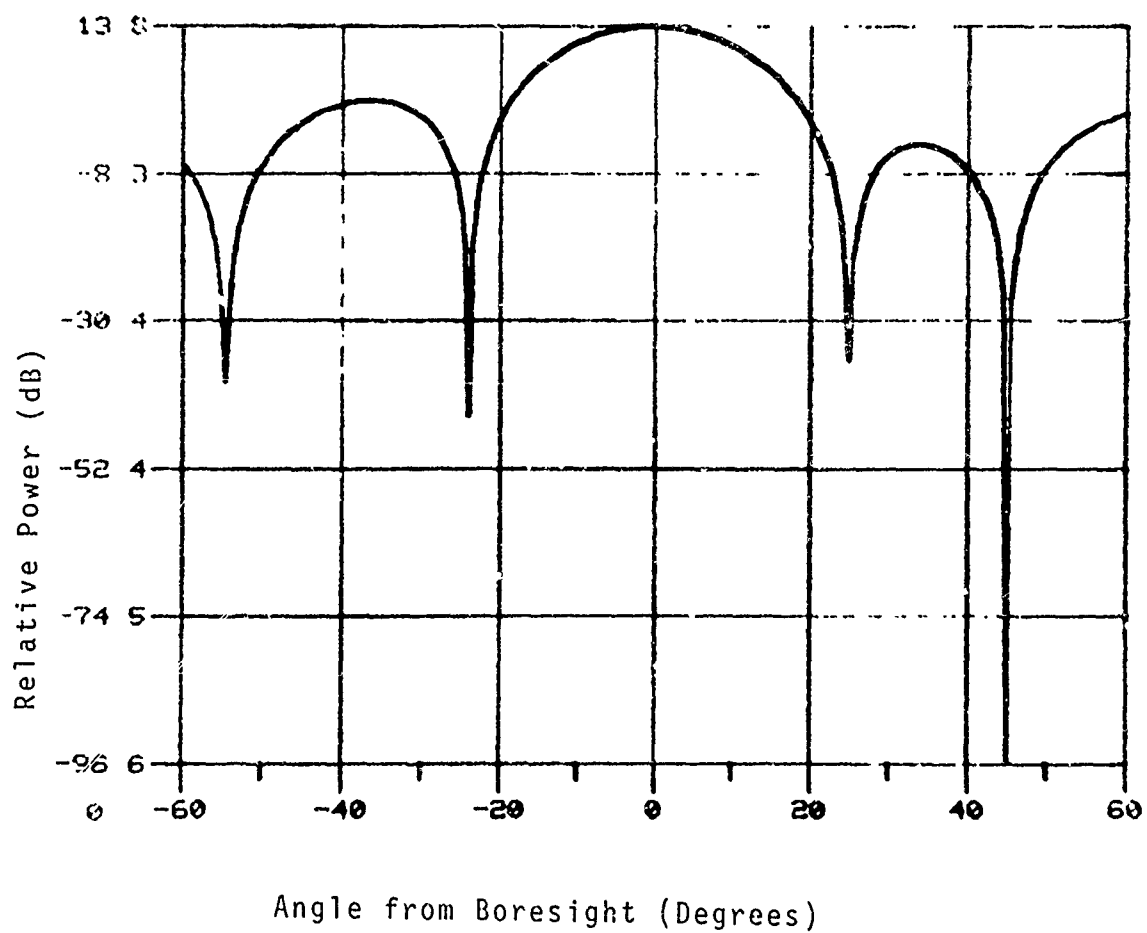
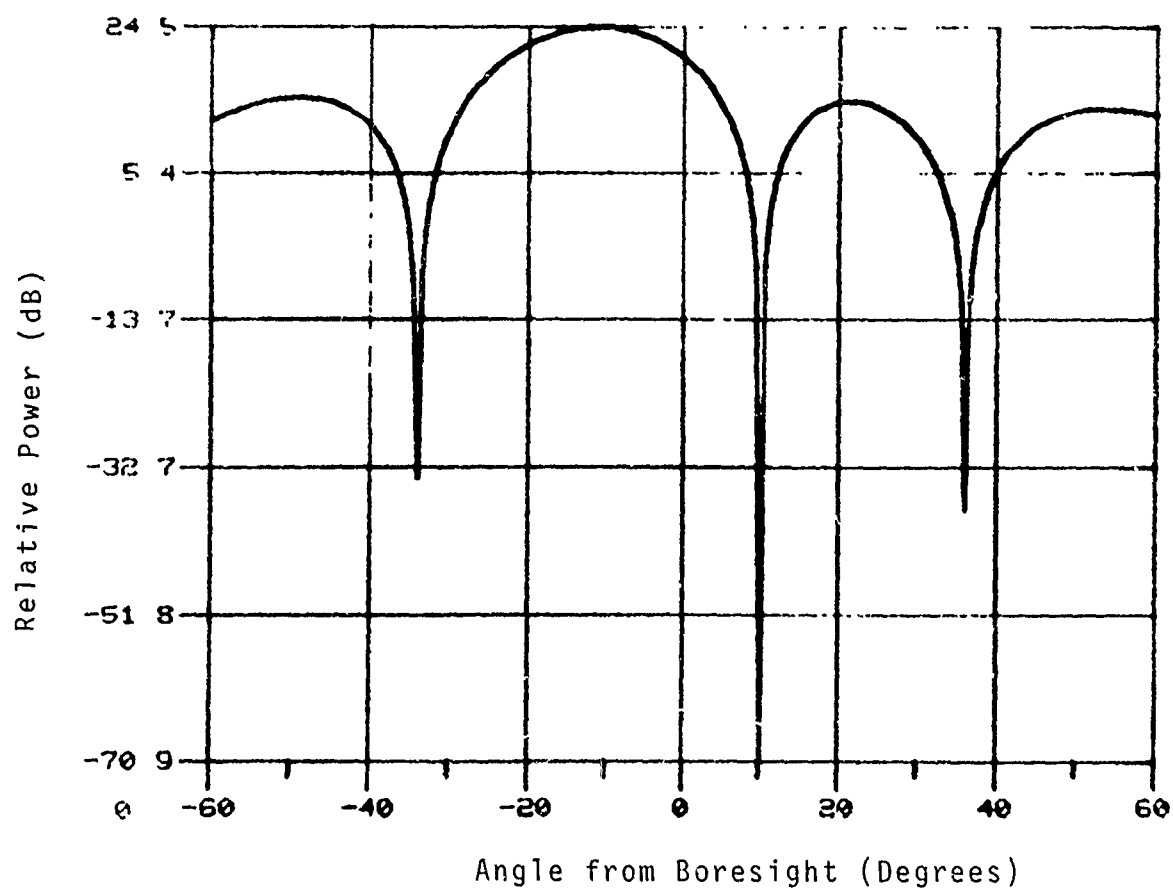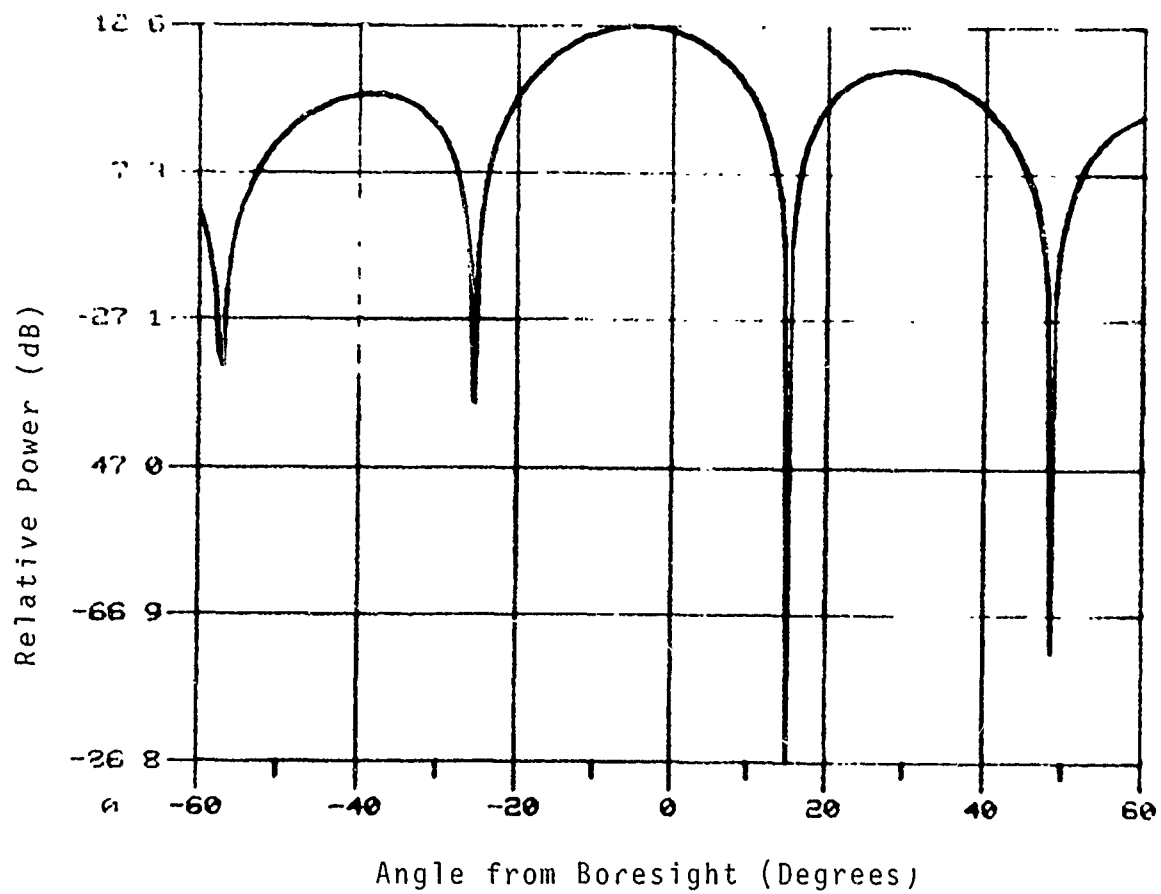Figure B-19 Adaptive Sum Pattern with Jammer at
45° from Boresight

167
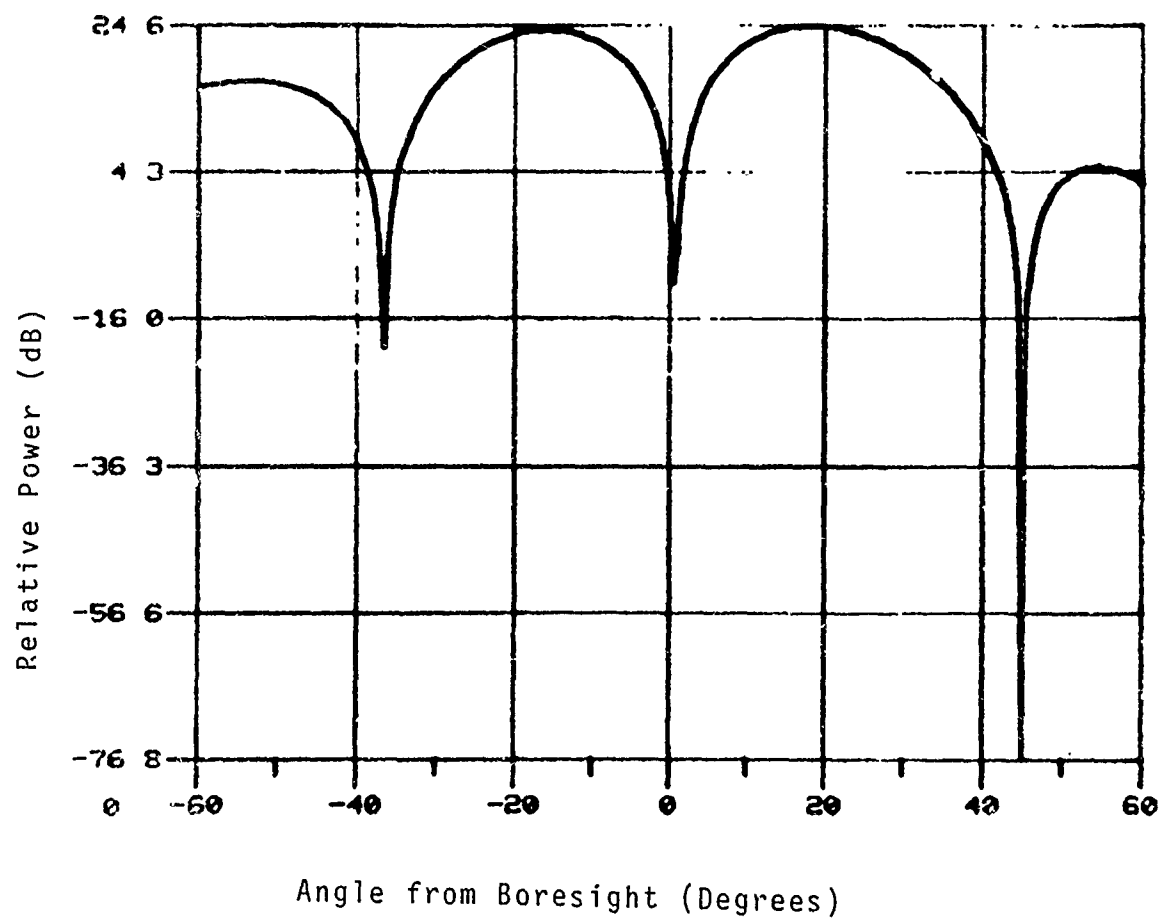
Figure B-20 Adaptive Difference Pattern with Jammer
at 45° from Boresight.

168
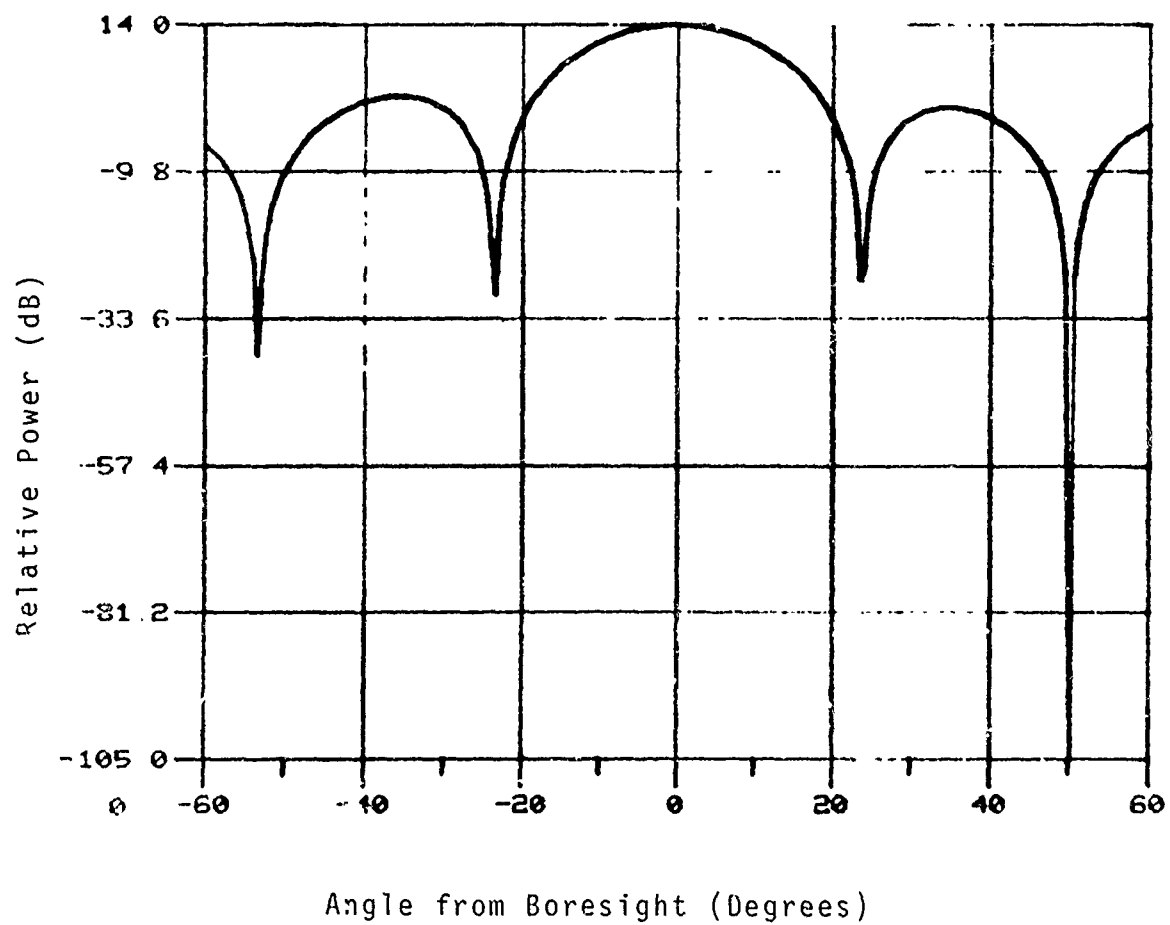
Figure B-21 Adaptive Sum Pattern with Jammer at 50° from Boresight.

169
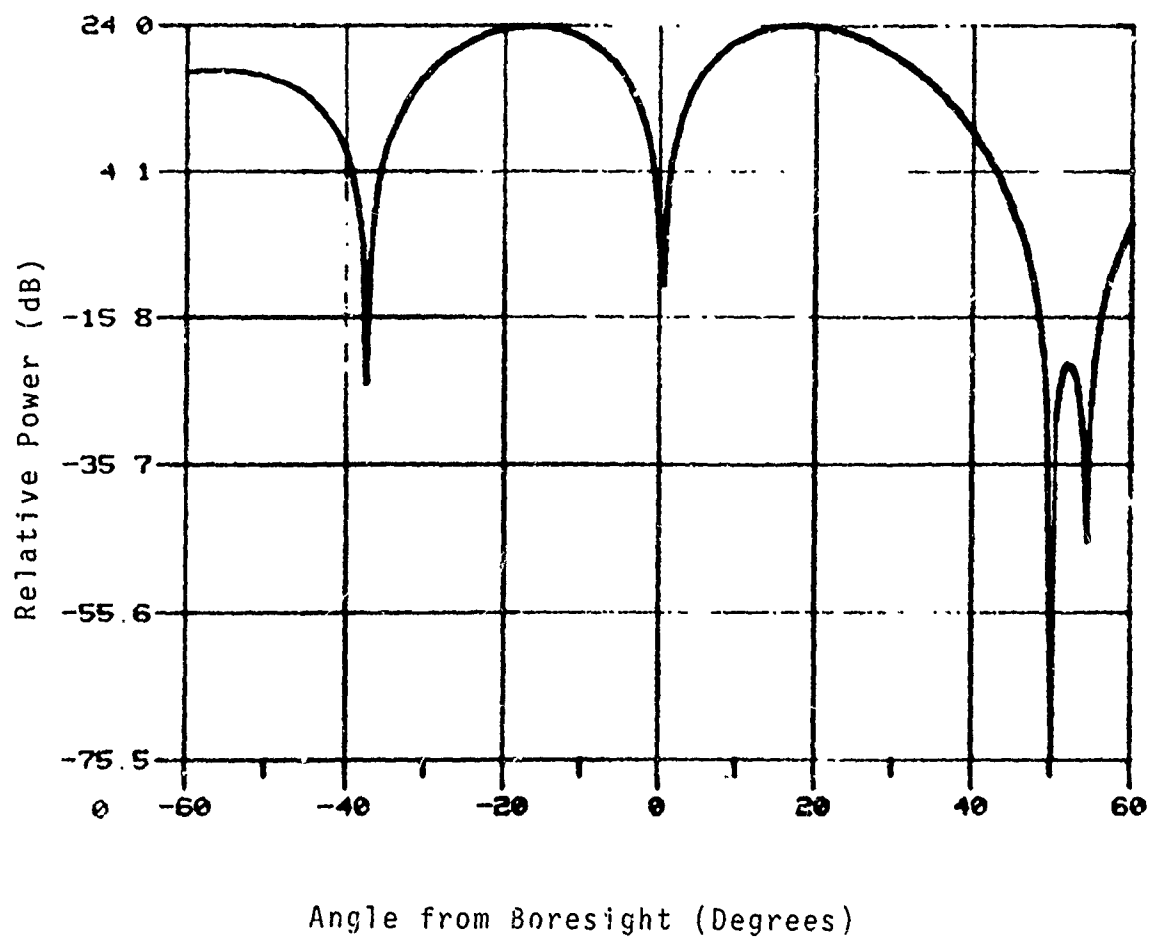
Figure B-22 Adaptive Difference Pattern with Jammer
at 50^0 from Boresight.

170
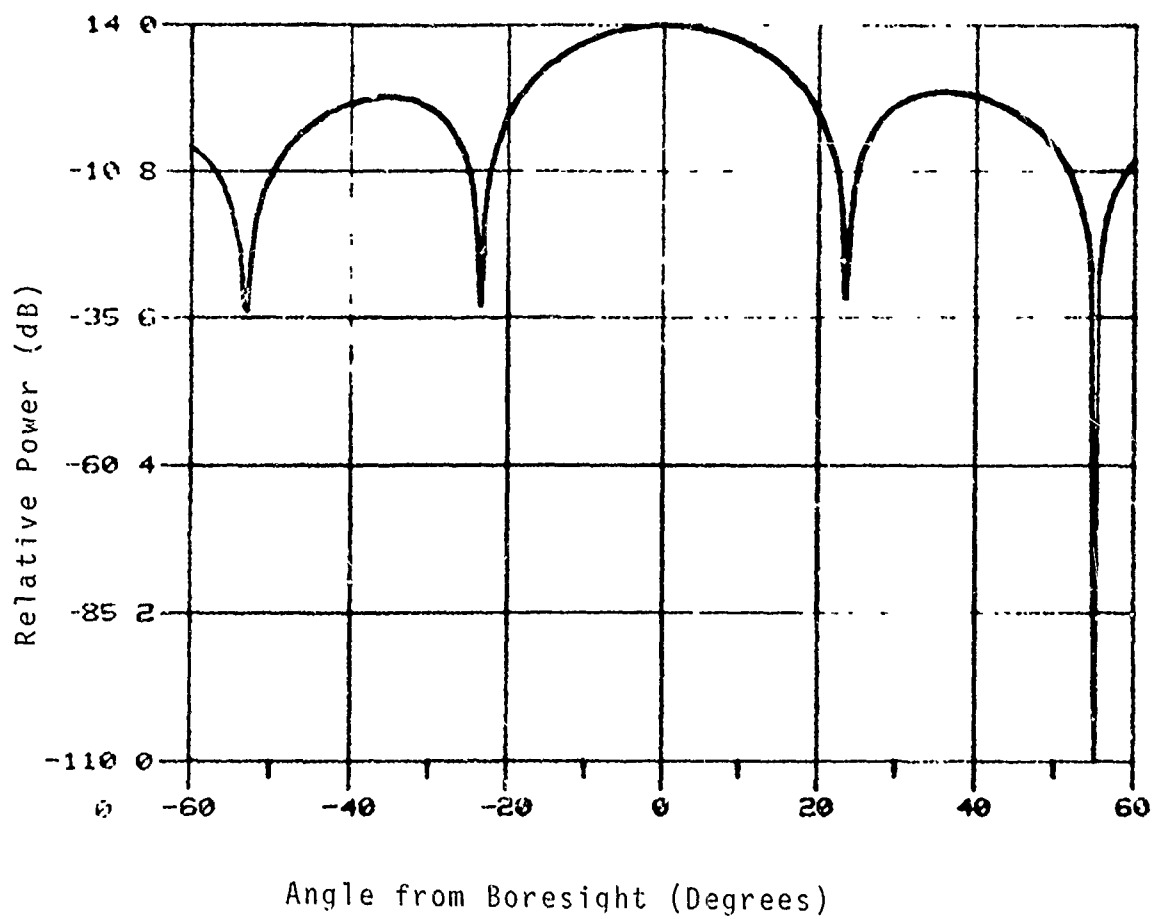
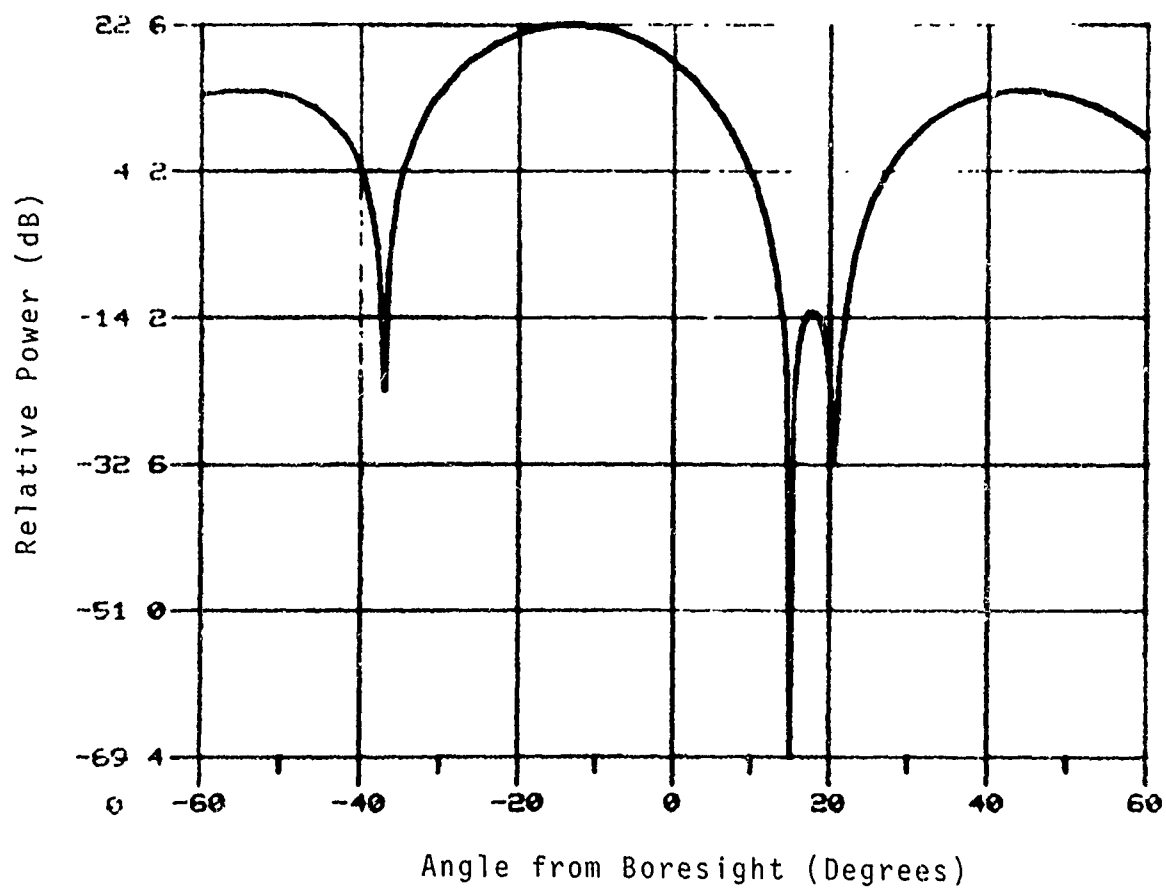Figure B-23 Adaptive Sum Pattern with Jammer at 55⁰
from Boresight.

171
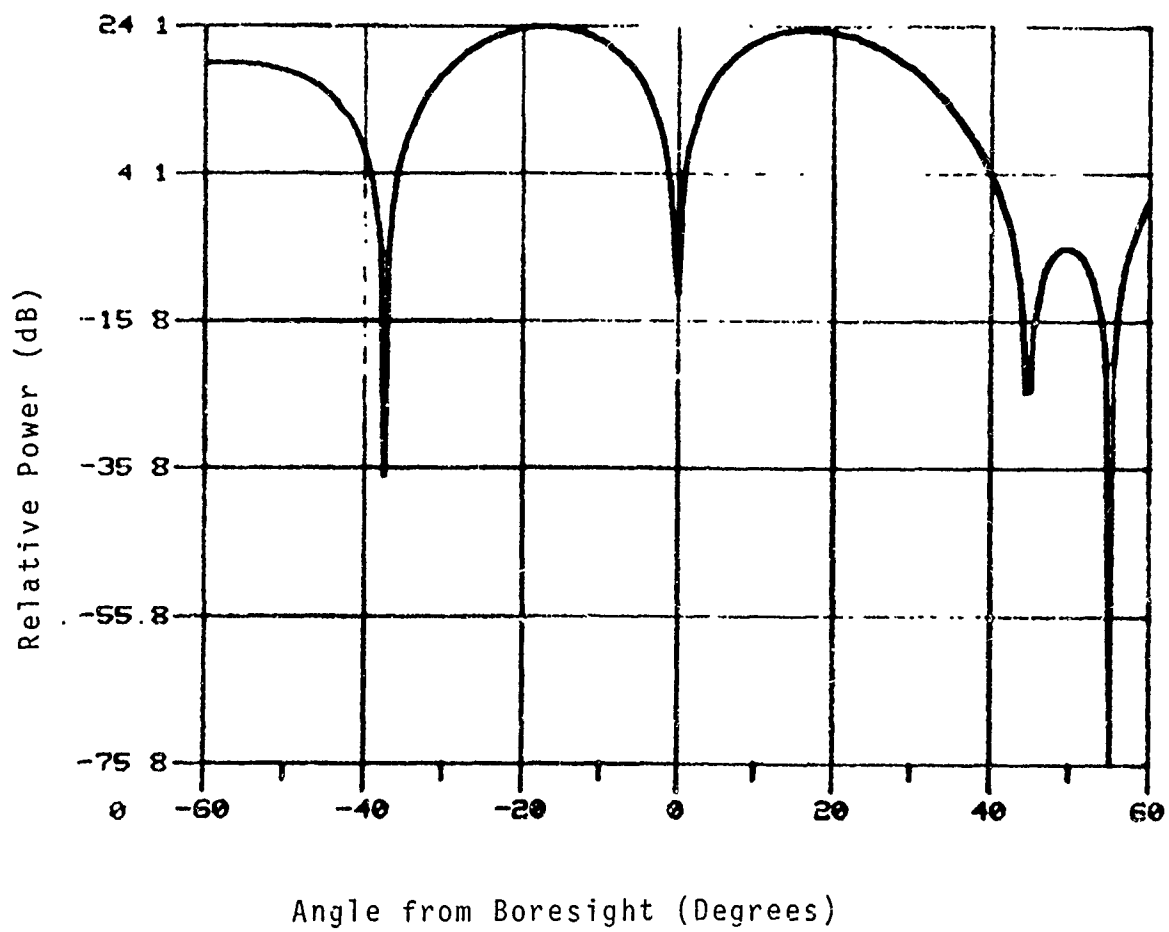
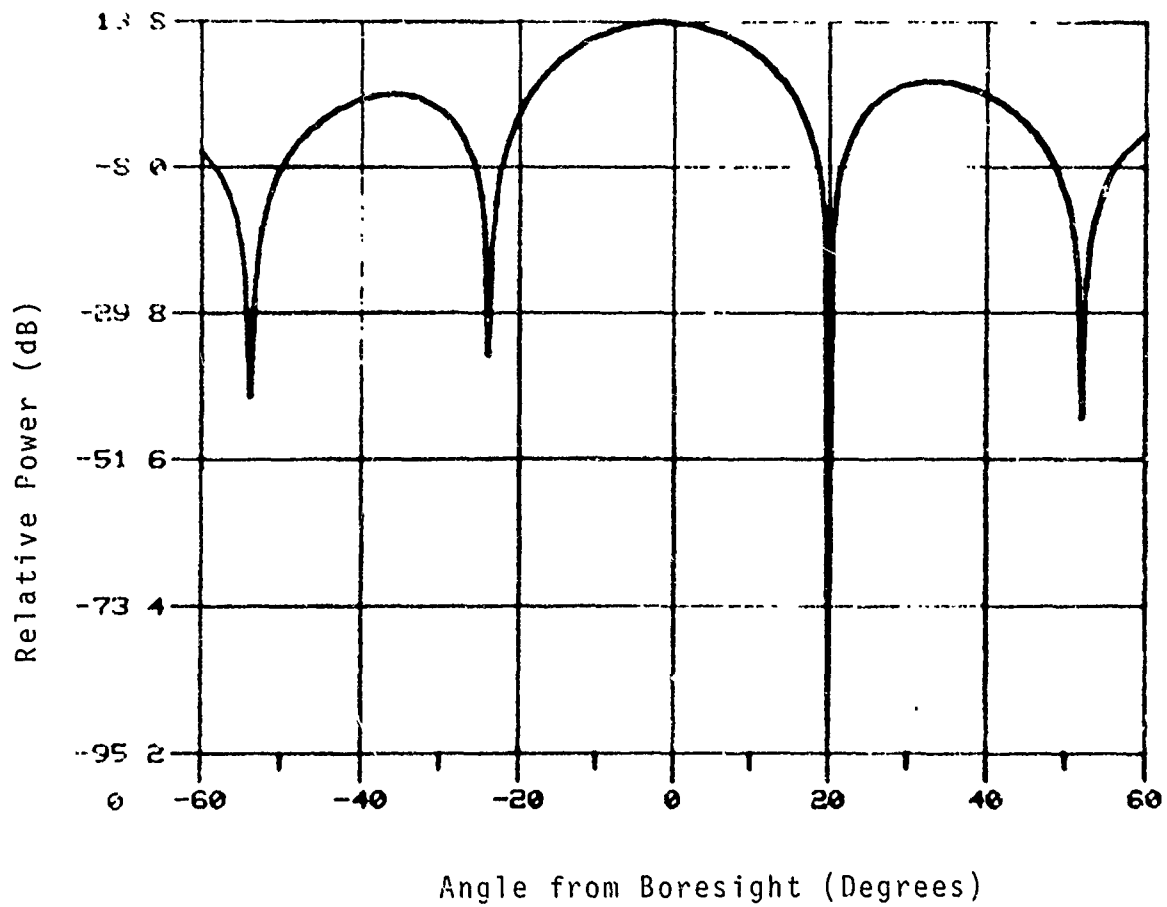Figure B-24 Adaptive Difference Pattern with Jammer
at 55⁰ from Boresight.

172
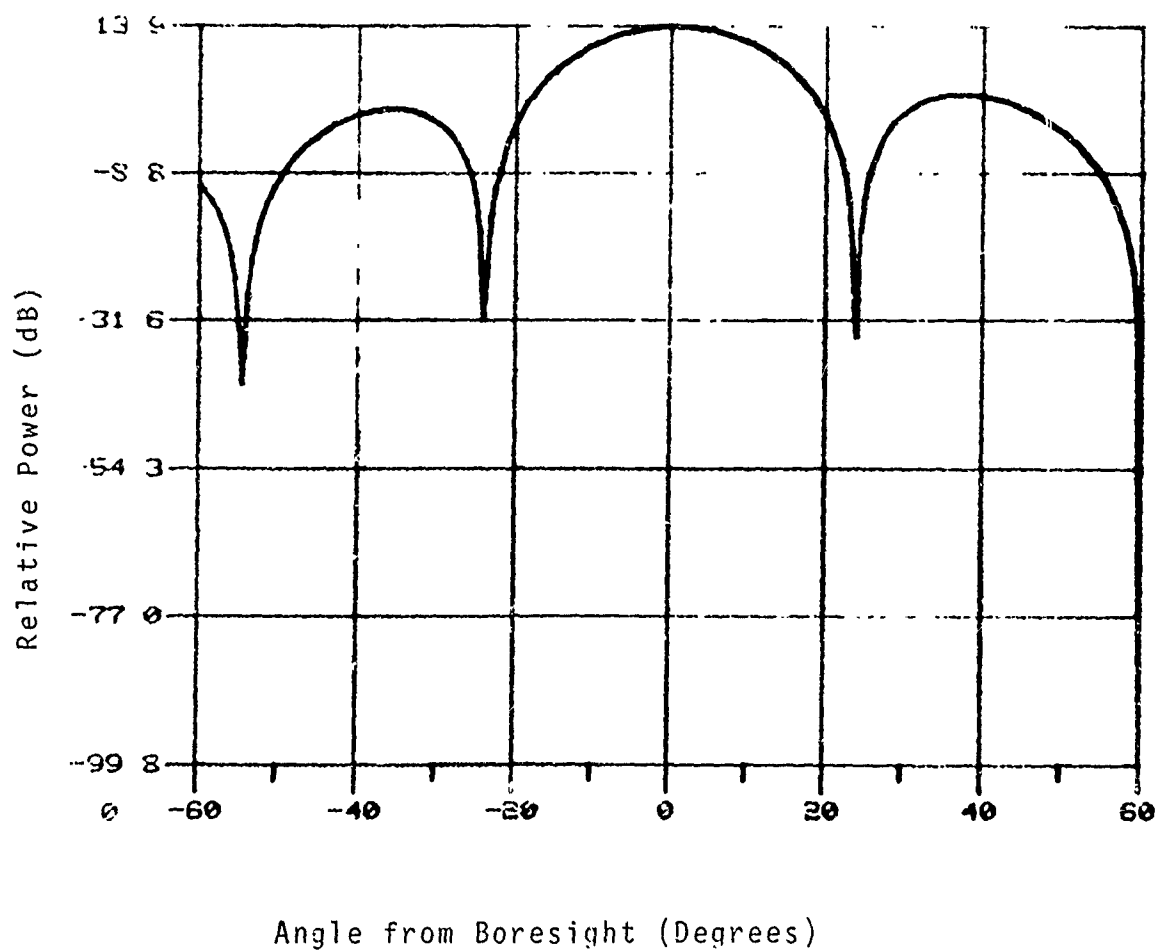
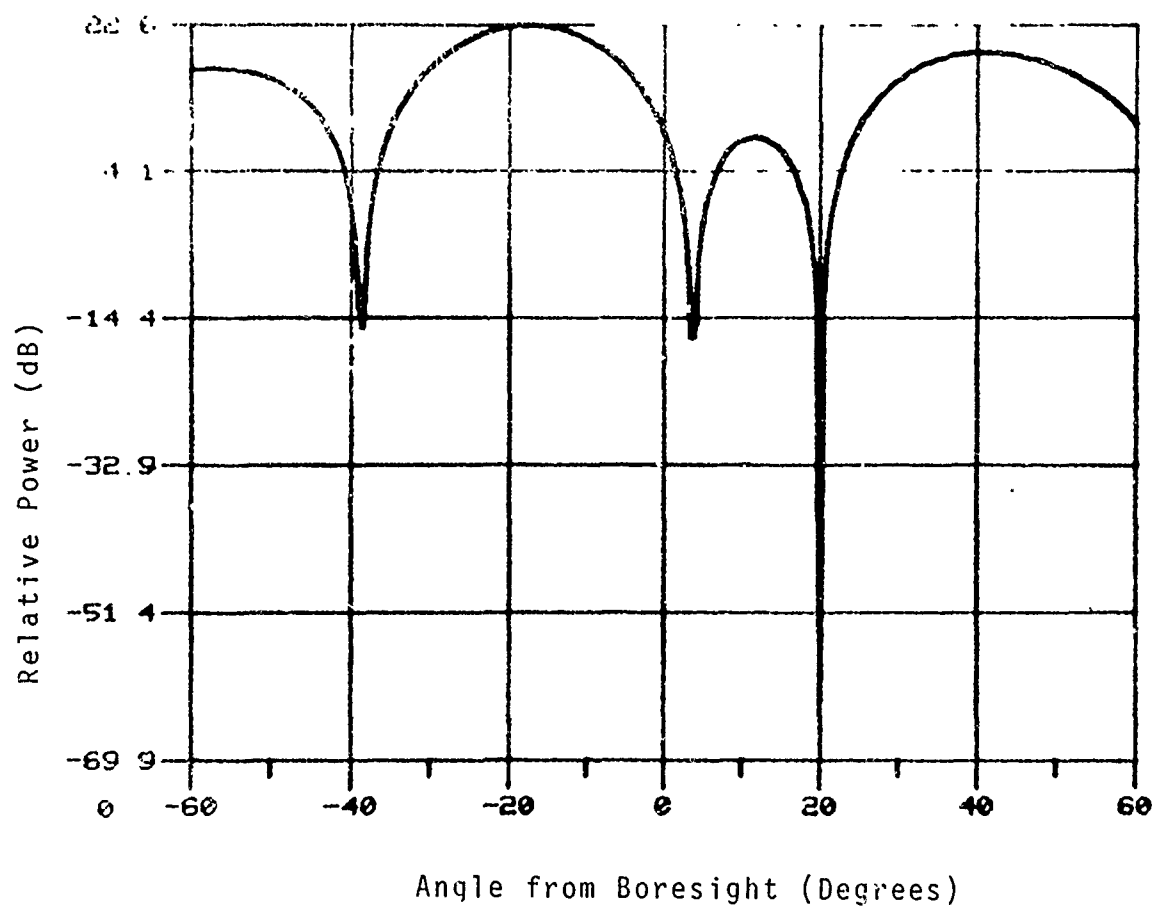Figure B-25. Adaptive Sum Pattern with Jammer
at 60° from Boresight
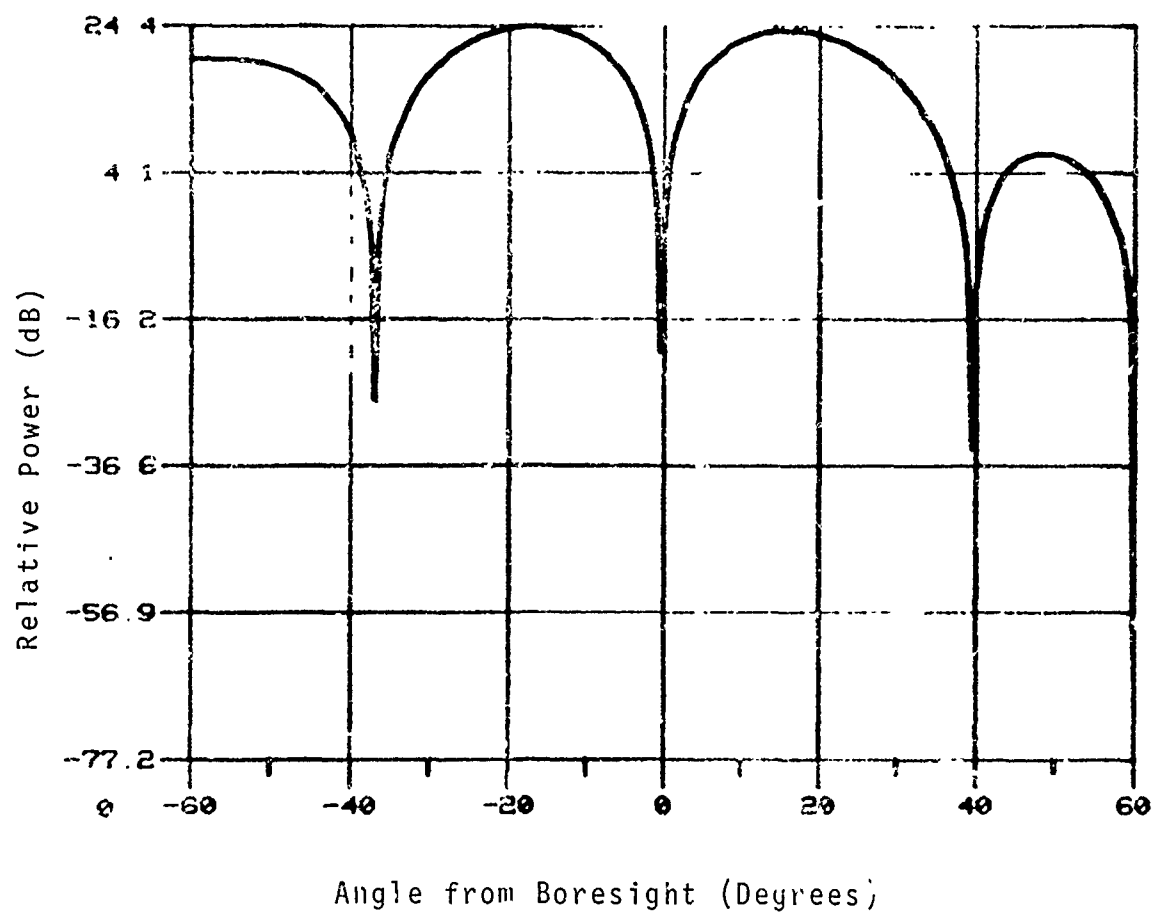
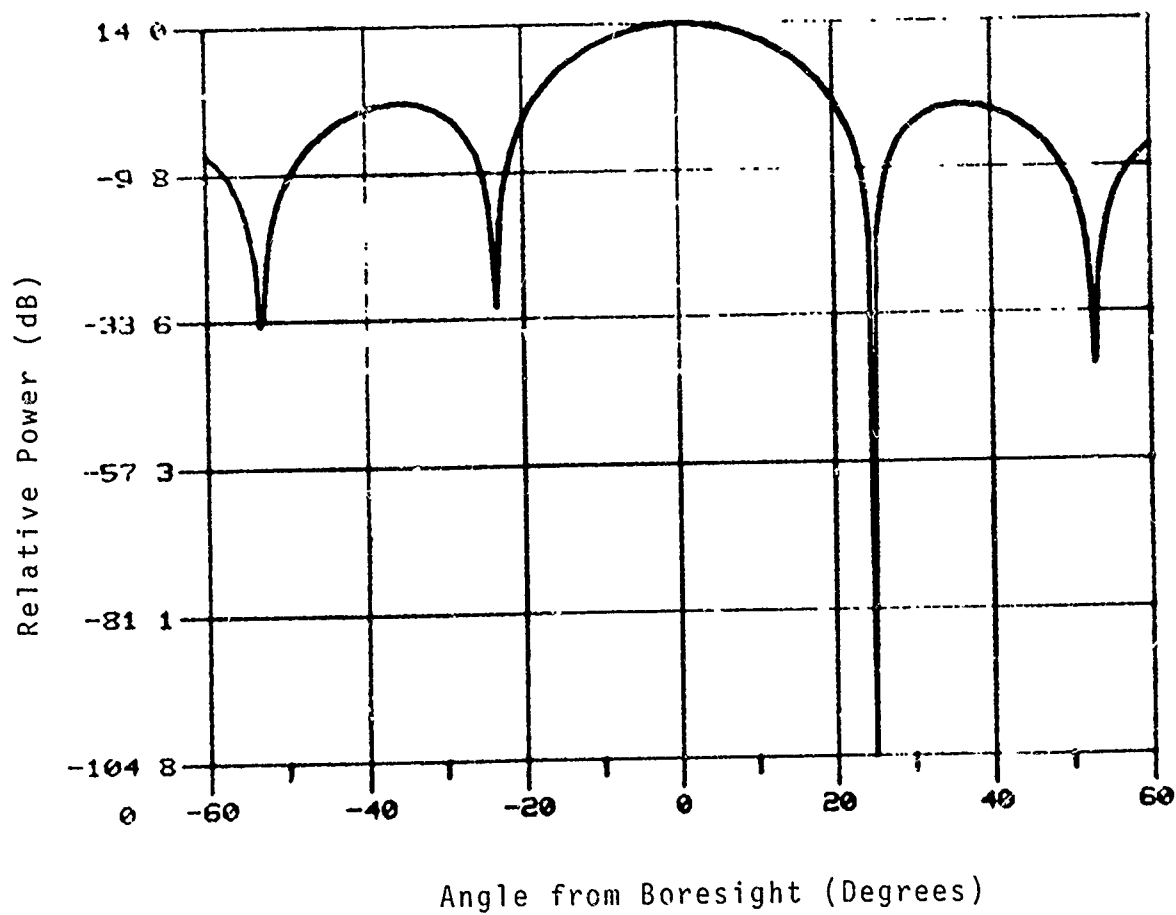Figure B-26. Adaptive Difference Pattern with Jammer
at 60° from Boresight.

174

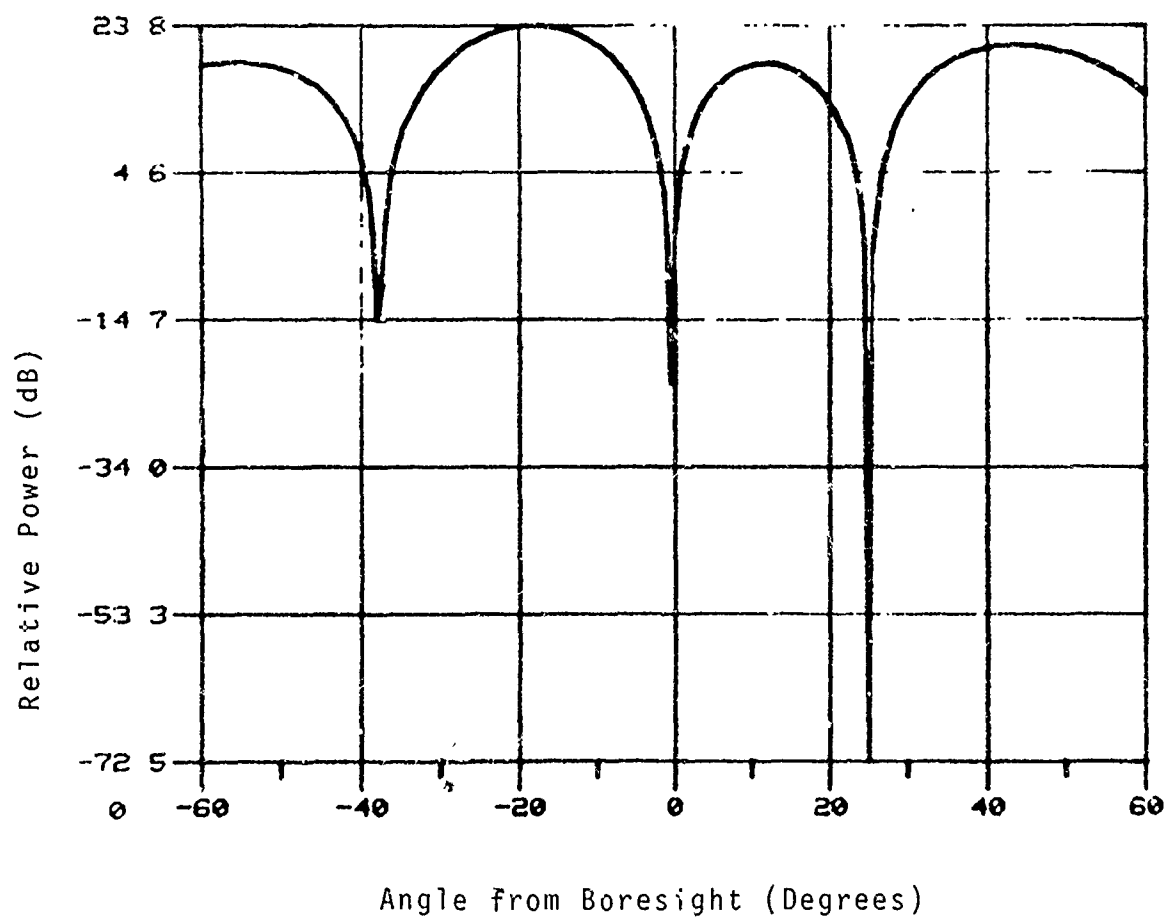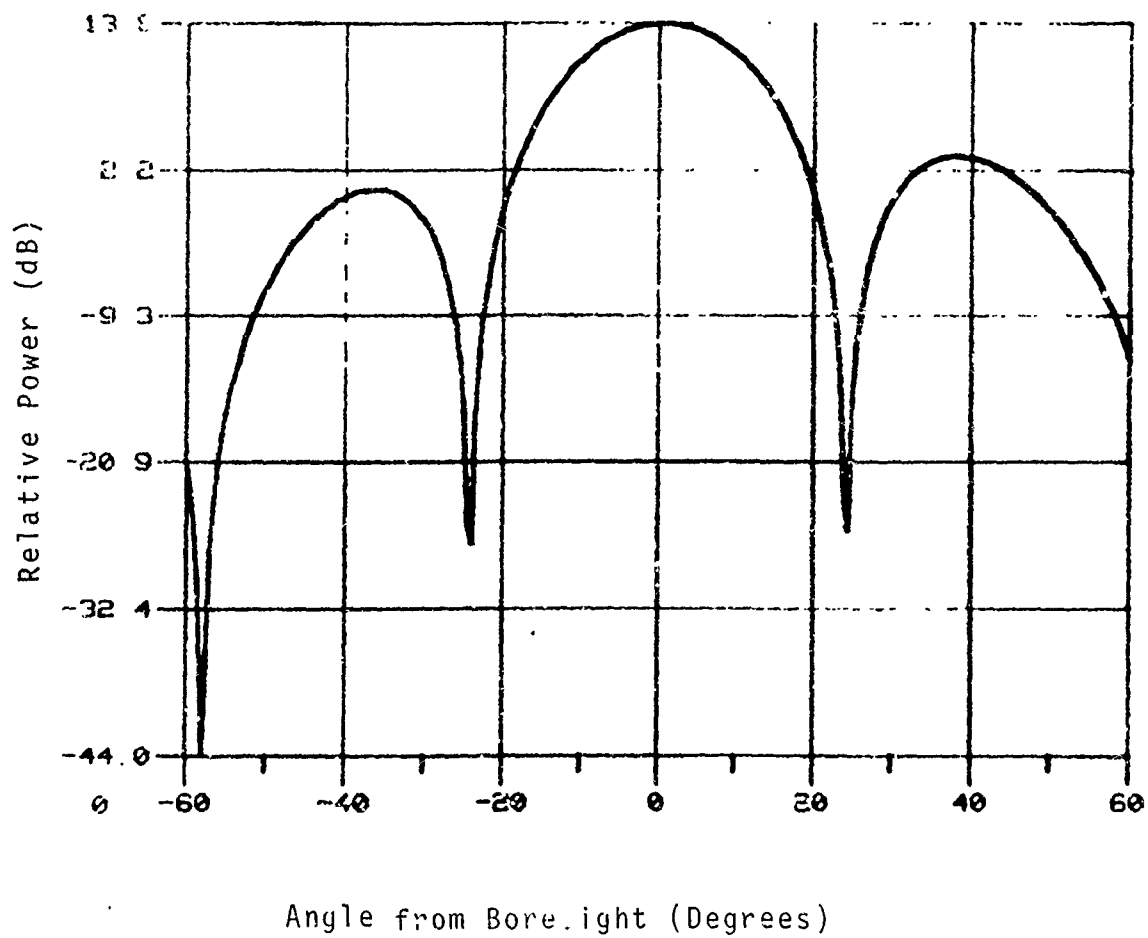Figure B-27. Adaptive Sum Pattern with Jammer
at 65° from Boresight.

175
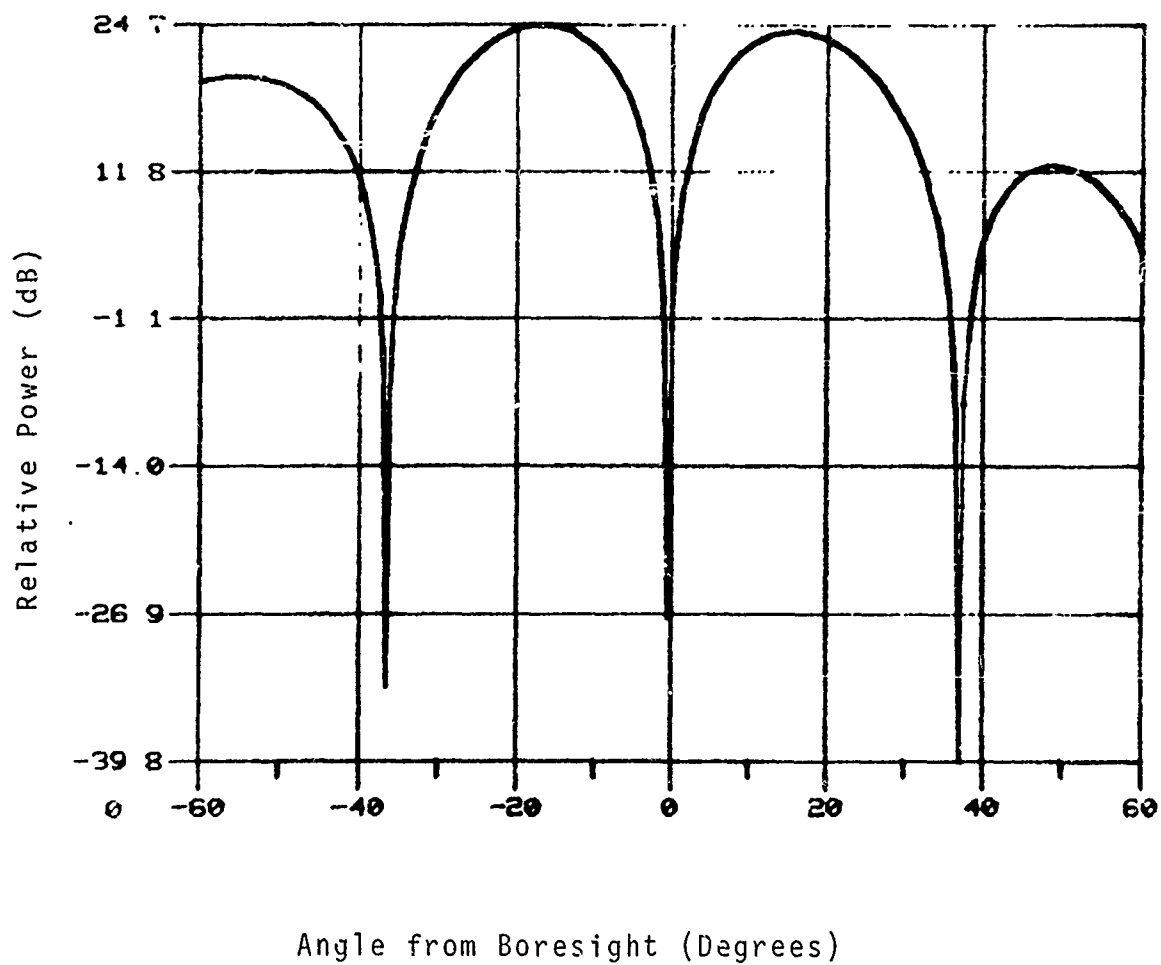
Figure B-28. Adaptive Difference Pattern with Jammer
at 65° from Boresight.

DELTA EPSILON
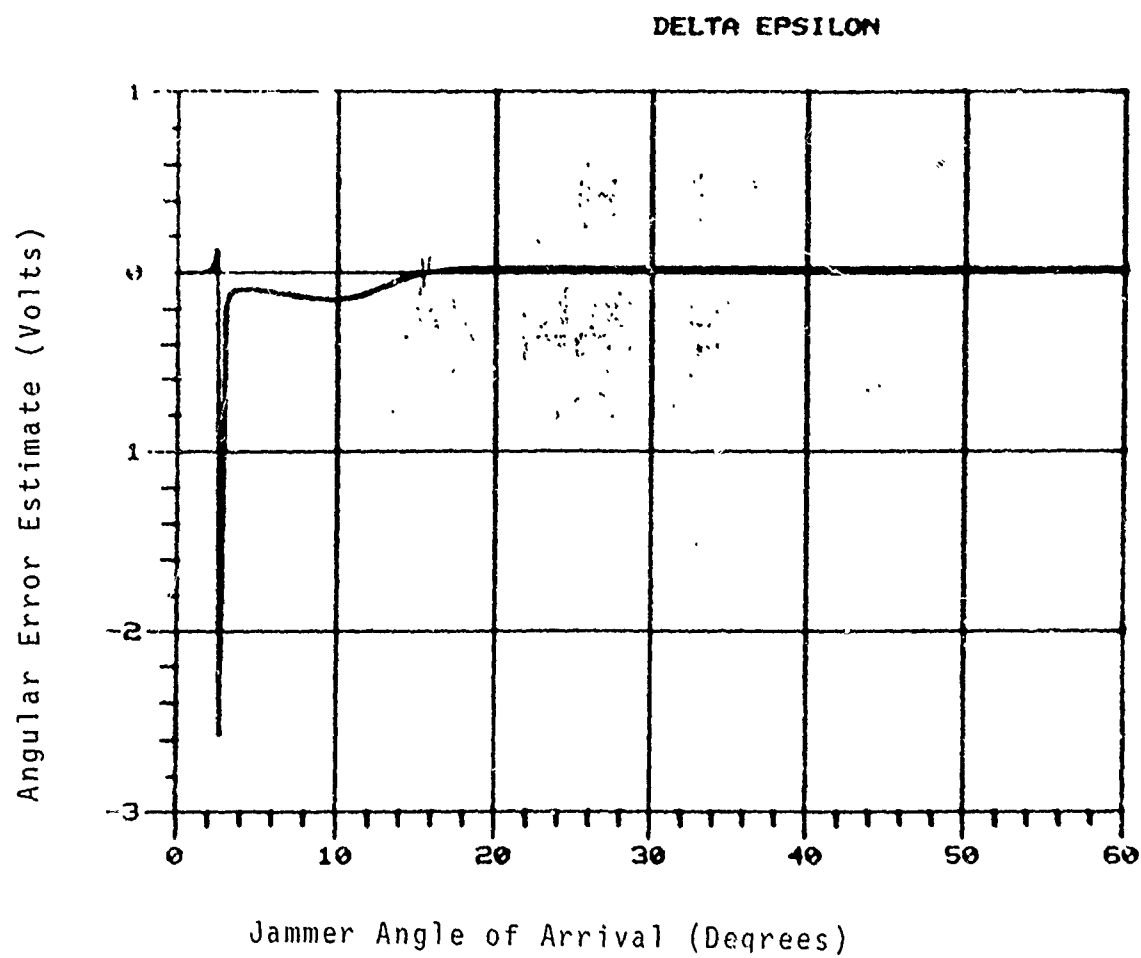
Figure B-29. Angular Error Estimate versus Jammer
Angle of Arrival (Target at 1°).

177

DELTA EPSILON
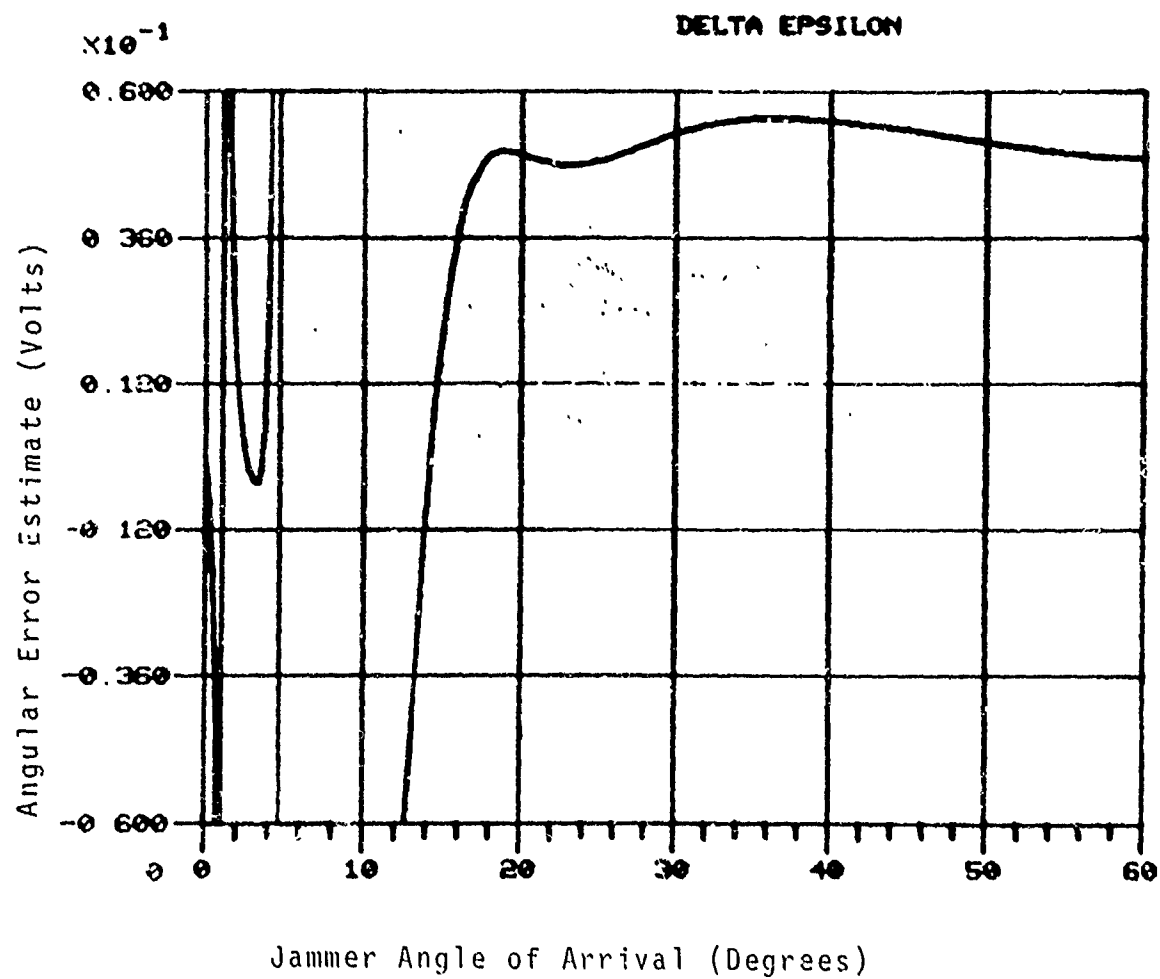
Figure B-30. Angular Error Estimate Versus Jammer
Angle of Arrival (Target at 3^0)

178

DELTA EPSILON
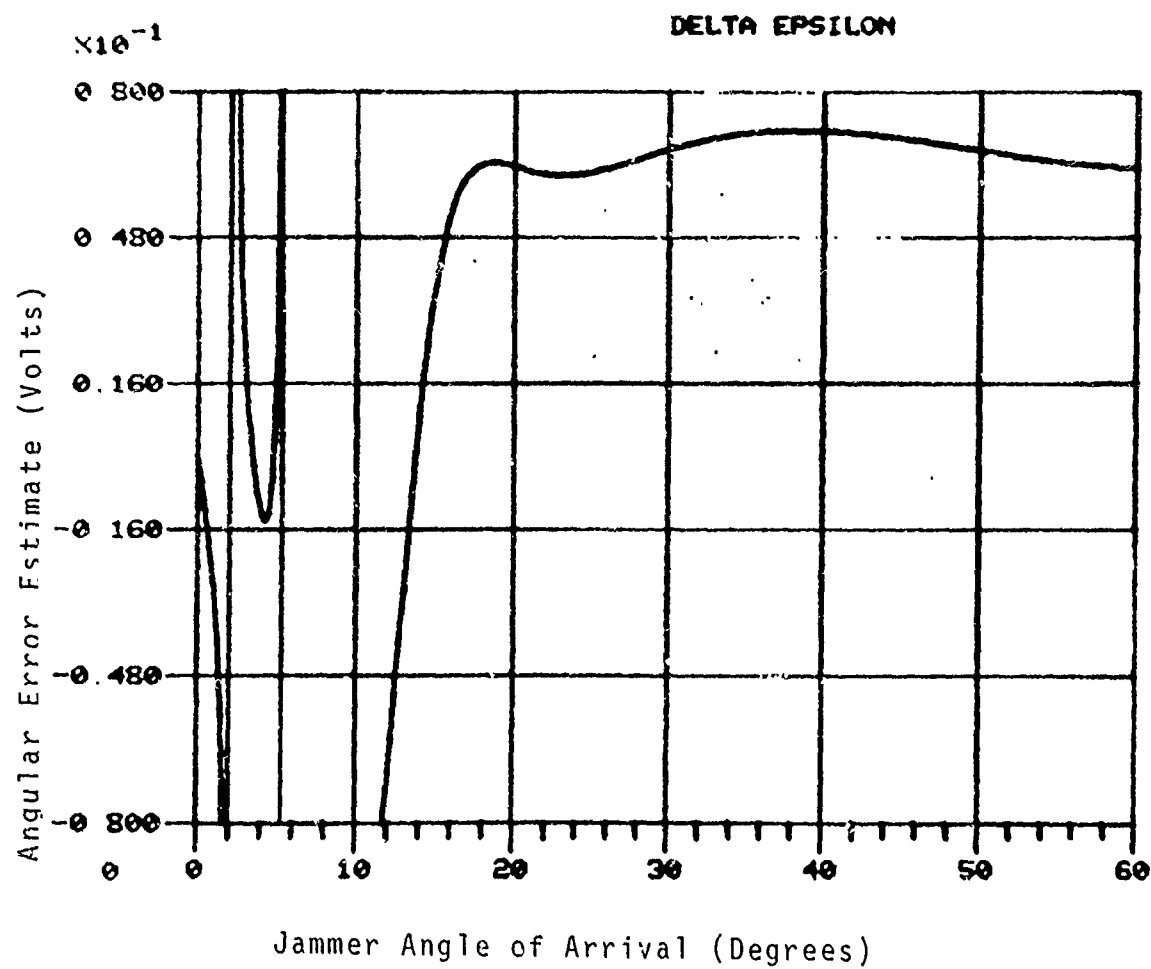
Figure B-31. Angular Error Estimate Versus Jammer
Angle of Arrival (Target at 4^0)

179

DELTA EPSILON
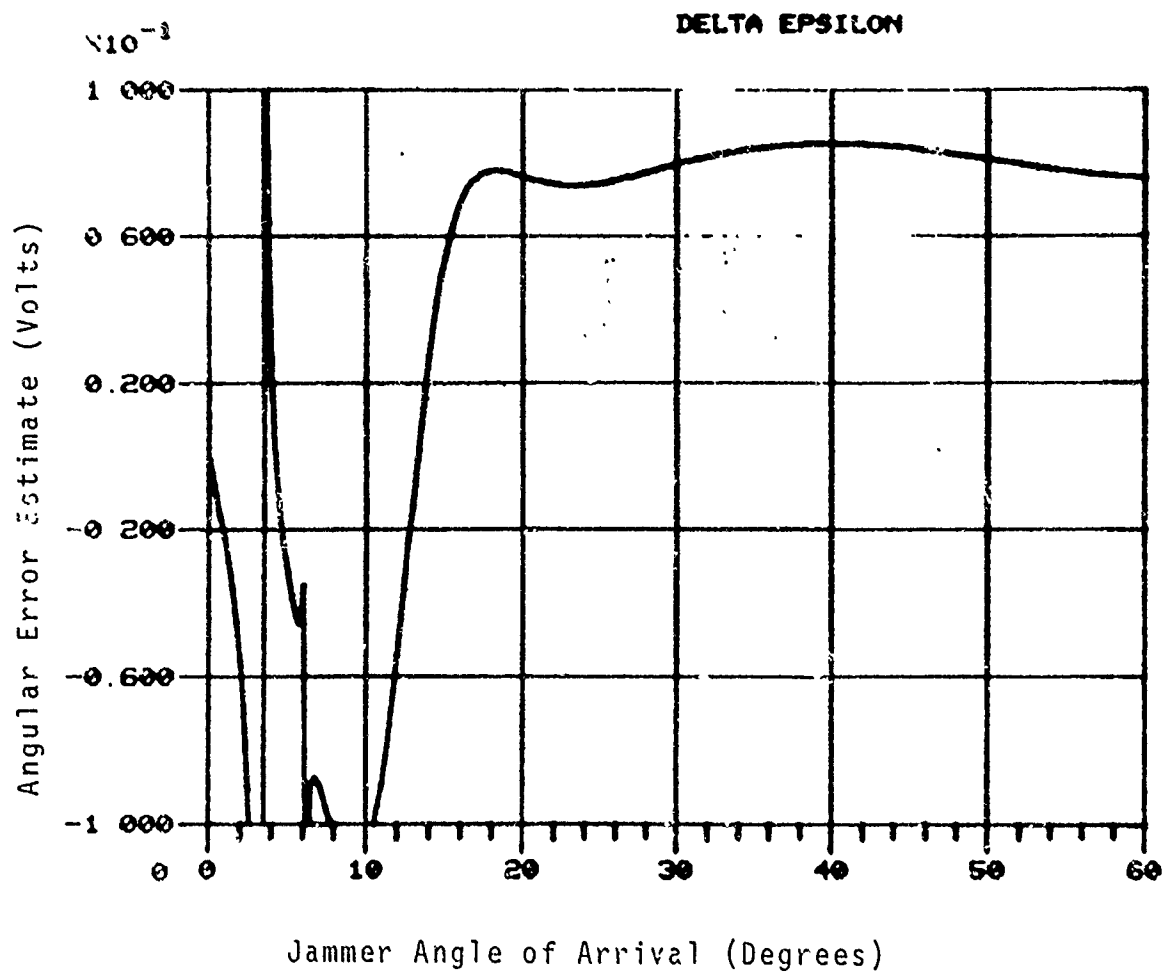
Figure B-32. Angular Error Estimate Versus Jammer
Angle of Arrival (Target at 5°)

DELTA EPSILON
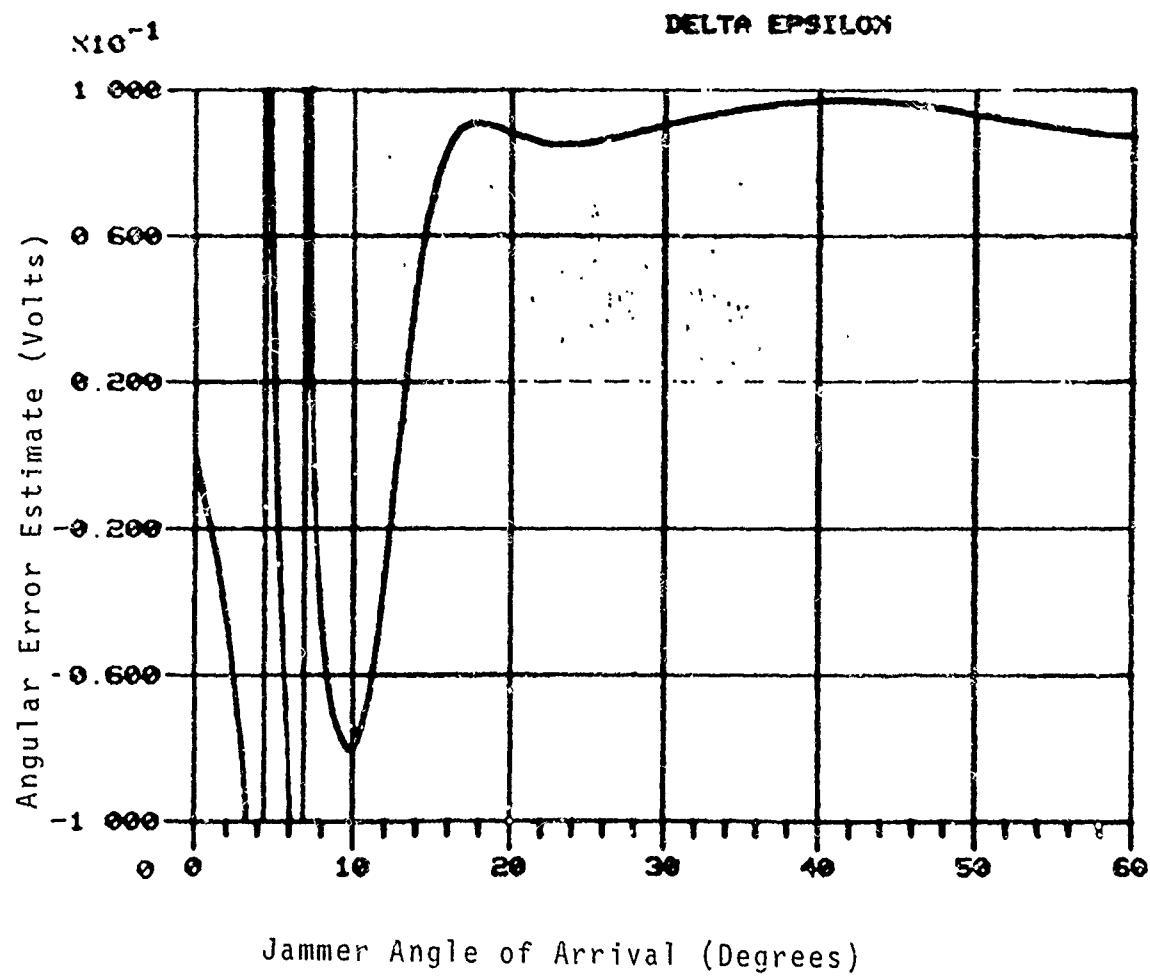
Figure B-33. Angular Error Estimate Versus Jammer Angle
of Arrival (Target at 6^0)

181

DELTA EPSILON
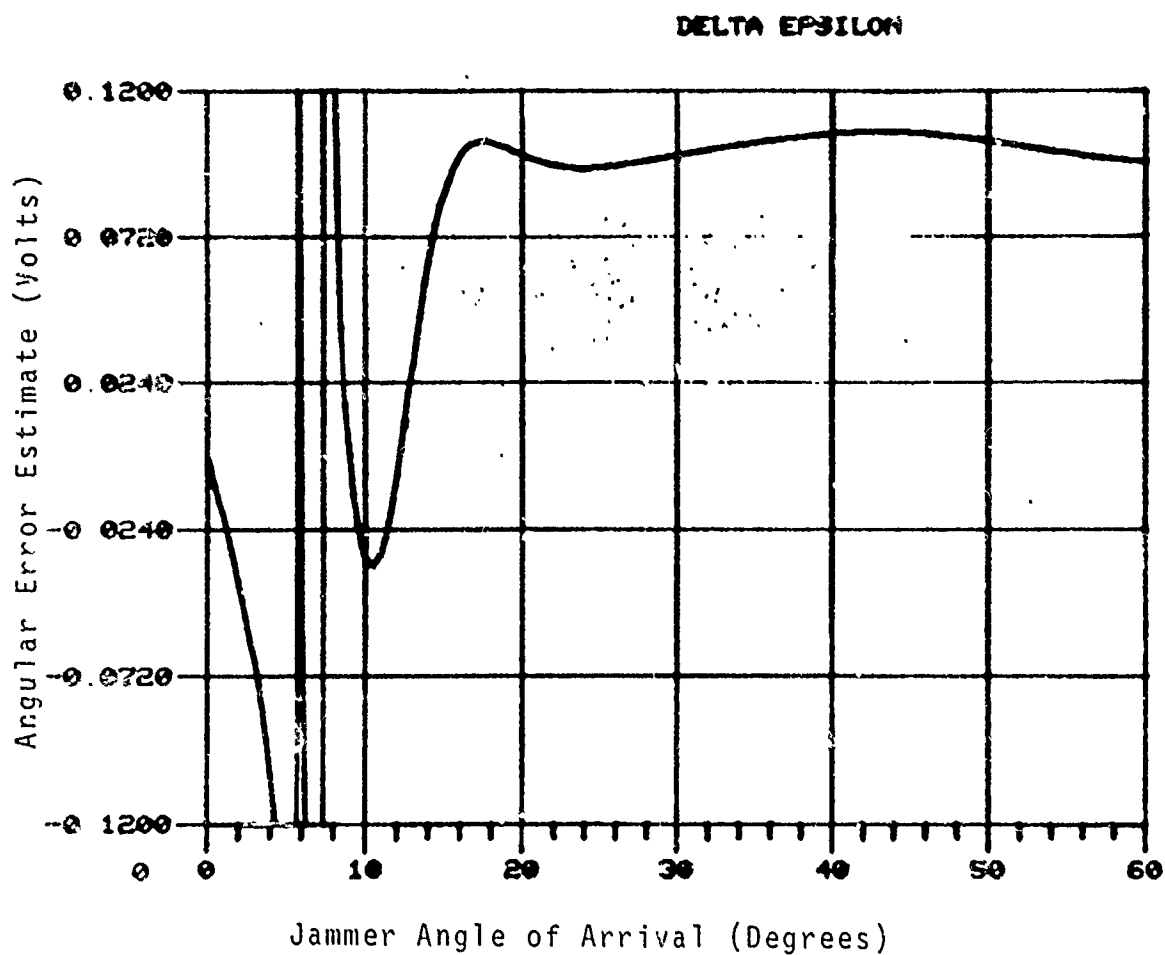
Figure B-34. Angular Error Estimate Versus Jammer
Angle of Arrival (Target at 7°)

DELTA EPSILON
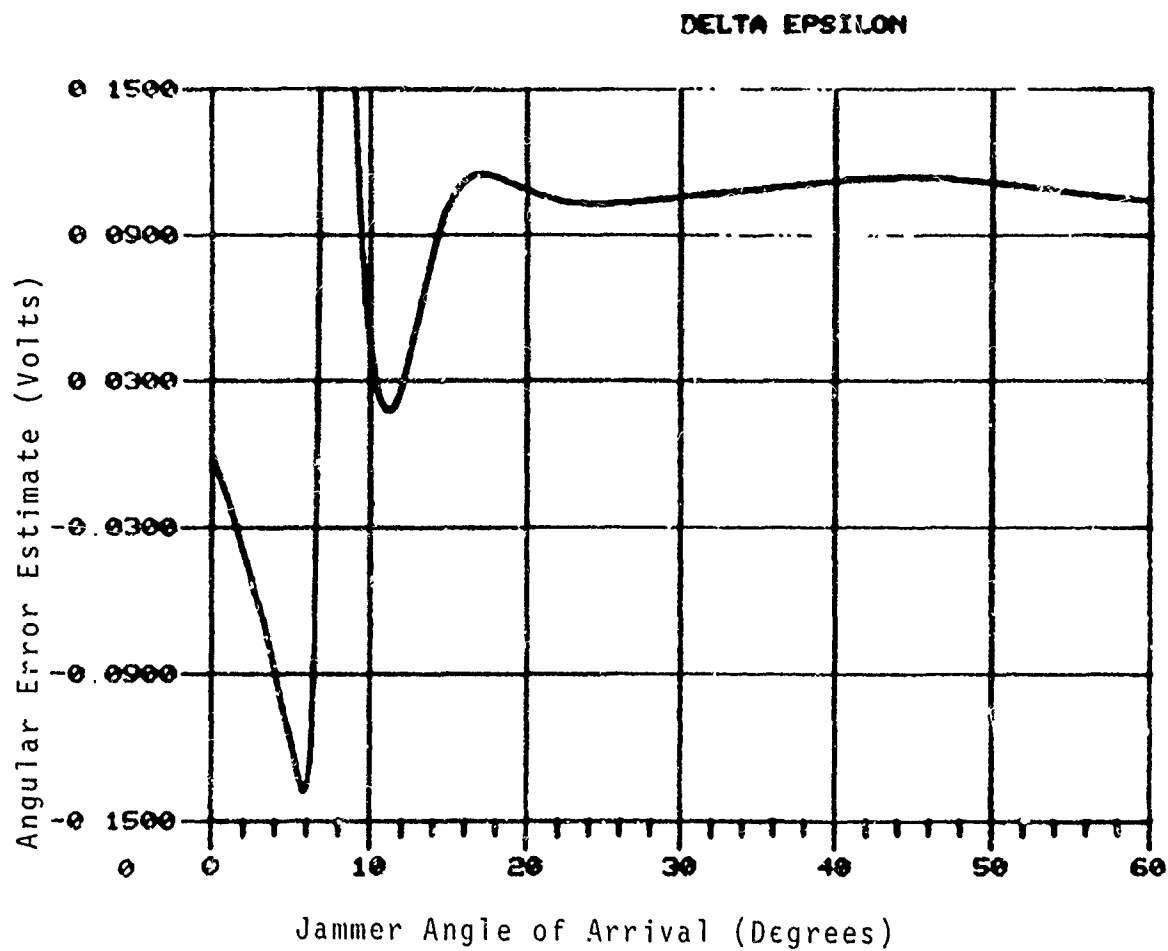
Figure B-35. Angular Error Estimate versus Jammer Angle
of Arrival (Target at 8^0)

183

DELTA EPSILON
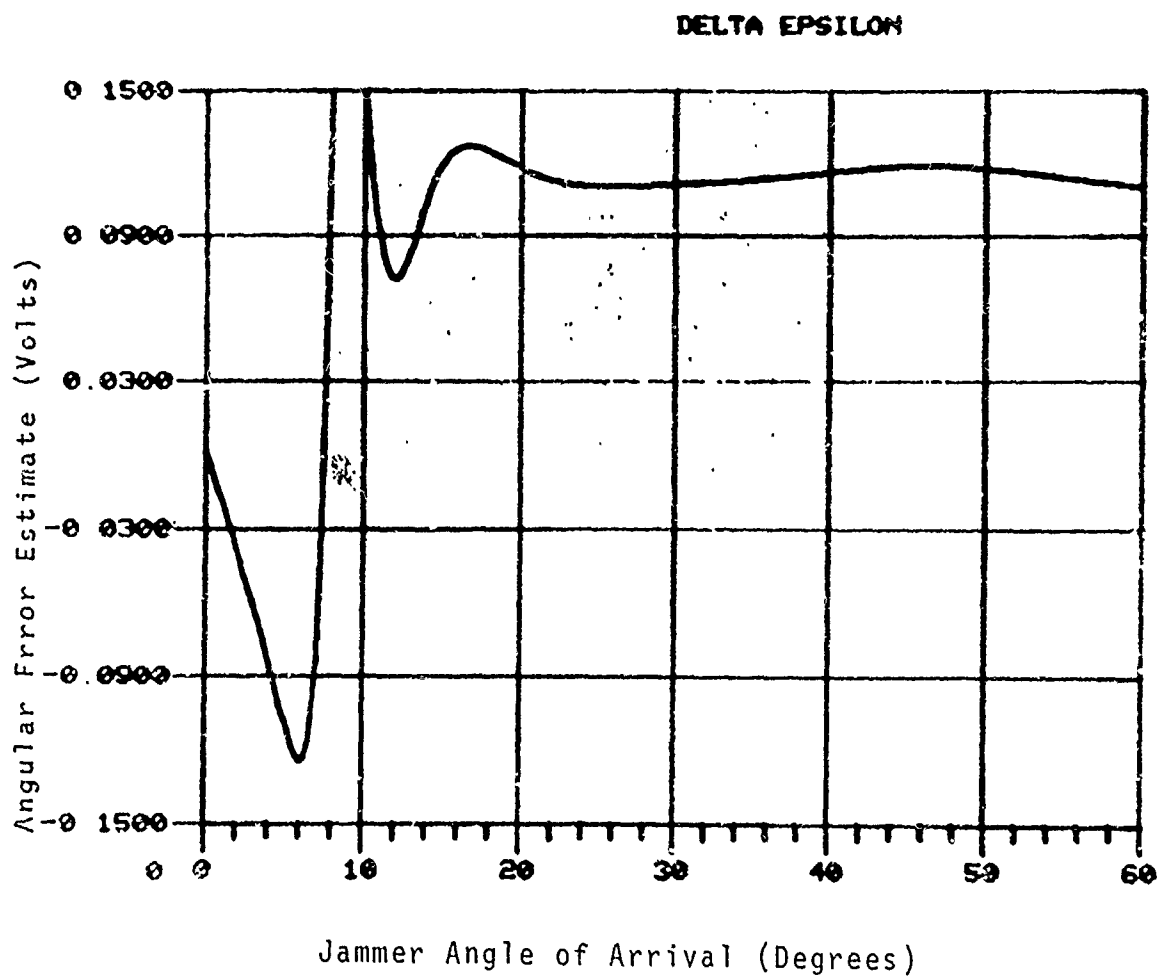
Figure B-36. Angular Error Estimate Versus Jammer
Angle of Arrival (Target at 9°)

184

DELTA EPSILON
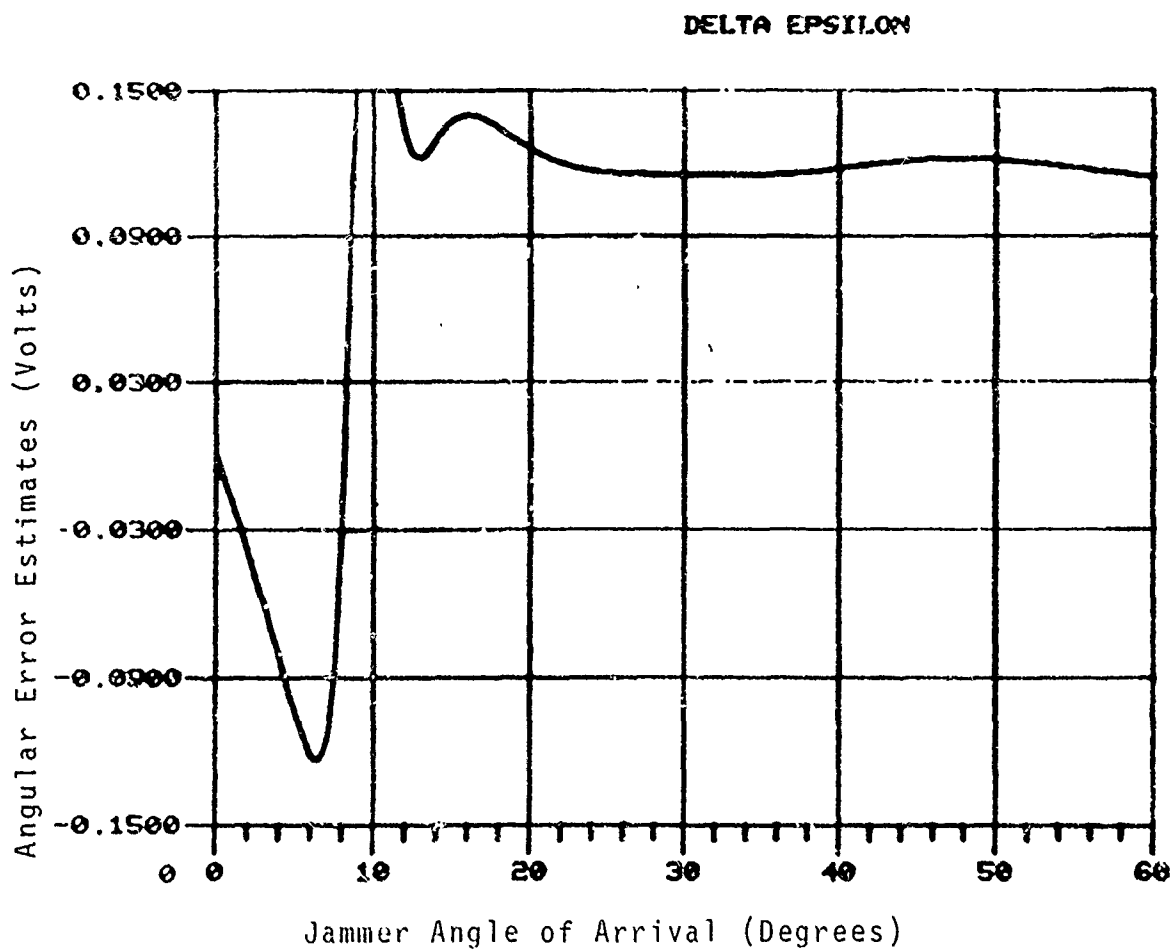
Figure B-37. Angular Error Estimate Versus Jammer
Angle of Arrival. (Target at 10°)

185

APPENDIX C

COMPUTER SIMULATION PROGRAM FOR ADAPTIVE
MONOPULSE CALCULATIONS

C1 General Model Description

This section describes the basic models and assumptions used
by the computer program. Also discussed are the advantages and
limitations of these models and the assumptions they were based
on. Also discussed are the model properties that significantly
impact computer system simulation.

C1.1 Array Geometry

A one dimensional linear antenna array with $\lambda/2$ element
spacing was used due to the computer memory limitations. The use
of a linear 1D array allows storage requirements for the complex
cross-correlation matrix necessary to model wideband signals to
be reduced to a single row. For a 100 element array, storage
requirements can be reduced from 10,000 complex numbers to 100
complex numbers. Thus, this geometry choice allows modeling
larger arrays than would otherwise be possible. This is
especially true for this study where computer time was free but
memory was limited to 32K.

Additional arguments can be made for this choice. There
was a need to control the large number of possible independent
variables to a reasonable number. This model is both general
and allows direct control of the effective aperture width through
the number of elements. Effective aperture dimensions in turn
directly relate to angular resolution and are thus fundamental
array variables. The focus of this study was adaptive array
performance relations and sensitivities to general parameters
rather than analysis of specific array configurations. It should

186

be stressed, however, that given sufficient computer storage for the associated cross-correlation matrices, arbitrary array geometries can be analyzed.

C1.2 Jammer and Target Geometry

The target and all jammers are stationary, far-field, and coplanar with the antenna array. It should be noted the choice of a 1D array geometry precluded any analysis of elevation performance or sensitivity. As all emitters are in the far field, received signal phase is not influenced by range but is only function of direction of arrival at the array. Range does effect received signal strength but it was felt that received in-band signal power was a more fundamental parameter. Thus, target and jammer ranges were indirectly incorporated into an in-band signal strength parameter. It should be noted that the interaction of array element patterns including mutual coupling effects and directions of arrival also influence in-band signal power. This complication was ignored due to its complexity. In essence the array model had idealized isotropic elements with no mutual coupling over the bandwidth. Thus jammer and target locations were reduced to a fixed angle of arrival and an influence on the received in-band power specified by the user.

C1.3 Signal Modulation

The target was assumed to use biphase PSK modulation of a known carrier. The bit period (i.e., data rate) is specified for signal simulation. Bit timing was assumed to be unavailable despite the possible presence of a modem bit sync. These ergodic assumptions yield a stationary ergodic stochastic process which allows a stochastic ensemble average to be used by the simulation. The baseband signal model is the Random Binary Signal*.

*See Papoalis, Probability, Random Variables, and Stochastic Processes, p.294.

It is also implicitly assumed that the index of modulation is low so that this baseband signal model is appropriate. At a high index of modulation significant amounts of aliasing occurs that is not accounted for in the baseband model.

This model does not allow simulation of signal processing gain. The control algorithms were restricted to the class of power suppression algorithms with constraints. Further, ensemble averages are equivalent to an infinite sampling period, i.e., infinite filtering, i.e., no jitter. Thus the basic model is not directly applicable to transient analysis or dynamic tracking capability assessment where the jitter due to finite sampling periods is an important factor. To remove this restriction jitter was artificially introduced as a zero mean Gaussian process with a user supplied sigma when needed.

C1.4 Jammer and Noise Models

All jammers modeled were constant amplitude noise jammers using biphase modulation with the same period as the target and at the same carrier frequency, i.e., with a signal spectrum identical to the target. Further all emitters were assumed to be uncorrelated, i.e., the jammers are all incoherent with each other and the target. This assumption allows the total signal cross-correlation matrix of the array to be computed as the sum of independent signal cross-correlation matrices plus a cross-correlation matrix due to thermal noise. Thermal noise is modeled as white noise. This total cross correlation matrix was used to model array performance. The individual emitters cross-correlation matrices were used to analyse individual emitter contributions.

C1.5 Array Filter Model

Each array element was assumed to have an ideal bandpass filter. As the signal spectrum is modeled at baseband these filters are modeled as ideal low pass filters. No other filtering was assumed to be present. The basic signal auto-correlation equations are presented below:

$$S \quad \boxed{LPF} \quad S'$$
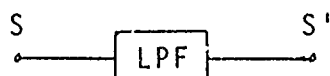
$$R_S(\zeta) = A_S \left(1 - \frac{|\zeta|}{T}\right), \quad |\zeta| \leq T \tag{1}$$

where A_S is the signal power and

T is the bit period

$$R_{S'}(\zeta) = \frac{A_S}{\pi} \left\{ \left(1 + \frac{\zeta}{T}\right) Si\left[\pi B(\zeta + T)\right] - \tag{2}\right.$$

$$\left(1 - \frac{\zeta}{T}\right) Si\left[\pi B(\zeta - T)\right] -$$

$$\frac{2}{\pi BT} Cos(\pi B\zeta) +$$

$$\left. \frac{1}{\pi BT} \left[Cos \, \pi B(\zeta - T) + Cos \, \pi B(\zeta + T)\right] \right\}$$

where B is the filter bandwidth and

Si is the sine integral

189

C1.6 Circuit Dispersion Model

No circuit dispersion was modeled. While circuit dispersion does dominate time of flight dispersion, it is complicated and varies with actual hardware.

C1.7 Stochastic Power Model

The total signal can be viewed as the sum of the signal present at each antenna array element times a complex weight that is a function of hardware. The amplitude of this complex weight represents amplitude weighting function. In our simulations this is a fixed number representing an amplitude taper and fixed hardware errors plus a small variable term dependent on phase state. The phase of the complex weights represents hardware implementation of phase commands from the tracking algorithm. Therefore:

$$P = \left\langle S_T^* \cdot S_T \right\rangle = \left\langle \sum_i W_i^* S_i^* \cdot \sum_j W_j S_j \right\rangle \tag{3}$$

$$P = \vec{W}^* \left\langle S_i^* S_j \right\rangle \vec{W}^T \tag{4}$$

where

$$\left\langle S_i^* \cdot S_j \right\rangle = \sum_{k_i} \left\langle S_{ik}^* S_{jk} \right\rangle = \sum_{k} R_{S'}(\zeta_{ijk}) \quad i \neq j \tag{5a}$$

$$= 1 + \sum_k R_{S'}(\zeta_{ijk}) \quad i = j \tag{5b}$$

where i and j are indices on the array elements and k is an indice on emitters.

Note that Equation (4) shows the average stochastic power is a function of a complex weight vector representing the array hardware including tracking phase commands and a cross-correlation matrix representing the emitters, the array element geometry, and array filtering. Equation (5a) shows that the cross-signal correlation between array elements can be decomposed into a contribution from each emitter. These contributions in turn are found by plugging the time delay between the two elements, ς_{ij} into the auto-correlation function modified by the array filtering, R'.

C2   Sum/Difference Networks

Four sum/difference power combiner networks were used to test various phase weights hardware implementation structures. The first consisted of separate networks for the sum and difference beam, each having a fixed amplitude taper. This allowed independent investigation of the adaptive process for the sum and difference beams. The second network was a phase comparison system with a uniform aperture illumination. The third network was an amplitude comparison network, again with an uniform aperture illumination. The fourth network was an improved amplitude comparison system having a fixed amplitude taper that allows better side lobe control of both the effective sum and difference beams.

C2.1 Independent Networks

A functional diagram of the independent sum and difference networks is shown in Figure C1. Note that each element has two fixed attenuators and two variable phase shifters. Equations (6a) and (6b) are the corresponding stochastic power equations. Note that W_Σ and W_Δ which are controlled by the tracking and adaptive process algorithms are independent. Thus the adaptive process for the sum and difference beam are decoupled.

191
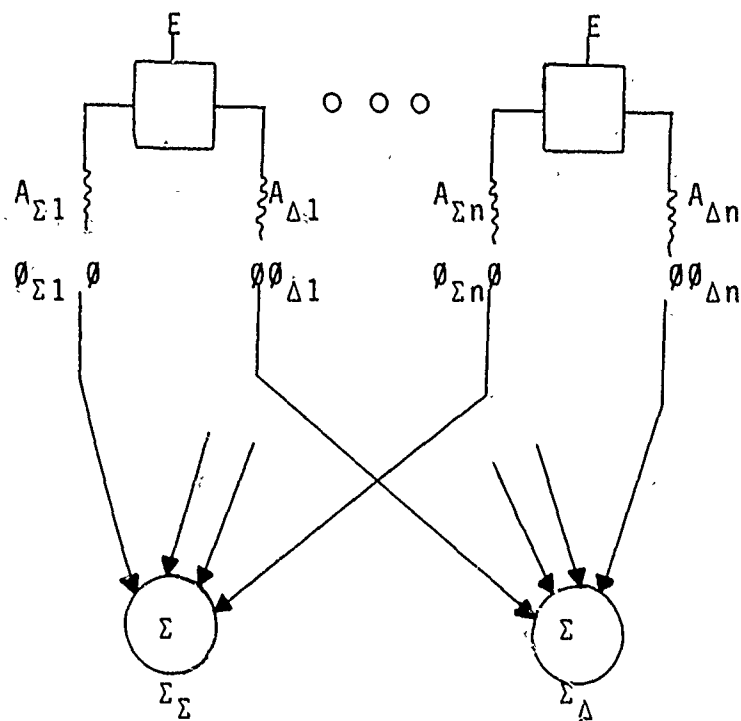
Figure C-1. Independent Sum and Difference Networks

$$P_\Sigma = W_\Sigma^* \underline{R} W_\Sigma^T \tag{6a}$$

$$P_\Delta = W_\Delta \underline{R} W_\Delta^T \tag{6b}$$

This network allowed independent investigation of the adaptive process for the sum and difference beams used for monopulse tracking. It was particularly useful for discovering the difficulties of using a beam space approach for direct nulling of jammers in the difference pattern. While mainly of theoretical interest due to implementation costs. it also allowed investigation of near 'optimum' amplitude tapers.

Several were tried including a cosine square illumination function. However, each taper required modification of the FORTRAN code and consequently was not extensively used. The importance of side lobe control through amplitude taper choice is discussed elsewhere in this report.

C2.2 Phase Comparison Network

A functional diagram of the phase comparison network is shown in Figure C-2 with its corresponding Equations given as (7a-d). Note that these equations show that the adaptive process for the sum and difference channels are coupled. In practice the array was divided into two subarrays, with adaptive nulling of jammers occurring at the output of the left and right subarrays prior to combination. Thus, two independent networks are used for adaptive control while the final sum and difference adaptation is coupled.
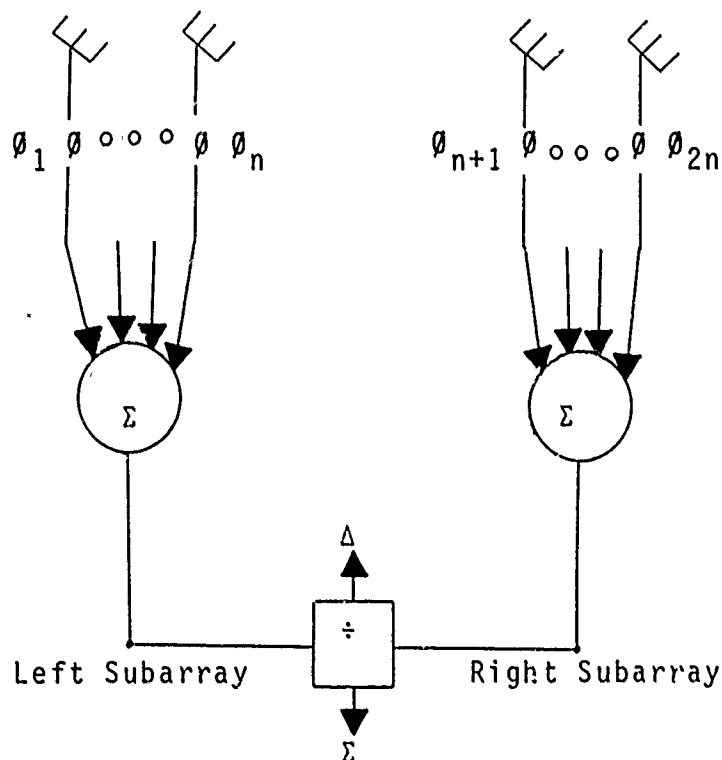
Figure C-2. Phase Comparison System

$$P_{\Sigma} = W^{+*} \ \underline{R} \ W^{+T} \tag{7a}$$

$$P_{\Delta} = W^{-*} \ \underline{R} \ W^{-T} \tag{7b}$$

$$W_i^+ = e^{j\emptyset i} \tag{7c}$$

$$W_i^- = \begin{array}{ll} e^{j\emptyset i} & 1 \le i \le n \\ -e^{j\emptyset i} & n+1 \le i \le 2n \end{array} \tag{7d}$$

This network has the advantage of requiring the least hardware per element (one phase shifter) of the four networks studied. For a fixed number of elements it also has the poorest performance of these four networks. It should be noted, however, that the control algorithm has only m degrees of freedom for a m element array with this network. The other networks allow 2m degrees of freedom.

C2.3 Uniform Amplitude Comparison System

A functional diagram of the uniform amplitude comparison network is shown in Figure C-3. Here there are left and right beams squinted to each side of the target as shown in Figure C-4. The equivalent sum beam aperture illumination function is a sampled cosine function while the equivalent difference beam aperture illumination function is a sampled sine function. The spacial frequency is controlled by the amount of beam squint. With an appropriate choice of spacial frequency these illumination functions yield good side lobe control of the sum and difference beams, respectively.

In practice the array was divided into a left and right beam, with adaptive nulling of jammers occurring at the output of these beams prior to combining to produce a sum and difference signal. Thus, two independent networks are again used for adaptive control while the final sum and difference adaptation is coupled.

C2.4 Improved Amplitude Comparison System

A functional diagram of the improved amplitude comparison network is shown in Figure C-5. The network is the same as the uniform amplitude comparison network with the exception of a common amplitude taper. Through the choice of the approximate taper for a given squint angle, the equivalent sum and difference aperture illuminations functions remain sampled cosine and sine functions, respectively, but of difference spacial frequencies. An appropriate choice of these two spacial frequencies further enhances side lobe control.
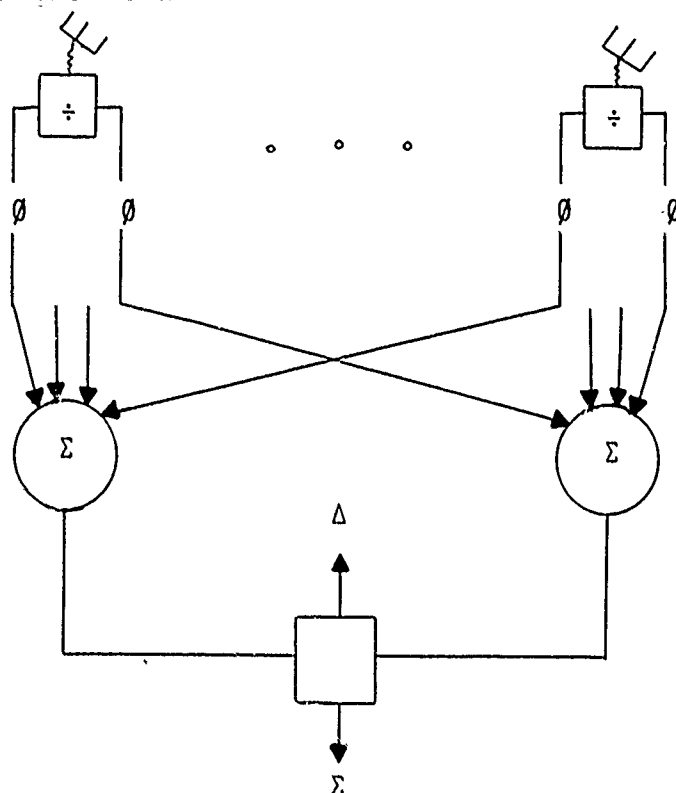
Figure C-5. Improved Amplitude Comparison Network

C3   Adaptive Array Control Algorithms

Two control algorithms were used in the study. Both were
basically power minimization algorithms. One was a constrained
random search. The other was a beam space coefficient search.
Both use tracking information. The figure of merit in all cases
was the average stochastic power output of an identifiable
network or subnetwork.

C3.1 Random Search

A constrained accelerating random search was used. This
algorithm starts with the phase command vector generated by the
tracking algorithm. A random vector is then generated using a
uniform probability function. This vector is added to the
present phase command vector. If there is no improvement the
vector is reversed. If the figure of merit improved (decreases)
the step size is increased. If after a previous improvement,
no improvement results, the phase command reverts to the previous
phase command and the step size is decreased. If no improvement
then occurs, a new random vector is generated. There is also a
constraint on how far the phase of each phase shifter can be
changed from the original phase command generated by the
tracking algorithm.

It should be noted that this algorithm requires no informa-
tion about the jammer or any target information other than
approximate angular position. However, if the target signal is
strong relative to the jammers this algorithm will reduce this
signal while ignoring the jammers. The amount of target signal
loss is determined by the phase constraint imposed.   The
constraint can be viewed as an M-dimensional box. Under this
condition this algorithm will result in a phase command vector
at one of the corners of this box.

196
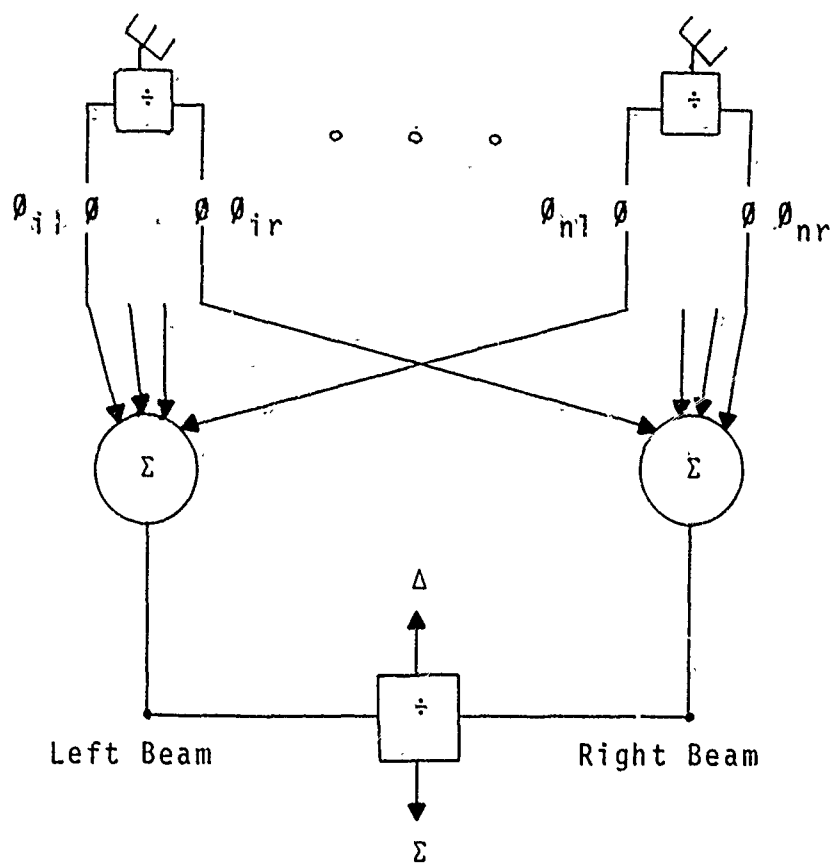
Figure C-3.   Uniform Amplitude Comparison Network
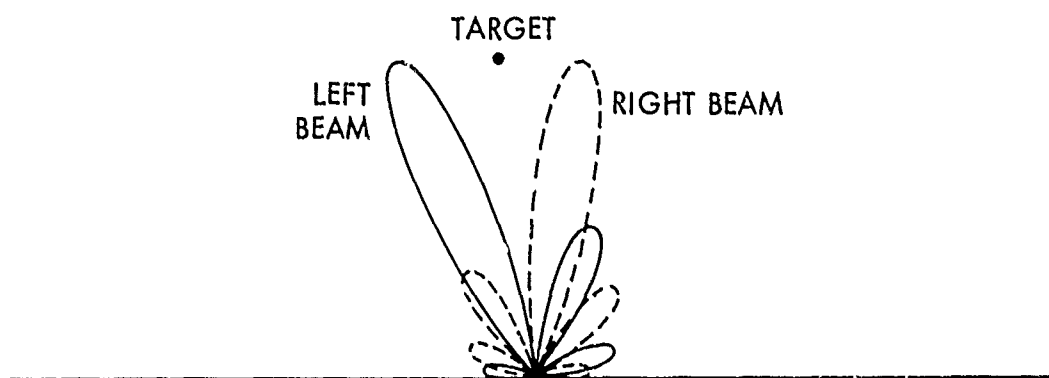
Figure C-4.   Left and Right Squinted Beams

197

C3.2 Beam Space Search

This algorithm forms a cancelling beam toward each jammer. It is an optimal algorithm in the sense that it results in the smallest change in the sum beam pattern while nulling the jammers. This algorithm needs the number of jammers present, their angular position, and the angular position of the target. The magnitude of the cancelling beam needed is determined by the side lobe level of the associated jammer. These levels are unknown by the algorithm which searches for this optimum set of coefficients. There is only one solution. This algorithm also uses the accelerated random search to search this coefficient space.

When no jitter is present, this algorithm is equivalent to a signal processing algorithm that maximizes the signal to noise ratio. This algorithm cannot handle jammers symmetrically located about the target when limited to phase only weights. This constraint requires an asymmetric beam relative to the target as shown in Figure C-6.
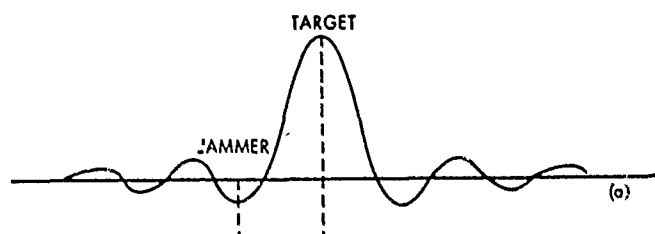
Figure C-6a. Main Beam Pattern
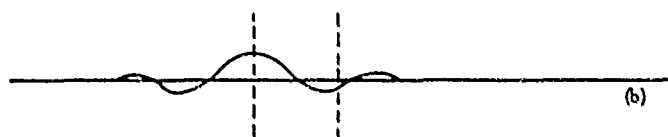
Figure C-6b. Cancelling Beam
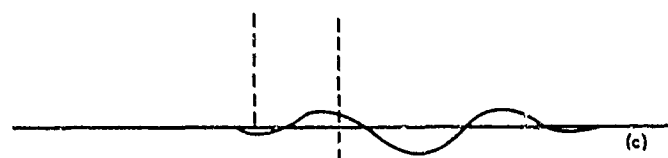
Figure C-6c. Additional Beam Due to Phase Weight Constraint
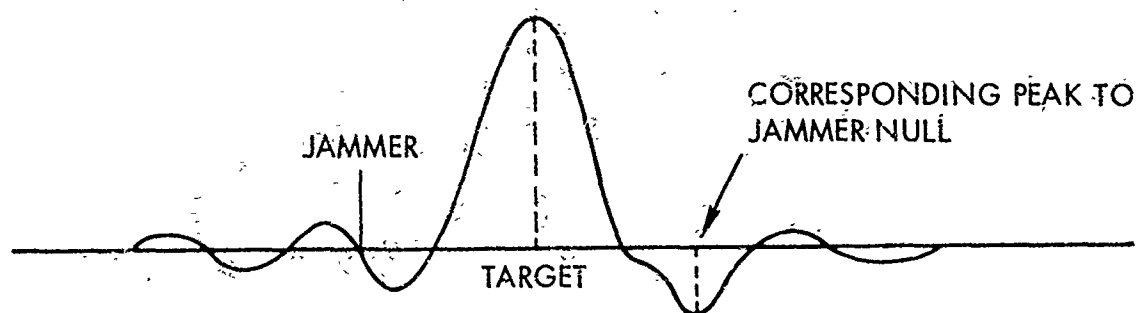
Figure C-6d.   Total Pattern After Adaptation

C4   Array Errors Modeled

The basic program without array errors was modified to
allow model verification by comparison with experimental results.
To achieve verification it was necessary to model quantization,
fixed errors in line phase length, fixed amplitude imbalance
errors, variable amplitude errors associated with phase shifter
state, and variable phase errors also associated with phase
shifter state that were found in the experimental hardware.

The majority of these errors had to be measured in the
experimental hardware. These measurements were then used as
data by the verification program. It should be stressed that
the control algorithm does not have access to these measurements
with the exception of the fixed errors in line phase length.
These measurements are used only to convert the control algorithms
phase commands into actual complex weights representing the
hardware including these errors.

C4.1 Quantization

The phase shifters used consist of a 4-bit/16-state (22.5^o)
p-i-n switched transmission line phase shifter plus a varactor
phase shifter controlled by a 5 bit DAC. The varactor is a non-
linear phase shifter, however, the varactor was modeled as a
linear phase shifter quantized to 0.7^o.

C4.2 Fixed Line Phase Length Errors

The phase length between the elements and the amplitude comparison network output is different for each element. It is assumed that the relative phase lengths have been measured and are known by the control algorithm. The phase shifter control algorithm compensates for these differences by modifying the phase commands from the adaptive control algorithm. Thus, the direct effects of these errors are compensated. However, this compensation can effect the p-i-n phase shifter states. These states in turn determine the variable amplitude and phase errors encountered. Thus, these fixed line phase length errors indirectly effect the variable amplitude and phase errors.

C4.3 Fixed Amplitude Errors

The path from each antenna element to the output port has different VSWR's, power divider losses, amplifier losses, etc. The total amplitude effect of these differences was measured for each path and the relative differences were considered to be fixed amplitude inbalance errors.

C4.4 Phase Shifter Amplitude Errors

Due to VSWR effects each of the 16 p-i-n switched line phase shifter states has different amplitude losses. These relative losses were measured for each state and incorporated into the model as variable amplitude errors.

C4.5 Phase Shifter Phase Errors

Due to VSWR effects each of the 16 p-i-n switched line phase shifter states is different from a multiple of 22.5°. These relative differences were measured for each state and incorporated into the model as variable phase errors.

C4.6 Phase Command Conversion to Actual Complex Weights

The phase commands from the control algorithm are adjusted to compensate for fixed phase length errors. These adjusted phase commands are then quantized. The quantized phase command are used to compute the phase state of each element's phase shifter. The amplitude associated with an array element is then computed as its nominal amplitude plus the fixed amplitude error associated with the element plus the variable amplitude error determined by the phase shifter state associated with the element. The phase associated with an element is then computed as its quantized value plus the fixed phase length error associated with the element plus the variable phase length error determined by the phase shifter state associated with the element.

C5   General Simulation Technique

The following is a top level function description of the simulation software sequence: a user supplied scenario is read. From this cross-correlation matrices for the target and all jammer(s) are computed. These are then combined with thermal noise into the total cross-correlation matrix. The initial phase commands are supplied by the tracking algorithm. The equivalent complex weights for the unadaptive sum and difference beams are calculated. These weights and the emitters cross-correlation matrices are used to calculate the initial contribution of each emitter to the total power.

Then for each independent network, i.e., subarray, left or right beam, an iterative series of calculations is performed. The actual complex weights, possibly including hardware errors. are computed from the phase commands. Using these weights and the total cross-correlation matrix the average stochastic power

is calculated. This is then fed to the adaptive control algorithm as the figure of merit. The adaptive control algorithm then produces a new set of phase commands.

When this adaptive nulling is completed the best phase commands found are used to calculate equivalent weights for the adaptive sum and difference beams. These weights and the emitters' cross-correlation matrices are used to analyze the contribution of each emiter to the total power after adaptation. These are compared to the contribution of each emitter in the unadaptive case. Then the adaptive sum and difference patterns are plotted. Following this the boresight error estimator is used on the difference between the unadaptive and adaptive weights to calculate the boresight shift experienced.

APPENDIX D

ACCURATE BORESIGHT SHIFT ERROR FORMULAS FOR COMPUTER SIMULATIONS

This section will develop an expression for the boresight error due to null steering.

The expression derived here was used in all simulations; and was found to give a reliable estimate of the boresight shift.

The far-field antenna patterns for the unadapted sum beam ($\Sigma(\theta)$) and the unadapted difference beam ($\Delta(\theta)$) are given in terms of the illumination functions $\Sigma(x)$ and $\Delta(x)$ as

$$\Sigma(\theta) = \int_{-\frac{1}{2}}^{\frac{1}{2}} \Sigma(x) e^{j(2\pi \sin \theta) x} \, dx \tag{1}$$

$$\Delta(\theta) = \int_{-\frac{1}{2}}^{\frac{1}{2}} \Delta(\theta) e^{j(2\pi \sin \theta) x} \, dx \tag{2}$$

After null steering, the illumination functions $\Sigma(x)$ and $\Delta(x)$ contain perturbations that can be written as

$t_1(x) e^{j\gamma_1 (x)}$ and $t_2(x) e^{j\gamma_2 (x)}$. The adapted sum and difference patterns can then be written as

$$\Sigma(\theta) = \int_{-\frac{1}{2}}^{\frac{1}{2}} \Sigma(x) \, t_1(x) e^{j\gamma_1 (x)} \, e^{j(2\pi \sin \theta) x} dx \tag{3}$$

$$\Delta(\theta) = \int_{-\frac{1}{2}}^{\frac{1}{2}} \Delta(x) \, t_2(x) e^{j\gamma_2 (x)} \, e^{j(2\pi \sin \theta) x} \, dx \tag{4}$$

Near boresight $2\pi \sin (\theta) x$ is small and

$$e^{j(2\pi \sin \theta) x} \doteq 1 + j(2\pi \sin (\theta) x) \tag{5}$$

Then

$$\Sigma(\theta) = \int_{-\frac{1}{2}}^{\frac{1}{2}} \Sigma(x)t_1(x)e^{j\gamma_1(x)} (1 + j(2\pi\sin(\theta) x)) \, dx \qquad (6)$$

$$\Delta(\theta) = \int_{-\frac{1}{2}}^{\frac{1}{2}} \Delta(x)t_2(x)e^{j\gamma_2(x)} (1 + j(2\pi\sin(\theta) x)) \, dx \qquad (7)$$

By expanding the remaining exponentials, the adapted patterns can be written as

$$\Sigma(\theta) = \int_{-\frac{1}{2}}^{\frac{1}{2}} \Sigma(x)t_1(x) \cos\gamma_1(x) \, dx - \sin\theta \int_{-\frac{1}{2}}^{\frac{1}{2}} 2\pi \Sigma(x)t_1(x)$$

$$\sin\gamma_1(x) \, x \, dx + j \int_{-\frac{1}{2}}^{\frac{1}{2}} \Sigma(x)t_1(x) \sin\gamma_1(x) \, dx +$$

$$\sin\theta \int_{-\frac{1}{2}}^{\frac{1}{2}} 2\pi\Sigma(x)t_1(x) \cos\gamma_1(x) \, x \, dx \qquad (8)$$

$$\Delta(\theta) = \int_{-\frac{1}{2}}^{\frac{1}{2}} \Delta(x)t_2(x) \cos\gamma_2(x) \, dx - \sin\theta \int_{-\frac{1}{2}}^{\frac{1}{2}} 2\pi\Delta(x)t_2(x)$$

$$\sin\gamma_2(x) \, dx + j \int_{-\frac{1}{2}}^{\frac{1}{2}} \Delta(x)t_2(x) \sin\gamma_2(x) \, dx +$$

$$\sin\theta \int_{-\frac{1}{2}}^{\frac{1}{2}} 2\pi\Delta(x)t_2(x) \cos\gamma_2(x) \, x \, dx \qquad (9)$$

The sum pattern can then be written as

$$\Sigma(\theta) = A - \sin\theta \, B + j(C + \sin\theta \, D) \qquad (10)$$

204

where

$$A = \int_{-\frac{1}{2}}^{\frac{1}{2}} \Sigma(x) t_1(x) \cos\gamma_1(x) \, dx \qquad (11)$$

$$B = 2\pi \int_{-\frac{1}{2}}^{\frac{1}{2}} \Sigma(x) t_1(x) \sin\gamma_1(x) \, x \, dx \qquad (12)$$

$$C = \int_{-\frac{1}{2}}^{\frac{1}{2}} \Sigma(x) t_1(x) \sin\gamma_1(x) \, dx \qquad (13)$$

$$D = 2\pi \int_{-\frac{1}{2}}^{\frac{1}{2}} \Sigma(x) t_1(x) \cos\gamma_1(x) \, x \, dx \qquad (14)$$

Similarly, for the difference pattern,

$$\Delta(\theta) = E - \sin\theta \, F + j(G + \sin\theta \, H) \qquad (15)$$

where

$$E = \int_{-\frac{1}{2}}^{\frac{1}{2}} \Delta(x) t_2(x) \cos\gamma_2(x) \, dx \qquad (16)$$

$$F = 2\pi \int_{-\frac{1}{2}}^{\frac{1}{2}} \Delta(x) t_2(x) \sin\gamma_2(x) \, x \, dx \qquad (17)$$

$$G = \int_{-\frac{1}{2}}^{\frac{1}{2}} \Delta(x) t_2(x) \sin\gamma_2(x) \, dx \qquad (18)$$

$$H = 2\pi \int_{-\frac{1}{2}}^{\frac{1}{2}} \Delta(x) t_2(x) \cos\gamma_2(x) \, dx \qquad (19)$$

The output of the product detector is

$$P(\theta) = \frac{\Sigma(\theta) \cdot j\Delta(\theta)}{|\Sigma(\theta)|^2} \tag{20}$$

The boresight error is the angle which drives the product detector output to zero:

$$P(\varepsilon) = 0 = \frac{\Sigma(\varepsilon) \cdot j\Delta(\varepsilon)}{\Sigma(\varepsilon)^2} \tag{21}$$

Expanding this expression,

$$Re(\Sigma(\varepsilon))\ Re(j\Delta(\varepsilon)) + Im(\Sigma(\varepsilon))\ Im(j\Delta(\varepsilon)) = 0 \tag{22}$$

Expanding (22) using (10) and (15) gives a quadratic in $sin\varepsilon$:

$$sin^2\varepsilon\ (DF - BH) + sin\ \varepsilon(AH + CF - BG - DE) +$$
$$(AG - CE) = 0 \tag{23}$$

Letting

$$Z_1 = DF - BH \tag{24}$$

$$Z_2 = AH + CF - BG - DE \tag{25}$$

$$Z_3 = AG - CE \tag{26}$$

the boresight error is expressed as

$$sin_\varepsilon = \frac{-Z \pm (Z_2^2 - 4Z_1 Z_3)^{\frac{1}{2}}}{2Z_1} \tag{27}$$

To calculate the boresight error, the illumination functions $\Sigma(x)$ and $\Delta(x)$ must be known. The right and left beams are linearly phased, and their far-field patterns can be expressed as

$$A^1(\theta) = \int_{-\frac{1}{2}}^{\frac{1}{2}} e^{-j\alpha x}\, e^{j(2\pi \sin\theta)\,x}\, dx \tag{28}$$

$$A^{11}(\theta) = \int_{-\frac{1}{2}}^{\frac{1}{2}} e^{j\alpha x}\, e^{j(2\pi \sin\theta)\,x}\, dx \tag{29}$$

where α is the electrical squint angle. Then

$$\Sigma(\theta) = A^1(\theta) + A^{11}(\theta) \tag{30}$$

$$\Delta(\theta) = A^1(\theta) - A^{11}(\theta) \tag{31}$$

and

$$\Sigma(\theta) = \int_{-\frac{1}{2}}^{\frac{1}{2}} 2\cos\alpha x\, e^{j(2\pi \sin\theta)\,x}\, dx \tag{32}$$

$$\Delta(\theta) = \int_{-\frac{1}{2}}^{\frac{1}{2}} (2j\,\sin\alpha x)\, e^{j(2\pi \sin\theta)\,x}\, dx \tag{33}$$

The illumination functions are then

$$\Sigma(x) = 2\cos\alpha x \tag{34}$$

$$\Delta(x) = 2j\sin\alpha x \tag{35}$$

It was found that (27) was not convenient for computational purposes because of round off errors, so a simplified expression was developed. Recalling (27),

$$\text{sine} = \frac{-Z_2 \pm (Z_2^2 - 4Z_1 Z_3)^{\frac{1}{2}}}{2Z_1} = \frac{-Z_2}{2Z_1} \left(1 \pm \sqrt{1 - 4Z_1 Z_3 / Z_2^2}\right)$$

Letting $4Z_1 Z_3 / Z_2^2 = x$, and expanding about $x = 0$,

$$\sqrt{1 - x} \doteq 1 - x/2 \tag{36}$$

then

$$\text{sine} \doteq \frac{-Z_2}{2Z_1} \left(1 \pm (1 - x/2)\right) \tag{37}$$

For the positive root,

$$\text{sine} \doteq \frac{-Z_2}{2Z_1} (2 - x/2) \tag{38}$$

This root was found in all cases to be greater than one and hence unphysical. The negative root of (37) is

$$\text{sine} \doteq \frac{-Z_2}{2Z_1} \left(\frac{2Z_1 Z_3}{Z_2^2}\right) = \frac{-Z_3}{Z_2} \tag{39}$$

This root was utilized for computational purposes.

208

APPENDIX E

BREADBOARD EQUIPMENT AND CALIBRATION MEASUREMENTS

E1   Bench Calibration

E1.1 Phase Shifters

A 9-bit phase shifter design was used in this program to provide vernier phase shifter control. The 9-bit phase shifter is derived from a 4-bit PIN diode digital phase shifter and an analog varactor phase shifter. A D/A converter is used to provide the equivalent of 5 bits of phase shift.

The insertion phase and amplitude of the phase shifters was measured on a Hewlett Packard 8410 network analyzer. The phase shifters were bench checked to see if all the circuits were working properly and to make necessary repairs. Table E1.1-1 is the insertion phase of the digital bits for the 16 phase shifters. Table E1.1-2 is the amplitude insertion loss for several phase commands. All analog phase shifters were allowed a 28⁰ minimum to maximum phase change. Figure E1.1-1 is a plot of the control voltage on the varactor diodes versus measured phase shift of circuit number 3. Figure E1.1-2 is a plot of the commanded phase versus measured phase of circuit number 3. Three circuits were checked using the same phase commands used on circuit number 3-all circuits were found to track to less than 0.3⁰ error.

E1.2 Array Reflection and Coupling Coefficients

The 16 element archimedean spiral array was measured for reflection and coupling coefficients using the Hewlett Packard 8410 network analyzer. Table E1.2-1 is the reflection coefficient measurements, referenced to the element input connector. Table E1.2-2 is the coupling coefficient

9 BIT PHASE SHIFTER

INSERTION PHASE

CIRCUIT NO.	BIT 1	BIT 2	BIT 3	BIT 4
1	183°	95°	50°	25
2	186	84	48	25
3	184	93	47	25
4	186	93	46	27
8	183	94	47	24
9	186	93	47	24
10	185	93	45	22
11	185	93	46	23
12	183	93	46	25
13	183	90	45	24
14	183	92	46	23
15	186	93	47	23
16	186	93	47	25
17	184	93	47	23
18	185	93	49	26
19	183	92	46	25

Table E1.1-1. Digital Bit Phase Shift
Bench Calibration

INSERTION LOSS (dB) 9 BIT PHASE SHIFTER

CIRCUIT NO.	0°	22°	45°	67°	90°	135°	157°	180°	225°	270°	315°	337°	28° (MAXIMUM ANALOG)
1	2.9	2.9	2.9	2.9	4.1	3.9	3.9	3.8	3.8	4.4	4.3	4.6	3.2
2	2.5	2.5	2.3	2.3	2.7	2.7	2.8	3.4	3.3	3.3	3.6	3.7	2.8
3	2.4	2.3	2.2	2.2	2.7	2.5	2.6	3.6	3.2	3.4	3.6	3.7	2.6
4	2.4	2.4	2.6	2.6	2.6	2.9	2.9	3.4	3.4	3.1	3.6	3.6	2.6
8	2.5	2.6	2.65	2.5	2.7	2.8	2.8	3.55	3.3	3.4	4.0	3.9	2.8
9	2.4	2.3	2.3	2.3	2.8	2.5	2.6	3.3	3.3	3.2	3.2	3.2	2.6
10	2.6	2.6	2.3	2.2	2.7	3.9	2.9	3.6	3.5	3.3	3.9	4.0	2.8
11	2.7	2.5	2.6	2.4	3.2	3.5	3.5	4.5	4.5	4.9	5.2	5.2	2.8
12	2.5	2.5	2.4	2.3	2.7	2.7	2.8	3.4	3.3	3.1	3.6	3.7	2.7
13	2.6	2.5	2.4	2.4	2.7	2.6	3.7	3.6	3.4	3.0	3.4	3.6	2.9
14	2.4	2.4	2.3	2.3	3.0	3.5	2.7	3.6	3.6	3.5	3.5	3.6	2.7
15	2.6	2.6	2.5	2.5	2.8	2.8	2.8	3.3	3.3	3.1	3.4	3.5	2.8
16	2.3	2.4	2.3	2.4	3.3	3.0	2.9	3.2	3.2	3.4	3.4	3.5	2.6
17	2.6	2.4	2.2	2.2	2.6	2.7	2.7	3.4	3.3	2.6	2.8	3.6	2.7
18	2.3	2.3	2.4	2.6	3.1	5.5	3.1	4.7	4.7	5.6	5.6	5.5	2.6
19	2.5	2.6	2.6	2.6	2.45	2.7	2.7	3.45	3.4	2.9	3.4	3.5	2.9

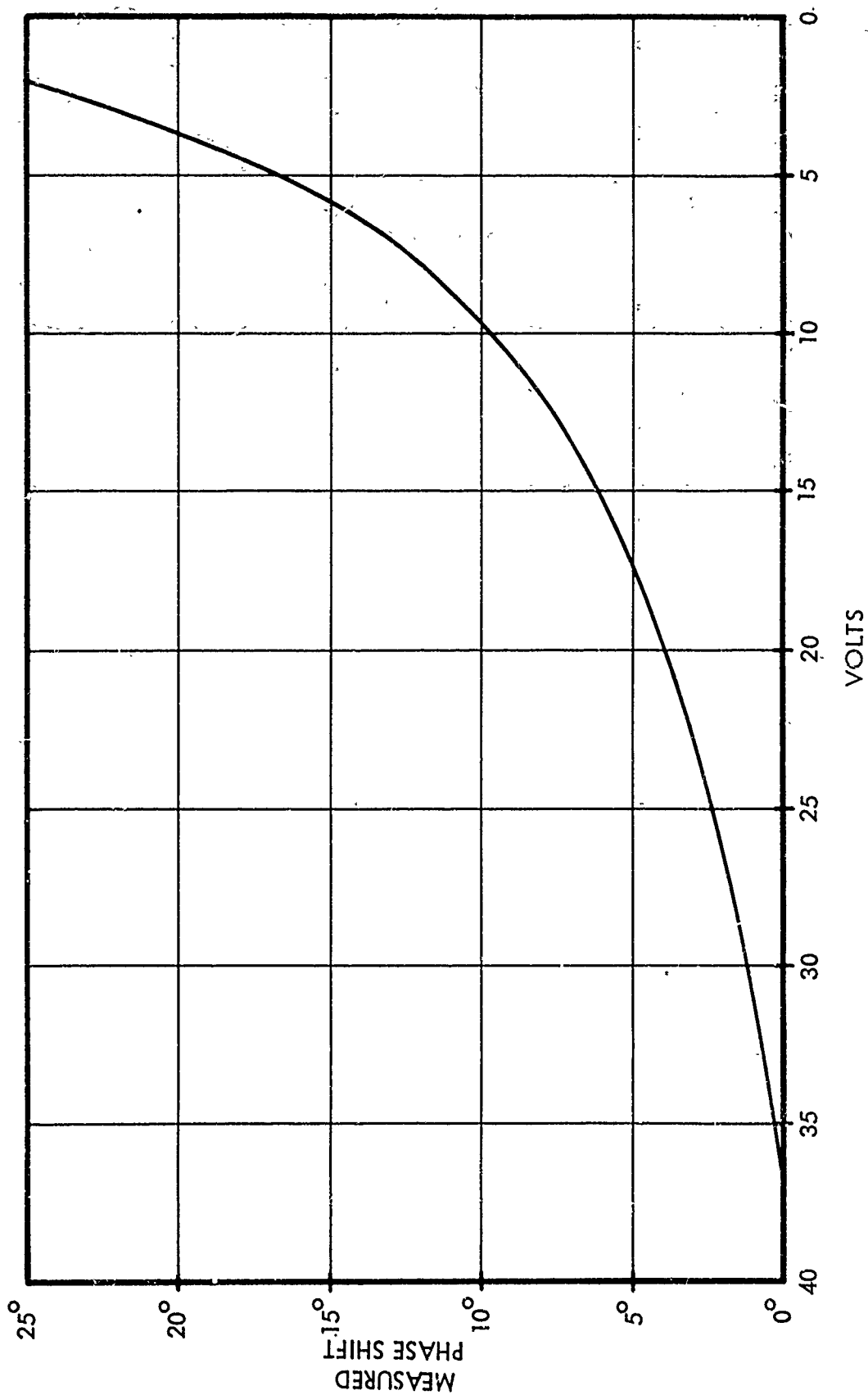Table E1.1-2. Amplitude Insertion Loss of Phase Shifters Bench Calibration

Figure E1.i-1 Analog Phase Shifter Varactor Control
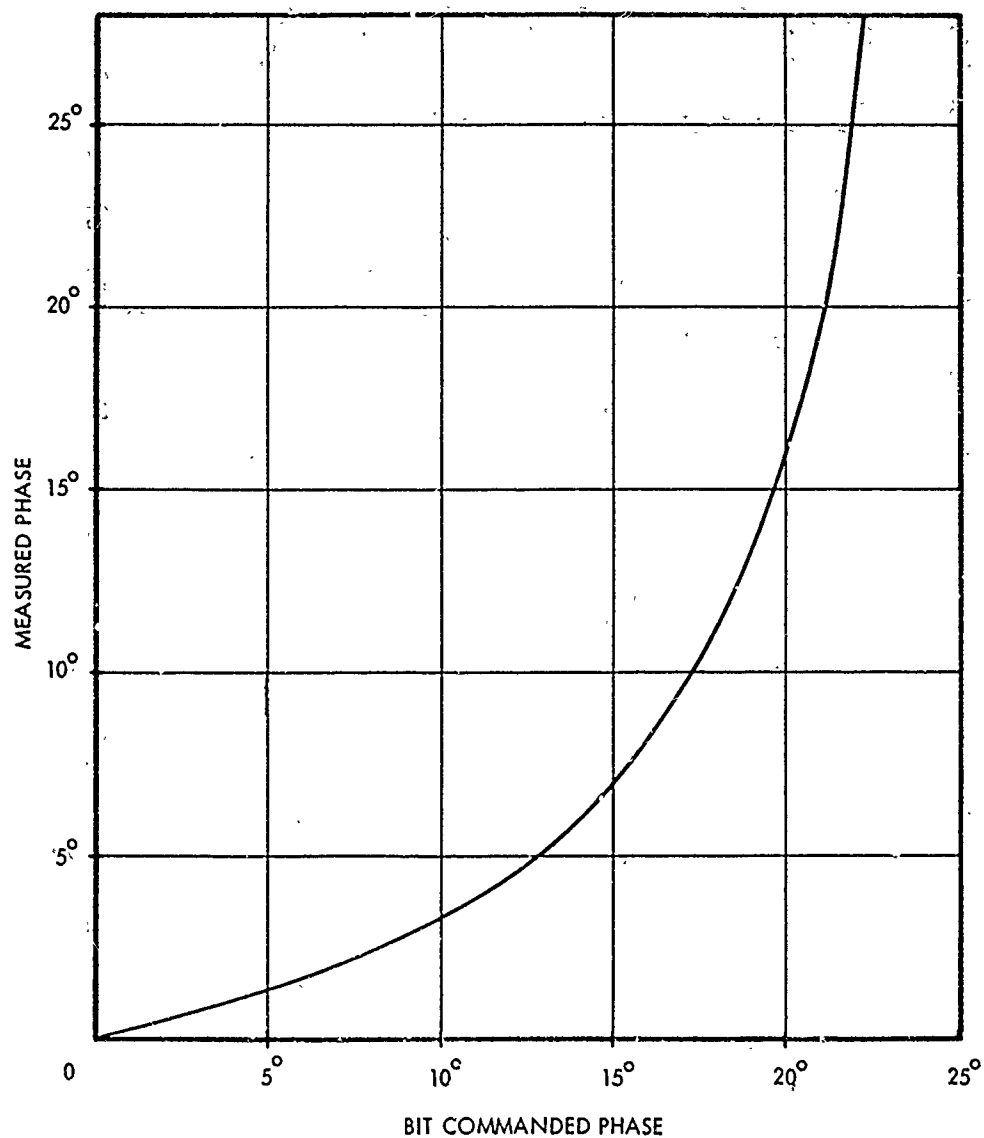Voltage vs. Phase Shift (Circuit #3).

212

Figure E1.1-2 Bit Commanded Phase Vs. Measured Phase
(Analog Phase Shifter)

REFLECTION COEFFICIENT

16 ELEMENT ARRAY (ARCHIMEDEAN ELEMENTS)

ELEMENT NO.	RETURN LOSS dB	SWR	PHASE
1	12 dB	1.67	-171^0
2	11 dB	1.78	-180^0
3	11 dB	1.78	-167^0
4	11 dB	1.78	-157.5^0
5	11 dB	1.78	-180^0
6	12 dB	1.67	-162^0
7	16 dB	1.38	-177^0
8	14 dB	1.5	-157^0
9	13 dB	1.58	-162^0
10	15 dB	1.43	-180^0
11	14 dB	1.5	-165^0
12	12 dB	1.67	-169^0
13	10 dB	1.92	-166^0
14	12 dB	1.67	-157^0
15	11 dB	1.78	-162^0
16	13 dB	1.58	-144^0

Table E1.2-1. Array Reflection Coefficient

COUPLING COEFFICIENT

16 ELEMENT ARRAY FROM ELEMENT NO. 8

TO ELEMENT NO.	AMPLITUDE	PHASE
9	-25 dB	-42^0
10	-29 dB	$+126^0$
11	-38 dB	-36^0
12	-38 dB	$+148^0$
13	-43 dB	$+27^0$
14	-42 dB	-162^0
15	-46 dB	$+72^0$
16	-46 dB	-135^0
7	-22 dB	-58^0
6	-30 dB	$+112^0$
5	-34 dB	-57^0
4	-36 dB	$+135^0$
3	-40 dB	-9^0
2	-42 dB	-170^0
1	-45 dB	$+54^0$

Table E1.2-2. Array Coupling Coefficient

measurements made from element number eight to all other elements in the array. Element number eight was selected for measurements because it is a center element. The reflection and coupling measurements were used to compute the active impedance of element number eight as the array is scanned. Figure E1.2-1 is the plot of the active impedance of element number eight.

E2   Range Calibration

E2.1 Amplitude Monopulse (Digital) Phase Shifter Calibration

The antenna range phase shifter calibrations were performed so the actual bit phases and the insertion loss could be used in the beam control program, both in the experimental test as well as the computer simulation.

All digital phase shifter calibrations were made using toggle switches to command the phase states.

The test configuration shown in Figure E2.1-1 was used to measure the phase and amplitude change with bit command of all 16 phase shifters.

The test configuration has a reference channel added for phase reference of the HP8405A vector voltmeter. The array was connected up in the amplitude monopulse configuration as shown in the figure. In order to test one phase shifter at a time only one of the beam 8-way power combiners was connected to the sum and difference hybrid and one phase shifter was connected to the remaining 8-way power combiner. All unused ports were terminated with a 50 ohm load. With this configuration each phase shifter under test will see the actual circuit match. All phase shifters were tested for 12 digital bit commands.
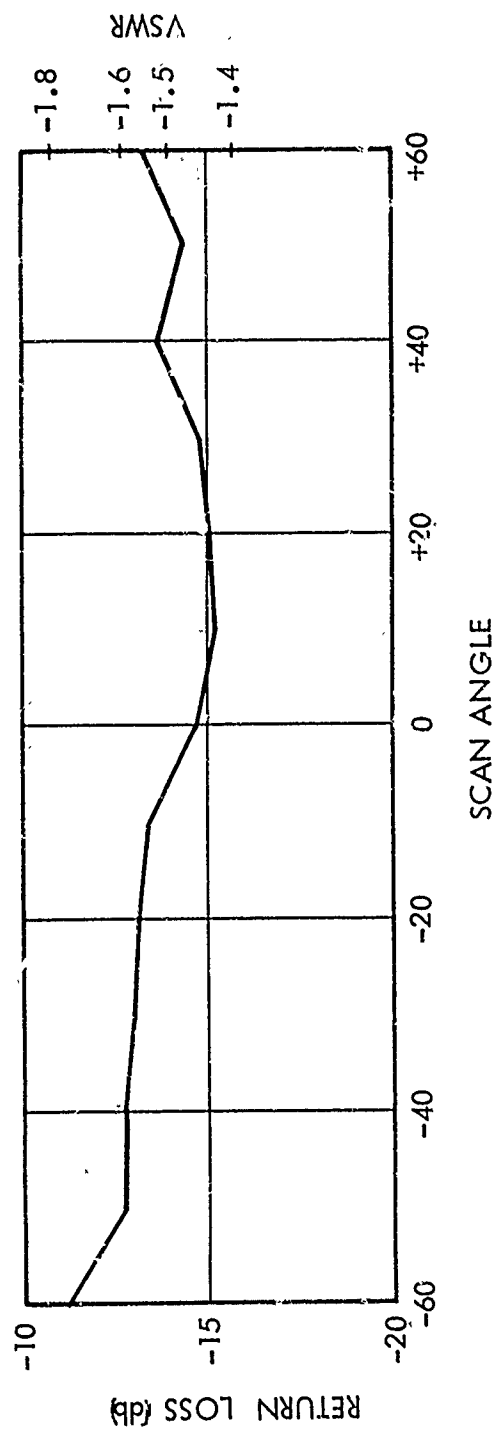
216

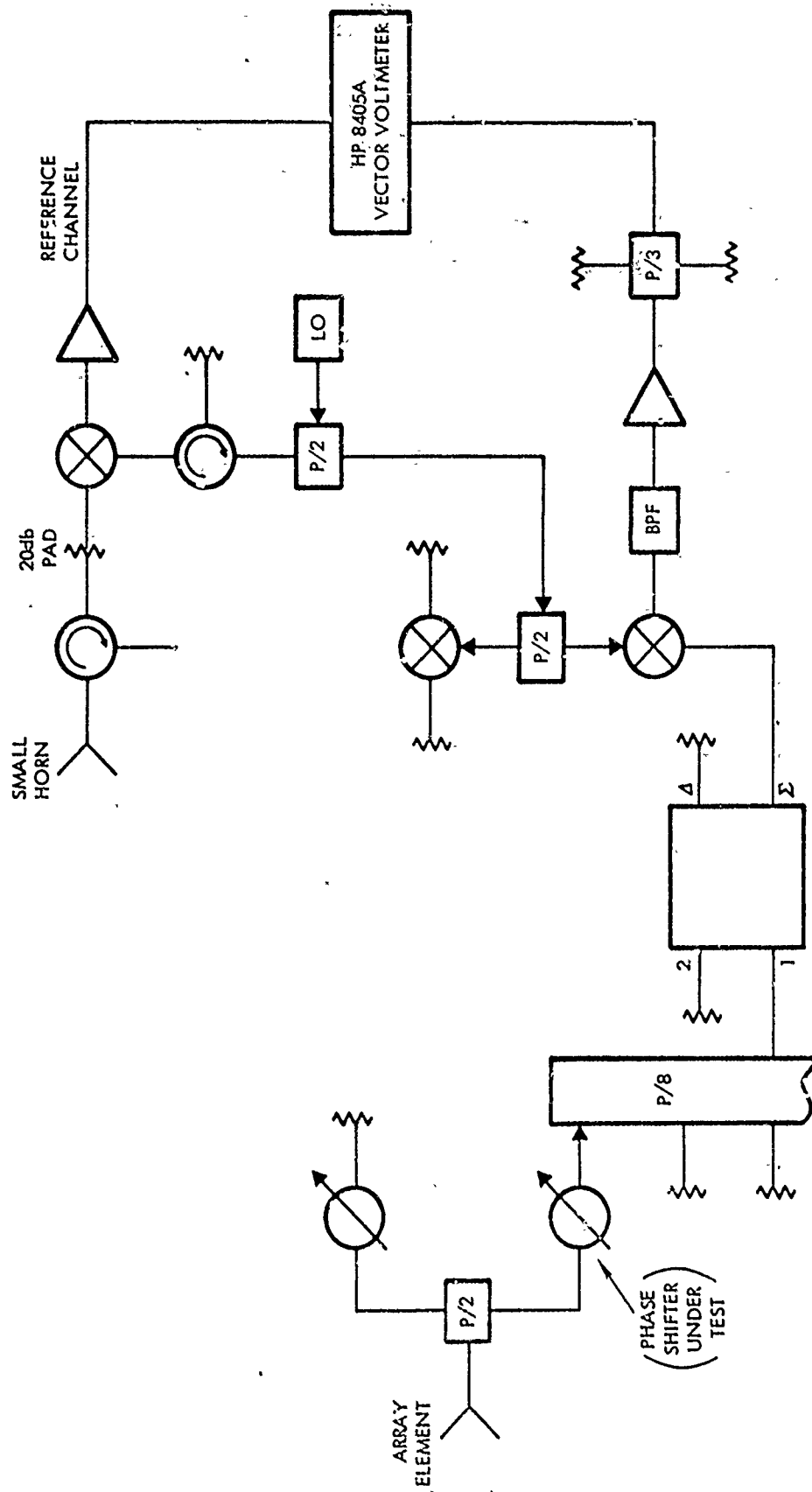Figure E1.2-1 Element Number 8 - Active Impedance

217

Figure E2.1-1   Amplitude Monopulse Range Calibration Configuration

Figures E2.1-2 and E2.1-3 are typical plots (for two phase shifters) of the commanded phase versus the measured phase for the left and right beams, respectively. Figures E2.1-4 and E2.1-5 are the commanded bit phase versus the measured insertion loss referenced from the 0^0 bit state.

E2.2 Analog Phase Shifter Calibration

One analog phase shifter was tested on the antenna range using toggle switches to command the D/A input of the analog phase shifter. Figure E2.1-1 is the test configuration used for antenna range calibration. Figure E2.2-1 is plot of bit commanded phase versus measured phase. The solid line is the plot of circuit number 3 phase shifter, measured on the bench using a network analyzer. The points marked (X) are measurements made on phase shifter number 18. These measurements were made on the antenna range using a vector voltmeter. Figure E2.2-2 is a plot of measured phase shifts versus amplitude change referenced to the 0^0 state of the analog phase shifter number 18.

The plot shown in Figure E2.2-1 shows that the commanded phases versus the measured phase is a nonlinear response. This non-linear response is compensated for in the computer software.

E2.3 0^0 Bit State Calibration

The test configuration shown in Figure E2.1-1 was used for the 0^0 bit calibration.

The phase shifter located in socket 16 was used as the phase and amplitude 0^0 reference for the vector voltmeter. All phase shifters were switched to the 0^0 bit state. The phase difference measured for each phase shifter was recorded in order to be used in the computer software for the electrical 0^0 phase reference. Figure E2.3-1 is a plot of the phase shifter socket location versus the 0^0 bit insertion phase, referenced to the phase shifter located in socket 16.
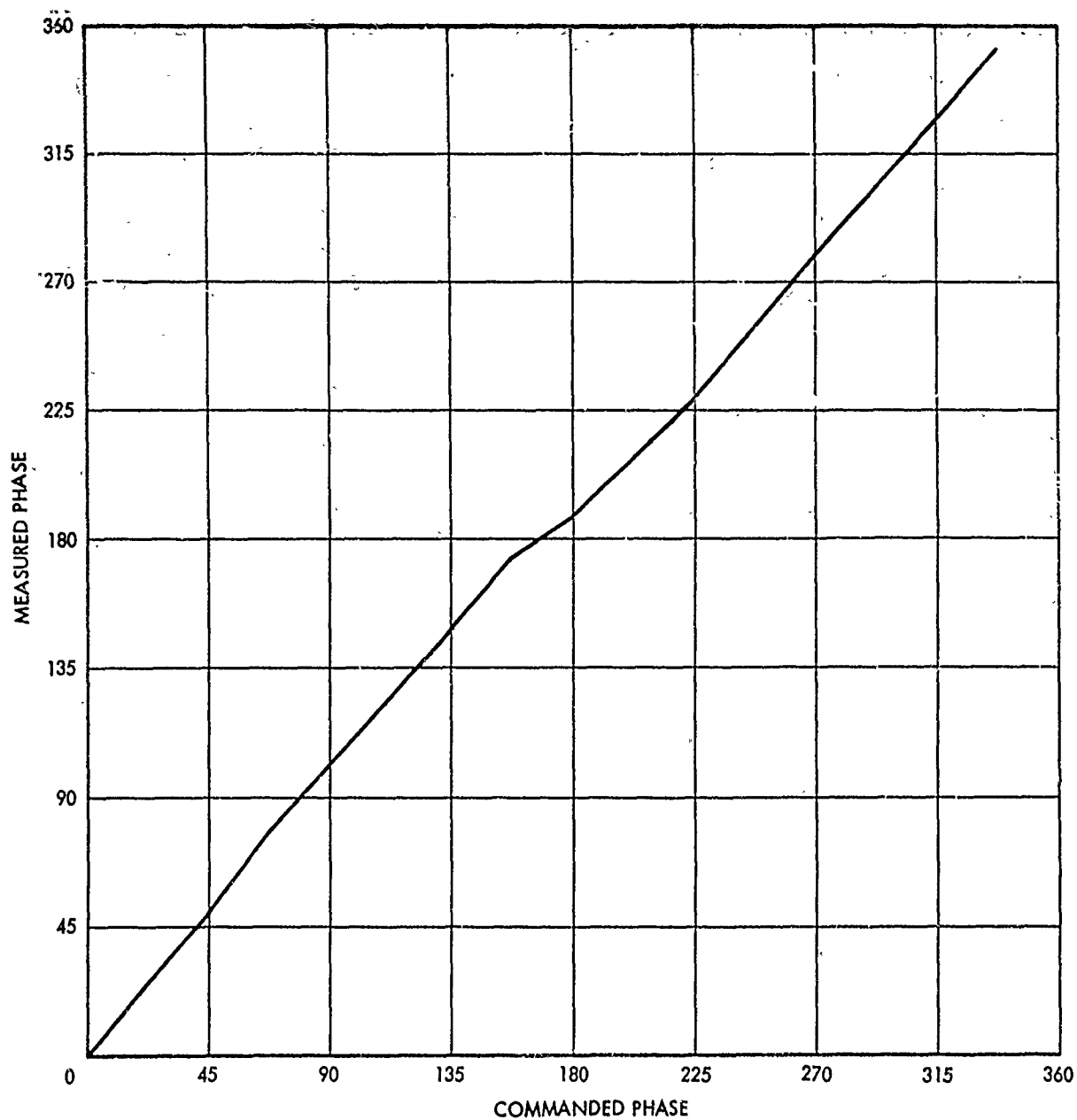
Figure E2.1-2. Commanded Phase vs. Measured Phase
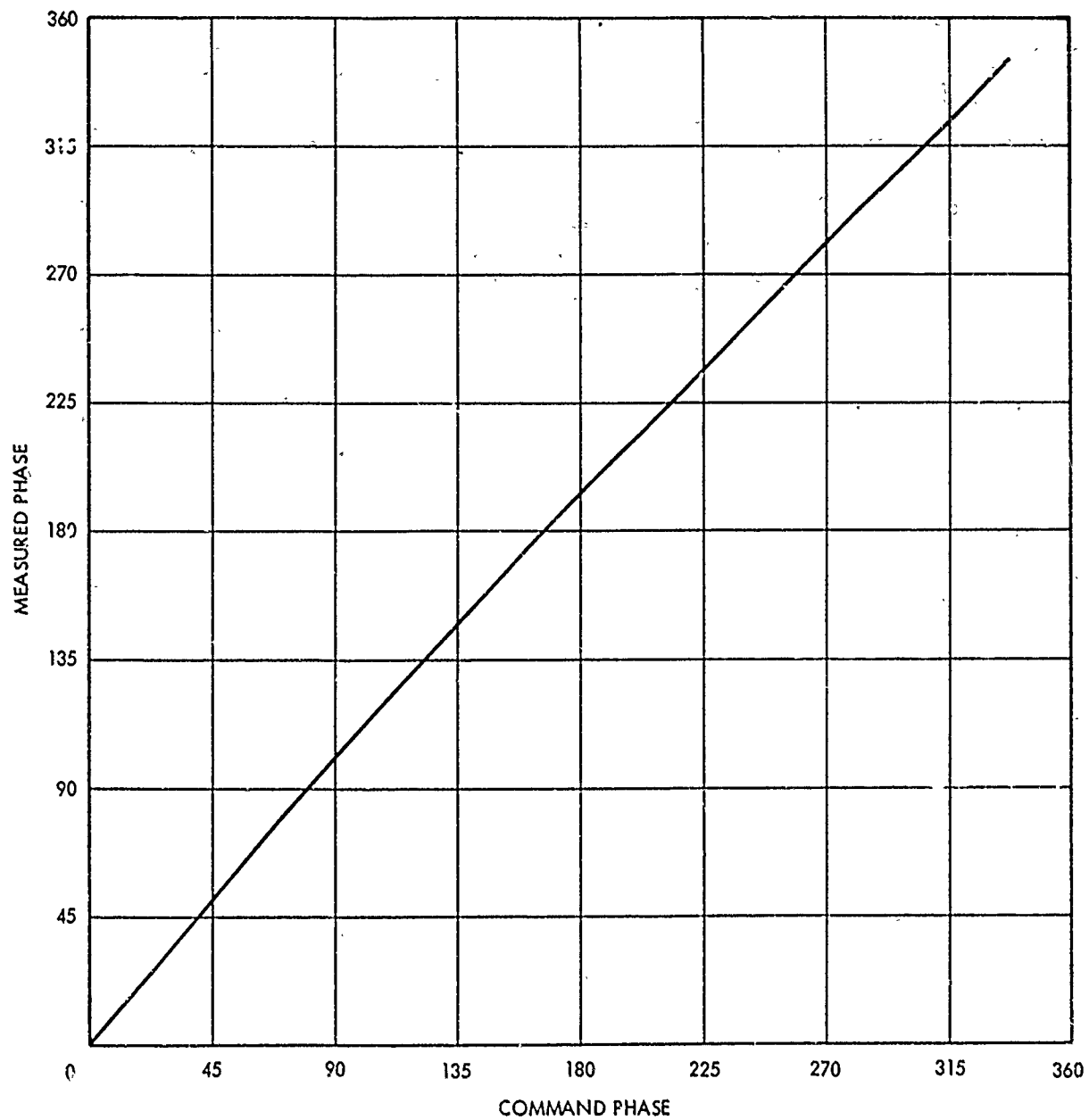For Phase Shifter Module Number 13

Figure E2.1-3. Commanded Phase vs. Measured Phase
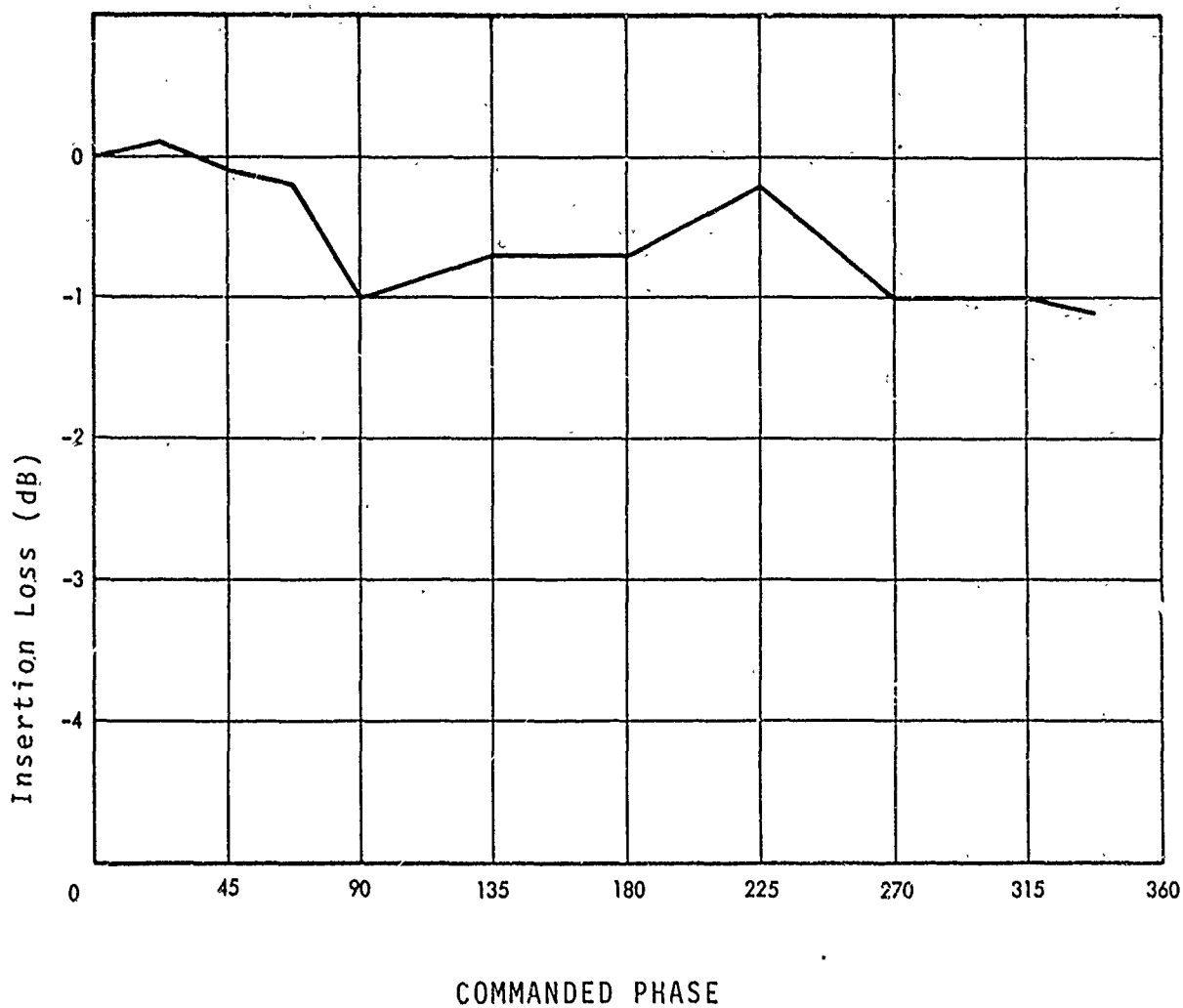For Phase Shifter Module Number 11

COMMANDED PHASE

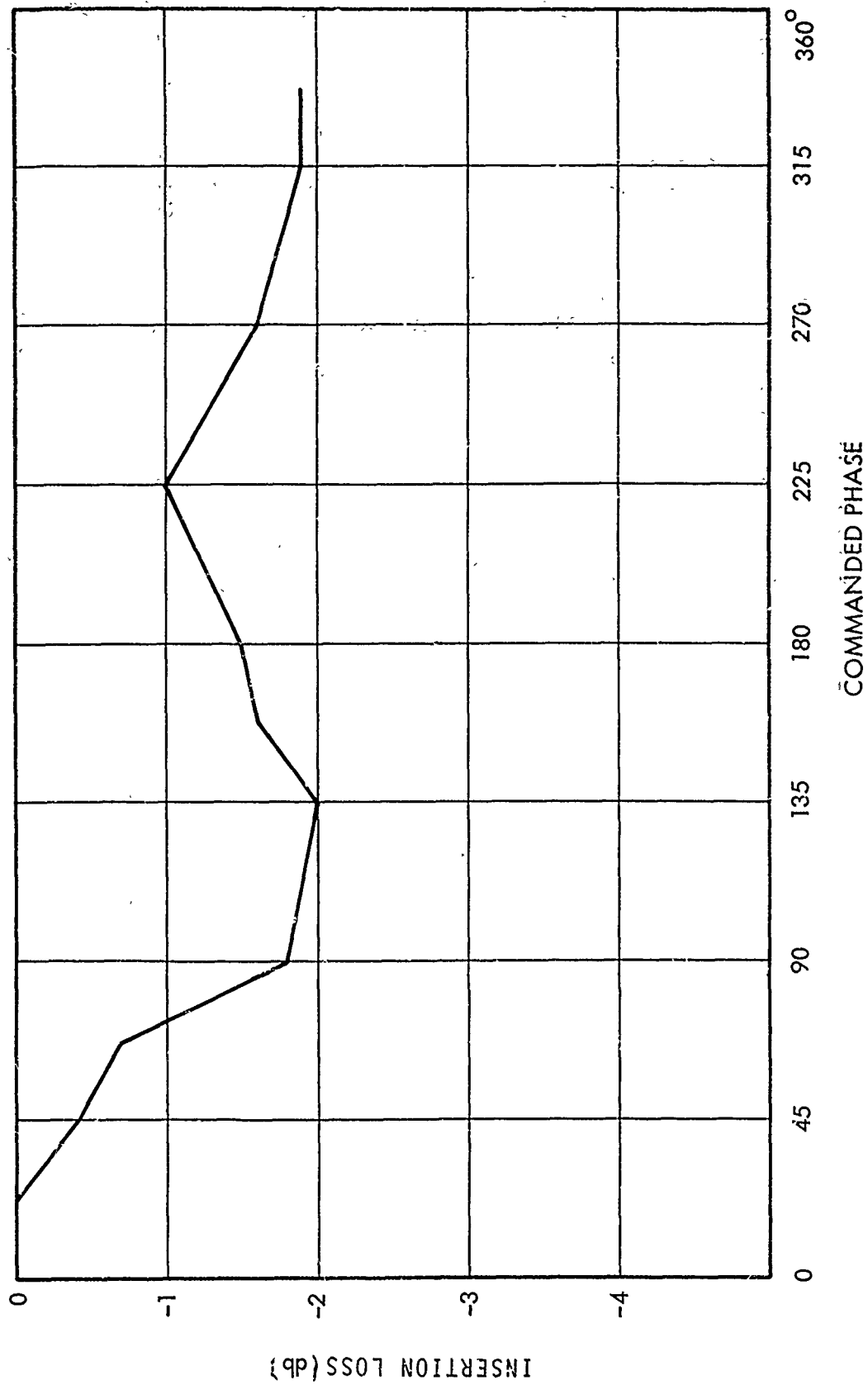Figure E2.1-4 Insertion Loss of Phase Shifter Module
Number 13

Figure E2.1-5 Insertion Loss of Phase Shifter Module Number 11
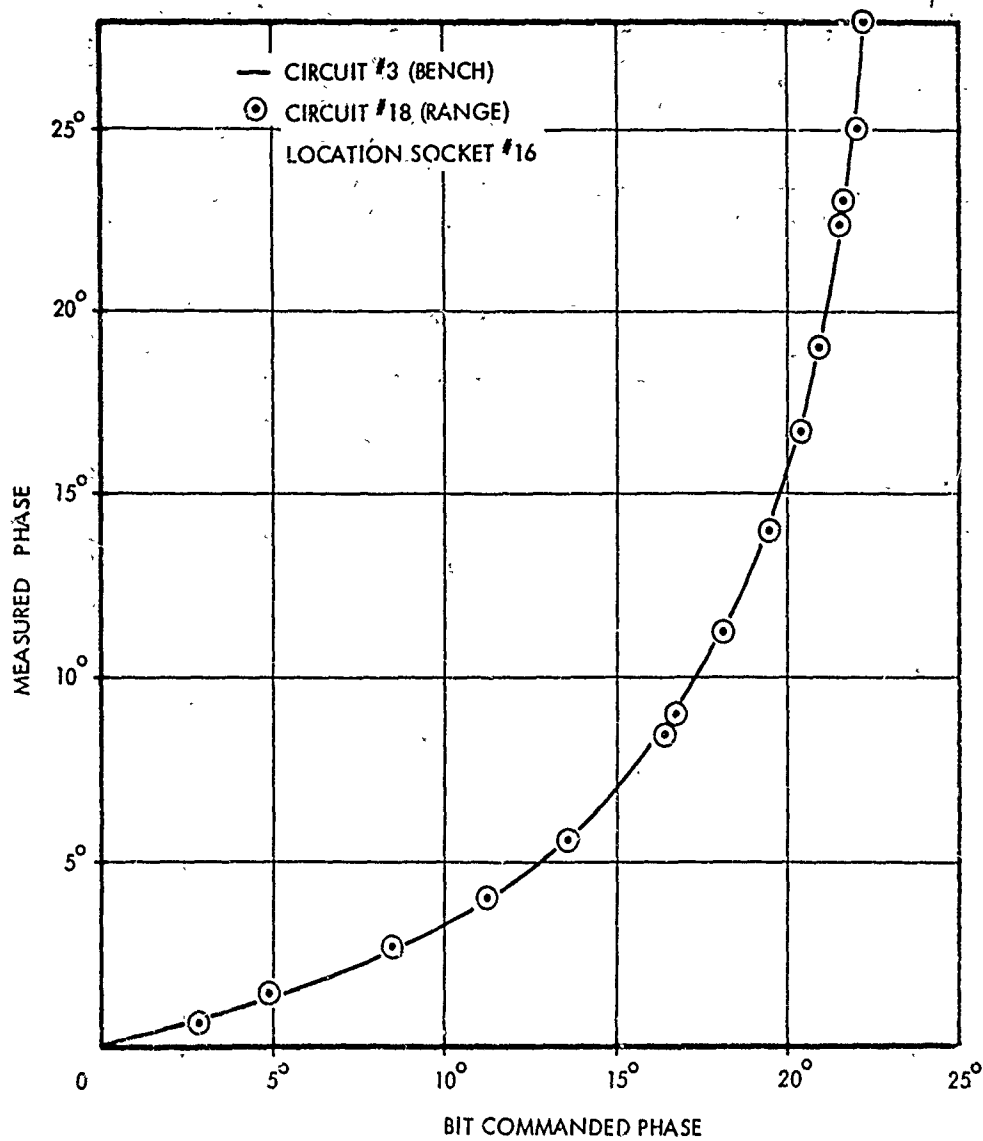
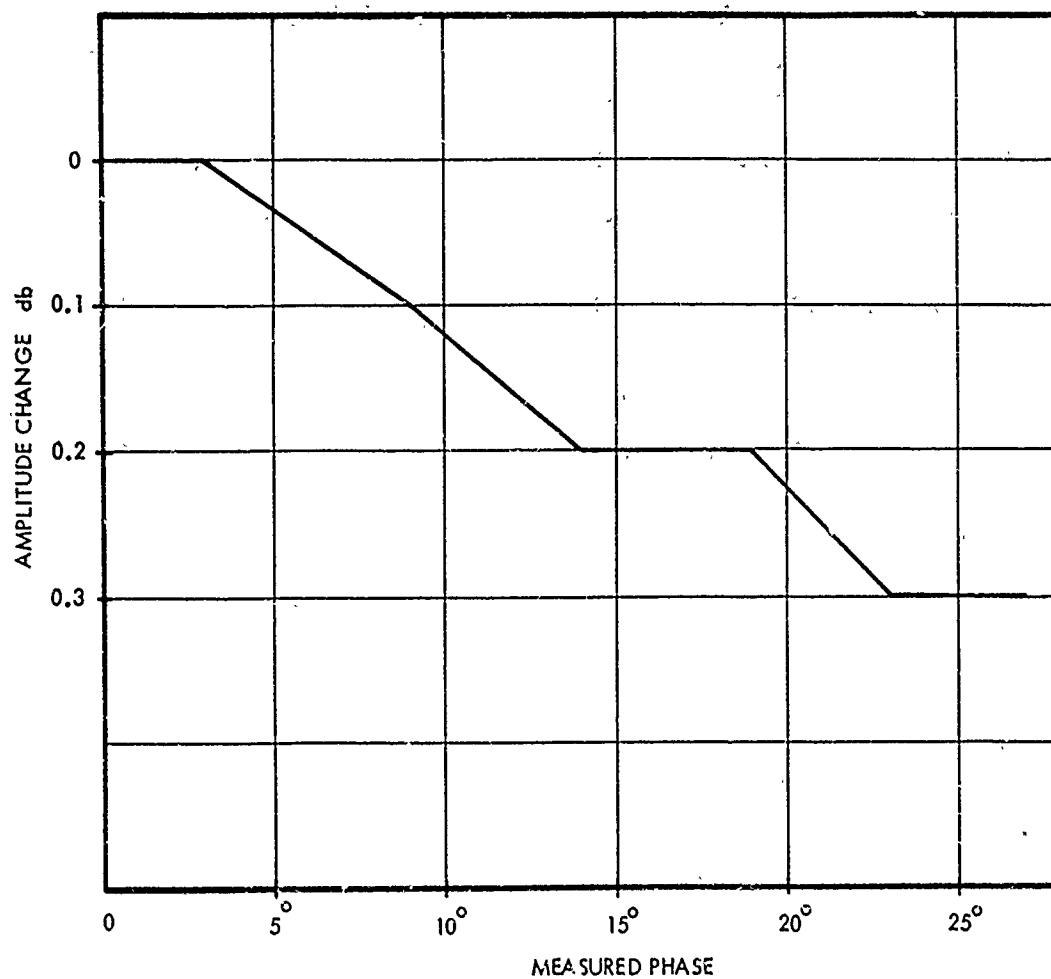Figure E2.2-1 Bit Commanded Phase vs. Measured Phase
(Analog Phase Shifter)

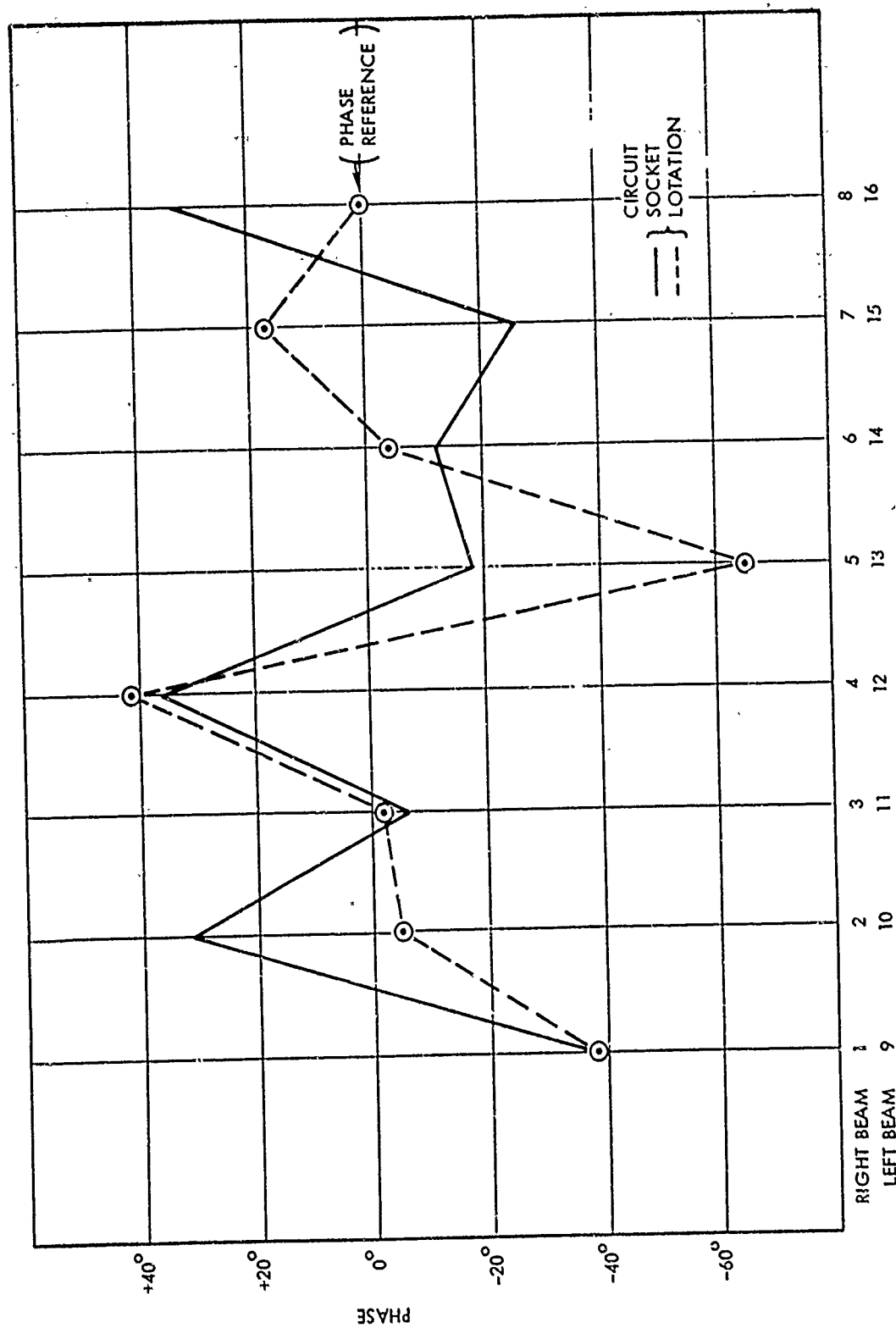Figure E2.2-2   Measured Phase vs. Amplitude Change
(Analog Phase Shifter)

Figure E2.3-1 0° Bit State Insertion Phase

Figure E2.3-2 is a plot of the phase shifters 0° bit state insertion loss, referenced the phase shifter located in socket 16. The phase shifter located in socket 13 had high insertion amplitude when measured and was repaired. The 0° bit state insertion loss measurements were used in the computer simulation.

E3   Antenna Measurement Configuration

Figure E3-1 is the block diagram of the antenna measurement configuration and reference geometry. The array was aligned to the reference geometry then mechanically attached to the positioner. The antenna beams and nulls were steered by the Datacraft 6024 software. Scientific Atlanta receiving and recording equipment was used to record the antenna pattern as the array was rotated. The 300 MHz array outputs were the outputs of the sum and difference circuit. A C-band standard gain horn was used as the transmitter source driven by a microwave amplifier.
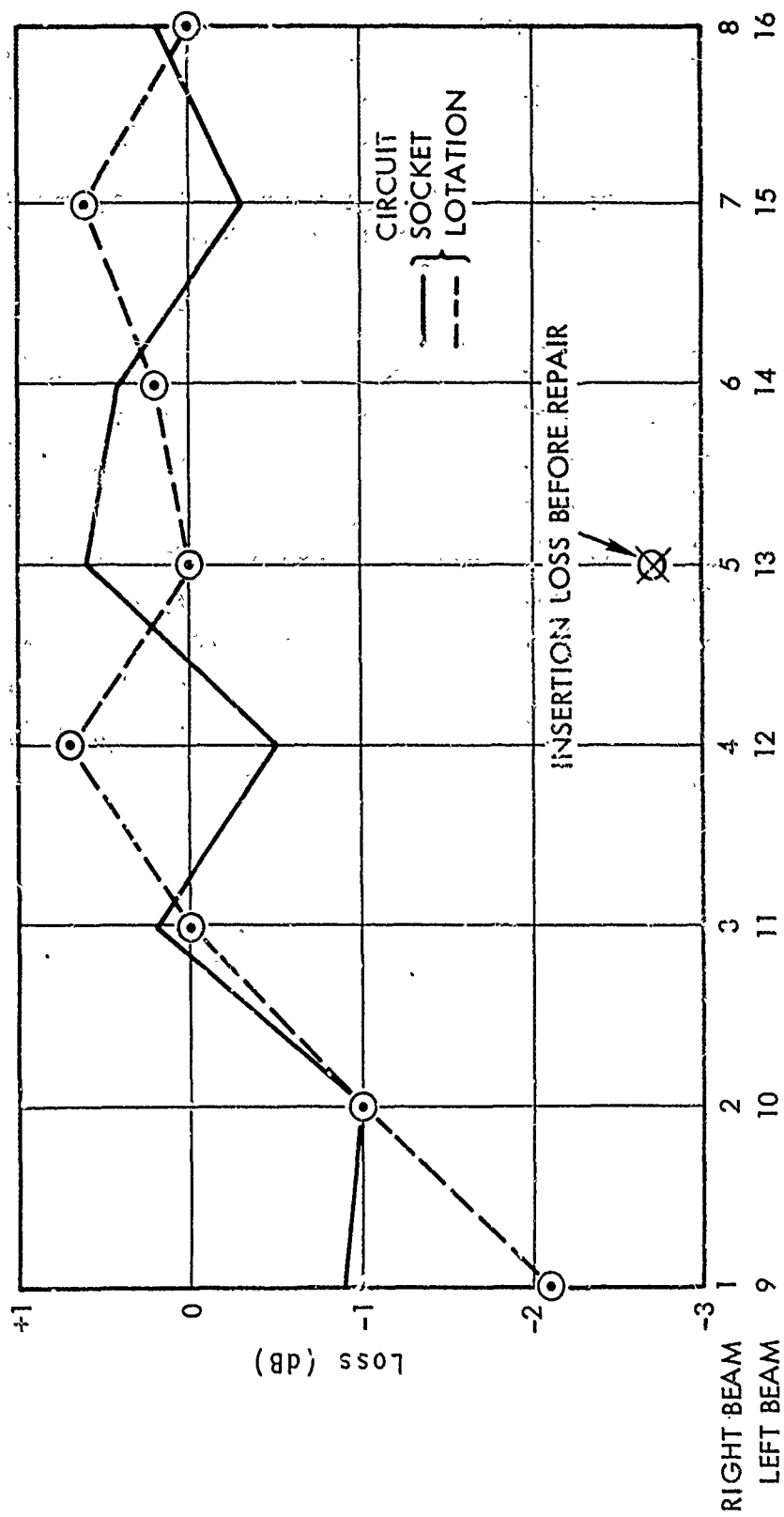
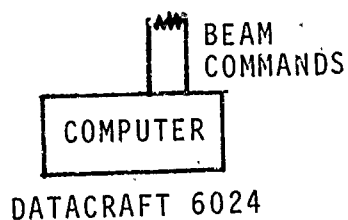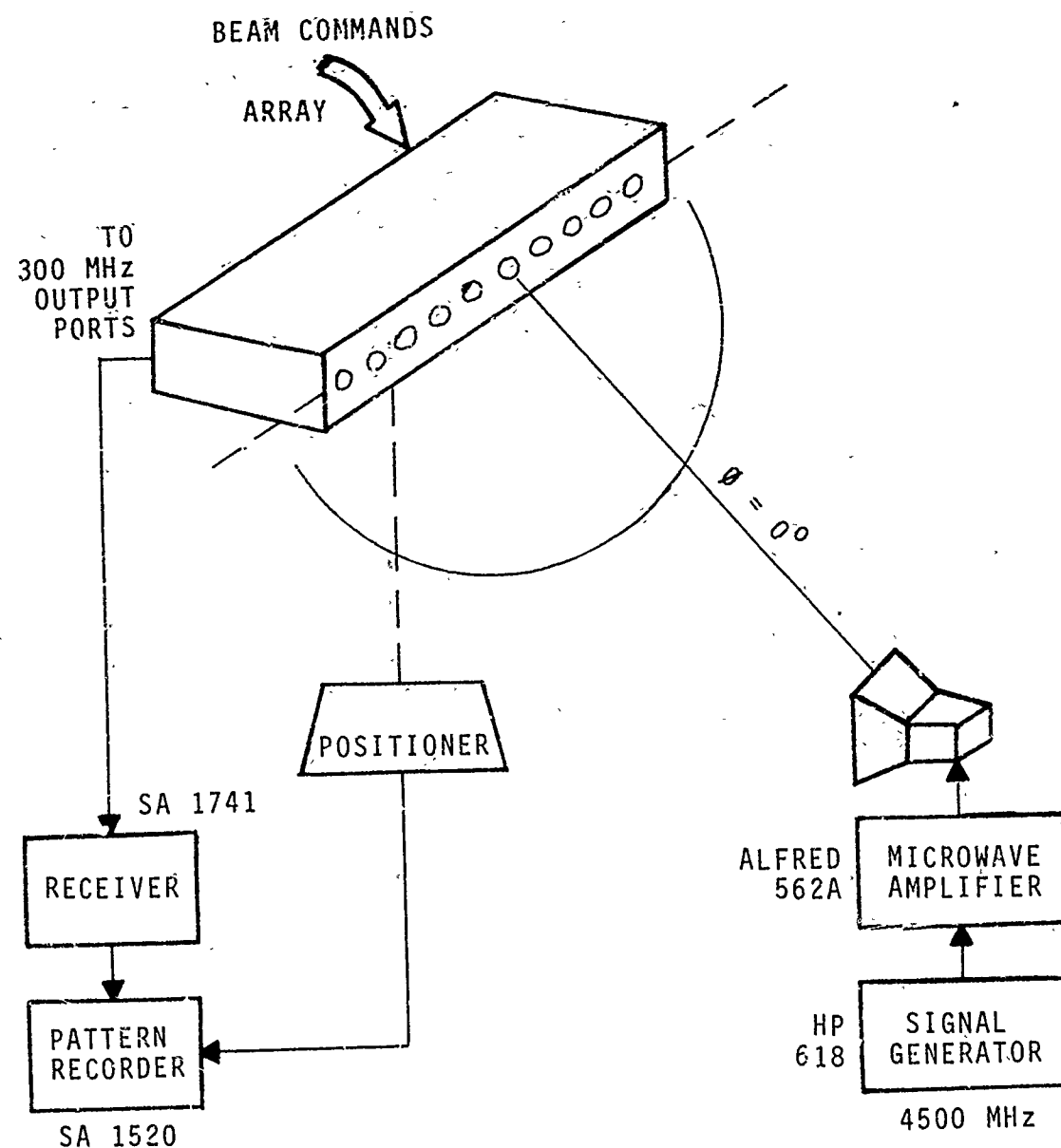Figure E2.3-2 0^0 Bit State Insertion loss

BEAM COMMANDS

ARRAY

TO
300 MHz
OUTPUT
PORTS

$\theta = 0^\circ$

POSITIONER

SA 1741

RECEIVER

ALFRED | MICROWAVE
562A | AMPLIFIER

PATTERN
RECORDER

HP | SIGNAL
618 | GENERATOR

SA 1520

4500 MHz

BEAM
COMMANDS

COMPUTER

Figure E3-1 Antenna Measurement
Configuration

DATACRAFT 6024

229

MISSION
of
Rome Air Development Center

RADC plans and conducts research, exploratory and advanced
development programs in command, control, and communications
(C^3) activities, and in the C^3 areas of information sciences
and intelligence. The principal technical mission areas
are communications, electromagnetic guidance and control,
surveillance of ground and aerospace objects, intelligence
data collection and handling, information system technology,
ionospheric propagation, solid state sciences, microwave
physics and electronic reliability, maintainability and
compatibility.